CFD Simulations of a Regenerative Process for Carbon Dioxide Capture in Advanced Gasification Based Power Systems

Final Scientific / Technical Report

August 1, 2010 – July 31, 2014

By

Hamid Arastoopour
Javad Abbasian

Work Performed Under Contract No. DE-FE0003997

For
U.S. Department of Energy
National Energy Technology Laboratory
P.O. Box 10940, Mail Stop 922-273C
626 Cochrans Mill Road
Pittsburgh, PA 15236-0940

By
Illinois Institute of Technology
3300 South Federal Street
Chicago, IL 60616-3793

Revision number1, Revision Date: April 13, 2016

DISCLAIMER

This report was prepared by Illinois Institute of Technology (IIT) as an account of work sponsored by the United States Government. Neither IIT, nor the United States, nor the National Energy Technology Laboratory (NETL), nor any of their employees, makes any warranty, expressed or implied, or assumes any legal liability or responsibility for the accuracy, completeness or usefulness of any information, apparatus, product, or process disclosed, or represents that its use would not infringe privately owned rights. Reference herein to any specific commercial product, process, or service by trade name, mark, manufacturer, or otherwise, does not necessarily constitute or imply its endorsement, recommendation, or favoring by the United States Government or any agency thereof. The views and opinions of authors expressed herein do not necessarily state or reflect those of the United States Government or any agency thereof.

ABSTRACT

This project describes the work carried out to prepare a highly reactive and mechanically strong MgO based sorbents and to develop a Population Balance Equations (PBE) approach to describe the evolution of the particle porosity distribution that is linked with Computational Fluid Dynamics (CFD) to perform simulations of the CO_2 capture and sorbent regeneration.

A large number of MgO-based regenerable sorbents were prepared using low cost and abundant dolomite as the base material. Among various preparation parameters investigated the potassium/magnesium (K/Mg) ratio was identified as the key variable affecting the reactivity and CO_2 capacity of the sorbent. The optimum K/Mg ratio is about 0.15. The sorbent formulation HD52-P2 was identified as the "best" sorbent formulation and a large batch (one kg) of the sorbent was prepared for the detailed study. The results of parametric study indicate the optimum carbonation and regeneration temperatures are 360° and 500°C, respectively. The results also indicate that steam has a beneficial effect on the rate of carbonation and regeneration of the sorbent and that the reactivity and capacity of the sorbent decreases in the cycling process (sorbent deactivation). The results indicate that to achieve a high CO_2 removal efficiency, the bed of sorbent should be operated at a temperature range of 370-410°C which also favors production of hydrogen through the WGS reaction.

To describe the carbonation reaction kinetics of the MgO, the Variable Diffusivity shrinking core Model (VDM) was developed in this project, which was shown to accurately fit the experimental data. An important advantage of this model is that the changes in the sorbent conversion with time can be expressed in an explicit manner, which will significantly reduce the CFD computation time.

A Computational Fluid Dynamic/Population Balance Equations (CFD/PBE) model was developed that accounts for the particle (sorbent) porosity distribution and a new version of the method of moments, called Finite size domain Complete set of trial functions Method Of Moments (FCMOM) was used to solve the population balance equations. The PBE model was implemented in a commercial CFD code, Ansys Fluent 13.0. The code was used to test the model in some simple cases and the results were verified against available analytical solution in the literature. Furthermore, the code was used to simulate CO_2 capture in a packed-bed and the results were in excellent agreement with the experimental data obtained in the packed bed. The National Energy Laboratory (NETL) Carbon Capture Unit (C2U) design was used in simulate of the hydrodynamics of the cold flow gas/solid system (Clark et al.[58]). The results indicate that the pressure drop predicted by the model is in good agreement with the experimental data. Furthermore, the model was shown to be able to predict chugging behavior, which was observed during the experiment.

The model was used as a base-case for simulations of reactive flow at elevated pressure and temperatures. The results indicate that by controlling the solid circulation rate, up to 70% CO_2 removal can be achieved and that the solid hold up in the riser is one of the main factors controlling the extent of CO_2 removal. The CFD/PBE simulation model indicates that by using a simulated syngas with a composition of 20% CO_2, 20% H_2O, 30% CO, and 30% H_2, the composition (wet basis) in the reactor outlet corresponded to about 60% CO_2 capture with and exit gas containing 65% H_2.

A preliminary base-case-design was developed for a regenerative MgO-based pre-combustion carbon capture process for a 500 MW IGCC power plant. To minimize the external energy requirement, an extensive heat integration network was developed in Aspen/HYSYS® to produce the steam required in the regenerator and heat integration. In this process, liquid CO_2 produced at 50 atm can easily be pumped and sequestered or stored. The preliminary economic analyses indicate that the estimated cost of carbon

capture is in the range of $31-$44/ton, suggesting that a regenerative MgO-Based process can be a viable option for pre-combustion carbon dioxide capture in advanced gasification based power systems.

TABLE OF CONTENTS

NOMENCLATURE

C_n	Coefficients in the size distribution function series expansion
C_e	Equilibrium CO_2 concentration
C_i	Concentration at reaction interface
D	Diffusivity
d_p	Particle diameter
E_{mni}	Coefficients in the moment equations
f	Number density function
$\overline{f}$	Dimensionless number density function
F_{mni}	Coefficients in the moment equations
K	Constant in the growth rate law
k	Reaction rate constant,
k_s	Conductivity of solid fluctuating
K_e	WGS equilibrium constant
K_s	Surface reaction rate
$\dot{m}$	Interface mass transfer
N^o_{MgO}	Initial number of moles of MgO, mole/m^3
p	Pressure
p_s	Solid phase pressure
r_{icarb}	Rate of species i in carbonation reaction
r_{iWSR}	Rate species I in water shift reaction
R	Particle radius
Re	Reynolds number
Re_p	particle Reynolds number
R_i	Rate of reaction of species i

S	Source term in PBE
t	Time
v	Velocity
u	Superficial velocity
X	Conversion
y_i	Mole fraction
Z	Expansion factor

Greek symbols

β	Aggregation kernel
β_0	Aggregation constant
β_{kj}	Drag coefficient between k phase and j phase
ε	Volume fraction
μ_i	i^{th} moment of the number density function
μ	Viscosity
η	Second internal coordinate in Smoluchowski equation
ξ	Internal coordinate in PBE
$\bar{\xi}$	Dimensionless internal coordinate in PBE
Υ_s	Collisional dissipation
ρ	Density
τ	Stress tensor
θ	Granular temperature
ϕ_n	Trial function associated with Legendre polynomials

EXECUTIVE SUMMARY

Advanced power generation technologies such as Integrated Gasification-Combined Cycle (IGCC) are among the leading contenders for power generation conversion in the 21st century, because such processes offer significantly higher efficiencies and superior environmental performance, compared to coal combustion processes. It is envisioned that these advanced systems can competitively produce low-cost electricity while achieving "near-zero discharge" energy plants, if the environmental concerns associated with these processes, including the climate change, can be effectively eliminated at competitive costs.

The commercially available clean-up processes (e.g., SELEXOL) operate at low temperatures, imparting a severe energy penalty on the system and, consequently, their use could significantly increase the costs of electricity production. Therefore, development of high temperature regenerative processes based on solid sorbents offer an attractive alternative option for carbon capture, at competitive costs. Computational Fluid Dynamics (CFD) provides an option to approach the reactor design in a systematic and economically feasible way. However, in order to use CFD to perform simulations of the CO_2 capture regenerative process, a model accounting for the variation of the particle porosity and its effects is required. This project describes the work carried out to prepare highly reactive and mechanically strong MgO based sorbents and to develop a Population Balance Equations (PBE) approach to describe the evolution of the particle porosity distribution and is linked with CFD to perform simulations of the CO_2 capture and sorbent regeneration.

To determine the optimum range of sorbent particle diameter, samples of the original sorbent in five different particle size ranges were prepared. The results of fluidization tests indicated that severe to moderate slugging occurs for the cuts smaller than 150-180μm. Therefore, the 150-180μm cut was selected for further investigation. Since it is known that half-calcined dolomite is generally not reactive toward CO_2, half-calcined dolomite was impregnated with potassium carbonate. The effects of various preparation parameters on the reactivity were studied and the potassium/magnesium (K/Mg) ratio was identified as the key variable affecting the CO_2 capacity of the sorbent. The result clearly indicates that the optimum K/Mg ratio is about 0.15. Furthermore, the optimum drying temperature during sorbent preparation appears to be in the range of 70°-100°C, while the optimum recalcination temperature is around 500°C. Based on the results obtained in this study, the sorbent formulation HD52-P2 was identified as the "best" sorbent formulation and a large batch (one kg) of the HD52-P2 sorbent was prepared for the detailed study.

The results of parametric study indicate that the rate of carbonation of the sorbent improves with increasing temperature in the range of 340° to 450°C, above which, thermodynamic equilibrium limitation results in lower reaction rate at higher temperatures. The order of the carbonation reaction with respect to CO_2 concentration was determined to be one with an activation energy of 134 kJ/mol. The results of carbonation tests also indicate that the presence of steam significantly enhances the sorbent reactivity and capacity and that the highest impact of steam occurs 360˚C.

To describe the carbonation reaction kinetics of MgO, the variable diffusivity shrinking core model (VDM) was developed in this project, which was shown to accurately fit the experimental data. An important advantage of this model is that the changes in the sorbent conversion with time can be expressed in an explicit manner, which will significantly reduce the CFD computation time.

The effect of operating variables on the sorbent regeneration was also investigated and the results indicate that, as expected, the reactivity of the regeneration reaction improves with increasing temperature (i.e. between 450° to 550°C). Furthermore, the results also indicate that steam has a beneficial effect on the rate of decomposition reaction, while the presence of CO_2 significantly decreases the rate and the extent

of regenerability of the sorbent. The long-term durability of the sorbent was investigated over several consecutive absorption/regeneration cycles, and the results indicate that the reactivity and capacity of the sorbent decreases in the cycling process (sorbent deactivation). Furthermore, the results indicate that the sorbents exposure to a higher regeneration temperature expedites the sorbent deterioration in the cyclic process. A number of tests were conducted in the lab-scale packed-bed reactor to evaluate the long-term durability of the sorbents and determine the catalytic activity of sorbent in the Water-Gas-Shift (WGS) reaction. The results indicate that to achieve a high CO_2 removal efficiency, the bed of sorbent should be operated at a temperature range of 370-410°C which is also favors production of hydrogen through the WGS reaction.

A computational fluid dynamic/population balance equations (CFD/PBE) model was developed in this project that accounts for the particle (sorbent) porosity distribution and of a numerical technique was developed to solve the CFD/PBE model. The population balance equation (PBE) is a balance equation, which accounts for the spatial and temporal evolutions of particulate phase internal variable, ξ, distribution function in a single control volume. Among the various available methods for solving the PBE, Method Of Moments (MOM) has received a lot of attention due to its relatively low computational costs. A new version of MOM called Finite size domain Complete set of trial functions Method Of Moments (FCMOM) was used to solve the population balance equations. In the formulation of PBE for CO_2 sorption process using solid sorbents the ξ_{min} and ξ_{max} can be considered as the density of fresh sorbent and the density of the sorbent with complete conversion, respectively. The PBE model was implemented in a commercial CFD code, ANSYS/ Fluent 13.0. The code was used to test the model in some simple cases and the results were verified against available analytical solution in the literature. Furthermore, the code was used to simulate CO_2 capture in a packed-bed and the results were in excellent agreement with the experimental data obtained in the packed bed.

To assess the performance of the sorbent for capturing CO_2 in a regenerative process and to provide a base case design for a circulating fluidized bed reactor, we used the NETL Carbon Capture Unit (C2U) design as our starting point to simulate the hydrodynamics of the cold flow gas/solid system. The results indicate that the pressure drop predicted by the model is in good agreement with the experimental data. Furthermore, the model was shown to be able to predict chugging behavior, which was observed during the experiment.

Following the cold flow simulations of the riser section of the NETL C2U circulating fluidized bed using our 3D Eulerian-Eulerian CFD model, the model was used as a base-case for simulations of reactive flow at elevated pressure and temperatures. To investigate the effect of different operating conditions on the CO_2 capture performance a set of simulations were performed at different solid circulating rates and also different reaction rates. In all the cases, gas inlet velocity was kept constant. The results indicate that at baseline condition the CO_2 removal is less than 15% and that by increasing the solid circulation rate by CO_2 removal increased to 70%, indicating that the solid hold up in the riser is one of the main factors controlling the extent of CO_2 removal. This can be attributed to the denser solid flow in the lower part of the riser and also denser solid flow in the transport zone. Following the implementation of the carbonation reaction in the model, the performance of the MgO-based solid sorbent in the sorbent enhanced water gas shift (SEWGS) reaction was studied by using a simulated syngas with a composition of 20% CO_2, 20% H_2O, 30% CO, and 30% H_2. The composition (wet basis) in the reactor outlet containing 65% H_2 corresponded to about 60% CO_2 capture. The model was also used to simulate a batch regeneration reactor in the process, using steam as the regeneration medium. The results indicate that the sorbent can be fully regenerated at 550°C in about 4 minutes.

A preliminary base-case-design was developed for a regenerative MgO-based pre-combustion carbon capture process that can be incorporated in a 500 MW Integrated Gasification Combined Cycle (IGCC) power plant. The coal used for this purpose is a typical Illinois #6 bituminous coal. To minimize the

external energy (e.g., natural gas) requirement of the process, an extensive heat integration network was developed in Aspen/HYSYS® produce the steam required in the regenerator. In this process, liquid CO_2 is produced at 50 atm, which can easily be pumped and sequestered or stored.

In the preliminary economic analyses performed in this project, the cost associated with the process consisted of operating costs and capital investment costs. The major components of the operating costs included sorbent cost, labor cost, and fuel cost, while the major components of the capital costs included those associated with the carbonators and regenerators and heat integration network. The cost of carbon capture (liquid CO_2 at 50 atm) was determined under three scenarios to range $31-$44/ton, indicating that a regenerative MgO-Based process can be a viable option for pre-combustion carbon dioxide capture in advanced gasification based power systems.

PROGRAM OBJECTIVE

The overall objective of this project is to develop a CFD model and to perform CFD simulations to describe the heterogeneous gas-solid absorption/regeneration and WGS reactions in the context of multiphase CFD for a regenerative magnesium oxide-based (MgO-based) process for simultaneous CO_2 capture and enhancement of H_2 production in coal gasification processes.

The specific objectives are: development of a computational fluid dynamics/population balance equations (CFD/ PBE) model accounting for the particle (sorbent) porosity distribution and of a numerical technique to solve the CFD/PBE model; determination of the key parameters of the absorption/regeneration and WGS reactions; CFD simulations of the regenerative carbon dioxide capture process; and optimization of operating conditions and reactor design.

INTRODUCTION

Coal-fired power plants currently account for about 50% of the electricity used in the United States[1]. With diminishing petroleum supplies, public concern regarding the overall safety of nuclear power, unpredictability of natural gas prices, and unavailability of alternative large-scale sources of energy, coal continues to play a leading role in the total energy picture. Advanced power generation technologies such as Integrated Gasification-Combined Cycle (IGCC) are among the leading contenders for power generation conversion in the 21st century, because such processes offer significantly higher efficiencies and superior environmental performance, compared to coal combustion processes. It is envisioned that these advanced systems can competitively produce low-cost electricity at efficiencies higher than 60% with coal while achieving "near-zero discharge" energy plants, if the environmental concerns associated with these processes, including the climate change, can be effectively eliminated at competitive costs[2].

Near-term applications of CO_2 capture from pre-combustion systems will likely involve physical or chemical absorption processes. However, these commercially available processes (e.g., SELEXOL) operate at low temperatures, imparting a severe energy penalty on the system and, consequently, their use could significantly increase the costs of electricity production. Therefore, development of high temperature regenerative processes based on solid sorbents offer an attractive alternative option for carbon capture, at competitive costs.

The Illinois Institute of Technology (IIT) has developed a regenerative high temperature CO_2 capture process that is capable of removing over 98% of CO_2 from a simulated WGS mixture at IGCC conditions using highly reactive and mechanically strong MgO based sorbents. Furthermore, the sorbent exhibited some WGS catalytic activity at 300°C, increasing hydrogen concentration from 37% (inlet) to about 70% in the reactor exit[3,4]. The results of theoretical modeling of the sorbent/catalyst performance in a packed bed indicated that hydrogen concentration in the simulated WGS mixture can achieve over 95% conversion. The cyclic chemical reactions for CO_2 capture involving magnesium oxide are:

$MgO + CO_2 \Rightarrow MgCO_3$ (CO_2 Absorption Reaction) (A)

$MgCO_3 \Rightarrow MgO + CO_2$ (Regeneration Reaction) (B)

$CO + H_2O \Leftrightarrow CO_2 + H_2$ (Water-Gas-Shift Reaction) (C)

The regenerability and long term durability of the sorbent has been demonstrated over 25 consecutive absorption/regeneration cycles, indicating that the sorbent is suitable for long-term applications. It was also shown that only the outer layer (40-50 μm thick) of the sorbent (particle diameter about 500 μm) reacted with CO_2.[3,5] Therefore, it is expected that by reducing the particle size to about 100-200 μm, the CO_2 absorption capacity of the sorbent can be significantly improved. The results of theoretical modeling of the sorbent/catalyst performance in a packed bed indicated that hydrogen concentration in the simulated WGS mixture can achieve over 95%.

Although the results obtained in the previous study was very promising, design of the process reactors (absorber and regenerator) and their configuration are hindered by the difficulties in design and operation of laboratory scale system to provide meaningful and applicable experimental data for scale up.

Computational Fluid Dynamics (CFD) provides an option to approach the reactor design in a systematic and economically feasible way. However, in order to use CFD to perform simulations of the CO_2 capture regenerative process, a model accounting for the variation of the particle porosity and its effects is required. In this project, a population balance equations approach is used to describe the evolution of the particle porosity distribution and is linked with the multiphase flow dynamics governing equations in order to perform simulations of the CO_2 capture regenerative process, taking into account the absorption/regeneration and the WGS kinetics.

The experimental section of the project will focus on determination of the key parameters needed for the CFD modeling of the absorption/regeneration reactor system. These key parameters include the absorption/regeneration and the WGS reaction rates and their dependence on the operating conditions (i.e., temperature, pressure, gas composition, catalyst/sorbent ratio, etc.).

Typically, in a coal gasification power plant, the coal gas is first cleaned from its contaminants (particulates, sulfur, etc.) and then is passed through the water-gas-shift (WGS) reactor and CO_2 capture unit. In the regenerative process considered in this study, both the WGS reaction and the CO_2 capture by sorbent absorption take place in the absorber. The H_2 rich syngas leaving the absorber can be converted to electrical or thermal power, while the reacted sorbent is regenerated in presence of the regeneration gas (steam), producing a high pressure CO_2 rich stream, which can be sequestered.

In the CFD/PBE model developed in this study, the sorbent porosity is defined by a particle porosity distribution (PPD), such that each sorbent particle (at each time and location inside the reactors) is defined by a different porosity (or density). Therefore, the gas and catalyst phases are described by standard multiphase governing equations,[6-10] while, an original approach is used based on a population balance equations (PBE) governing the evolution of particle porosity distribution is used for the sorbent phase.

WORK PERFORMED

The work performed in this project (August 1, 2010 through July 31, 2014) is summarized

below.

Task 1. Project management and planning

The objective of this task is to revise and maintain the Project Management Plan and to manage and report on activities in accordance with the plan.

The project management plan was prepared and submitted to USDOE on Oct 1, 2010. Reporting on the progress of the project including adherence to the project management plan and results was done on a quarterly basis.

Task 2. Development of a CFD/PBE model accounting for the particle (sorbent) porosity distribution and of a numerical technique to solve the CFD/PBE model

The objective of this task is to develop CFD/PBE model in which the sorbent phase transport phenomena properties will be a function of the particle porosity (density), and to extend the FCMOM numerical technique, used to solve the PBE for CFD/PBE model.

A comprehensive literature survey was initiated to define physical description of a single particle. A simplified version of mathematical model (uniform particles with constant size and density) was evaluated for a similar process to determine the model potential and applicability in simulation of a CO_2 capture process using a solid sorbent in the riser section of a circulating fluidized bed.

Simplified Model

The simplified CFD model is based on a two-dimensional Eulerian-Eulerian approach in combination with the kinetic theory of granular flow (Arastoopour [8,11] and Benyahia et al.,[7]). Other assumptions of our numerical simulation include the isothermal condition for the process, and the ideal gas description of the gas phase. Fluent® 6.3 code was used to solve a set of governing equations including:

Mass conservation

For gas phase: $$\frac{\partial}{\partial t}(\varepsilon_g \rho_g) + \nabla.(\varepsilon_g \rho_g v_g) = \dot{m}_g \quad (1)$$

For solid phase: $$\frac{\partial}{\partial t}(\varepsilon_s \rho_s) + \nabla.(\varepsilon_s \rho_s v_s) = \dot{m}_s \quad (2)$$

Momentum conservation

For gas phase: $$\frac{\partial}{\partial t}(\varepsilon_g \rho_g v_g) + \nabla.(\varepsilon_g \rho_g v_g v_g) = -\varepsilon_g \nabla P + \nabla.\tau_g + \varepsilon_g \rho_g g - \beta_{gs}(v_g - v_s) \quad (3)$$

For solid phase: $$\frac{\partial}{\partial t}(\varepsilon_s \rho_s v_s) + \nabla.(\varepsilon_s \rho_s v_s v_s) = -\varepsilon_s \nabla P + \nabla.\tau_s + \varepsilon_s \rho_s g + \beta_{gs}(v_g - v_s) \quad (4)$$

Species conservation

For gas phase: $$\frac{\partial}{\partial t}(\varepsilon_g \rho_g y_i) + \nabla.(\varepsilon_g \rho_g v_g y_i) = R_j \qquad i=1, 2, 3 \quad (5)$$

For solid phase: $$\frac{\partial}{\partial t}(\varepsilon_s \rho_s y_i) + \nabla.(\varepsilon_s \rho_s v_s y_i) = R_j \qquad i=1, 2, 3 \quad (6)$$

And conservation of solid phase fluctuating energy:

$$\frac{3}{2}[\frac{\partial}{\partial t}(\varepsilon_s \rho_s \theta) + \nabla.(\varepsilon_s \rho_s \theta) v_s] = (-\nabla p_s I + \tau_s) : \nabla v_s + \nabla.(\kappa_s \nabla \theta) - \gamma_s \quad (7)$$

Where κ_s and γ_s are conductivity of fluctuating energy and collisional dissipation of solid fluctuating energy, respectively.

For gas-solid inter-phase exchange coefficient β_{gs} there are different correlations available in the literature. Garg et al.[12] showed that using an EMMS based model as proposed by Li et al., [13] gives better results compared to the drag model proposed by Gidaspow.[14] Nikolopoulos et al.[15] has also shown that EMMS model increased accuracy of simulation at the lower part of riser and results in better prediction for solid concentration and pressure distribution and also is able to account for heterogeneous solid structures and cluster formation in the riser.

The EMMS based drag model has been used in this study as follow:

$$\beta_{sg} = \begin{cases} \frac{3}{4}\frac{(1-\varepsilon_g)\varepsilon_g}{d_p}\rho_g|v_g - v_s|C_{D0}\omega(\varepsilon_g) & \varepsilon > 0.74 \quad (8a) \\ 150\frac{(1-\varepsilon_g)^2\mu_g}{\varepsilon_g d_p{}^2} + 1.75\frac{(1-\varepsilon_g)\rho_g|v_g - v_s|}{d_p} & \varepsilon \le 0.74 \quad (8b) \end{cases}$$

Where $\omega(\varepsilon_g)$ which is called heterogeneity factor and defined as

$$\omega(\varepsilon_g) = \begin{cases} -0.5760 + \frac{0.0214}{4(\varepsilon_g - 0.7463)^2 + 0.0044} & 0.74 < \varepsilon_g \le 0.82 \quad (9a) \\ -0.0101 + \frac{0.0038}{4(\varepsilon_g - 0.7789)^2 + 0.0040} & 0.82 < \varepsilon_g \le 0.97 \quad (9b) \\ -31.8295 + 32.8295\varepsilon_g & \varepsilon > 0.97 \quad (9c) \end{cases}$$

And

$$C_{D0} = \frac{24}{\mathrm{Re}_p}(1 + 0.15\,\mathrm{Re}_p{}^{0.687}) \quad \text{for } Re_p<1000 \quad (10a)$$

$$C_{D0} = 0.44 \quad \text{for } Re_p>1000 \quad (10b)$$

In addition, $k-\varepsilon$ turbulent model has been used to take care of turbulent fluctuations of gas-solid mixture.

Simulation results of the simplified CFD model

To simulate the hydrodynamic behavior of the riser, it was assumed that there was no solid in the riser and the concentration of CO_2 was zero at time zero. A second order discretization scheme was used to discretize the governing equations throughout the domain including 34x1200 uniform rectangular cells.

Figure 1. shows contours of CO_2 concentration and solid sorbent volume fraction at the lower part of the riser. Based on the results of our simulation the 2-D Eulerian-Eulerian CFD simulation based on kinetic theory of granular flow in combination with deactivation kinetic model was able to predict the overall hydrodynamic behavior of the system in addition to cluster formations along the riser. Furthermore, the simulation was able to predict CO_2 removal percentage at the riser outlet at different gas flow rate in good

agreement with experimental data. Our simulation was also able to predict the pressure drop in the riser and dependency of the CO_2 conversion to gas flow rate in line with available experimental data.

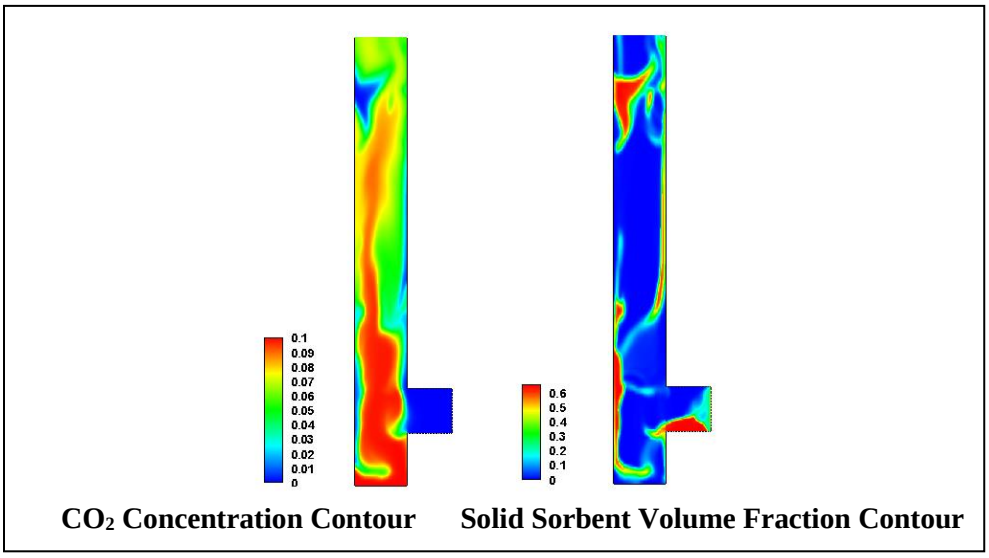

Figure 1. Contours of CO_2 concentration and solid sorbent volume fraction at the lower part of the riser.

The simulation results for the extent of CO_2 removal and sensitivity analysis of the model to the changes in gas flow rate and pressure drop along the riser are presented below. Simulations were performed for 200 seconds of the processing time and, as it takes about 90 seconds for the solid inventory in the riser to become stable, the first 100 seconds of the simulations were not considered in the calculation of the time averaged results. Our results were compared with the experimental data of KIER provided by Yi et al. [19]. In the experiments a very slender 2.5 cm ID and 6 m height riser, with an expanded 3.5 cm ID mixing zone at the first 0.6 m of the bottom of the riser as the absorber and a 10 cm ID and 1.28 m height bubbling bed as the regenerator reactor, were used. Differential pressure was measured at four different elevations along the riser. In addition, CO_2 concentration at the riser outlet was monitored continuously. In this study, our focus has been on the simulation of the riser and the carbonation (absorption) process. Figure 2 shows the simulated axial profile of time averaged CO_2 mass fraction and CO_2 removal percentage at the different elevations in the riser at the baseline operating condition. The CO_2 removal percentage at the outlet of the riser is 58%, which is very close to the reported 54% removal in the experimental data.

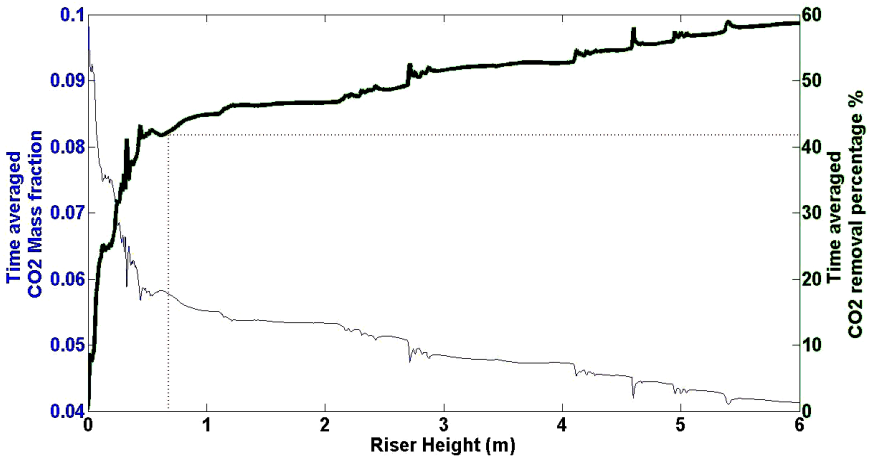

Figure 2. Simulated time averaged CO_2 mass fraction and CO_2 removal percentage

In addition, the axial profile of the time averaged CO_2 mass fraction showed that about 60% of CO_2 removal takes place in the first 0.6 m of rise (mixing zone), which is due to the higher solid concentration and solid circulation in this region. Furthermore, the effect of gas flow rate on the percentage of CO_2 removal has been investigated. The results showed that the increasing inlet gas flow rate (inlet gas velocity) decreases the CO_2 removal percentage, which is in-line with the experimental data. The higher gas flow rate means shorter residence time, which results in reduction of surface time, τ, in the Deactivation Kinetic Model and, in turn, increases the deactivation factor and decreases the CO_2 removal (see Figure 3). Moreover, our model was able to capture the sensitivity of the CO_2 removal process to the gas flow rate much better than Garg et al., [12] who used the homogeneous reaction model. Sensitivity of CO_2 removal to the changes in the solid circulation rate was also investigated. As was expected, increasing the solid circulation rate resulted in increased CO_2 removal percentage. Similar to the experimental data and the simulation of Garg et al.,[12] the results of our simulation were also sensitive to the variations in the solid circulation rate.

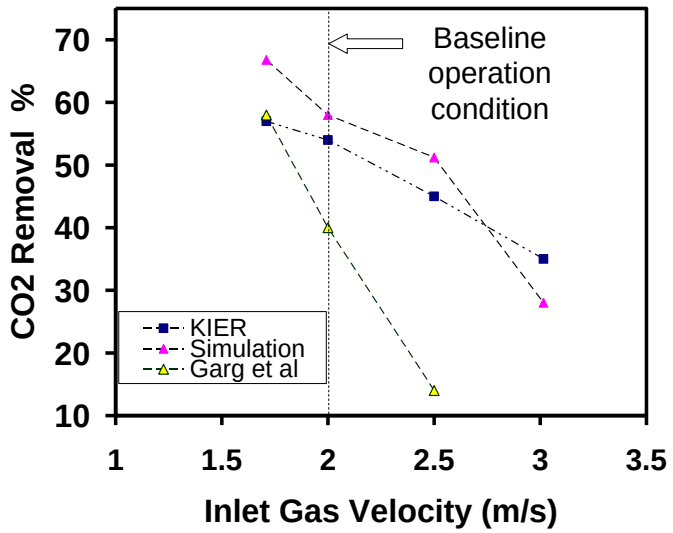

Figure 3. Effect of inlet gas velocity on CO_2 removal percentage

Table 1 shows the comparison between the pressure drop predicted using our simulation with the experimental results of Yi et al.,[19] at 4 different elevations of 0.52 m, 2.27 m, 4.07 m, and 5.87 m which are referred to as DP1, DP2, DP3, and DP4, respectively. Our simulation closely predicted the pressure drop over the DP1, DP2, and DP4 sections and over predicts the pressure drop over the DP3 section. This can be attributed to the sudden reduction over the DP2 and DP3 sections at around the 11th hour of operation that remains up to the end of the experiment. This reduction in pressure drop is apparently due to an undisclosed change in the operating condition that cannot be implemented in our simulation. Another possible reason can be due to the inaccuracy of the EMMS drag model in predicting a wide range of solid phase concentration and heterogeneities.

Table 1. Differential pressure at different elevations

	Differential Pressure (mm H_2O) KIER Experiments, Yi et al [19]	Differential Pressure, (mm H_2O) Simulation
DP1	100	107
DP2	200-500	335
DP3	100-210	270
DP4	70	67

Development of the CFD/PBE model

The population balance equation (PBE) is a balance equation based on the number density function $f(\boldsymbol{\xi}; \mathbf{x}, t)$ accounts for the spatial and temporal evolutions of particulate phase internal variable, $\boldsymbol{\xi}$, distribution function in a single control volume. For an inhomogeneous particulate system the governing equation is (Randolph and Larson:[20]

$$\frac{\partial f(\boldsymbol{\xi};\mathbf{x},t)}{\partial t} + \frac{\partial}{\partial x_i}[u_p(t,\mathbf{x})\, f(\boldsymbol{\xi};\mathbf{x},t)] + \frac{\partial}{\partial x_i}[D_{pt}(\boldsymbol{\xi};\mathbf{x},t)\frac{\partial f(\boldsymbol{\xi};\mathbf{x},t)}{\partial x_i}] + \frac{\partial}{\partial \xi_j}[\frac{\partial \xi_j}{\partial t}\, f(\boldsymbol{\xi};\mathbf{x},t)] = h(\boldsymbol{\xi};\mathbf{x},t) \tag{11}$$

The terms in the left hand side are accumulation term, convective term, diffusive term and convective term with respect to the internal coordinate, respectively. The source term $h(\boldsymbol{\xi};\mathbf{x},t)$ in the right hand side accounts for the net rate of introduction of new particles into the system (Hulburt and Katz,[21]). D_{pt} is the turbulent diffusivity and $\frac{\partial \xi_j}{\partial t}$ term is the flux in $\boldsymbol{\xi}$-*space* (Marchisio et al.,[22,23]), or in other words, the growth rate of internal variable. It is assumed that the sorbent particles are convected with the same sorbent phase velocity $u_p(\mathbf{x},t)$ therefore the sorbent phase convective velocity is independent of the particle density.

Depending on the system of interest, the number density function $f(\xi; x, t)$ may have only one internal coordinate (i.e. particle size or volume) or multiple coordinates such as particle size and surface area (Marchisio et al.,[22,23]). The system of our interest is a monovariate system with the particle density being the only internal coordinate. Ramkrishna[24] and Vanni[25] provide a comprehensive review of the subject of PBE in terms of formulation of PBE, solution techniques, PBE applications, and theoretical considerations. Among the various available methods for solving the PBE, Method of Moments (MOM) has received a lot of attention due to its relatively low computational costs. In this method the key is the formulation of the transport equation in terms of the lower-order moments of the, *f*, in closed form (Marchisio et al.,[22,23]). For a homogeneous system, the k^{th} moment is defined as:

$$\mu_k = \int_0^{\infty} \xi^k . f(\xi; x, t) d\xi \qquad (12)$$

Based on Strumendo and Arastoopour (Strumendo and Arastoopour,[9]) one can summarize the various forms of MOM in four categories.

The first category includes methods in which the functional form of the property (i.e. size) distribution function *f is* assumed while the unknown parameters in *f* are independent of the internal variables and can be computed as a function of the moments. Although in some cases these methods can provide good results and at the same time are not computationally intensive, the obvious drawbacks are that they are not general and they require that the functional form of the distribution function does not change during the process (Strumendo and Arastoopour,[9]).

The second category is represented by the quadrature method of moments (QMOM) where no explicit assumption is made regarding the form of the size distribution function; this technique was first presented by McGraw [26] and later applied different processes by others (Barrett and Webb [27] and Marchisio et al.,[22]). Using this approach, McGraw[26] computed the moments evolution correctly and efficiently (from a computational point of view). Different from the methods of the first category, this method can be considered general since no explicit assumption is made regarding the functional form of *f*. On the other hand, in the QMOM, the solution is given in terms of the moments, while the size distribution function *f* disappears from the governing equations. The reconstruction of the distribution function from the moments (Diemer and Olson,[28,29]), if possible, can be rather complex (Strumendo and Arastoopour, [9)].

The third category includes a version of QMOM called DQMOM (direct quadrature method of moments) which has been proposed by Marchisio and Fox [30] for the purpose of overcoming some disadvantages of the QMOM when dealing with: (1) multivariate distributions; (2) systems with a strong dependency of the dispersed phase velocity on the internal variables (Strumendo and Arastoopour, [9]).

Recently, Strumendo and Arastoopour (Strumendo and Arastoopour [9,10,31]) introduced a new version of MOM called Finite size domain Complete set of trial functions Method Of Moments (FCMOM) which could be the fourth category of these methods.

The main advantages of FCMOM compare to the other methods are (Strumendo and Arastoopour, [9]):

1- There is no specific assumption for the size distribution function *f* ;
2- It gives *f* in an explicit form;
3- The computed *f* converges to the solution of the PBE;
4- The convergence is reasonably fast.

Using FCMOM, the solution of the PBE is sought, instead of the [0,∞] range, in the finite interval between the minimum and maximum values of the particle property (i.e. density). The evolution of *f* is tracked by imposing moving boundaries conditions. After reformulating the PBE in the standard interval [−1, 1] by a coordinate transformation as

$$\bar{\xi} = \frac{\{\xi - [\xi_{\min}(t) + \xi_{\max}(t)]/2\}}{[\xi_{\min}(t) + \xi_{\max}(t)]/2} \qquad \text{and} \qquad \bar{\xi} \in [-1,1] \qquad (13)$$

The dimensionless (divided by an appropriate scale factor) size distribution function $\overline{f(\bar{\xi}; x, t)}$ is represented as a series expansion by a complete system of orthonormal functions (i.e. Legendre Polynomials). Writing distribution function in terms of series expansion of *Legendre Polynomials* gives

$$\overline{f'(\bar{\xi},x,t)} \approx \sum_{n=0}^{M-1} c_n(t,x)\phi_n(\bar{\xi}) \tag{14}$$

While coefficients c_n can be expressed in terms of the moments as:

$$c_n = \sqrt{\frac{2n+1}{2}}.\frac{1}{2^n}.\sum_{v=0}^{n}(-1)^{n-v}.\frac{(2v)!}{[(2v-n)!]}.\{\frac{1}{[(n-v)!].[(v)!]}\}.\mu_{2v-n} \tag{15}$$

Where the terms with negative moments order are to be omitted (Strumendo and Arastoopour, [10]), and $\phi_n(\bar{\xi})$ are the orthonormal functions associated with the Legendre polynomials $P_n(\bar{\xi})$ as:

$$\phi_n(\bar{\xi}) = \sqrt{\frac{2n+1}{2}}.P_n(\bar{\xi}) \tag{16}$$

Then the moments evolution equations can be developed from the PBE in the interval [−1, 1] as follow (Strumendo and Arastoopour, [9,10]):

$$\frac{\partial \mu_i}{\partial t} + \mu_i \frac{\partial v_{p,j}}{\partial x_j} + v_{p,j}\frac{\partial \mu_i}{\partial x_j} - \frac{\partial}{\partial x_j}[\int_{-1}^{+1} D'_{pt}\frac{\partial \overline{f'}}{\partial x_j}(\bar{\xi})^i d\bar{\xi}] = \\ -(MB + MB_{Conv} + MB_{Diff\,1} + MB_{Diff\,2} + MB_{Diff\,3} + IG) + S \tag{17}$$

A detailed explanation of the FCMOM method and derivation of the governing equations can be found in the literature (Strumendo and Arastoopour [9,10, 31]). In the right hand side of the moments evolution equations, *S* is the integral source term due to the introduction of new particles into the system. The first five terms are due to the coordinate transformation and the *IG* is due to the *Integration* of property (i.e. density) *Growth* term. These terms are as follow:

$$MB = -\{[\overline{f'_{+1}} - (-1)^i.\overline{f'_{-1}}] - i.\mu_{i-1}\}.\frac{1}{(\xi_{\max} - \xi_{\min})}.(\frac{d\xi_{\min}}{dt} + \frac{d\xi_{\max}}{dt}) \\ -\{[\overline{f'_{+1}} - (-1)^{i+1}.\overline{f'_{-1}}] - (i+1).\mu_i\}.\frac{1}{(\xi_{\max} - \xi_{\min})}.(-\frac{d\xi_{\min}}{dt} + \frac{d\xi_{\max}}{dt}) \tag{18}$$

$$MB_{Conv} = -\{[\overline{f'_{+1}} - (-1)^i.\overline{f'_{-1}}] - i.\mu_{i-1}\}.\frac{v_{p,j}}{(\xi_{\max} - \xi_{\min})}.(\frac{\partial\xi_{\min}}{\partial x_j} + \frac{\partial\xi_{\max}}{\partial x_j}) \\ -\{[\overline{f'_{+1}} - (-1)^{i+1}.\overline{f'_{-1}}] - (i+1).\mu_i\}.\frac{v_{p,j}}{(\xi_{\max} - \xi_{\min})}.(-\frac{\partial\xi_{\min}}{\partial x_j} + \frac{\partial\xi_{\max}}{\partial x_j}) \tag{19}$$

$$MB_{Diff\,1} = \frac{1}{(\xi_{\max} - \xi_{\min})}(\frac{\partial\xi_{\min}}{\partial x_j} + \frac{\partial\xi_{\max}}{\partial x_j})\int_{-1}^{+1}\frac{\partial D'_{pt}}{\partial x_j}\frac{\partial\overline{f'}}{\partial\bar{\xi}}(\bar{\xi})^i d\bar{\xi} + \\ \frac{1}{(\xi_{\max} - \xi_{\min})}(-\frac{\partial\xi_{\min}}{\partial x_j} + \frac{\partial\xi_{\max}}{\partial x_j})\int_{-1}^{+1}\frac{\partial D'_{pt}}{\partial x_j}\frac{\partial\overline{f'}}{\partial\bar{\xi}}(\bar{\xi})^{i+1} d\bar{\xi} \tag{20}$$

$$MB_{Diff\,2} = \frac{2}{(\xi_{\max} - \xi_{\min})}\left(\frac{\partial \xi_{\min}}{\partial x_j} + \frac{\partial \xi_{\max}}{\partial x_j}\right)\int_{-1}^{+1} D'_{pt}\,\frac{\partial^2 \overline{f'}}{\partial x_j \partial \bar{\xi}}(\bar{\xi})^i\, d\bar{\xi} +$$

$$\frac{2}{(\xi_{\max} - \xi_{\min})}\left(-\frac{\partial \xi_{\min}}{\partial x_j} + \frac{\partial \xi_{\max}}{\partial x_j}\right)\int_{-1}^{+1} D'_{pt}\,\frac{\partial^2 \overline{f'}}{\partial x_j \partial \bar{\xi}}(\bar{\xi})^{i+1} d\bar{\xi} -$$

$$\frac{1}{(\xi_{\max} - \xi_{\min})^2}\left[\left(\frac{\partial \xi_{\min}}{\partial x_j} + \frac{\partial \xi_{\max}}{\partial x_j}\right)\right]^2 \int_{-1}^{+1} D'_{pt}\,\frac{\partial^2 \overline{f'}}{\partial \bar{\xi}^2}(\bar{\xi})^i\, d\bar{\xi} -$$

$$\frac{1}{(\xi_{\max} - \xi_{\min})^2}.2.\left(\frac{\partial \xi_{\min}}{\partial x_j} + \frac{\partial \xi_{\max}}{\partial x_j}\right)\left(-\frac{\partial \xi_{\min}}{\partial x_j} + \frac{\partial \xi_{\max}}{\partial x_j}\right)\int_{-1}^{+1} D'_{pt}\,\frac{\partial^2 \overline{f'}}{\partial \bar{\xi}^2}(\bar{\xi})^{i+1} d\bar{\xi} -$$

$$\frac{1}{(\xi_{\max} - \xi_{\min})^2}\left(-\frac{\partial \xi_{\min}}{\partial x_j} + \frac{\partial \xi_{\max}}{\partial x_j}\right)^2 \int_{-1}^{+1} D'_{pt}\,\frac{\partial^2 \overline{f'}}{\partial \bar{\xi}^2}(\bar{\xi})^{i+2} d\bar{\xi} -$$

$$\frac{2}{(\xi_{\max} - \xi_{\min})^2}\left(-\frac{\partial \xi_{\min}}{\partial x_j} + \frac{\partial \xi_{\max}}{\partial x_j}\right)\left(\frac{\partial \xi_{\min}}{\partial x_j} + \frac{\partial \xi_{\max}}{\partial x_j}\right)\int_{-1}^{+1} D'_{pt}\,\frac{\partial \overline{f'}}{\partial \bar{\xi}}(\bar{\xi})^i\, d\bar{\xi} +$$

$$\frac{1}{(\xi_{\max} - \xi_{\min})}\left(\frac{\partial^2 \xi_{\min}}{\partial x_j^{\,2}} + \frac{\partial^2 \xi_{\max}}{\partial x_j^{\,2}}\right)\int_{-1}^{+1} D'_{pt}\,\frac{\partial \overline{f'}}{\partial \bar{\xi}}(\bar{\xi})^i\, d\bar{\xi} -$$

$$\frac{1}{(\xi_{\max} - \xi_{\min})}.\left[\left(\frac{\partial^2 \xi_{\min}}{\partial x_j^{\,2}} - \frac{\partial^2 \xi_{\max}}{\partial x_j^{\,2}}\right) + \frac{2}{(\xi_{\max} - \xi_{\min})}\left(-\frac{\partial \xi_{\min}}{\partial x_j} + \frac{\partial \xi_{\max}}{\partial x_j}\right)^2\right]\int_{-1}^{+1} D'_{pt}\,\frac{\partial \overline{f'}}{\partial \bar{\xi}}(\bar{\xi})^{i+1} d\bar{\xi} \tag{21}$$

$$MB_{Diff\,3} = \frac{1}{(\xi_{\max} - \xi_{\min})}\left(\frac{\partial \xi_{\min}}{\partial x_j} + \frac{\partial \xi_{\max}}{\partial x_j}\right)\int_{-1}^{+1} \frac{\partial D'_{pt}}{\partial \bar{\xi}}\frac{\partial \overline{f'}}{\partial x_j}(\bar{\xi})^i\, d\bar{\xi} +$$

$$\frac{1}{(\xi_{\max} - \xi_{\min})}\left(-\frac{\partial \xi_{\min}}{\partial x_j} + \frac{\partial \xi_{\max}}{\partial x_j}\right)\int_{-1}^{+1} \frac{\partial D'_{pt}}{\partial \bar{\xi}}\frac{\partial \overline{f'}}{\partial x_j}(\bar{\xi})^{i+1} d\bar{\xi} -$$

$$\frac{1}{(\xi_{\max} - \xi_{\min})^2}\left[\left(\frac{\partial \xi_{\min}}{\partial x_j} + \frac{\partial \xi_{\max}}{\partial x_j}\right)\right]^2 \int_{-1}^{+1} \frac{\partial D'_{pt}}{\partial \bar{\xi}}\frac{\partial \overline{f'}}{\partial \bar{\xi}}(\bar{\xi})^i\, d\bar{\xi} - \tag{22}$$

$$\frac{1}{(\xi_{\max} - \xi_{\min})^2}.2.\left(\frac{\partial \xi_{\min}}{\partial x_j} + \frac{\partial \xi_{\max}}{\partial x_j}\right)\left(-\frac{\partial \xi_{\min}}{\partial x_j} + \frac{\partial \xi_{\max}}{\partial x_j}\right)\int_{-1}^{+1} \frac{\partial D'_{pt}}{\partial \bar{\xi}}\frac{\partial \overline{f'}}{\partial \bar{\xi}}(\bar{\xi})^{i+1} d\bar{\xi} -$$

$$\frac{1}{(\xi_{\max} - \xi_{\min})^2}\left(-\frac{\partial \xi_{\min}}{\partial x_j} + \frac{\partial \xi_{\max}}{\partial x_j}\right)^2 \int_{-1}^{+1} \frac{\partial D'_{pt}}{\partial \bar{\xi}}\frac{\partial \overline{f'}}{\partial \bar{\xi}}(\bar{\xi})^{i+2} d\bar{\xi}$$

and

$$IG = \frac{2}{(\xi_{\max} - \xi_{\min})}.\left\{\left[G'_{+1}\,\overline{f'_{+1}} - (-1)^i.G'_{-1}\,\overline{f'_{-1}}\right] - i.\int_{-1}^{1} G'\,\overline{f'}.(\bar{\xi})^{i-1}.d\bar{\xi}\right\}, \text{ where } G' = \frac{d\bar{\xi}}{dt} \tag{23}$$

In all the above terms, the subscripts of -1 and +1 refer to the value of that term at minimum and maximum limits of the range [-1, +1], respectively.

In general from, Moments evolution equations must be coupled with the moving boundary conditions providing the governing equations for $\xi_{min}(t,\mathbf{x})$ and $\xi_{max}(t,\mathbf{x})$ (Strumendo and Arastoopour,[10]).

The moments evolution equations coupled with the moving boundaries conditions form a set of partial differential equations whose variables are the moments $\mu_i(t,\mathbf{x})$, $\xi_{min}(t,\mathbf{x})$ and $\xi_{max}(t,\mathbf{x})$. The initial conditions for the moments are computed from the initial particle density distribution function. To apply the FCMOM method in the application of interest in this work, to simulate the temporal and spatial evolution of sorbent density distribution, the complexity of the eq. 17 can be reduced by cancellation of some of the terms.

Experimental data in the literature on fresh, carbonated and regenerated sorbent particles in the CO_2 capture process using solid sorbents have shown that the sorbent particle size distribution remains almost constant during carbonation and regeneration processes. However, the density of sorbent particle as a function of particle porosity changes during both sorption and regeneration processes. The structural changes in the particles are due to the reaction between CO_2 and sorbent and lead to the changes in density of particles.

In the formulation of PBE for CO_2 sorption process, using solid sorbents the ξ_{min} and ξ_{max} can be considered as the density of fresh sorbent and the density of the sorbent with complete conversion, respectively. Therefore, the values of these variables are constant and consequently the problem is no more a moving boundary problem. As a result the terms due to the moving boundaries (eq. 18 to 22) will be cancelled out.

Moreover, the assumption of incompressible particle phase set the second term in the left hand side of eq. 17 to zero (Strumendo and Arastoopour, [10]). In addition, in this specific application the source term S in the right hand side of eq. 17 is zero. Considering above mentioned assumptions, the final form of governing equation for evolution of moments becomes;

$$\frac{\partial \mu_i}{\partial t} + \frac{\partial}{\partial x_j}[v_{p,j}\mu_i - D'_{pt}(\bar{\xi},x,t)\frac{\partial \mu_i}{\partial x_j}] = -\frac{2}{(\xi_{max}-\xi_{min})}.\{[G'_{+1}\overline{f'_{+1}} - (-1)^i.G'_{-1}\overline{f'_{-1}}] - i.\int_{-1}^{1} G'\overline{f'}.(\bar{\xi})^{i-1}.d\bar{\xi}\} \quad (24)$$

In eq. 24, G' is the rate of change in the density of sorbent particles which will be determined from the rate of the carbonation and regeneration reactions.

The PBE model was implemented in a commercial CFD code, Ansys Fluent 13.0. The code was used to test the model in some simple cases and the results were verified against available analytical solution in the literature. To derive the final form of Population Balance Equations accounting for the temporal and spatial evolution of the sorbent density distribution, following assumptions have been made:

1- Uniform and constant particle size distribution.
2- Density of the sorbent particles is defined as a function of particle porosity which is changing during the process due to the reaction between the sorbent and the gas phase.
3- Density distribution function is defined in the range of $[\xi_{min}, \xi_{max}]$ and then using a coordinate transform is changed to [-1,+1].

4- Incompressible particle phase ($\mu_i \frac{\partial v_{p,j}}{\partial x_j} = 0$).

5- Constant maximum sorbent density, $\xi_{\max}$, corresponding to the completely reacted sorbent.

6- Variable minimum sorbent density, $\xi_{\min}$, corresponding to the fresh sorbent. The rate of change is related to the rate of reaction.

Considering assumption 6, we need to add two terms to the right hand side of the Equation 24:

to account for the changes in the minimum density value. These two terms are as follow:

$$MB = -\{[\overline{f'_{+1}} - (-1)^i.\overline{f'_{-1}}] - i.\mu_{i-1}\}.\frac{1}{(\xi_{\max} - \xi_{\min})}.(\frac{d\xi_{\min}}{dt} + \frac{d\xi_{\max}}{dt}) \\ -\{[\overline{f'_{+1}} - (-1)^{i+1}.\overline{f'_{-1}}] - (i+1).\mu_i\}.\frac{1}{(\xi_{\max} - \xi_{\min})}.(-\frac{d\xi_{\min}}{dt} + \frac{d\xi_{\max}}{dt}) \quad (25)$$

$$MB_{Conv} = -\{[\overline{f'_{+1}} - (-1)^i.\overline{f'_{-1}}] - i.\mu_{i-1}\}.\frac{v_{p,j}}{(\xi_{\max} - \xi_{\min})}.(\frac{\partial\xi_{\min}}{\partial x_j} + \frac{\partial\xi_{\max}}{\partial x_j}) \\ -\{[\overline{f'_{+1}} - (-1)^{i+1}.\overline{f'_{-1}}] - (i+1).\mu_i\}.\frac{v_{p,j}}{(\xi_{\max} - \xi_{\min})}.(-\frac{\partial\xi_{\min}}{\partial x_j} + \frac{\partial\xi_{\max}}{\partial x_j}) \quad (26)$$

Therefore, the population balance equation in the absence of diffusion term becomes:

$$\frac{\partial\mu_i}{\partial t} + \frac{\partial}{\partial x_j}[v_{p,j}\mu_i] = -\frac{2}{(\xi_{\max} - \xi_{\min})}.\{[G'_{+1}\overline{f'_{+1}} - (-1)^i.G'_{-1}\overline{f'_{-1}}] - i.\int_{-1}^{1} G'\overline{f'}.(\bar{\xi})^{i-1}.d\bar{\xi}\} - \\ \{[\overline{f'_{+1}} - (-1)^i.\overline{f'_{-1}}] - i.\mu_{i-1}\}.\frac{1}{(\xi_{\max} - \xi_{\min})}.(\frac{d\xi_{\min}}{dt}) - \\ \{[\overline{f'_{+1}} - (-1)^{i+1}.\overline{f'_{-1}}] - (i+1).\mu_i\}.\frac{1}{(\xi_{\max} - \xi_{\min})}.(-\frac{d\xi_{\min}}{dt}) - \\ \{[\overline{f'_{+1}} - (-1)^i.\overline{f'_{-1}}] - i.\mu_{i-1}\}.\frac{v_{p,j}}{(\xi_{\max} - \xi_{\min})}.(\frac{\partial\xi_{\min}}{\partial x_j}) - \\ \{[\overline{f'_{+1}} - (-1)^{i+1}.\overline{f'_{-1}}] - (i+1).\mu_i\}.\frac{v_{p,j}}{(\xi_{\max} - \xi_{\min})}.(-\frac{\partial\xi_{\min}}{\partial x_j}) \quad (27)$$

In all the above terms, the subscripts of -1 and +1 refer to the value of that term at minimum and maximum limits of the range [-1, +1], respectively.

Moments evolution equations must be coupled with the moving boundary conditions to provide the governing equations for $\xi_{\min}(t,x)$. When there is a source term due to the reaction, $\xi_{\min}(t,x)$ changes because of the convective particle movement in the presence of spatially inhomogeneous conditions. The definition of the moving boundary conditions for $\xi_{\min}(t,x)$ is based on the evaluation of the following:

(a) The spatial derivatives of $\xi_{\min}(t,x)$.

(b) The velocity $v_{p,\min}(t,x)$ of the particles whose densities are equal to $\xi_{\min}(t,x)$.

The moving boundary condition for $\xi_{\min}(t,x)$ is then given by

$$\frac{\partial \xi_{\min}}{\partial t} = \sum_{i=x,y,z} \left(-\frac{\partial \xi_{\min}}{\partial x_i} v_{p,i,\min}\right) + G \qquad (28)$$

where *G* is the density growth rate due to the reaction.

Implementation in CFD code

In Fluent it is possible to add and solve additional transport equations through User-Defined Scalars (UDS). The equation for a generic scalar ϕ_d^k associated to the dispersed (solid) phase is:

$$\frac{\partial \varepsilon_s \rho_s \phi_s^i}{\partial t} + \nabla.(\varepsilon_s \rho_s v_p \phi_s^i - \varepsilon_s D_s^i \nabla \phi_s^i) = S_{\phi s}^i \qquad (29)$$

where ε_s , ρ_s and v_p are volume fraction, physical density and velocity of the solid phase, respectively.

By neglecting the diffusive term and defining each scalar as:

$$\phi_s^i = \frac{\mu_i}{\varepsilon_s} \qquad (30)$$

and by considering $\rho_s S_{\phi s}^i$ as the moment source term, it is possible to obtain the moment transport equation (PBE) reported in Eq. (27) from Eq.(29).

The source terms for the different moment equations are calculated and returned by a proper user-defined function (UDF) in Fluent.

Case studies

To ensure proper implementation of the moment transport equation sets in CFD code, we applied our approach to two specific cases, for which the analytical solutions are available.

A. Linear Growth

The first case is pure density growth in absence of velocity field while the rate of growth in density is proportional to the particle density itself.

Therefore the growth term becomes:

$$G = \frac{d\xi}{dt} = K.\xi \qquad (31)$$

and in the transformed coordinate:

$$G' = K.\left[\frac{(\xi_{\min} + \xi_{\max})}{2} + \frac{(\xi_{\max} - \xi_{\min})}{2}.\bar{\xi}\right] \qquad (32)$$

If we start with an initial dimensionless density distribution of the following form

$$I(\xi,0) = (1+\xi)^2.(1-\xi)^8 \qquad (33)$$

an exact analytical solution for the particle density distribution will be (McGraw, 1997):

$$I(\xi,t) = I(\xi,0).\exp(K.t) \qquad (34)$$

With growth rate of eq. (32) the set of moments transport equations resulting from eq.(27) becomes:

$$\frac{\partial \mu_i}{\partial t} = \mu_i.K \qquad i=0,1,2,\ldots \qquad (35)$$

The set of equations were discretized using a second order time discretization scheme with a fully implicit integration formula. The advantage of the fully implicit scheme is that it is unconditionally stable with respect to time step size.

The simulation results are shown in Figure 4, which shows the initial dimensionless particle density distribution, $I(\xi)$, and the comparison between the numerical simulation $f(\xi)$ and the exact solution $A(\xi)$. The results show that by solving 10 moments equations one can predict the exact final density distribution accurately. The values of *K* and *t* were 0.05 (s^{-1}) and 10 (s), respectively.

B. Linear Growth and Convection

In the second case FCMOM method was applied to a case with simultaneous linear growth, similar to the first case, and particle convection. The application considered is the gas-solid flow in a pipe with 1m length and 10cm diameter, with the same initial density distribution as Equation 33. The problem is solved in a 2-D geometry according to Figure 5. The moments transport equations were coupled with the equations governing the gas-phase fluid dynamics (mass and momentum balances) presented above.

The gas phase is in a laminar regime, and the particles move only due to the convection. In this specific case we assumed that the particles closely follow the gas flow field (low Stocks number). Therefore the particle phase velocity is equal to the gas phase velocity. Such assumption was made because, in this way, it is straightforward to confirm that the simulation results (the particle density distribution) are correct. At the inlet the gas velocity and the values for the first 10 moments calculated based on the initial density distribution are prescribed.

The simulation results after 5 seconds are reported in Figure 6. The particle size distribution (PSD) at different locations are different for different values of the radial coordinate *r*. In fact, because of the existing velocity profile, the inlet PSD is different radial positions. As a result, the final outlet PSD at the wall has the value of zero which is due to no slip boundary condition at the wall. Again, the moment values and the density distribution itself are predicted correctly by the numerical method.

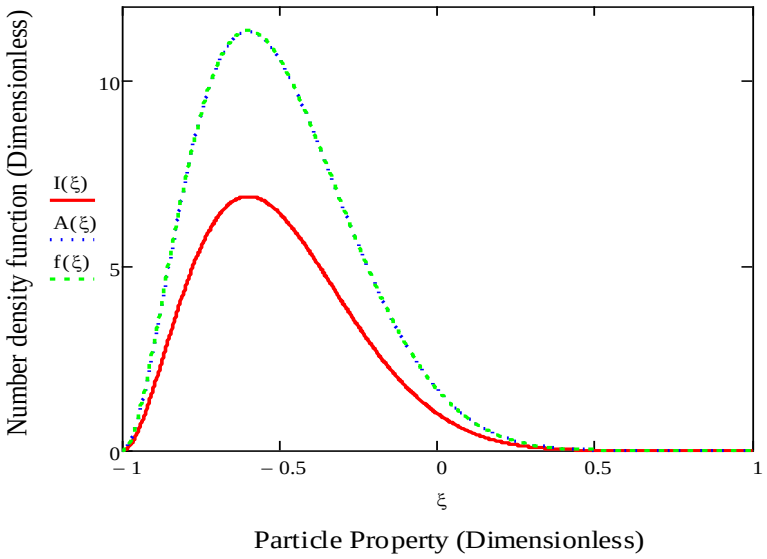

Figure 4. Particle density distribution vs. particle property (density)

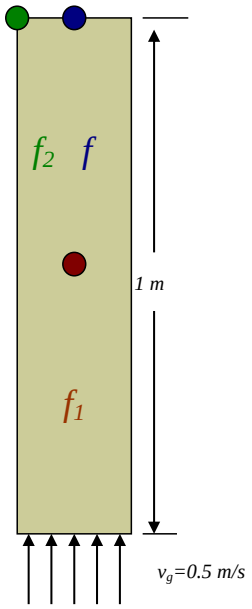

Figure 5. Corresponding geometry for Case 2. The color dots refer to the different locations that the density distributions are reported for in Figure 6.

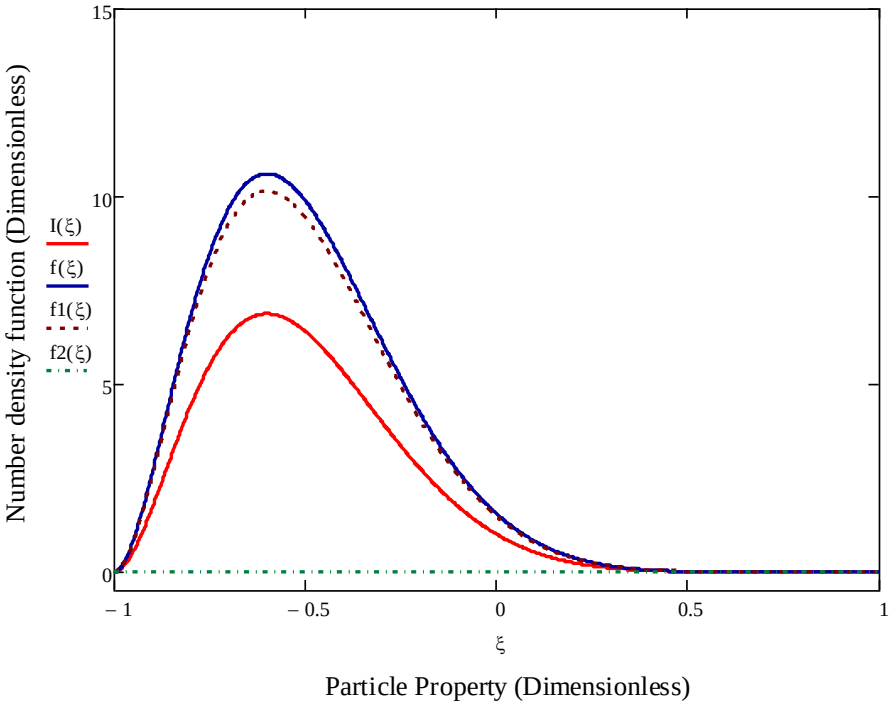

Figure 6. Initial and final density distribution at different locations inside the pipe.

Reaction Model

To describe the evolution of the state of a particle, due to the transport of CO_2 through the porous particle and its reaction a mathematical model is needed to be incorporated in the CFD/PBE model. A realistic particle mathematical model requires a physical description of the particle behavior, in terms of chemical components, phases present in the particle, diffusivity and reaction properties, etc.

The MgO (magnesium oxide) based sorbents considered in this project were prepared following a procedure developed by Hassanzadeh and Abbasian[5]. Starting from the base material (dolomite) to the final product (the MgO sorbents) to be used in the CO_2 capture process, it is possible to distinguish four main stages to define the material:

1) base material, i.e. the dolomite;
2) product after half-calcination;
3) product after impregnation in potassium salts solution (and re-calcination);
4) sorbents used in the CO_2 capture process.

Dolomite is the base material. A dolomite particle can be described essentially as a crystalline material with a porous structure. The crystalline material is divided in grains, and grains are separated by grain boundaries (line imperfections). Within each grain, the dolomite crystals are defined by the chemical formula $CaMg(CO_3)_2$ and have a well-defined chemical structure.

Partial calcination (Half-calcination) of dolomite is a key-step in the preparation of the sorbents and we are interested in the dolomite modifications after half-calcination. In the process of half-calcination, the dolomites particles are heated to release CO_2. The extent of the conversion of this process depends on the temperature and on the CO_2 partial pressure (Beruto et al [16] and Galari et al [17]). Typical decomposition temperatures are around 920-970K. According to a simple reaction models, half-calcination can be described by the following reaction (D):

$$CaMg(CO_3)_2 = CO_2 + CaCO_3 + MgO \qquad (D)$$

In Reaction D, one gas phase CO_2 and three solid phases ($CaMg(CO_3)_2$, $CaCO_3$, and MgO) are present simultaneously. However, Beruto et al. [16] showed evidence that an additional solid phase can be present in specific operative conditions, namely a solid solution of $CaCO_3$ and MgO, according to the reaction (E):

$$CaMg(CO_3)_2 = CO_2 + xCaCO_3 + yMgO + (1-x)CaCO_3\ (1-y)MgO \qquad (E)$$

An important modification of the dolomite due to the half-calcination is the variation of the particle porosity, which increases significantly. When dolomite particles (98% purity) are half-calcined at 1 atmosphere carbon dioxide partial pressure and at 973K, the experimental determined porosity value is about 0.10 cm^3/g. Clearly, the modification of the particle porous structure is crucial for improving the CO_2 absorption/capture by the sorbents.

The mechanisms of formation and growth of the new solid phases (i.e., MgO and $CaCO_3$), according to reaction (D) in the half-calcination process have not been fully understood in literature and are still a subject of discussion and investigation. Even though the mechanisms presently proposed in the literature are not definitive, it is very useful to review them for several reasons, including qualitative prediction of the spatial distribution of the different phases within each grain of the dolomite particles. The articles by Hashimoto et al [18] and by Galai et al [17] have revealed some of the issues related to the mechanism of growth of the product solid phases. According to the mechanism proposed by Hashimoto et al [18], the carbon dioxide is released at the dolomite surface (interface dolomite/gas phase), creating O^{2-} ions. Magnesium Mg^{2+} ions move towards the O^{2-} ions to form MgO. Simultaneously, calcium Ca^{2+} ions move in a direction opposite to the Mg^{2+} ions, forming calcite at the interface with the dolomite. The shortcoming of the model by Hashimoto et al [18] is that it cannot predict the reaction rate experimental dependency on the CO_2 partial pressure. A more complex model was proposed by Galai et al [17], which includes eight elementary steps and defines three interfaces, a) interface dolomite/$CaCO_3$; b) interface $CaCO_3$/MgO; c) interface MgO/ CO_2. The first interface moves internally, the second interface is stationary, the third one moves externally. They showed that, assuming the transport of magnesium

through MgO as the rate controlling step, the reaction rate dependency on the CO_2 partial pressure can be predicted.

The results of literature review suggest that, although a physical description of the half-calcined dolomite particles can be sketched using some of the literature results above outlined; this physical description is not to be taken as definitive and/or established. A half-calcined dolomite particle has a porous structure, with porosity values significantly higher than the base material. The solid material in the half-calcined particles is distributed in three phases. These three phases are: MgO, $CaCO_3$, and dolomite. The MgO phase is formed at the surface of the particle, the $CaCO_3$ grows internally, and the dolomite remains un-reacted in the core of the particle.

To describe the carbonation reaction kinetics of the MgO based sorbent at elevated temperatures, a modified version of the classical shrinking core model [Yagi and Kunii[32], Levenspiel,[33]] was developed[34] in this project. The schematic diagram of the model is presented in Figure 7. The fundamental assumptions of the classical shrinking core model [Yagi and Kunii,[32]] include the presence of the following resistances:

1- Diffusion of gaseous reactant through the gas film around the particle to the surface of the solid
2- Diffusion of a gaseous reactant through the porous product layer to the surface of unreacted sorbent
3- Surface reaction of gaseous reactant at the surface of the unreacted sorbent

However, due to the high concentration of CO_2 in the bulk and the significant flow rate of gas during the experiments (Hassanzadeh and Abbasian,[5]) the mass transfer resistance of gas film surrounding the particle is negligible.

In addition to the above assumptions, it is assumed that because of the difference between the molecular volume of the solid reactant and the product the radius of the spherical particles is increasing as the reaction proceeds. Additionally, based on SEM/EDS results reported by Hassanzadeh[4], there are two distinct reactive zones inside the particle due to presence of potassium carbonate as a promoter for the carbonation reaction. Therefore, considering two different zones with different reaction rate constants, k_1 and k_2 in the model is essential. The values of k_1 and k_2 has been adopted from the recent work of Hassanzadeh and Abbasian.[5].

Another important assumption in our model is that of a variable diffusivity of gaseous reactant through the product layer. The strong dependency of product layer diffusivity on the temperature, concentration and depth in the product layer has been reported in the similar processes by many researchers (Haul and Stein[35], Anderson[36], Szekely and Evans[37], Krishnan and Sotirchos[38] and Stendardo and Foscolo[39]).

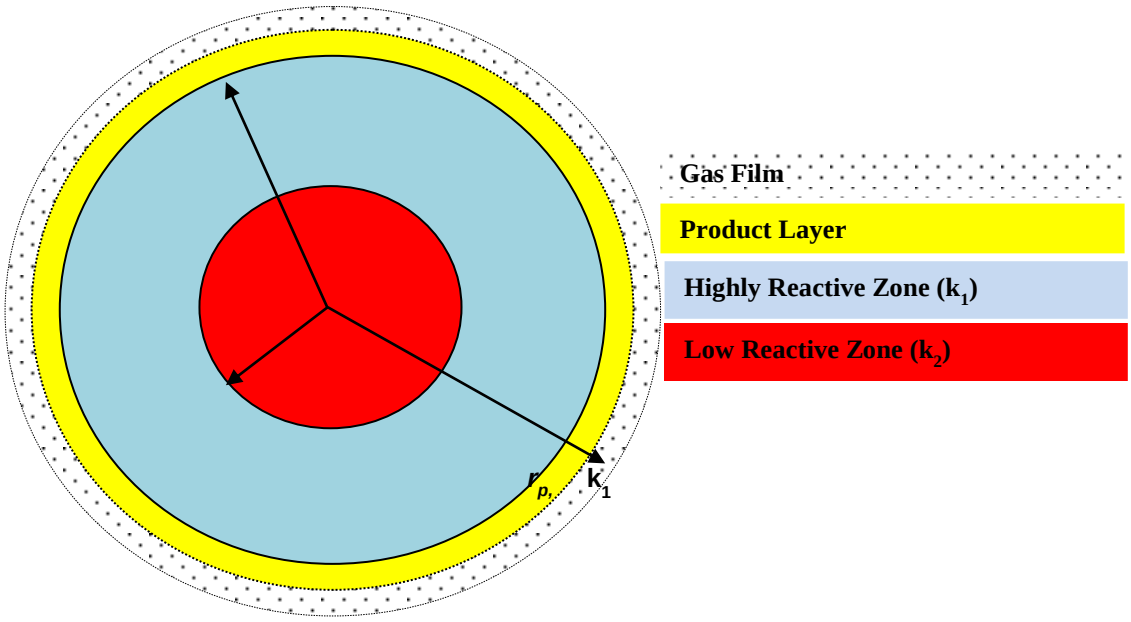

Figure 7. Schematic of the Two-Zone Variable Diffusivity Shrinking Core Model

The general governing equation for the temporal changes in the reaction front, r_i, in each of the two reactive zones can be easily derived by writing a mass balance around the spherical particle as presented by Levenspiel.[33] By neglecting the mass transfer resistance through the gas film surrounding the particle:

$$-\frac{dr_i}{dt} = \frac{(C_b - C_e)/N^o_{MgO}}{\underbrace{\frac{(r_p - r_i)r_i}{r_p D_g}}_{\text{Product Layer}} + \underbrace{\frac{1}{k_s}}_{\text{Reaction}}} \tag{36}$$

which gives

$$\frac{dr_i}{dt} = -\frac{k_s}{N^o_{MgO}}\left[\frac{(C_b - C_e)}{1+\frac{k_s}{D_g} r_i (1-\frac{r_i}{r'_p})}\right] \tag{37}$$

where, C_b is the CO_2 concentration in the bulk gas, C_e is the equilibrium CO_2 Concentration, D_g is the product layer Diffusivity of CO_2, r_i is the radial coordinate of the reaction front inside the particle, r'_p is the radius of the expanded grain, k_s is the surface reaction constant rate at each zone and N^o_{MgO} is the initial number of moles of *MgO* per unit volume.

In Equation 37, the local surface reaction rate (moles of carbon dioxide captured per unit time and particle volume) is assumed to depend linearly upon the CO_2 concentration in excess of equilibrium $(C_b\text{-}C_e)$.

For a spherical particle overall conversion is defined by:

$$X = 1 - (\frac{r_i}{r_p})^3 \tag{38}$$

and having the relationship between the initial particle radius and the expanded particle radius as:

$$r'_p = r_p \sqrt[3]{(1-X) + ZX} \tag{39}$$

where Z is the expansion factor, the rate of change in the conversion is:

$$\frac{dX}{dt} = -\frac{\frac{3}{r_p}\frac{k_s}{N^o_{MgO}}(C_b - C_e)(1-X)^{\frac{2}{3}}}{1 + \frac{k_s}{D_g} r_p (1-X)^{\frac{1}{3}} (1 - \sqrt[3]{\frac{1-X}{1-X+XZ}})} \tag{40}$$

$$k_s = \begin{cases} k_1 & for\ r_i \geq r_c \quad \text{or} \quad t \leq t_c \\ k_2 & for\ r_i < r_c \quad \text{or} \quad t > t_c \end{cases}$$

Since Equation 40 has to be solved over two reactive zones; an outer highly reactive zone with $k_s=k_1$ expanded from r_c to r'_p and an inner low reactive zone with $k_s=k_2$, a critical time, t_c must be defined as the required time for reaction front, r_i, to reach to the surface of the inner low reactive zone at $r_c=r_p-\delta$, where δ is the thickness of the highly reactive zone. The required reaction time, t_c can be obtained by integration of Equation 37, when $r_i = r_c$:

$$t_c = \frac{N^o_{MgO}}{k_1(C_b - C_e)}\left[r'_p\left(1 + \frac{k_1}{6D_g} r'_p\right) - r_c - \frac{k_1}{D_g}\left(\frac{r_c^{\,2}}{2} - \frac{r_c^{\,3}}{3r'_P}\right)\right] \tag{41}$$

In the modified model, the dependence of the diffusion coefficient through the porous product layer with respect to conversion was assumed to follow the following exponential function:

$$D_g = D_{g0}(-\alpha X^{\beta}) \tag{42}$$

Where D_{g0} is the initial diffusion coefficient and α and β are two adjustable model parameters. The optimum values of these adjustable parameters were determined using a multi-variable regression method (Marquaradt[40], Kuester and Mize[41]). The reaction kinetics model developed in this project was used to describe sorbent performance in carbonation reaction at different operating conditions based on a set of HP-TGA experimental data, and to calculate the model parameters.

The linear ordinary differential equations along with the governing equations of two-zone variable diffusivity shrinking core model were also used to fit the experimental results obtained in the high-pressure TGA unit at different operating temperatures. Table 2 provides the variable diffusivity model parameters used in this study. There are two adjustable model parameters, D_{g0} and α, which were obtained by determination of the best fit to the experimental results through minimization of the least squares of the errors. Figure 8 provides a comparison of the best models fit to the experimental data with the variable and constant diffusivity models. The results clearly indicate that the data cannot be described by a constant diffusivity model, while the results predicted by the variable diffusivity model closely match the experimental data.

Figure 8 Shows the model predictions as a function of the thickness of the outer reactive zone, when the thickness of the higher reactivity zone is not sufficiently large, resulting in two distinct regions in the conversion versus time curve. Furthermore, the results obtained by the model also indicate that, with a

reactive thickness layer of $\delta \geq 40 \mu m$, the reaction rate will be independent of the thickness of the outer reactive zone because pore closures reduce the product layer diffusivity to the point that does not allow the gaseous reactant to penetrate through the pores to reach the remaining reactive surfaces and the conversion curve reaches a plateau.

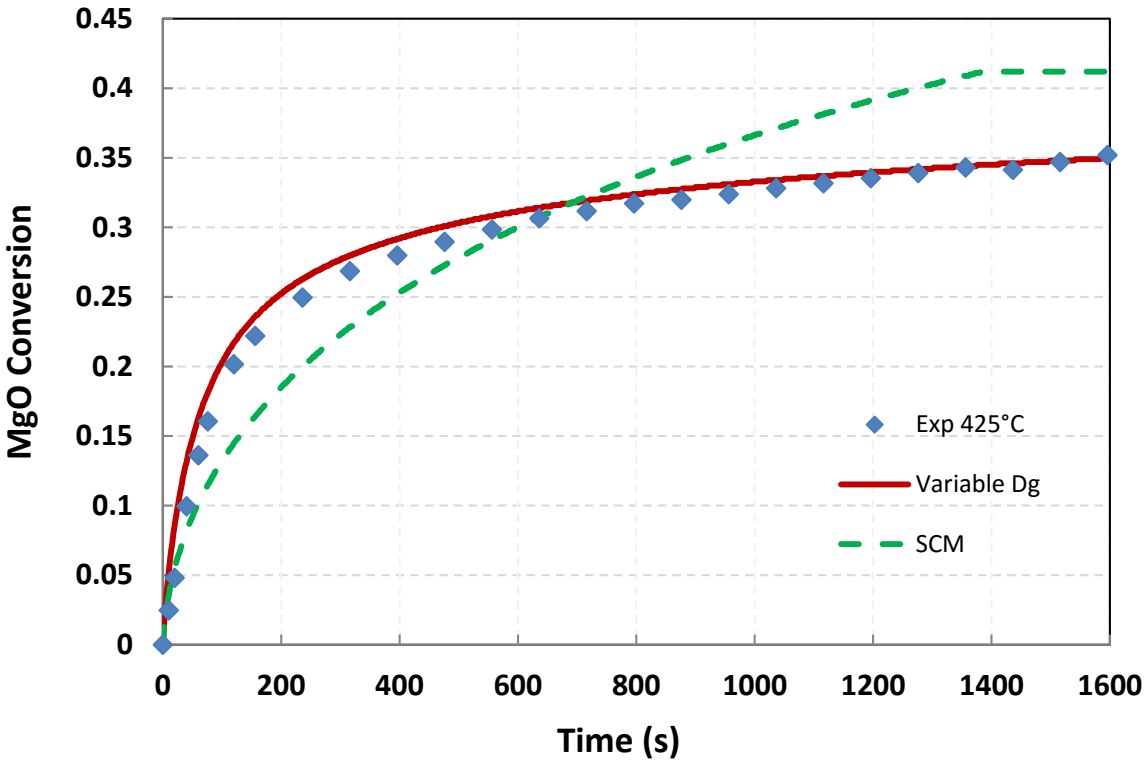

Figure 8. Comparison of the constant diffusivity (SCM) and variable diffusivity two-zone shrinking core models

Table 2. Values of parameters used in the model

Parameter	Value
r_p, μm	255
δ, μm	40
N^o_{MgO}, $mole/m^3$	1.671e+4
$C^o_{b,}$ $mole/m^3$	174.6
C_e , $mole/m^3$	41.7
ρ, kg/m^3	2570
Z,-	1.15

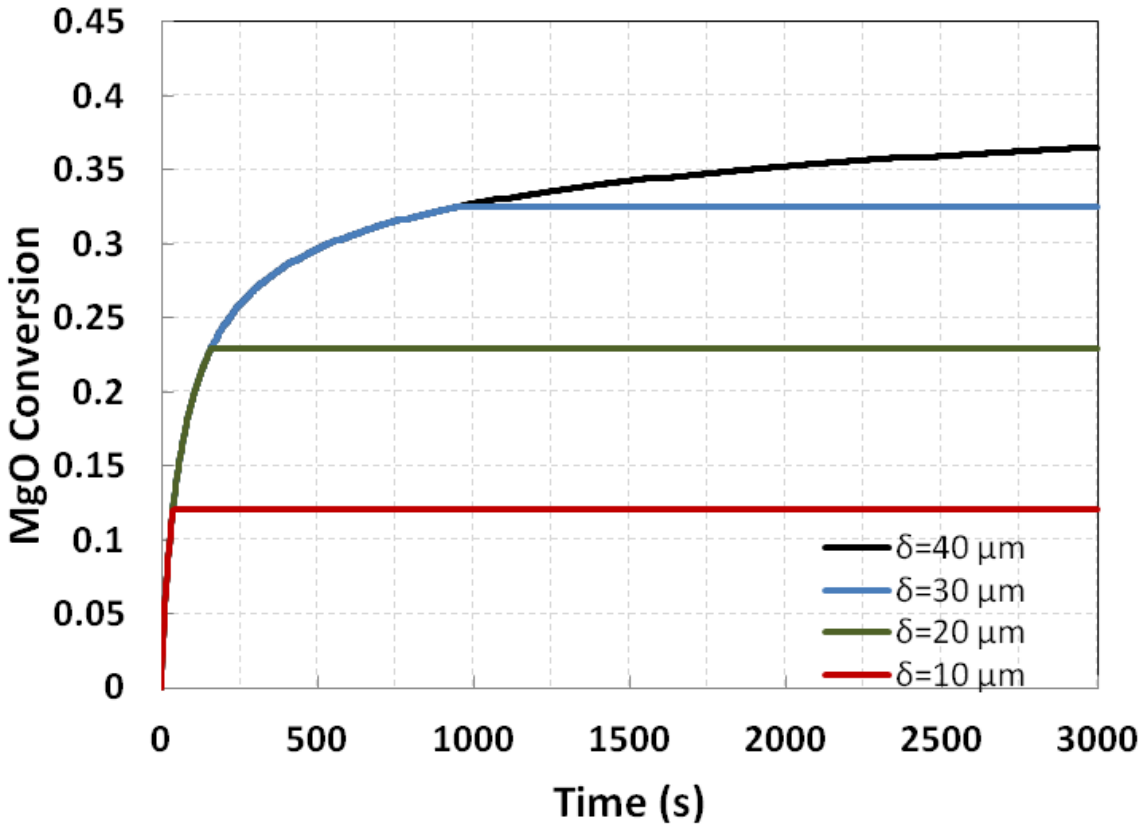

Figure 9. Model prediction for the reaction rate of sorbents with different thickness of the highly reactive zone

A comparison of the model predictions with the experimental results at different temperatures is shown in Figure 10, indicating that the model provides an excellent fit to the experimental data with R^2=0.99.

The dependency of D_{g0} and α on the reaction temperature is shown in Figure 11 and Table 3, indicating that in the temperature range of 350° to 450°C, the product layer diffusivity (D_{g0}) is in the range of 2.1E-9 to 5.0E-11 m^2/s, which is within the range of the reported diffusivity in literature for dolomite- and limestone-based sorbents.[42-44]

Figure 12 shows calculated values of the product layer diffusivity D_g, as the reaction front moves toward the center of the particle. Similar behavior has been reported by Adanez and co-workers[43] in sulfidation of a dolomite based sorbent and by Mess and co-workers[45] in CaO carbonation. The results presented in Figure 12 also indicate that diffusivity through the product layer sharply decreases to very low levels, limiting the sorbent conversion to about 40%, which corresponds to a product layer thickness of about 40 µm.

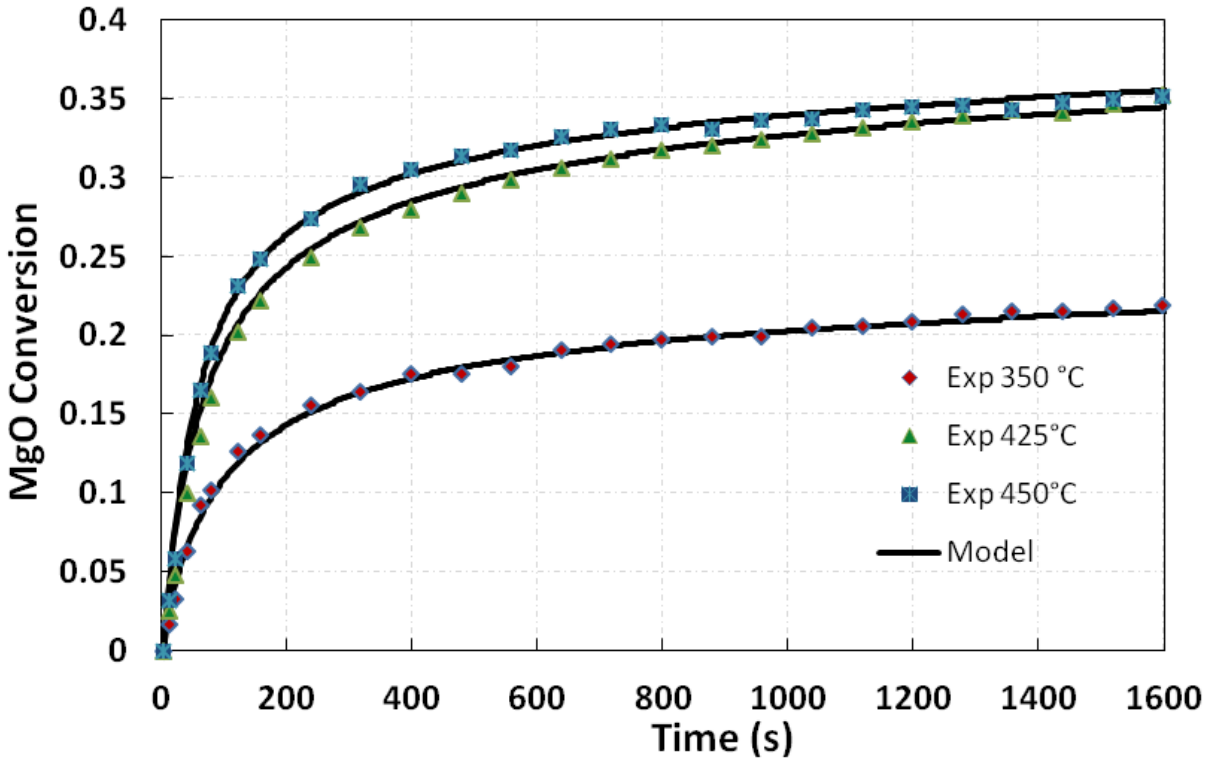

Figure 10. Comparison of model and experimental data at different temperatures

Table 3. Effect of temperature and steam treatment on the model parameters

Model Parameter	Without Steam			With Steam
	350 °C	425 °C	450 °C	425 °C
D_{g0}	1.1E-10	6.0E-10	1.2E-9	2.1E-9
α	3.5E+2	8.1E+1	5.7E+1	4.6E+1
β	3	3	3	3

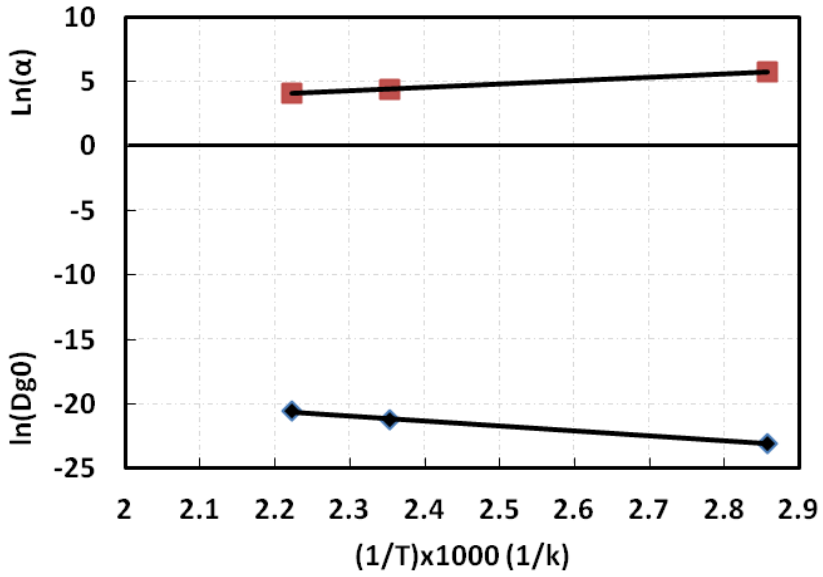

Figure 11. Temperature dependence of initial product layer diffusivity and diffusivity decay rate

The model was also used to predict the experimentally observed improved sorbent reactivity in the presence of steam[4], resulting from the higher porosity, surface area and changes in the pore size distribution shown in Table 4. Similar changes in the properties of dolomite and limestone has also been reported by others[46-48]. These changes can be translated to a higher initial product layer diffusivity to represent a more permeable porous product layer for the gaseous reactant diffusion and a lower tendency to pore closure at the wet condition. A comparison of the experimental results with and without the presence of steam with those predicted by the model is presented in Figure 13. The intrinsic reaction rate constant was assumed to be the same for both cases and the two model parameters were determine based on the best fit to the experimental data. The model parameters for the runs with and without the presence of steam are presented in Table 3, indicating higher initial diffusivity and lower rate of decline (i.e., smaller values for α) in the presence of steam.

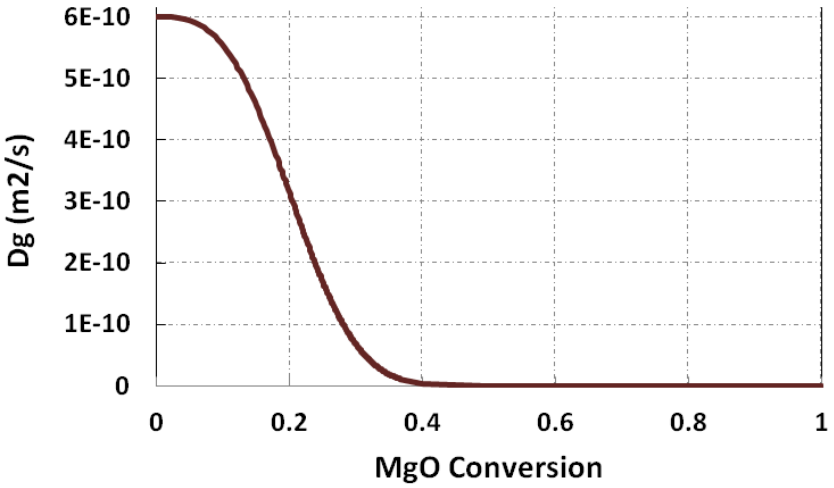

Figure 12. Product layer diffusivity vs. MgO conversion at 425 ^{o}C

Table 4. Effect of Steam on physical properties of the sorbent

Particle	BET Surface Area m^2/g	Porosity %	Particle Radius μm
Fresh	5.36	13.2	255
Treated with H_2O	6.32	17.0	259

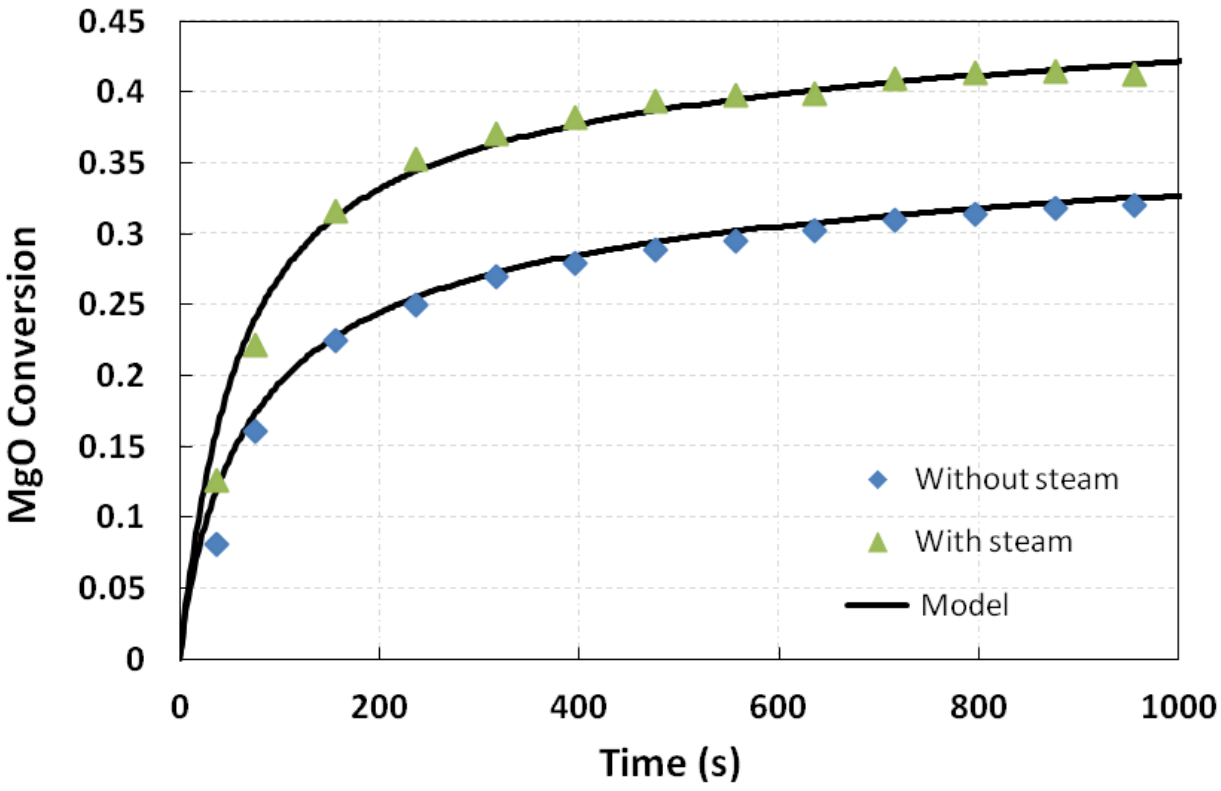

Figure 13. Comparison of model and experimental data at 425°C with and without steam

Hassanzadeh[5] also reported that the reactivity of the sorbent gradually decreases in the cyclic process resulting from the decrease in the sorbent porosity and surface area (see Table 5), which was attributed to sorbent agglomeration and pore closure when the sorbent is exposed to high-temperature/high-pressure operating conditions. Figure 14 compares the experimental TGA data in the cyclic process with those predicted by the model, while the values of the two adjustable parameters are presented in Table 6. The model provides excellent fit to the experimental data and indicates a decreasing trend in the initial diffusivity and an increasing trend in the rate of decline of the diffusivity, which are consistent with the declining surface area and porosity in the cyclic process presented in Table 4 above.

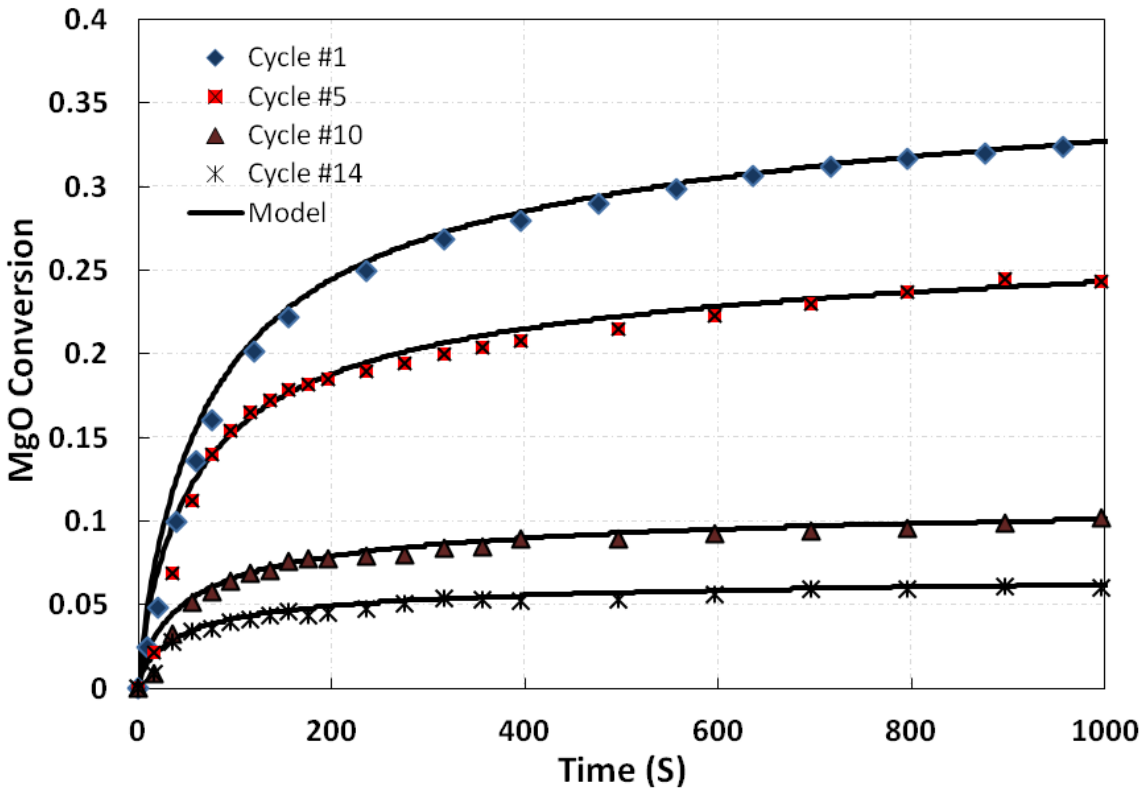

Figure 14. Comparison of model and experimental data in different cycles

Table 5. Changes in sorbent characteristics in cycling process

Sorbent	BET Surface Area, m^2/g	Porosity, %
Fresh	5.36	20.1
1-Cycle	3.07	9.1
9-Cycle	2.87	8.4
25-Cycle	1.49	3.8

Table 6. Effect of cycling on the model parameters

Model Parameter	Cycle Number			
	1	5	10	14
D_{g0}	6.0E-10	3.5E-10	5.0E-11	1.0E-11
α	8.1E+1	2.12E+2	3.3E+3	1.5E+4
β	3	3	3	3

Based on the above results, it is concluded that a two-zone variable diffusivity shrinking core model with expanding product layer is capable of describing the gas/solid carbonation reaction involving carbon dioxide and potassium-promoted half-calcined dolomite sorbent and the model predictions are very similar to those provided by the two-zone expanding grain model. Although both models can correctly capture the trends on the effects of operating conditions on the physical properties of the sorbent observed in the experiments, the two-zone variable diffusivity shrinking core model with expanding product layer is more suitable for CFD applications due to its explicit formulation.

Coupling the Population Balance Model and the CFD Model

Figure 15 shows the algorithm developed for coupling the population balance model and the CFD model, indicating that the CFD model provides the phase velocity and volume fraction for each of the two phases at each time and location. These values are used to define the source terms of the moments transport equations describing the temporal and spatial evolution of the sorbent density distribution. In addition, as discussed above, the rate of change in density due to the chemical reaction between the two phases is fed to the model through chemical reaction kinetics model.

By defining the essential terms in the population balance model and solving the set of equations derived above using FCMOM numerical method, the values of the moments, μ_i, are known at each time and location throughout the domain. In the next step, Equation 43 was used to calculate the mean solid density and update the solid density in the CFD model for the next time step.

$$\rho_s = \frac{(\frac{\mu_1}{\mu_0})(\xi_{\max} - \xi_{\min}) + (\xi_{\min} + \xi_{\max})}{2} \tag{43}$$

In Equation 43, μ_0, μ_1, are the first and second moments of the particle density distribution, respectively. ξ_{min} refers to the minimum value of the particle density at each time and location and ξ_{max} is the density of the fully reacted particle.

To ensure proper implementation of the coupling algorithm in the CFD code, ANSYS Fluent 13.0, the algorithm was applied to a test case of a reactive solid-gas flow with changes in solid phase density distribution due to the chemical reaction in a pipe with 1m length and 10cm diameter, with an initial density distribution of--

$$I(\xi,0) = (1+\xi)^2.(1-\xi)^8 \tag{44}$$

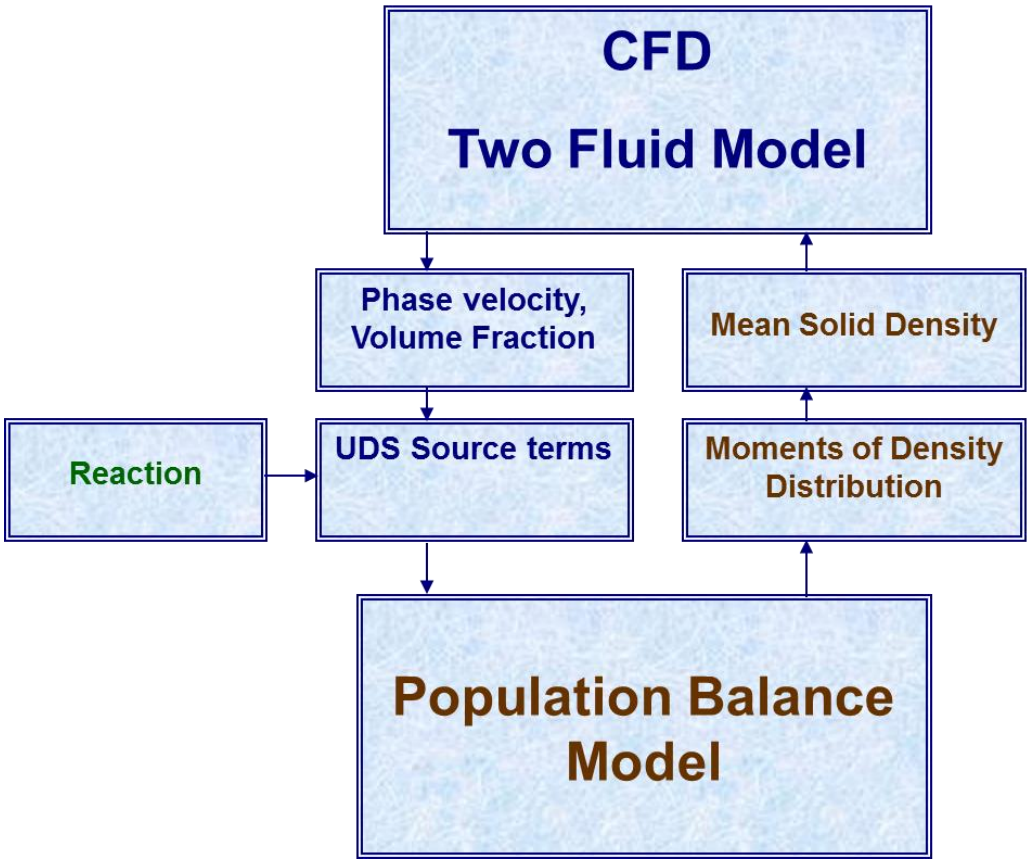

Figure 15. Schematic diagram of the coupling algorithm

The problem was solved in a 2-D geometry shown in Figure 16. The moments transport equations were coupled with the equations governing the gas-phase fluid dynamics (mass and momentum balances) according to our coupling algorithm. In this case the particles were assumed to be convected with the mixture velocity and the rate of change in the density was assumed to be constant. At the inlet the gas velocity and the values for the first 10 moments calculated based on the initial density distribution were prescribed.

The simulation results after 10 seconds are reported in Figure 17 and Figure 18. The contours of the first and second moments of the particle density distribution inside the domain are presented in Figure 17, while the contours for the minimum value of the solid density, solid volume fraction, and the solid density inside the domain are presented in Figure 18, respectively. It should be noted that, in this specific case, due to the low reaction rate and short length of the domain, the solid density changes are not significant. However the results confirm the proper implementation of the algorithm in the CFD code.

A series of available high-pressure/high-temperature packed-bed experimental data with the dry regenerable MgO-based sorbent was simulated using our two zone variable diffusivity shrinking core model presented above to investigate the effects of operating temperature and inlet CO_2 concentration on the performance of the sorbent in a packed-bed reactor, with and without water gas shift reaction.

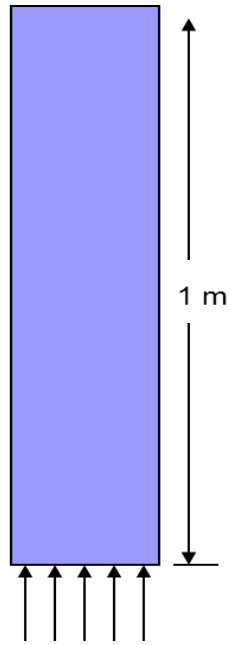

Figure 16. Schematic diagram of the test case domain

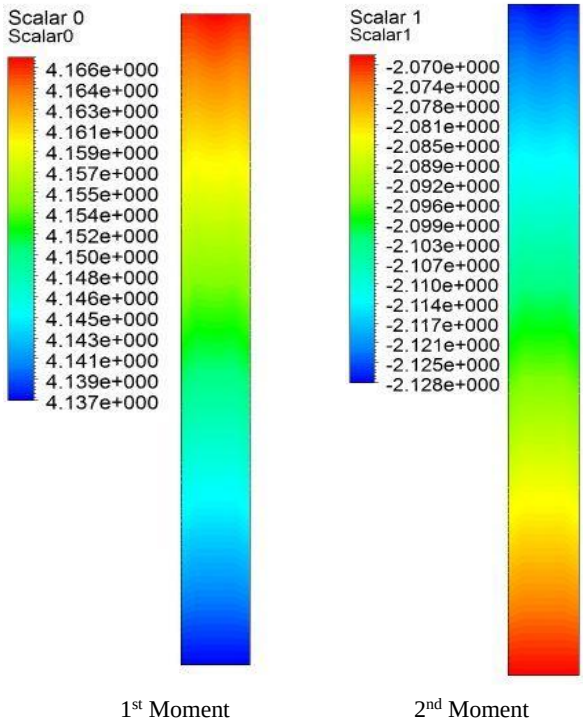

Figure 17. Contours of the first and second moments after 10 sec.

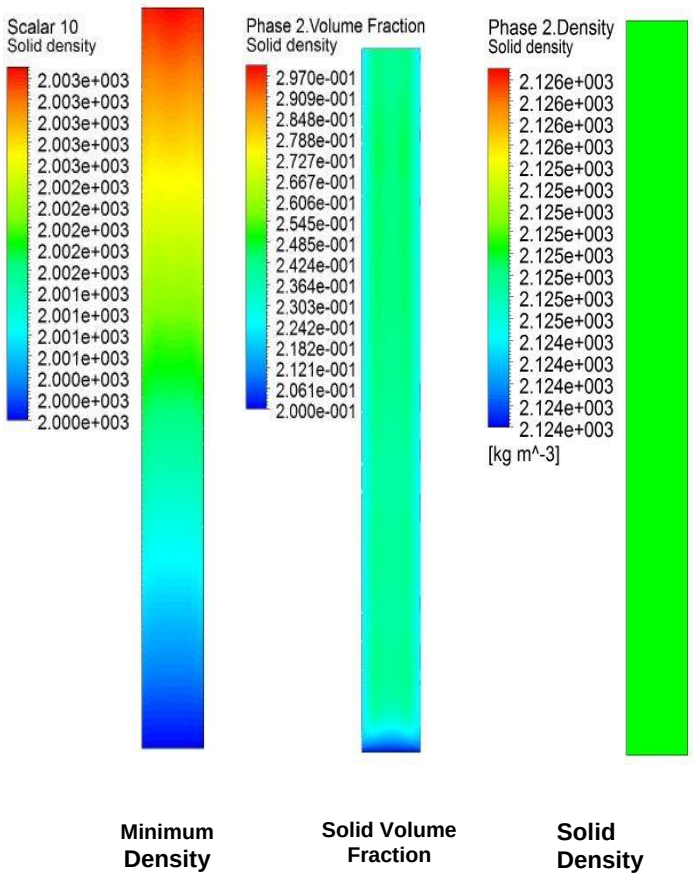

Figure 18. Contours of minimum solid density, solid volume fraction and solid density after 10 sec.

The schematic of the packed-bed reactor used to obtain the experimental data (Hassanzadeh [4]) is shown in Figure 19. The experimental data includes two sets of runs in the packed-bed unit. The first set included the absorption/regeneration cycles in the presence of different concentrations of CO_2, N_2, and steam at different operating conditions to study CO_2 absorption without the water-gas-shift reaction, while in the second set, syngas mixtures with different compositions were fed into the reactor to evaluate simultaneous CO_2 absorption and enhancement of hydrogen production through the water-gas-shift reaction. The operating conditions of each of these experimental sets are shown in Table 7. A mathematical model was developed to represent the single phase multicomponent reactive flow in the packed bed which is treated as a porous media. The model includes the following transport equations for mass, momentum and different species, respectively:

$$\nabla . u = 0 \tag{45}$$

$$\frac{\partial(\rho u)}{\partial t} + \nabla . (\rho u u) = -\nabla p + \nabla . \tau + S \tag{46}$$

$$\frac{\partial C}{\partial t} + \nabla . (uC) = -\nabla . (\mathrm{D} . \nabla \mathrm{C}) + R \tag{47}$$

$$R = \rho_{sorbent} (1-\varepsilon) . (r_{CO2,cbn} + r_{CO2,WGS}) \tag{48}$$

$$r_{CO2,cbn} = \frac{y_{MgO}}{MW_{sorbent}} \frac{dX}{dt} \tag{49}$$

Where, u is the velocity vector, ρ is the gas density, p is the pressure, τ is the stress tensor, S is the momentum source term, C is the concentration of species in gas phase, R is the net rate of the reaction, ε is the porosity, and ρ sorbent is the sorbent density. Equation 46 describes the Navier-Stokes flow with an additional sink of momentum (S) representing the Darcy viscous loss of a porous media and is given by:

$$S = -\frac{\mu}{K}u \tag{50}$$

Where. μ is the dynamic viscosity and K is the permeability tensor. Therefore the flow is physically represented in both the fluid and the porous media.

$r_{CO2,cbn}$ and $r_{CO2,WGS}$ represents the reaction rate of CO_2 involving carbonation and water gas shift reactions, respectively. The rate of carbonation reaction can be calculated from the rate of sorbent conversion, obtained from the two zone variable diffusivity shrinking core model with expanding product layer which gives the dX/dt in the following correlation.

$$r_{cbn} = \frac{y_{MgO}}{MW_{sorbent}}\frac{dX}{dt} \tag{51}$$

This model was implemented in a commercial finite volume based CFD code, ANSYS Fluent, for simulations of the packed bed reactor and investigation of the sorbent's performance at different operating condition as described in Task 4.

Table 7. Ranges of high-pressure packed-bed operating parameters

Operating Parameter	Experimental Set #1		Experimental Set #2	
	CO_2 Removal	Regeneration	CO_2 Removal/ H_2 Production	Regeneration
Temperature, ℃	300-450	500	300-425	500
Pressure, atm	20	20	20	20
Space Velocity, hr^{-1}	1000	2500	1000	2500
Gas Composition, *mol%*				
CO_2	25-50	0	10-30	0
N_2	Balance	Balance	-	-
CO	-	-	30	0
H_2O	0-10	0-10	10-30	10-30
H_2	-	-	30	Balance

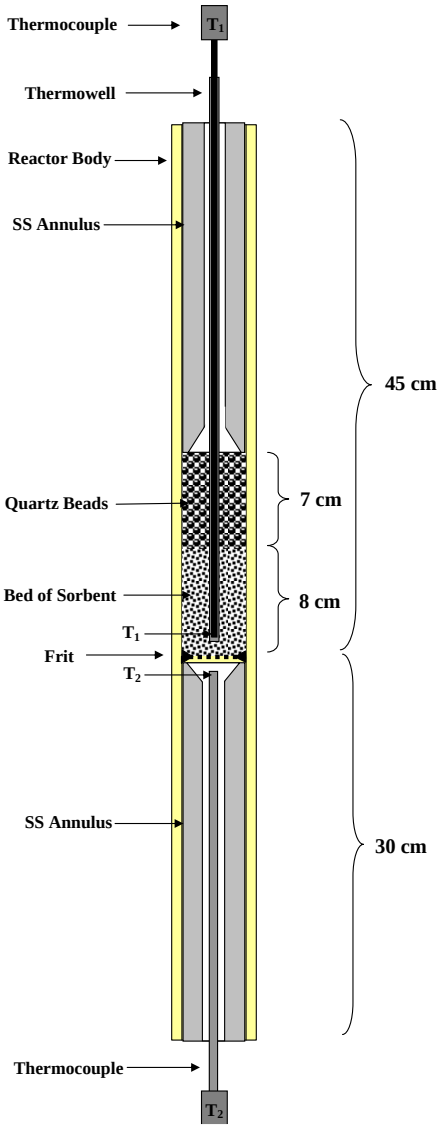

Figure 19. Schematic diagram of the packed-bed reactor

Task 3. Determination of the key parameters of the absorption/regeneration and WGS reactions

The objective of this task is to experimentally determine the key gas-solid reaction parameters for the absorption/regeneration and WGS reactions, which are needed for CFD simulation of the sorbent/catalyst performance in the regenerative process.

In order to determine the optimum range of sorbent particle diameter, samples of the original sorbent in five different particle size ranges were prepared. The ranges of particle diameter included 75-100, 100-125, 125-150, 150-180, 180-250μm. The fluidization behavior of each of the five cuts at ambient condition (i.e., 25 °C, 1 bar) was investigated in an existing glass fluidization column. The results of these tests indicate that severe to moderate slugging occurs for the cuts smaller than 150-180μm. Therefore, given that, it is desirable to use the smallest suitable particle size to increase the sorbent capacity, the 150-180μm cut was selected for further investigation.

To determine the ranges of flow rates of the feed gas components (i.e., CO, CO_2, H_2, N_2, and H_2O) at the process condition prevailing in the MgO-based regenerative process, the minimum fluidization velocities of a dolomite and a half-calcined dolomite (representing fresh and reacted sorbents, respectively) with the particle size range of 150-180μm were determined at the ambient condition. The results are presented in Figures 20 and 21, indicating that, in general, the fluidization velocity of the sorbent is in the range of 1-1.5 cm/s for the fresh/reacted sorbent, respectively). The experimentally determine fluidization velocities are in good agreement with those predicted by various correlations available in the literature (see Table 8). These correlations were used to estimate the fluidization velocity of the feed gas mixture at 20 bar and 400°C. Based on the fluidization tests, the sorbent with a particle diameter in the range of the 150-180μm was selected for further investigation.

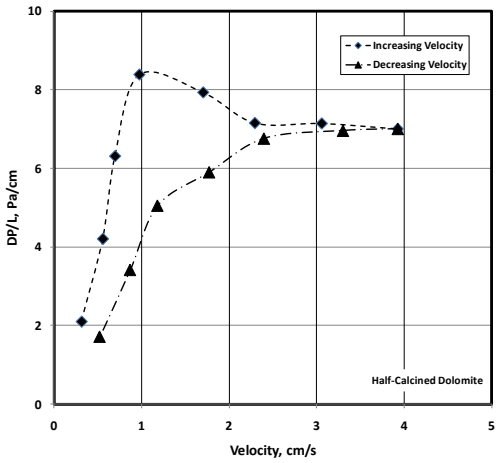

Figure 20. Fluidization velocity of half-calcined dolomite (representing fresh sorbent)

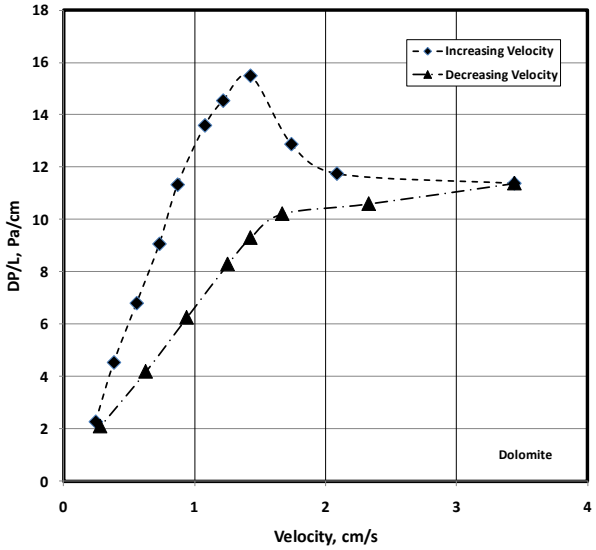

Figure 21. Fluidization velocity of dolomite (representing reacted sorbent)

A five-gallon batch of the same dolomite (from Thornton quarry located in Illinois) used in the earlier study (Hassanzadeh[4]) was obtained from Hansen Material Services Corporation. The dolomite was crushed, sized, dried, and a representative sample in the desired particle size (150-180μm) was obtained for further testing.

Experimental tests were carried to prepare the sorbents in the desired particle size range by modifying the dolomite using the same preparation procedure developed in the earlier study (Hassanzadeh and Abbasian[3]). The first step in preparation requires half-calcinations of the dolomite at 550°C and 4 hours to decompose magnesium carbonate through the following reaction:

$$CaMg(CO_3)_2 = CaCO_3 + MgO + CO_2 \quad (D)$$

Table 8. Comparison of Measured and Calculated Umf

u_{mf}, cm/s	T=25 °C, P=1 bar		T=400 °C, P=20 bar	
	Dolomite	Half Calcined Dolomite	Dolomite	Half Calcined Dolomite
MEASURED	1.5	1.0	N/A	N/A
Wen & Yu	2.2	1.6	1.20	0.83
Richardson	2.5	1.9	1.40	0.96
Saxena & Vogel	4.0	3.0	2.21	1.52
Babu	4.6	3.5	2.51	1.73
Grace	2.7	2.0	1.48	1.02
Chitester	3.1	2.3	1.69	1.17
Experiment	3.8	1.2	2.07	0.62

However the results obtained at this operating condition indicated a very low conversion (i.e., 37%) in Reaction (D). It has been reported that because of the complex crystal structure of the dolomite, depending on the dolomite properties, the half-calcinations temperature can vary over a relatively wide range. (Cater and Buseck[49]). To ensure accurate temperature measurement, the calcinations oven temperature was calibrated using two external thermocouples (in addition to the oven thermocouple), using two temperature indicators (the oven and the external unit) and the results are presented in Figure 22, oven temperature measurement by the three thermocouples are similar, but the oven temperature determined by the temperature indicator of the oven is about 30°C lower than those obtained from the external indicators.

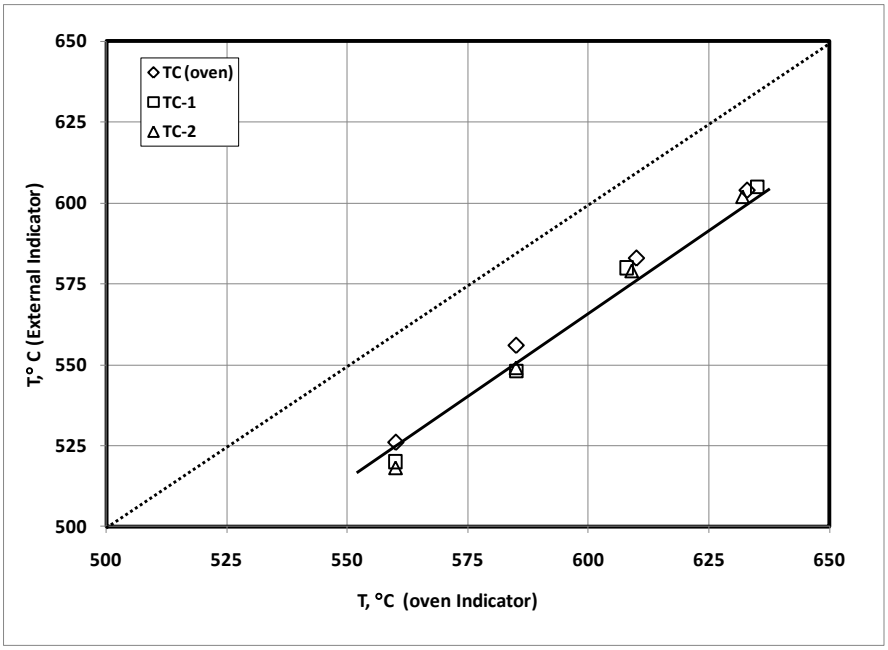

Figure 22. Oven temperature calibration

To determine the optimum calcinations temperature, several batches of uncalcined dolomite were calcined at different temperatures and the results are presented in Figure 23, indicating that the extent of conversion improves by increasing the calcination temperature and calcination time. However, based on the results obtained in a previous study, the extent of conversion is lower than expected.

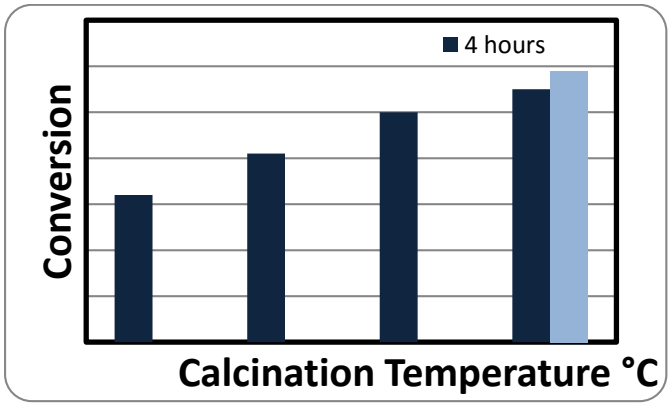

Figure 23. Effect of calcination temperature on the extent of calcination

Six samples were calcined at three different temperatures and two different calcination time. The results are presented in Table 9; indicating that at any given temperature, the extent of calcination slightly increases with calcination time.

Table 9. Deviation of dolomite weight during different calcination process

	Type	Calcination Temperature (C)	Calcination Duration (hr)	Weight Loss %
Sample 1	Half-Calcined	560	6	16.38
Sample 2	Half-Calcined	560	10	17.46
Sample 3	Half-Calcined	600	6	17.31
Sample 4	Half-Calcined	600	10	21.54
Sample 5	Half-Calcined	650	6	27.69
Sample 6	Half-Calcined	650	10	30.00

To determine the chemical composition of the calcined sorbents, several samples of the calcined sorbents were analyzed by XRD. The results of the XRD tests are presented in Table 10, indicating that at temperature above 625 °C $CaCO_3$ starts to decompose. Furthermore, the results also indicate that in the temperature range of 580-600°C, a new phase [i.e., $(Ca_{1-x}Mg_x)CO_3$]with unknown structure forms.

The XRD spectra of several samples are shown in Figure 24. In Sample A, the calcite peaks all have a weak broad shoulder on the high-angle side. The best explanation for these shoulders is the presence of a calcite which contains a small concentration of Mg. The lattice parameters of the calcite in these samples do not differ significantly, and are identical to those expected for pure $CaCO_3$. The calcite peaks are also dominated by strain broadening, and the strain is similar in all samples. The calcites exhibit some preferred orientation, probably reflecting large size of some grains. The refined lattice parameters of this phase in sample A suggest that the composition is $Ca_{0.93}Mg_{0.07}CO_3$. As expected for such a solid solution, the degree of strain broadening is high. A similar magnesian calcite is probably present in Sample F, but the shoulders are broader and weaker, making extracting details about its composition difficult. The calcined samples contain about 20-30 wt% periclase, MgO. The cubic lattice parameters suggest that this phase is pure MgO. The periclase peaks are dominated by size broadening, and the average crystallite sizes are ~300 Å. Lime (CaO) was detected in Samples B. A very weak peak at 25.2E in the pattern of Sample F may indicate the presence of a trace of anhydrite, CaSO4.

Table10. Calcination of dolomite at different temperatures

Sample	A	B	C	D	F	G
Calcination Time, hrs	6	6	6	-	6	6
Calcination Temp., °C	600	650	560	-	580	625
Type	Half-Calcined	Half-Calcined	Half-Calcined	Fresh Dolomite	Half-Calcined	Half-Calcined
CaMg (CO3)2 (wt %)	31.4	8.2	37.2	100	29.5	12.1
CaCO3 (wt %)	43.4	59.9	43.8	0	45.6	62
$(Ca_{1-x}Mg_x)CO3$ (wt %)	6.6	0	0	0	5.7	0
*MgO (*wt %)	18.5	28.1	19	0	18.9	25.9
*CaO (*wt %)	0	3.7	0	0	0	0
Other (wt %)					0.3	
Conversion (%)	75.62%	-	70.14%	0.00%	76.78%	90.78%

Based on XRD results, sample G has highest conversion with no CaO, thus this sample was selected to use in reactor. About 1 kg of half calcined dolomite was prepared at this condition.

As shown in the earlier study (Hassanzadeh and Abbasian[3]), half-calcined dolomite is generally not reactive toward CO_2, and to increase the reactivity of the sorbets, it is necessary to impregnate an alkali salt, such as potassium carbonate, into the sorbent. Therefore, a large quantity of half-calcined sorbent was prepared by calcination at 625°C for 6 hrs (HD15). The calcined sorbent was subsequently impregnated with potassium carbonate by placing the sample in a 2M of potassium carbonate solution for 24 hours followed by calcination at 625 °C (HDP15). The results of the XRD analyses of these samples are presented in Table 11, indicating that the sample contains 1.2% potassium carbonate that is significantly lower than those reported in the earlier study.

To carry out the experimental work detailed in this task, an existing packed-bed unit was modified to allow testing the sorbent in a dispersed-bed, as well as packed-bed reactormode. A schematic diagram of the packed-/fluidized-/dispersed-bed reactor unit is presented in Figure 25. The unit consists of three main subsections; the gas feeding section, the reactor section, and the gas effluent section. For the tests

involving N_2 /CO_2 mixtures, the feed gases are supplied by the pressurized cylinders flow through pre-calibrated Mass Flow Controllers (MFCs) to accurately achieve the desired mixture composition before entering the reactor. Stainless steel tubing with 1/8" (0.318 *cm*) OD is used to deliver the gas mixture to the reactor.

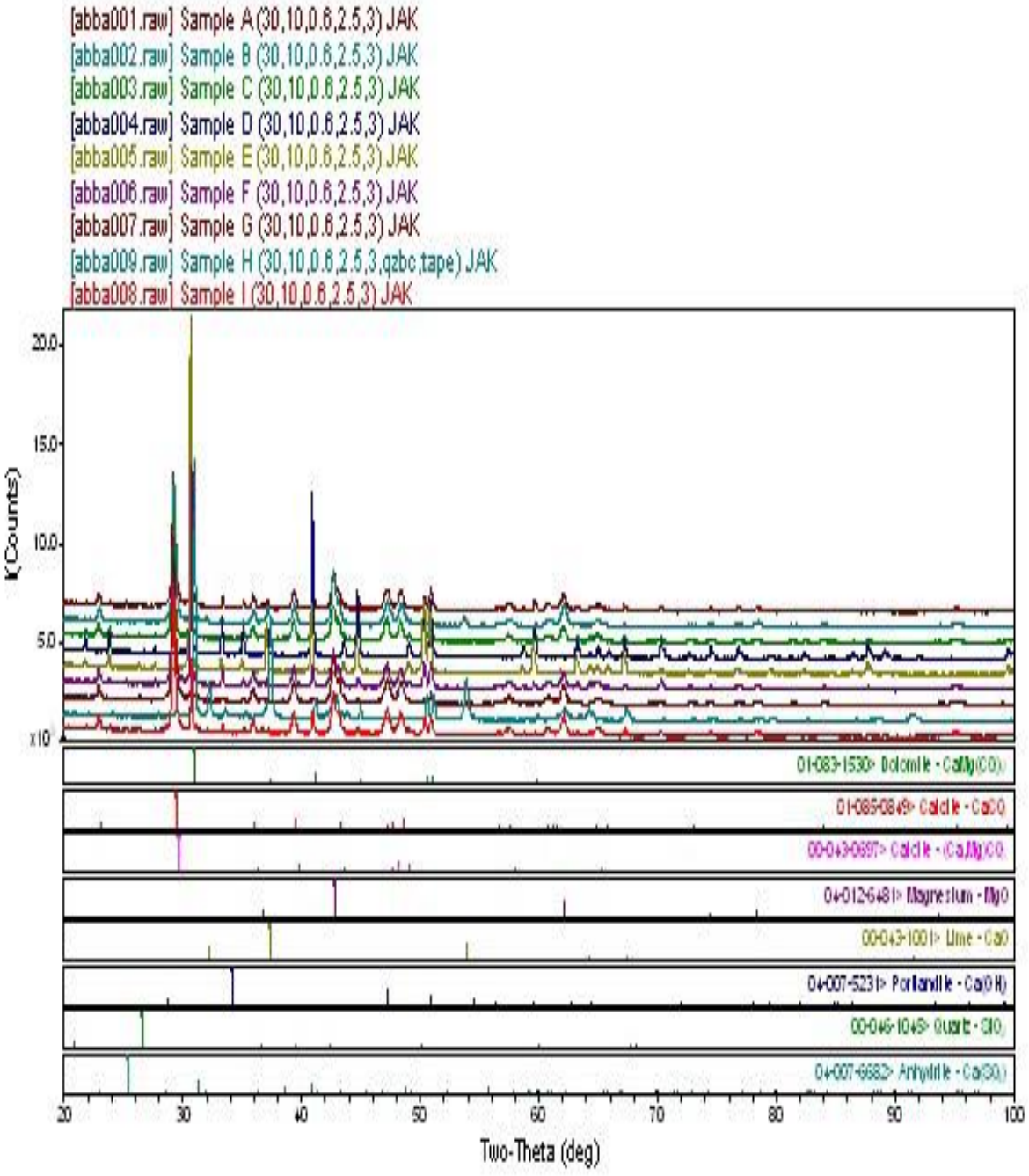

Figure 24. XRD results of prepared sorbents

Table 11. Analyses of calcined and impregnated sorbents

Sample	HD15	HDP15
Calcination Duration, hrs	6	6
Calcination Temperature,°C	625	625
CaMg $(CO_3)_2$ (wt %)	0.7	0
$CaCO_3$ (wt %)	68.5	64
MgO (wt %)	30.8	31.3
$K2CO_3$ (wt %)	0	2.2
$KHCO_3$ (wt %)	0	1.2
Ca $(OH)_2$ (wt %)	0	1.2
Conversion (%)	99.51%	-

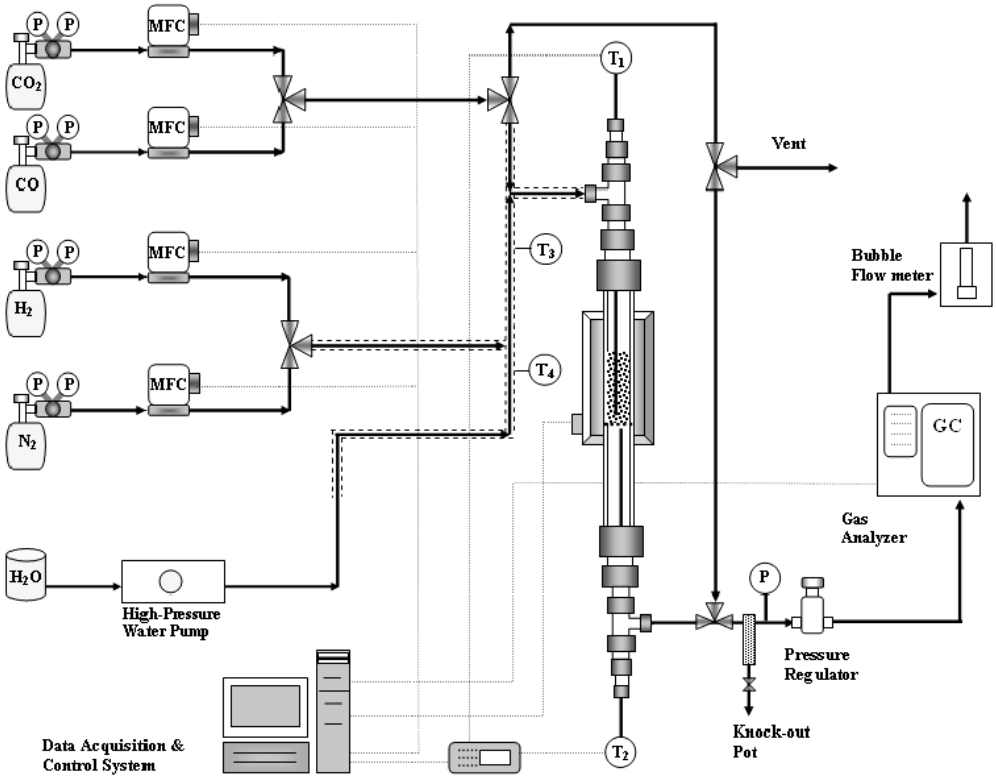

Figure 25. Schematic diagram of the high-pressure packed-bed unit

A highly-sensitive backpressure regulator was installed downstream of the reactor to maintain the total pressure of the reactor at a pre-determined setting. This regulator is comprised of a wide diaphragm-sensing area, which increases its accuracy, and a low-flow rate seat assembly, which dampens flow fluctuations. A manual bubble flow meter was placed at the very end of the unit to measure the changes in the flow rate of the reactor effluent.

The reactor is a custom made 316 stainless steel tubular reactor with 1" (2.54 *cm*) OD × 0.75" (1.905 *cm*) ID and 75 *cm*. A porous frit with two-micron openings made of Hastelloy®-276 alloys was welded 30 *cm* above the bottom of the reactor. Approximately 45 *cm* of the reactor is externally heated with a single-

zone electric tubular furnace. Two thermocouples were placed inside the bed of sorbents and below the porous frit and were connected to the data acquisition system (Figure 25). The thermocouple inside the bed, with 0.04" (0.102 *cm*) OD, is placed inside a 1/8" (0.318 *cm*) thermo-well and is moved along the bed during each run to measure the temperature of the bed at different axial positions.

To evaluate the sorbent in a well dispersed differential reactor, about 1 gram of the sorbent was distributed in 8 cm of quartz beads (dia = 850-1200μm) along the reactor (see figure 26). To enhance a uniform radial distribution of the gas composition, as well as the gas flow rate (plug flow), 7 cm of quartz beads were placed on the top of the sorbent bed. The test is initiated by setting the backpressure regulator at the desired value and feeding nitrogen to the reactor until the reactor reaches the desired pressure and stabilized. At this point, the tube connections (fittings) are checked for any possible gas leakage to prevent any error in the mass balance calculations. Following the leak test, the bed temperature is gradually increased to reach the desired settings.

To determine the bed temperature during the CO_2 adsorption, the bed temperature was monitored and measured at seven locations along the sorbent bed. The results indicates that approximately one hour is required to reach a steady state condition using an inert feed gas (i.e., nitrogen). The steady state temperature profile along the bed is shown in Figures 27.

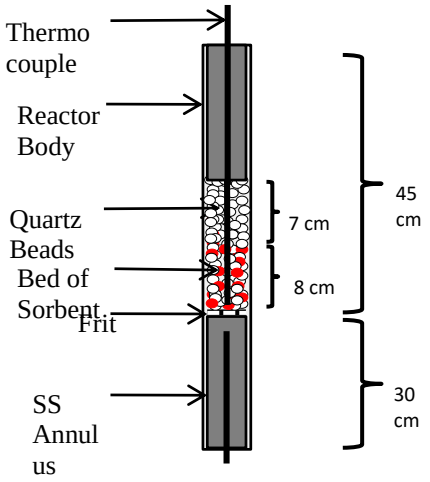

Figure 26. Schematic diagram of the packed-bed reactor

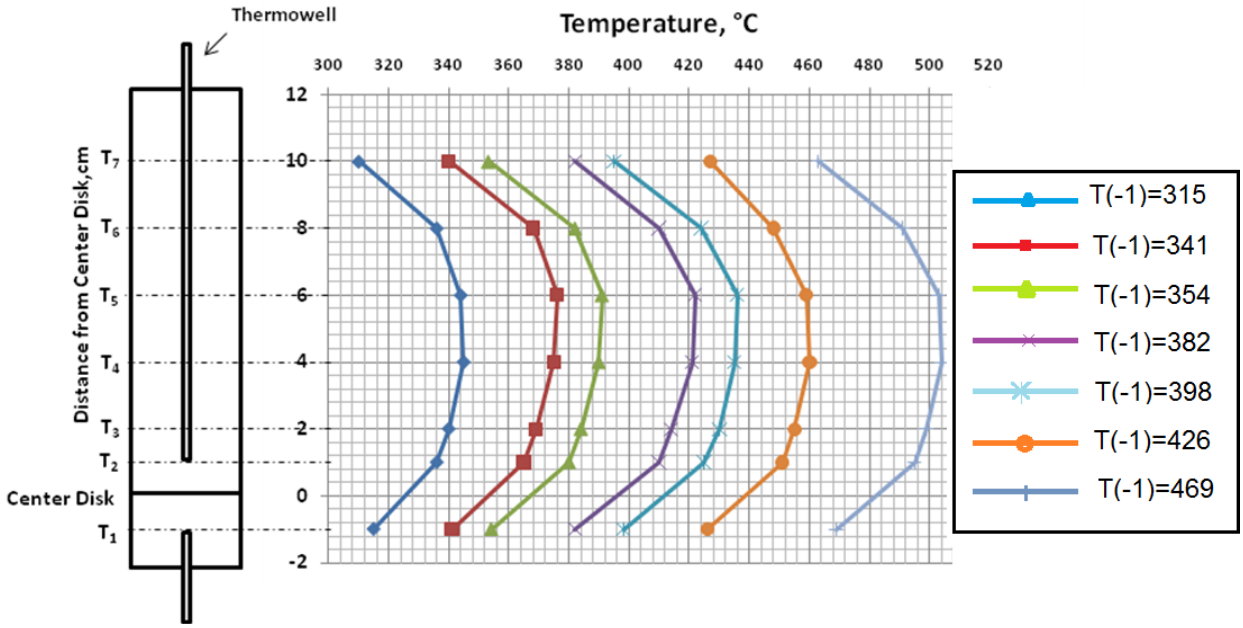

Figure 27. Temperature profile along reactor

Following the preparation and characterization of various sorbent formulations, the "most promising" sorbent formulation was selected and a larger batch of the sorbent was prepared and evaluated in the packed-bed reactor. In this test, the selected sorbent [i.e., HD-15(7)-P1(5)] was exposed to pure CO_2 at 425°*C* and 20 atm for 6.40 min. Following the test, the sorbent was removed from the reactor and analyzed using XRD. The XRD results of the fresh and the "reacted" sorbents are shown in Table 12, indicating that the amount of MgO in reacted sorbent was essentially the same as fresh sorbent, leading to the conclusion that the sorbent was not reactive toward CO_2. To determine the reason of the lack of reactivity, the specific surface area and pore volume of the sorbent was determined BET analysis. The results (shown in Table 13) indicates that the sorbent has a much lower than expected BET surface area, which may be attributed to pore closure during impregnation or sorbent agglomeration during the re-treatment after the impregnation.

Table 12. Fresh and treated sorbent analysis

Sample	Fresh	"Reacted"
CaCO3, wt%	42.7	44.5
MgO, wt%	26.6	28.1
$K_2Ca_2(CO_3)_3$, wt%	27.7	25.6
$K_2Ca(CO_3)_2$, wt%	2.9	1.7

Table 13. Sorbent physical characteristics

Sample	BET Surface area, m^2/g	Total Pore Volume, ml/g
"Reacted"	1.895	0.0072

To improve the sorbent reactivity and absorption capacity, the sorbent preparation procedure was further refined by increasing the surface area of the sorbent through modification of calcination conditions before and after impregnation by potassium carbonate.

Thirteen samples were calcined at six different temperatures and three different calcination times. The prepared sorbents were subjected to BET analysis to determine the effects of calcination conditions on the surface area and pore size distribution of the sorbent. The results are presented in Figure 28; indicating that, up 580°C, the surface area of the sorbents improves with the increasing calcination temperature and calcination time. However, above this temperature, the surface decreases with both the increasing temperature and calcination time, which may be attributed to partial sintering and agglomeration within the sorbent.

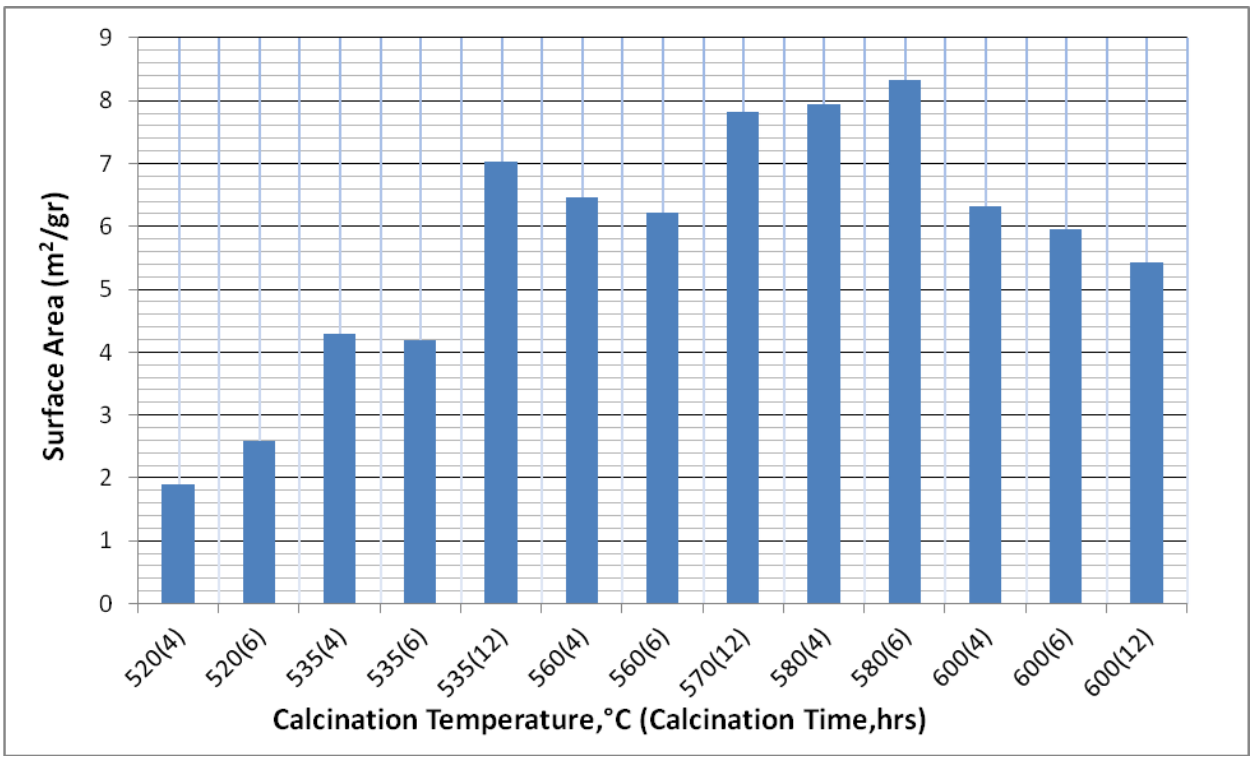

Figure 28. Effect of calcination condition on the surface area

As shown in the earlier study (Hassanzadeh and Abbasian[3]), half-calcined dolomite is generally not reactive toward CO_2, and to increase the reactivity of the sorbents, it is necessary to impregnate an alkali salt, such as potassium carbonate, into the sorbent. Therefore, calcined samples were impregnated using two different potassium solutions followed by re-calcination at 30°-50°C above the calcination temperatures used in the first calcination step. The results of the BET analyses performed on the impregnated sorbents are presented in Figure 29, indicating that the surface area of the sorbents calcined at lower temperatures (i.e., T< 550°C) improved after impregnation followed by re-calcination at the higher temperatures, while the surface areas for sorbent calcined above these temperatures decreased after impregnation and re-calcination. Furthermore, the results also indicate that longer exposure during the re-calcination step generally results in lowering of the surface area of the sorbents. As indicated above, the reduction in the surface area at higher temperatures and longer exposure time may be attributed to partial sintering and agglomeration within the sorbent at these conditions. Additionally, it can be postulated that the increase in the surface areas of the sorbent calcined at the lower temperature is probably due to

formation of new pore resulting from the calcination of the partially–calcined sorbents during the re-calcination at higher temperatures.

To confirm the observed effects of the calcination and re-calcination temperatures on the surface area of the sorbents, four identical dolomite samples were calcined at four different temperatures for 6 hours, followed by impregnation using 1 M potassium carbonate solution for 24 hours, which were followed by re-calcination at 570 °C for four hours. The results of the BET analyses of these samples are presented in Figure 30, confirming the conclusion that, while the impregnation step generally leads to pore closure, any additional calcination during the re-calcination step results in generating pores , and hence, higher surface areas.

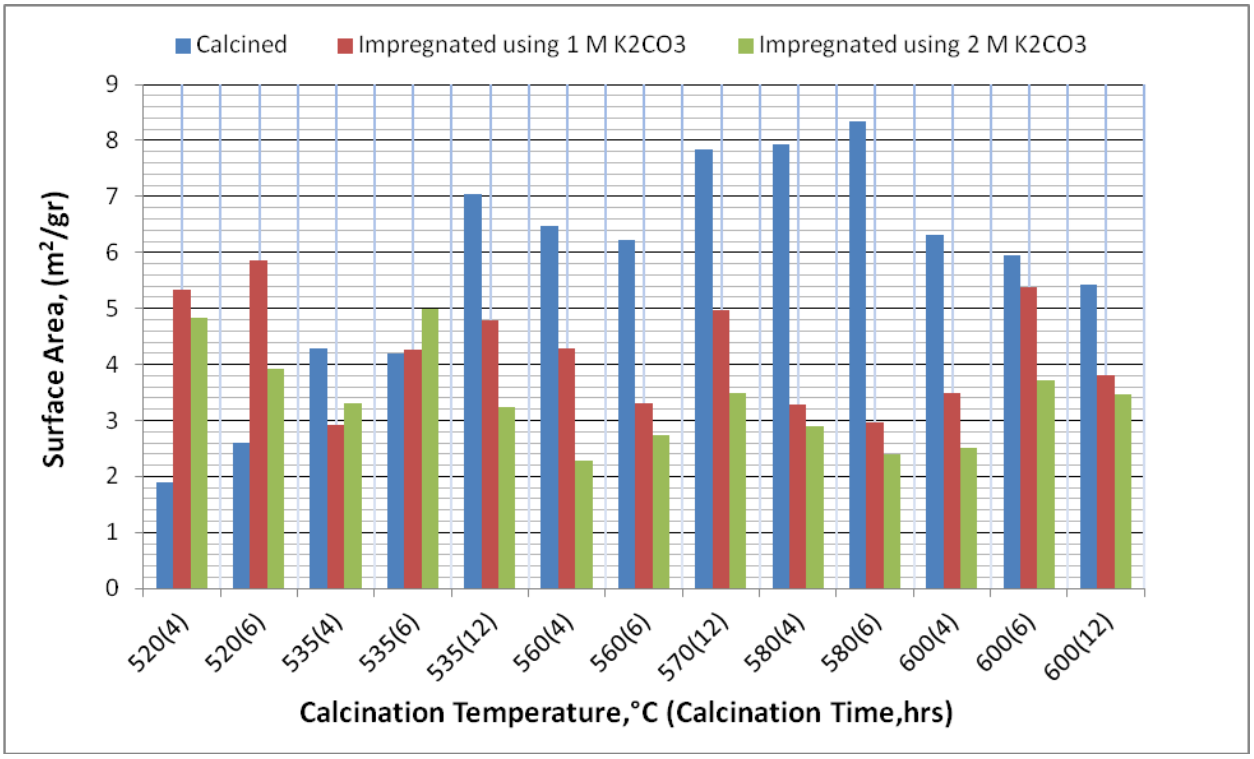

Figure 29. Effect of impregnation on the extent of surface area

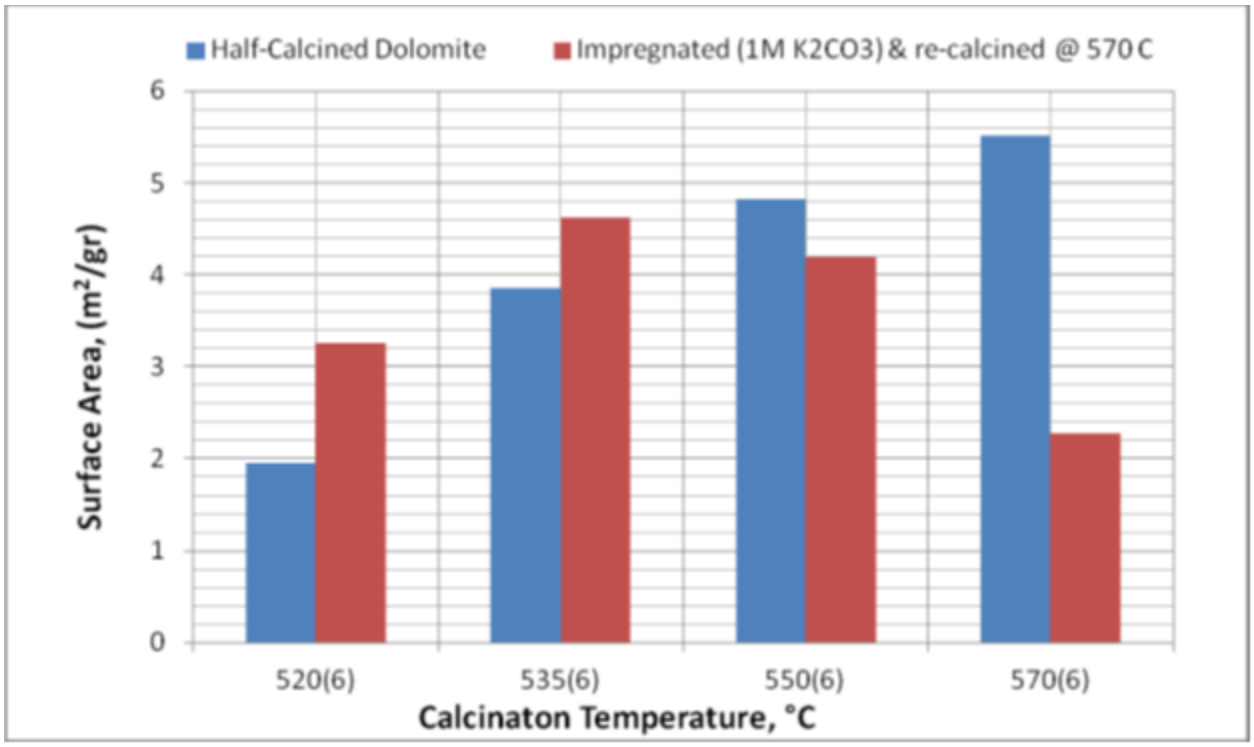

Figure 30. Effect of impregnation & re-calcination on the surface area

The CO_2 absorption capacity of these four samples [i.e., 520(6), 535(6), 550(6), 570(6)] was determined in the dispersed-bed reactor. In these tests, the selected sorbents were exposed to pure CO_2 at 425°*C* and 20 atm for 40 min. Following the test, the sorbent was removed from the reactor and analyzed using XRD. The XRD results of the "reacted" sorbents are shown in Table 14, indicating that the amount of potassium component in reacted sorbents was nominal, leading to the conclusion that the reactivity of the sorbent was low toward CO_2. In order to improve the reactivity of the sorbent, calcined samples subsequently will be impregnated by 2 M potassium carbonate solution.

Table14. XRD Analysis of the treated sorbents

Sample	520(6)	535(6)	550(6)	570(6)
$CaCO_3$ (wt %)	55.9	59.4	54.5	62.9
MgO (wt %)	23.8	23.1	21.7	26
$CaMg(CO_3)_2$(wt %)	9.2	2.1	9.0	4.2
$MgCO_3$ (wt %)	11.0	11.3	12.1	6.9
0.4 CaO.7.7 $K_2Ca_2(CO_3)_2$		Trace	-	
1 CaO.0.4 $Ca(OH)_2$			Trace	

Five samples were heated at a rate of 5°C/min to a maximum calcination temperature of 520°C and maintained at this calcination temperature for four hours. The calcined samples were cooled and impregnated using 2M potassium carbonate solution for 24 hours. The impregnated samples were filtered and re-heated at a rate of 5°C/min to a maximum re-calcination temperature of 570°C and maintained at this calcination temperature at four different re-calcination times. The prepared sorbents were subjected to BET analysis to determine the effects of exposure time at the re-calcination temperature on the surface area and pore size distribution of the sorbent. The results are presented in Table15; indicating that, after

one hour at the maximum re-calcination temperature, the surface area essentially remains constant with calcination time.

Table 15. Effect of re-calcination temperature on the surface area of the sorbents

Sample / Steps	**A**	**B**	**C**	**D**	**E**
1st Calcination-Temp ramp, °C/min	5	5	5	5	5
1st Calcination-Max Temp, °C	520	520	520	520	520
1st Calcination Time @ T_{max} , hr	4	4	4	4	4
Impregnation Salt	K_2CO_3	K_2CO_3	K_2CO_3	K_2CO_3	K_2CO_3
Impregnation solution molarity	2M	2M	2M	2M	2M
Drying Temperature, °C	N/A*	N/A*	N/A*	N/A*	N/A*
Re-calcination-Temp ramp, °C/min	5	5	5	5	5
Re-calcination-Max Temp, °C	570	570	570	570	570
Re-calcination Time @ T_{max} , hr	**0**	**1**	**2**	**3**	**4**
Surface Area, m^2/gr	1.69	3.58	3.68	3.28	3.63

*Sample was only filtered (not dried)

To investigate the effect of heating rate on the surface area and pore size distribution of the sorbent, three additional samples were heated at different heating rates to a maximum calcination temperature of 520°C and maintained at this calcination temperature for four hours. The calcined samples were cooled and impregnated using 2M potassium carbonate solution for 24 hours. The impregnated sample was filtered and re-heated at the same heating rate as the previous step to a maximum re-calcinations temperature of 570°C and maintained at this calcinations temperature at one hour. The results are presented in Table 16; indicating that the extent of surface area slightly increases with increasing temperature ramp rate, which may be attributed to a higher extent of sorbent agglomeration at higher temperature ramp rates.

Table 16. Effect of temperature ramp rate on the surface area of the sorbents

Sample / **Steps**	**F**	**G**	**H**
1st Calcination-Temp ramp, °C/min	**5**	**2**	**1**
1st Calcination-Max Temp, °C	520	520	520
1st Calcination Time @ T_{max} , hr	4	4	4
Impregnation Salt	K_2CO_3	K_2CO_3	K_2CO_3
Impregnation solution molarity	2M	2M	2M
Drying Temperature, °C	N/A*	N/A*	N/A*
Re-calcination-Temp ramp, °C/min	5	2	1
Re-calcination-Max Temp, °C	570	570	570
Re-calcination Time @ T_{max} , hr	1	1	1
Surface Area, m^2/gr	3.22	3.36	3.73

*Sample was only filtered (not dried)

Finally, two samples were calcined at the same condition as sample H but with different drying procedures. These samples were dried at different temperatures for 24 hours after impregnation before re-calcination. The results of the BET analyses of these samples are presented in Table 17, indicating that the extent of surface area decreases with drying temperature. The significant drop in the BET surface area and porosity of the sorbent is believed to be mainly due to the sorbent's agglomeration and pore closure

as the sorbent is exposed to simultaneous drying and re-calcination following impregnation. Pore closure occurs by of the deposition of potassium carbonate on the entrance of the pores in the sorbent.

Table17. Effect of drying procedure on the extent of surface area

Steps \ Sample	H	I	J
1st Calcination-Temp ramp, °C/min	1	1	1
1st Calcination-Max Temp, °C	520	520	520
1st Calcination Time @ T_{max} , hr	4	4	4
Impregnation Salt	K_2CO_3	K_2CO_3	K_2CO_3
Impregnation solution molarity	2M	2M	2M
Drying Temperature, °C (24 hr duration)	N/A*	**80**	**25**
Re-calcination-Temp ramp, °C/min	5	5	5
Re-calcination-Max Temp, °C	570	570	570
Re-calcination Time @ T_{max} , hr	1	1	1
Surface Area, m^2/gr	3.73	4.8	5.81, 5.53

*Sample was only filtered (not dried)

The CO_2 absorption capacity of sample J was determined in the dispersed-bed reactor. In this test, the sorbent was exposed to pure CO_2 at 425°C and 20 atm for 40 min. Following the test, the sorbent was removed from the reactor and analyzed using XRD. The results are presented in Table 18, indicating that the conversion of carbonation reaction increased by 33% compared to the earlier results reported above.

Table 18. XRD analysis of the treated sorbents

Composition \ Sample	550(6)	J
$CaCO_3$ (wt %)	54.5	45.1
MgO (wt %)	21.7	18.7
$CaMg(CO_3)_2$ (wt %)	9.0	18.6
$MgCO_3$ (wt %)	12.1	13.7
K_2CO_3 (wt %)	-	1.0
K_6MgO_4 (wt %)	-	2.8
1 CaO.0.4 $Ca(OH)_2$ (wt %)	Trace	-
Conversion(%)	29.0	40.7

Based on the results reported above, a large batch of dolomite was calcined at 520°C for four hours. The calcined sorbent was impregnated using 2M potassium carbonate solution for 24 hours and the impregnated sorbent was re-calcined at with one hour at 570°C . The CO_2 absorption capacity of the sorbent was determined in the dispersed-bed reactor.

To evaluate the sorbent in a well dispersed differential reactor, about 1 gram of the sorbent was distributed in 8 cm of quartz beads (see Figures 25 & 26). The sorbent was exposed to pure CO_2 at 425°*C* and 20 atm for pre-determined periods (i.e., 5, 10, 20 and 40 min]. Following each test, the sorbent was removed from the reactor and analyzed using XRD. To assess the reproducibility of the packed-bed carbonation tests, one additional test was conducted in which the sorbent was exposed to the reactant gas for 40 minutes.

The XRD results of the "reacted" sorbents are shown in Table 19, indicating significant differences in the composition of the reacted sorbents, especially with respect to MgO carbonation. The conversion of the sorbent was calculated based on the XRD analysis in Table 19 and the results are presented in Figure 31. The observed variability in the sorbent conversion may be attributed to possible differences in the key operating parameters, experimental procedure, and/or XRD analysis procedure. To determine the impact of XRD analysis, one of the reacted samples ["Reacted" for 10 min] was micronized and mixed with Silica prior to XRD analysis. The results are shown in Table 20, indicating that there are amorphous materials inside the sample, which may lead a systematic error in XRD analysis.

Table 19. Fresh and treated sorbent analysis

Sample wt%	Fresh	"Reacted" 5 min	"Reacted" 10 min	"Reacted" 20 min	"Reacted" 40 min	"Reacted" 40 min
CaCO3	48.8	46	40.9	41.7	34.2	33.1
MgO	29.1	22.9	22.9	20.2	18.8	15.5
$CaMg(CO_3)_2$	-	11.3	14.0	12.1	25.6	29.5
$MgCO_3$	-	5.6	8.6	11.8	9.9	11.2
$K_2Ca_2(CO_3)_3$	21	13.6	13.2	14	11.1	10.2
$K_2Ca(CO_3)_2$	-	0.5	0.5	0.2	0.4	0.4

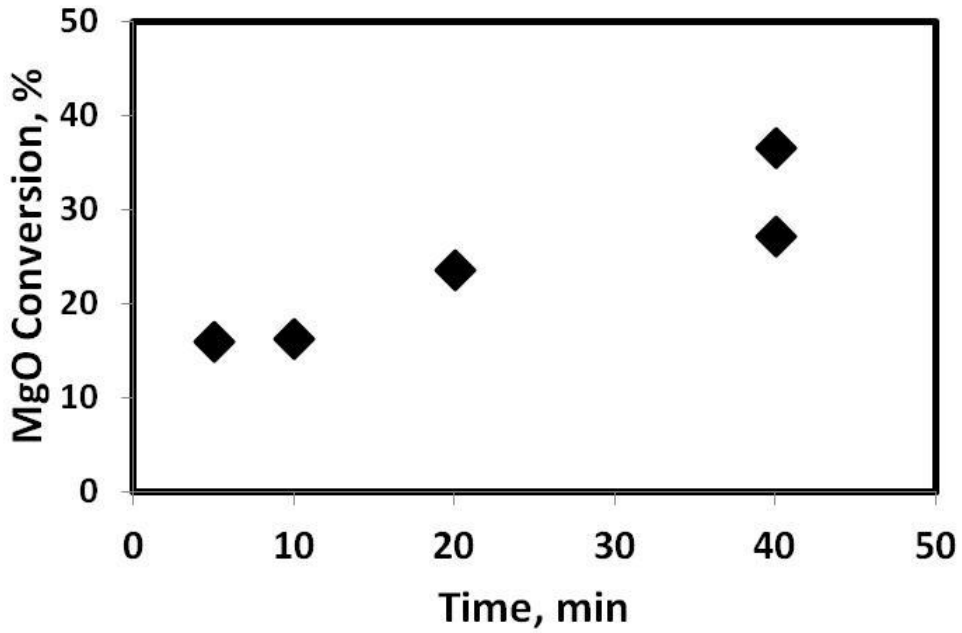

Figure 31. Reactivity of the sorbent (packed-bed)

Table 20. Effect of sorbent particle size on XRD analysis

Sample Wt%	"Reacted" 10 min	Micronized "Reacted" 10 min
$CaCO_3$	40.9	43.8
MgO	22.9	20.3
$CaMg(CO_3)_2$	14.0	14.0
$MgCO_3$	8.6	8.5
$K2Ca_2(CO_3)_3$	13.2	6.0
$K_2Ca(CO_3)_2$	0.5	0.2
Amorphous	-	7.2

To emulate half-calcined, fresh sorbent, and reacted sorbent, several mixtures of known composition (without amorphous phases) were prepared and subjected to XRD analysis to more conclusively assess the accuracy of the XRD analysis.

To determine the effect of drying condition after impregnation on the sorbent's reactivity and CO_2 sorption capacity, six identical dolomite samples were calcined at 550°C for 4 hours followed by impregnation using 2 molar (2M) potassium carbonate solution for 24 hours. The prepared samples were dried at different conditions (shown Table 21) followed by re-calcination at 600 °C for one hour. The evaporation rates were measured by weight loss using BLUE M ELECTRIC drier with an accuracy of 0.1g. In a typical test, a tared pan is loaded on the balance, and sorbent is poured into the tray, and the weight loss is measured over time. In this series of experiments, three major variables were selected to control the rate of evaporation. These variables included the drying temperature, the exposed surface area at the air/sorbent interface, and the relative humidity of the air.

Table 21. Drying conditions of sorbent at different conditions

Sample	A	B	C	D	E	F
Drying Temperature, °C	50	50	15	15	80	120
Drying Humidity, %	13	55	90	90	Ambient	Ambient
Exposed Surface area to weight, cm^2/gr	10.4	10.4	0.74	10.4	0.74	10.4

The CO_2 absorption capacity of these six samples [i.e, A through F] was determined in the dispersed-bed reactor. In these tests, the selected sorbents were exposed to pure CO_2 at 425°C and 20 atm. Following the test, the sorbent was removed from the reactor and analyzed using XRD. Another series of tests were conducted with sorbents A and F at temperature of 425°C and 20. Table 22 shows the composition of the six model sorbents determined by gravimetric measurement. Samples 20307-18-1, 20307-18-2, 20307-18-3 and 20307-20 represent expected ranges of composition in the fresh sorbent (before being exposed to CO_2). Sample 20307-19 emulates half-calcined dolomite and Sample 20307-21 represents carbonated sorbent (after being exposed to CO_2).

Table 22. Gravimetric concentrations in mixtures

Sample	20307-18-1	20307-18-2	20307-18-3	20307-19	20307-20	20307-21
CaCO3, wt%	41.59	35.77	31.74	24.05	47.7	41.21
MgO, wt%	24.98	22.16	16.39	9.81	29.9	19.2
$CaMg(CO_3)_2$, wt%	14.83	22.72	30.95	66.14	0	0
$MgCO_3$, wt%	5.88	6.78	7.42	0	0	13.27
$K_2Ca_2(CO_3)_3$, wt%	10.87	10.76	11.56	0	19.1	22.63
$K_2Ca(CO_3)_2$, wt%	1.82	1.81	1.94	0	3.3	3.72
Sum	99.97	98.19	98.06	100	96.7	100.03

Rietveld refinements were carried out using data for each of the "pure" components, to optimize the lattice parameters, profile coefficients, and structural models. These were all fixed in the first Rietveld refinements using data for the mixtures 20307-18-n. These refinements yielded an average concentration error of 1.4 wt% absolute. Refining additional parameters (cells and profiles) did not change the errors much. This result was disappointing, therefore, an attempt was made to investigate the details of the errors by mainly focusing on the negative errors, since it is generally easier to increase the concentration of a phase by refining additional parameters than to decrease it. The largest errors were positive for the concentration of MgCO3. This phase was present in relatively low concentrations, and its peaks are broad. Refining the profile *X* (size broadening) coefficient tended to result in values which were too high, based on examining the difference curve. The correlation between the profile coefficient and the background parameters made it hard to describe the tails of the weak magnesite peaks. Better concentrations were obtained by fixing the magnesite profile coefficient to a reasonable value based on visual examination of the raw patterns. The most accurate concentrations were obtained by slightly modifying the CaCO3 and MgO structural models, and including preferred orientation corrections for dolomite and fairchildite. The final results are reported in Table 23. The average concentration error is 0.8 wt% absolute. However, the average error on the MgO concentration is 0.3 wt% absolute. A comparison of the calculated sorbent conversion before and after XRD re-calibration is presented in Figure 32, indicating that the effect of XRD analysis error on the extent of conversion is negligible. The results obtained in the drying tests are presented in Figure 33, indicating that rate of evaporation in sample C is significantly lower than the other samples.

Table 23. Quantitative error analyses for mixtures

Sample	20307-18-1	20307-18-2	20307-18-3	20307-19	20307-20	20307-21
CaCO3, wt%	0.21	-0.57	-0.54	0.05	0.6	0.49
MgO, wt%	-0.38	-0.56	0.21	-0.21	0.4	0.3
$CaMg(CO_3)_2$, wt%	0.77	1.08	1.25	0.16	0	0
$MgCO_3$, wt%	0.92	1.42	1.38	0	0	1.33
$K_2Ca_2(CO_3)_3$, wt%	-0.32	-0.41	-0.74	0	-0.8	-1.63
$K_2Ca(CO_3)_2$, wt%	-1.27	-1.46	-1.56	0	-0.2	-0.52
Sum	-0.07	-0.50	0.00	0.00	0.00	-0.03

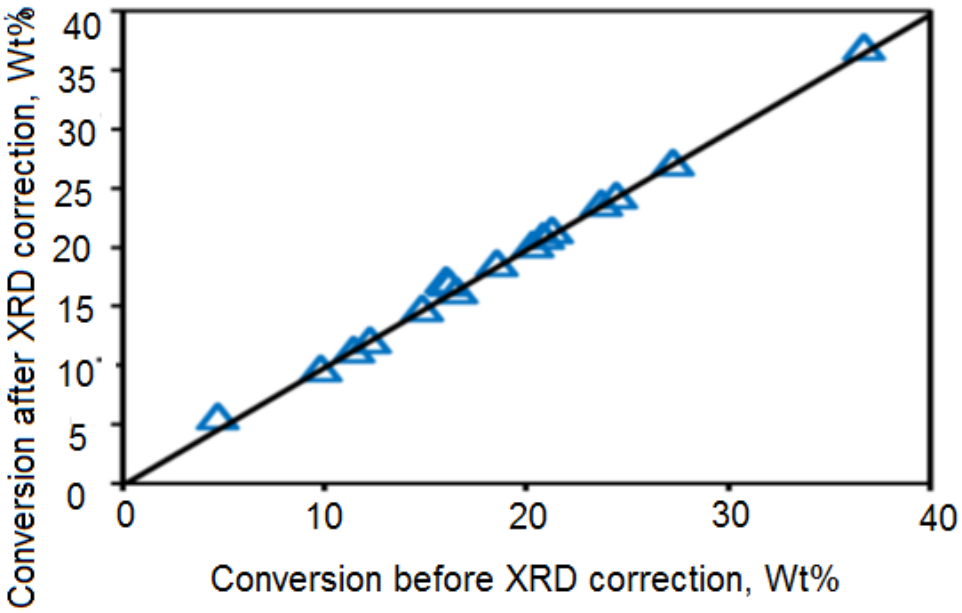

Figure 32. Calibration of XRD analysis

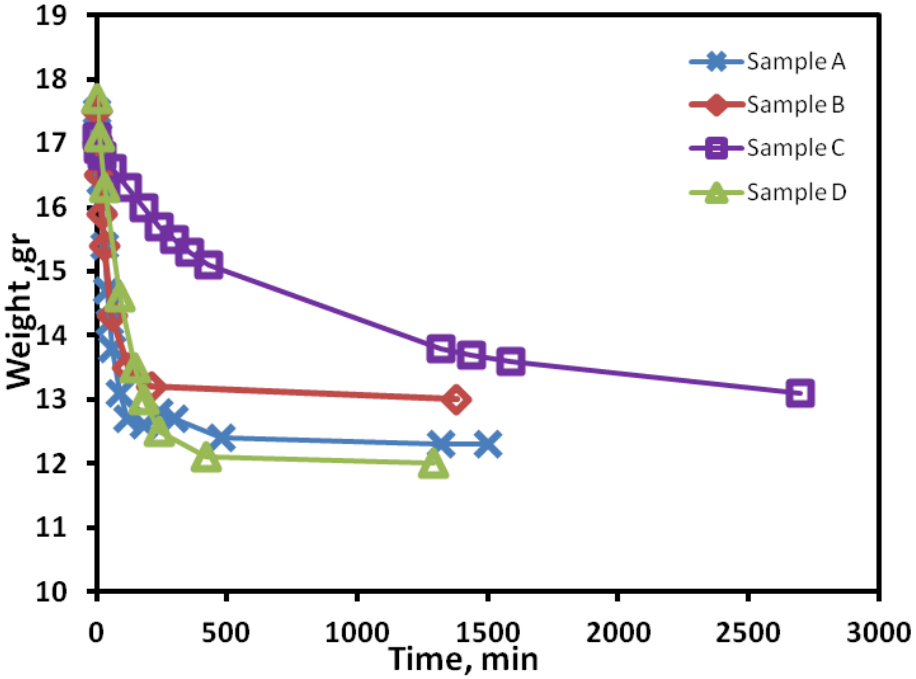

Figure 33. Effect of drying condition on weight loss of sorbent

The sorbent conversion in the dispersed-bed reactor tests for various sorbents, calculated based on the XRD analysis of the “fresh” and “reacted” sorbents are presented in Figure 34, indicating that sample E has the highest conversion leading to the conclusion that optimum drying temperature is about 90°C. The

results of the reproducibility tests conducted in the dispersed-bed reactor are presented in Table 24, indicating that the dispersed-bed test results can be reproduced with a good degree of accuracy.

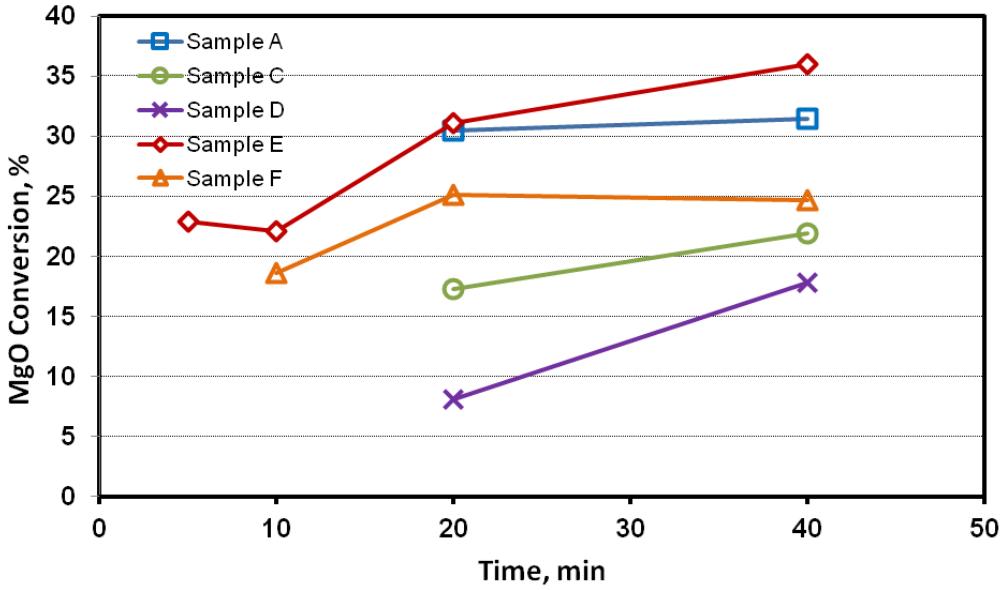

Figure 34. Effect of drying procedure on sorbent reactivity

Table 24. Reproducibility of the packed-bed tests

Sample	A	F
CO_2 Exposed time, min	10	40
Conversion (Run1), %	16.3	31.5
Conversion (Run2), %	17.5	30.7
Conversion (Run3), %	18.6	28.3

To determine the optimum sorbent preparation procedure, several sorbent formulations were prepared and evaluated in the dispersed-bed reactor. The "best" sorbent formulation developed in the earlier study[3,4] (i.e., EP 68) was reproduced and evaluated to confirm the reproducibility of the sorbent preparation technique. To produce this duplicate sorbent formulation (HD37-P1), a batch of the same dolomite (i.e., D245) with a particle diameter of 425-600µm was prepared and calcined at 550 ºC for four hours. The calcined sorbent was impregnated using 2M potassium carbonate solution for 20 hours and dried in the oven at 120°C for four hours. The dried impregnated sorbent was recalcined at 550°C for four hours.

The CO_2 absorption capacity of the HD-37-P1 sorbent was determined in the dispersed-bed reactor. In these tests, the sorbent was exposed to pure CO_2 at 425°C and 20 atm for 40 min. To improve the accuracy of the results obtained in these tests, duplicate tests were conducted with the sorbent. Following each test, the reacted sorbent was removed from the reactor and analyzed using XRD. A comparison of the CO_2 capacities of various reacted sorbents obtained from dispersed-bed reactor and determined from the XRD analysis are presents in Table 25. The results indicate that the CO_2 capacity of the HD37-P1sorbent was 9.7%, which is close to that reported with EP68 sorbent (9.3%), confirming the reproducibility of the sorbent preparation procedure.

Table 25. CO_2 capacities of various sorbents

Sorbent property	EP68	HD37-P1	HD38-P1	HD43-P2
CO_2 Capacity, gr/100gr of sorbent	9.3	9.7	8.2	8.7
Particle diameter, μm	425-600	425-600	150-180	150-180
Impregnation Solution Molarity, M	2	2	2	1
RE-Calcination Temperature, °F	550	550	550	500
K/Mg , molar ratio		0.14	0.25	

The effect of the particle size on the CO_2 absorption capacity of the sorbents was investigated by preparing a new sorbent (HD38-P1) in the particle diameter of 150-180μm using the same dolomite (D245) and preparation procedure used for HD37-P1sorbent. The CO_2 absorption capacity of these sorbents are also presented in Table 25, indicating that the CO_2 capacity of the sorbents decreases with decreasing particle size, which may be attributed to the higher potential for pore closure caused by the higher potassium incorporated into the sorbent during impregnation.

To minimize sintering during re-calcination and possible pore closure during impregnation, another sorbent formulation (HD43-P2) was prepared at a lower re-calcination temperature of 500°C using a lower molarity potassium carbonate solution (1M) during impregnation. Comparison of the XRD results obtained with HD43-P1 and HD-38-P1 (Table 1) indicate that by lowering the potassium carbonate concentration in the impregnation solution and reducing the re-calcination temperature, the CO_2 capacity of the sorbent increases from 8.2% to 8.7%.

As shown in the earlier study (Hassanzadeh and Abbasian[3]), the depth of penetration of potassium carbonate solution was limited to a relatively thin outer layer (about 40 μm thick), which limited the sorbent capacity. The short depth of penetration in the sorbent may be attributed to the low porosity of the uncalcined inner core of the sorbent following the initial calcination stage before impregnation. Therefore, to confirm this postulate, the HD43-P2 sorbent was exposed to XRD test before impregnation by potassium carbonate. The XRD results indicate that a major fraction of dolomite does not decompose during the 4-hr calcination, and that the residual dolomite from half-calcination process is decomposed during re-calcination process. The effect of calcination time on the depth of potassium carbonate penetration (and consequently on sorbent capacity) during impregnation was investigated by preparing three additional sorbents (HD50-P2, HD45-P2, and HD46-P2) using identical preparation procedure (1M potassium carbonate impregnation and 500 °C re-calcination), except at different duration of calcination at 550°C (4, 8, and 12 hours, respectively). The effect of the duration of initial calcination on the CO2 capacities of the sorbents is presented in Figure 35; indicating that the capacity of the sorbent generally increases by increasing the duration of the initial calcination stage.

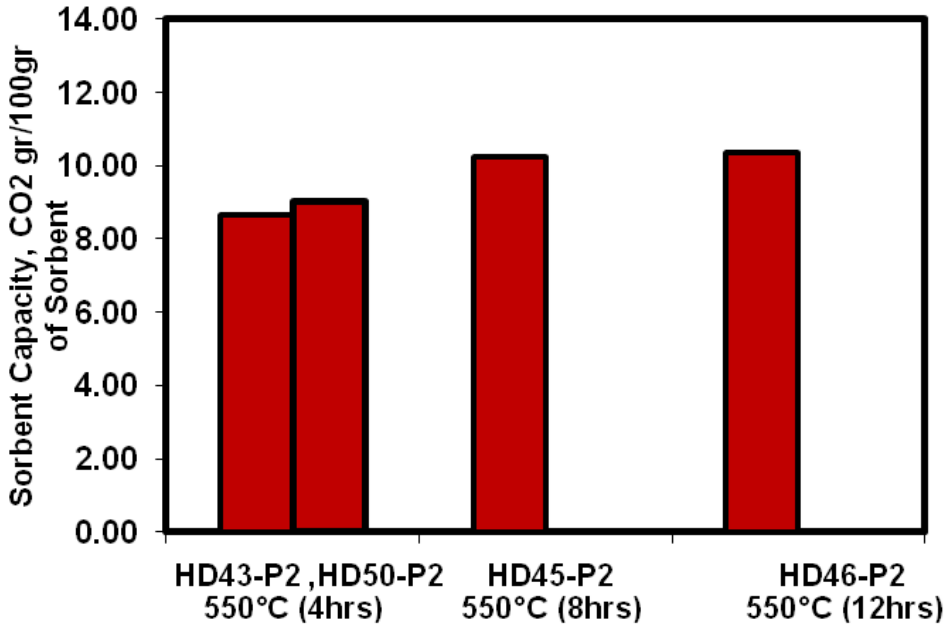

Figure 35. Effect of calcination time on the capacity of the sorbent

The effect of sorbent residence time during carbonation on the extent of sorbent carbonation is Figure 36; indicating that the extent of sorbent carbonation is not affected by the sorbent residence time beyond 40 minutes, which can be attributed to pore closure of the sorbent in the outer layer of the sorbent during the carbonation reaction.

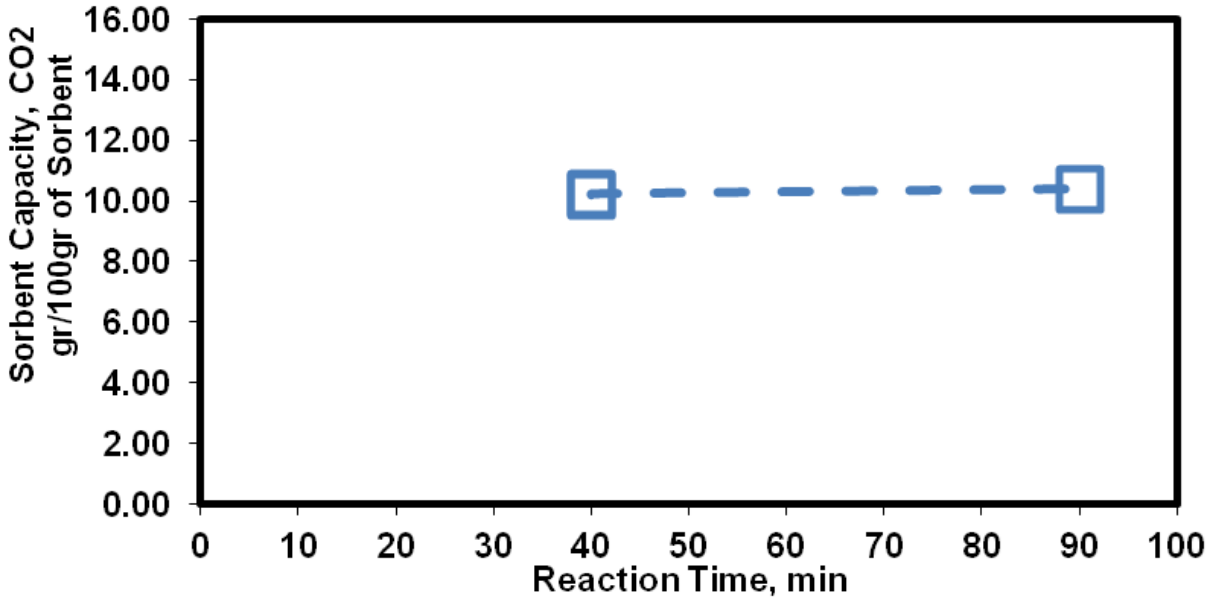

Figure 36. Effect of reaction time on the capacity of the sorbent HD45-P2

Among all the preparation parameters studied above, the potassium/magnesium (K/Mg) ratio was identified as the key variable affecting the CO_2 capacity of the sorbent. The effect of Potassium/Magnesium (K/Mg) ratio on the CO_2 capacity of all sorbents after 40 minutes residence time in

the dispersed-bed reactor in shown in Figure 37. The result clearly indicates that the optimum K/Mg ratio is about 0.15 that has generally been achieved when the sorbent was impregnated using a 1M solution of potassium carbonate. Furthermore, as shown in Figure 38, that the optimum drying temperature during sorbent preparation appears to be in the range of 70°-100°C. Additionally, as shown in Figure 39, the CO_2 capacity of the sorbent decreases as the re-calcination temperature is increased from 500°C to 550°C, suggesting possible sintering of the sorbent at the higher temperature.

Based on the results obtained in this study, the sorbent formulation HD52-P2 was identified as the "best" sorbent formulation and a large batch (one kg) of the HD52-P2 sorbent was prepared for the parametric study. The preparation parameters for the HD52-P2 are presented in Table 26.

The effect of the reaction temperature on the carbonation reaction rate involving HD52-P2 sorbent was investigated in a series of tests in which the sorbent was exposed to pure CO_2 and 20 atm at different temperatures and sorbent residence times. The extent of sorbent conversion at each operating condition was determined by analyzing the reacted sorbent using XRD. The results obtained in this series of tests are presented in Figure 40, indicating that as long as the absorption temperature is below 450°C, the reactivity of the sorbent improves with increasing temperature (i.e. 340° to 450°C). The lower conversion in the sorbent reactivity at 490°C is due to the significantly higher equilibrium CO_2 partial pressure in carbonation reaction at higher temperatures, as shown in Figure 41. The higher equilibrium CO_2 partial pressure results in lower concentration driving force, which is the difference between the CO_2 partial pressure in the gas mixture and the CO_2 equilibrium pressure at the reaction operating temperature (PCO_2-P_e), leading to lower reaction rate at higher temperatures.

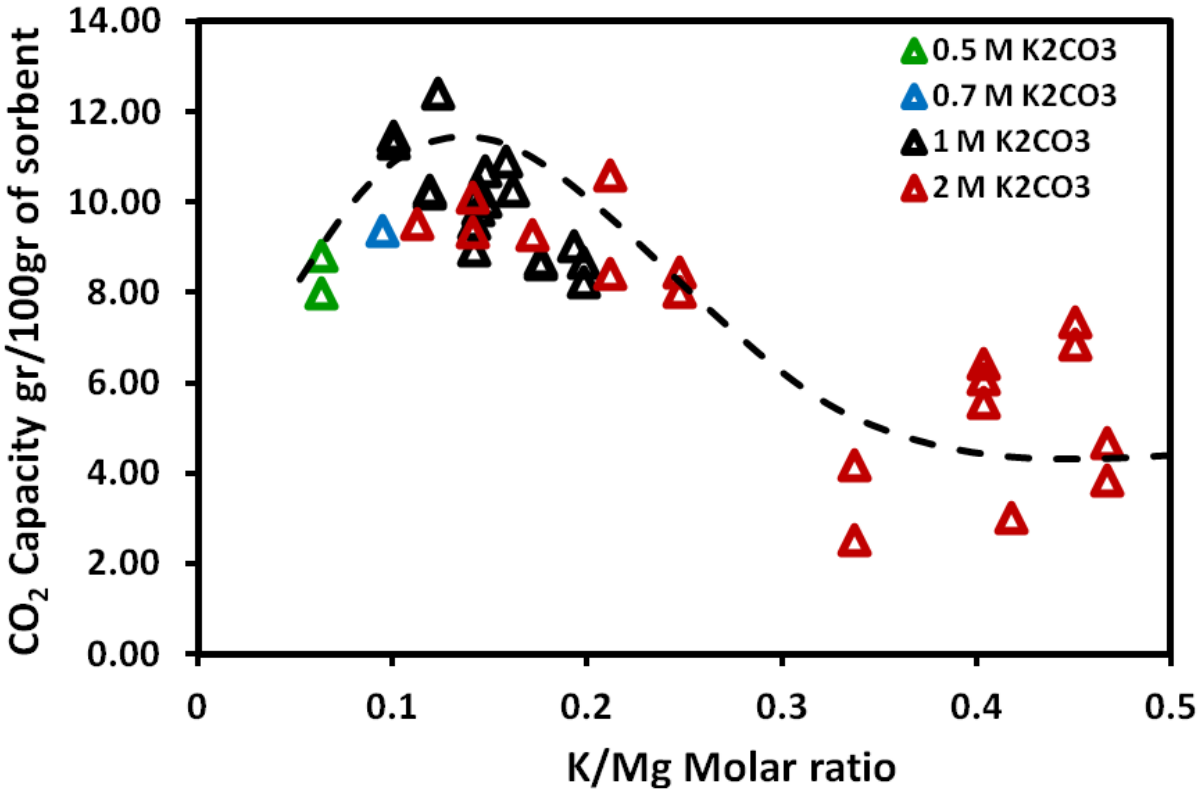

Figure 37. Effect of K/Mg ratio on the capacity of the sorbent

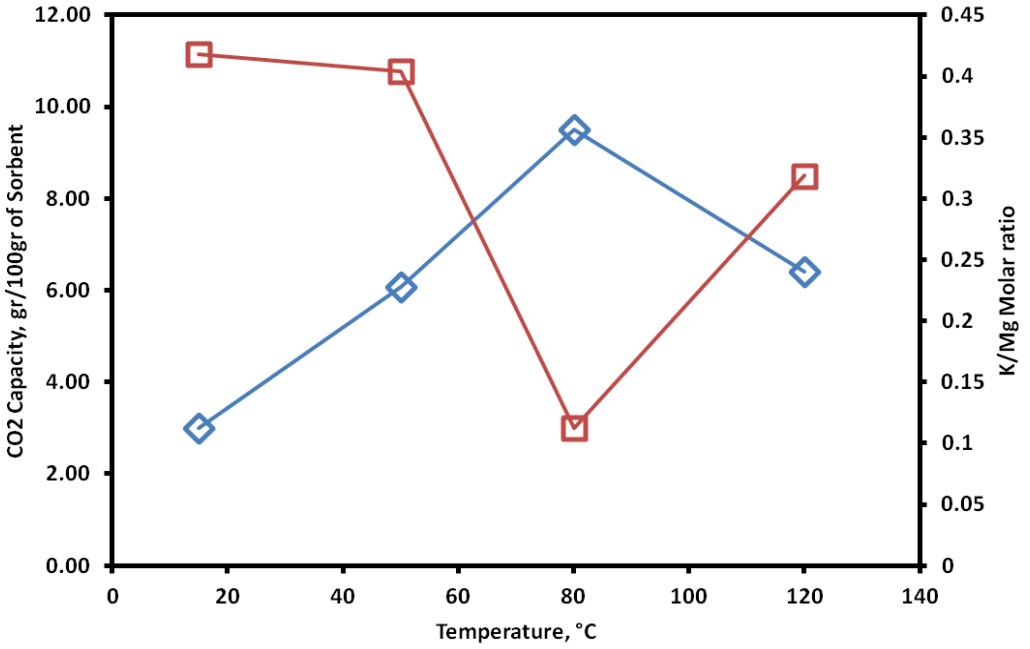

Figure 38. Effect of drying temperature on K/Mg ratio and CO_2 capacity of the sorbent

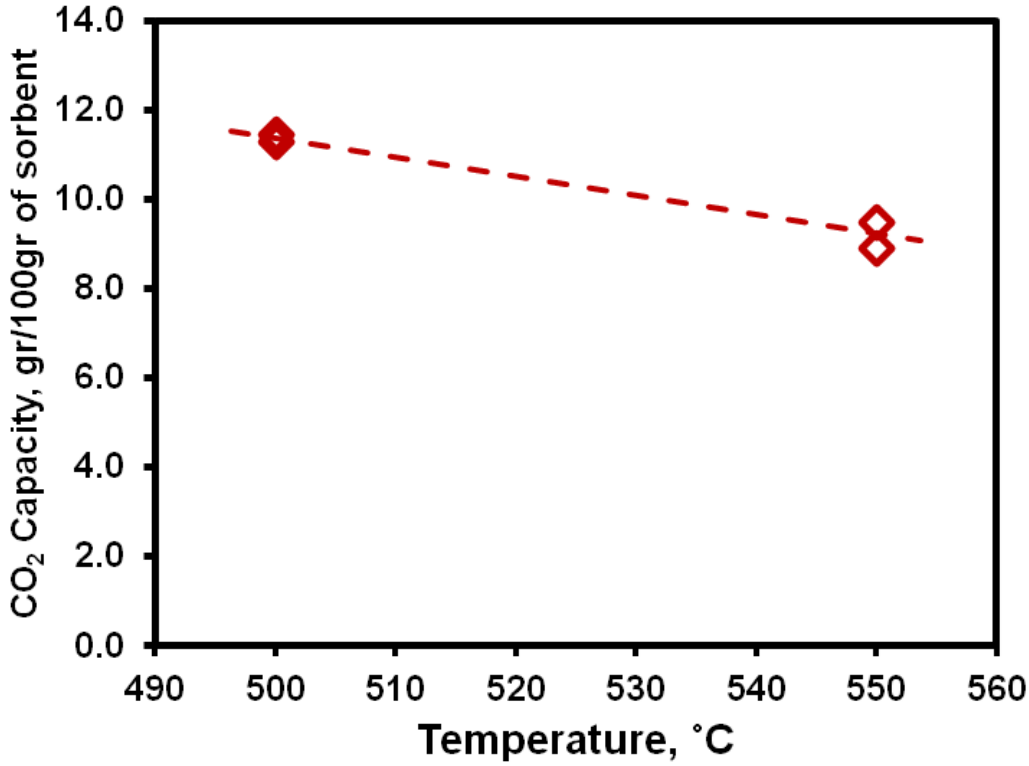

Figure 39. Effect of re-calcination temperature on CO_2 capacity of the sorbent

Table 26. Preparation parameters for HD52-P2 sorbent

Preparation Parameters	HD52-P2
Sorbent particle diameter, μm	150-180
Calcination temperature, °C	520
Calcination temperature ramp, °C/min	1
Duration of calcination, hr	8
Concentration of potassium carbonate in the impregnation solution, mol/lit (M)	1
Duration of impregnation, hr	20
Drying temperature, °C (post-impregnation)	90
Humidity during drying, %	ambient
Duration of drying, hr	24
Re-calcination temperature, °C (post-drying)	470
Calcination temperature ramp, °C/min	1
Duration of re-calcination, hr	4

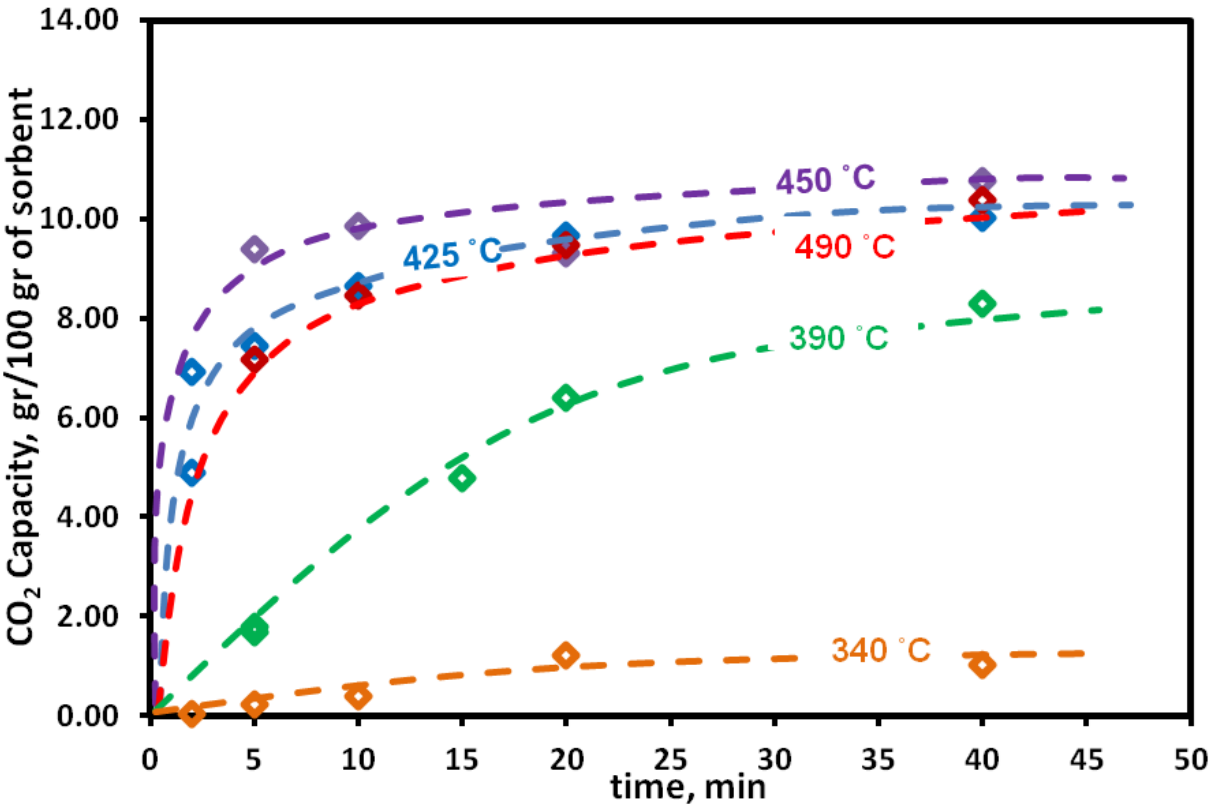

Figure 40. Effect of temperature on the absorption reactivity of the HD52-P2 sorbent

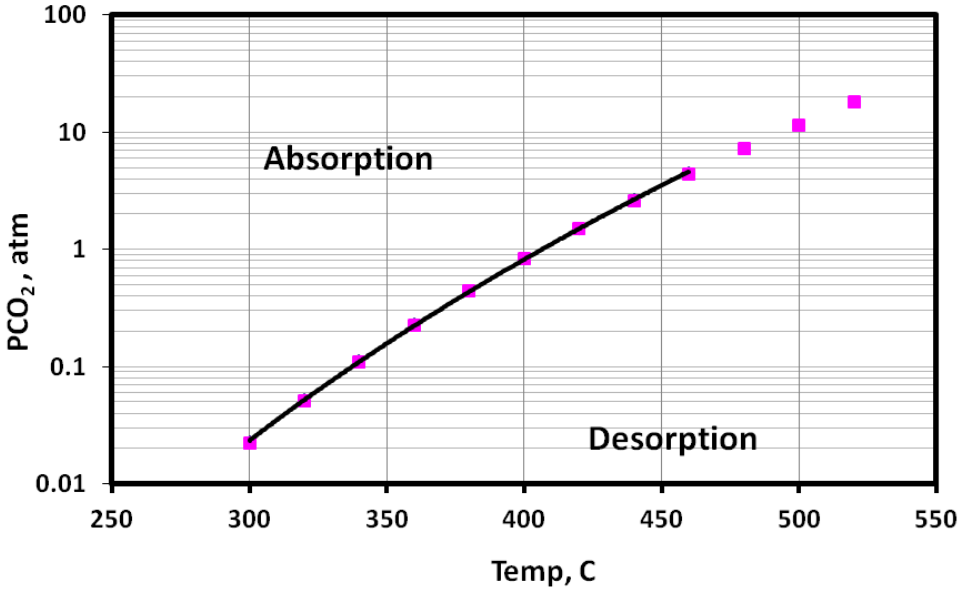

Figure 41. MgO-CO_2 reaction equilibrium
(data obtained from JANAF Tables, 1986)[50]

The reversible chemical reaction between the porous MgO-based sorbent and CO_2 can be expressed as follow:

$$MgO(s) + CO_2(g) = MgCO_3(s) \quad (A)$$

The intrinsic rate of reaction can generally be described by the following equation:

$$r_{MgO} = -[1/(4\pi r_i^2)].[(dN_{MgO})/dt] = k_s.(C_i-C_e)^n \quad (51)$$

The dependence of the intrinsic reaction rate constant k_s on temperature is expressed in terms of the Arrhenius equation:

$$k_s = k_{s0}.e^{(-Ea/RT)} \quad (52)$$

To determine the order of reaction (n), the intrinsic reaction rate constant (k_s), and the activation energy (E_a), the initial slopes of the conversion curves [i.e., $(dX/dt)_{t=0}$] were obtained from the dispersed- bed experimental data (see Figure 42) and the order of reaction was obtained by the slope of $Ln(dX/dt)_{t=0}$ vs. $Ln(C_b-C_e)$. The results presented in Figure 43 indicate that the order of the carbonation reaction with respect to CO_2 concentration can be assumed to be one. Similar gas/solid reactions involving alkali/alkaline material with reactant gases such as CO_2 and SO_2, has been generally reported as first order in literature. The activation energy of the reaction was obtained by the Arrhenius plot of the intrinsic rate (see Figure 44) to be 134 kJ/mol for the temperature range of 350° to 420°C.

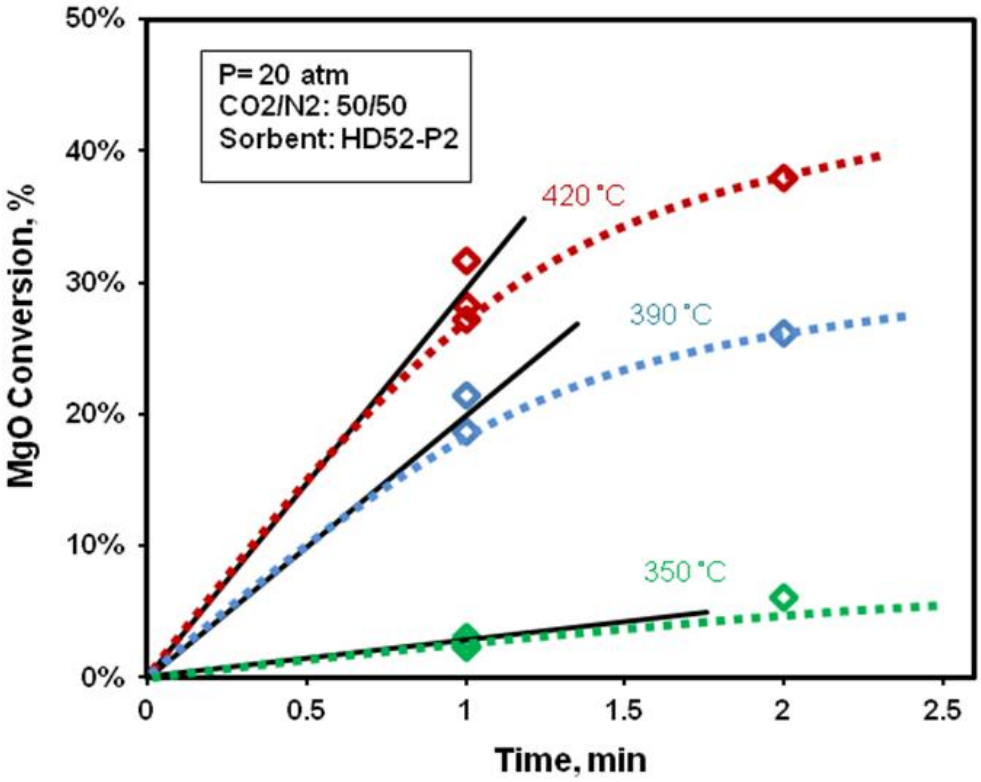

Figure 42. The initial slopes of the carbonation curves at different temperatures

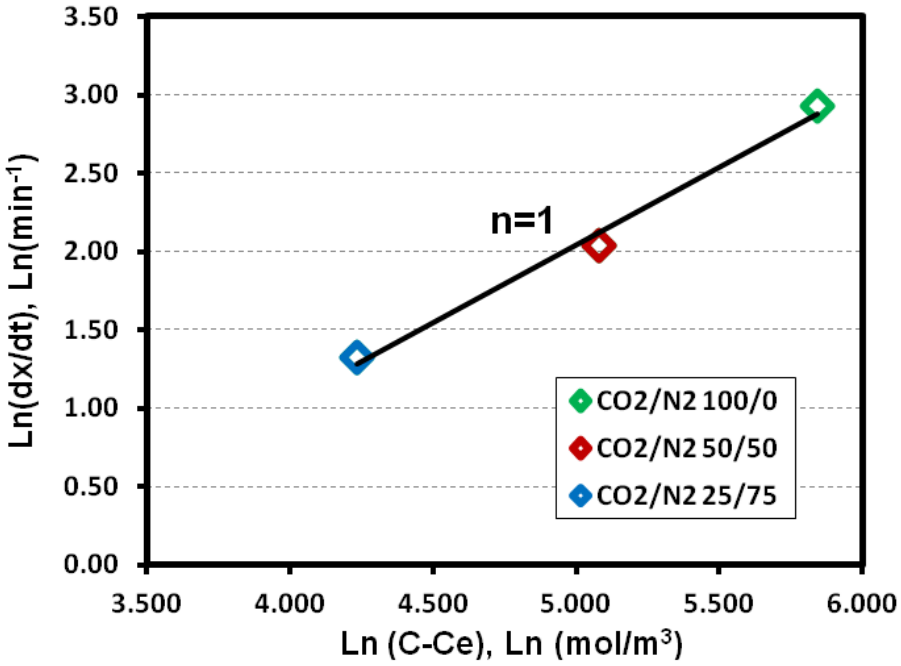

Figure 43. Determination of the order of carbonation reaction with respect to CO_2 concentration

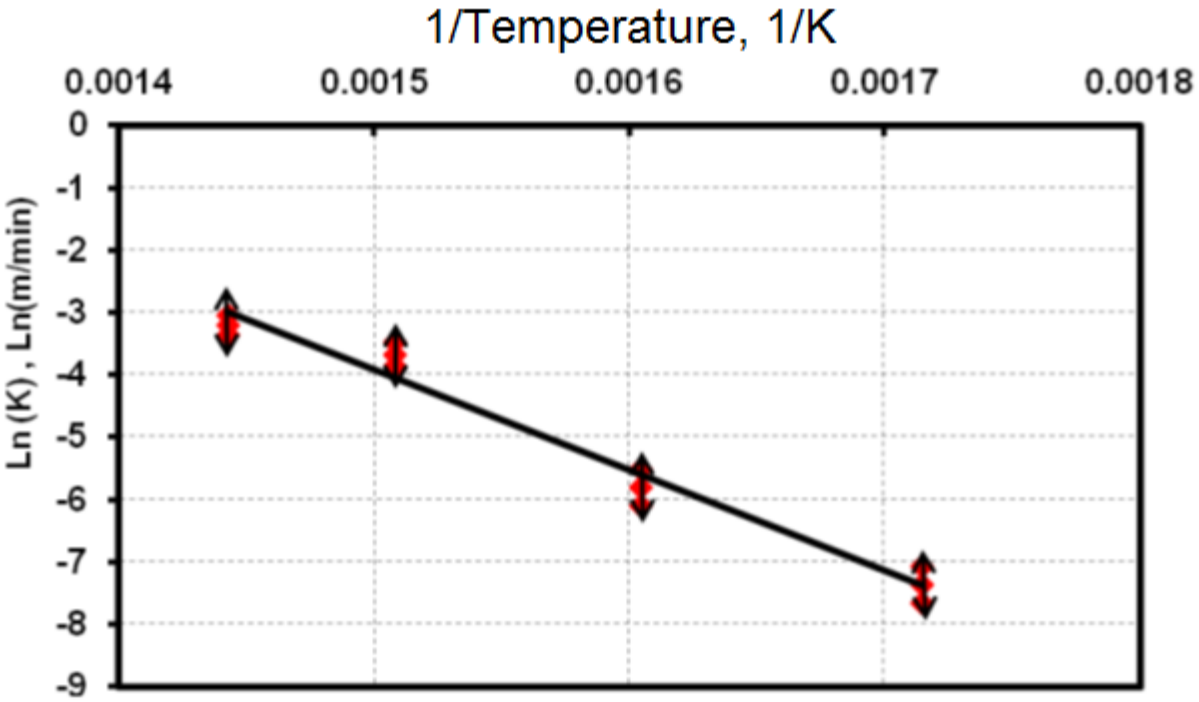

Figure 44.Determination of activation energy of reaction

***Activation Energy* = 134** *kJ/mol*

To determine the impact of steam on the reactivity of the sorbent, samples of the sorbent were exposed to nitrogen environment containing 10, 20 and 30%mol steam at 420˚C and 20 atm for 1 hour. Following the pretreatment, the sorbents were exposed to a $CO_2/N_2/H_2O$ mixture at 420 °C and 20 atm, with the same H_2O content of the pretreatment, 50% CO_2 and balanced with N_2. Following each test, the sorbent was removed from the reactor and analyzed using XRD. X-ray diffraction measurements were conducted with a Bruker D2 Phaser diffractometer. Quantitative phase analyses were determined by the Rietveld method using GSAS and peak assignments were determined through comparison with X-ray databases.

A comparison of the CO_2 capacities of reacted sorbents with different steam content obtained from dispersed-bed reactor and determined from the XRD analysis is presents in Figure 45. The results indicate that the presence of steam significantly enhances the sorbent reactivity and capacity. The effect of steam in increasing the porosity and changing the pore size distribution has been reported for dolomite and limestone by others (Dobner, Hughes, and Laursen)[51-53]. Wolf and at el [54] found that the adsorption of H_2O on the surface of Pt/MgO catalyst, used for water-gas shift reaction, is very strong, and a transient $Mg(OH)_2$ component is created as the catalyst is exposed to the H_2O environment. Liu and Shih[55], who studied calcium sulfation reactions in the presence of humid simulated flue gases, postulated that H_2O enhances the carbonation reaction by forming a region of dense water vapor around the reacting MgO particles where CO_2 reacts to form carbonate ions and H^+ ions, and the released Mg^{2+} ions can react with the carbonate ions to form $MgCO_3$.
To determine the impact of steam on the reactivity of the sorbents at different temperatures, the HD52-P2 sorbent was directly exposed to reactant gas mixtures containing 50% CO_2, 10% & 30% H_2O, and N_2 (without pretreatment with H_2O/N_2 mixture) in the temperature 300-430 °C and 20 atm for 5 minutes. The results are presented in Figure 46; indicating that the CO_2 capacity of the sorbent increases with steam concentration in the reactant gas mixture. The results also indicate that the highest conversion is achieved at 360˚C.

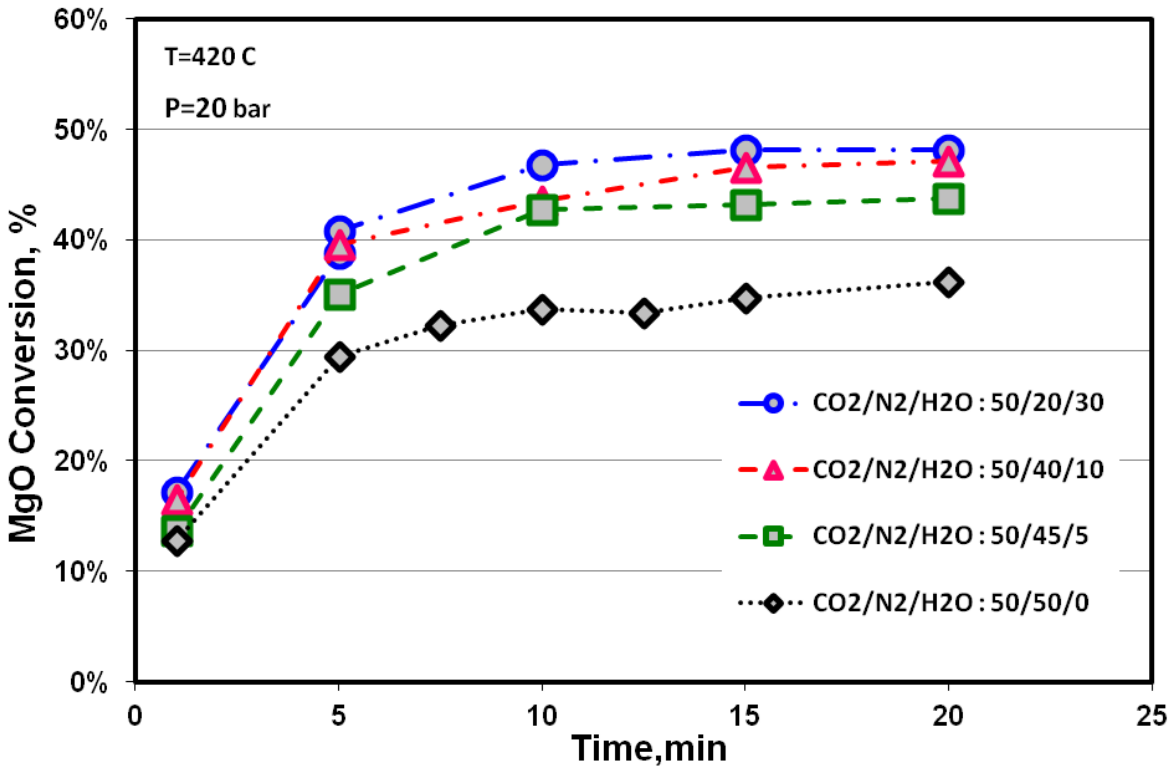

Figure 45. Effect of steam on sorbent reactivity and capacity

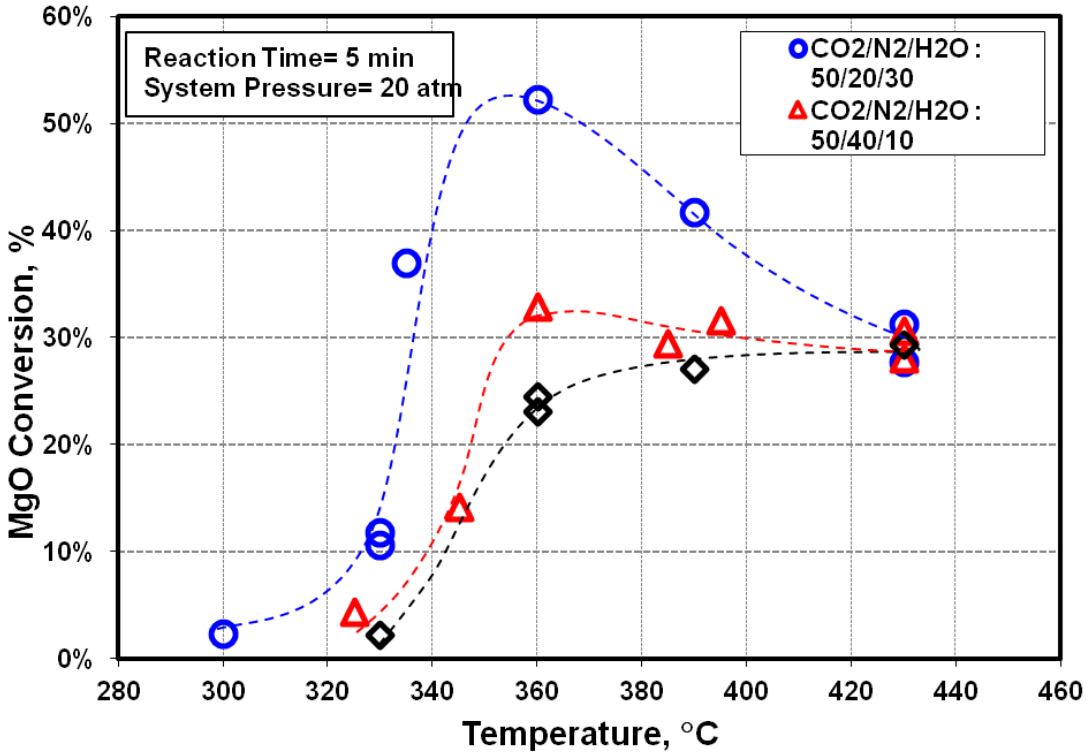

Figure 46. Effect of steam on sorbent reactivity at different temperatures

Based on our own experimental results, as well as on work by others (Kato[56] and Liu[55]), the following reaction mechanism for MgO carbonation in the presence of steam is assumed:

$MgO + CO_2 = MgCO_3$ (A)

$MgO + H_2O = MgO.H_2O^*$ (F)

$MgO.H_2O^* + CO_2 = MgCO_3 + H_2O$ (G)

When steam is not present in the reacting gas mixture, the carbonation reaction pathway is through Reaction (A), and the carbonation reaction rate of MgO monotonically increases with increasing temperatures. However, with the presence of steam in the reacting gas, the carbonation reaction pathways include all three reactions. Under this condition, because of the thermodynamic limitation, the extent of MgO hydration in Reaction (F) decreases with increasing temperatures, while the rate of carbonation of the hydrated MgO [i.e., Reaction (G)], significantly increases with increasing temperatures, resulting in maximum conversion at 360°C. Above this temperature, as the extent of MgO hydration decreases, the contribution of Reaction (G) also decreases, and appears to diminish in the vicinity of 420°C.

To determine the effect of water pretreatment on the sorbent reactivity at different temperatures, another series of tests were conducted, where samples of the sorbent were first exposed to N_2/H_2 mixture 30% steam at 300 ˚C and 20 atm for 1 hour. Following the pretreatment, the sorbents were exposed to $CO_2/N_2/H_2O$ mixture containing 50% CO_2 and 30% H_2O (balance N_2) at different temperatures (300-430 ˚C) and 20 atm. The results are presented in Figure 47; indicating that the CO_2 capacity of the sorbent

increases with stream pretreatment. The difference in the extent of capacity between the two experiments may be attributed to structural changes in the pore size distribution of the sorbent.

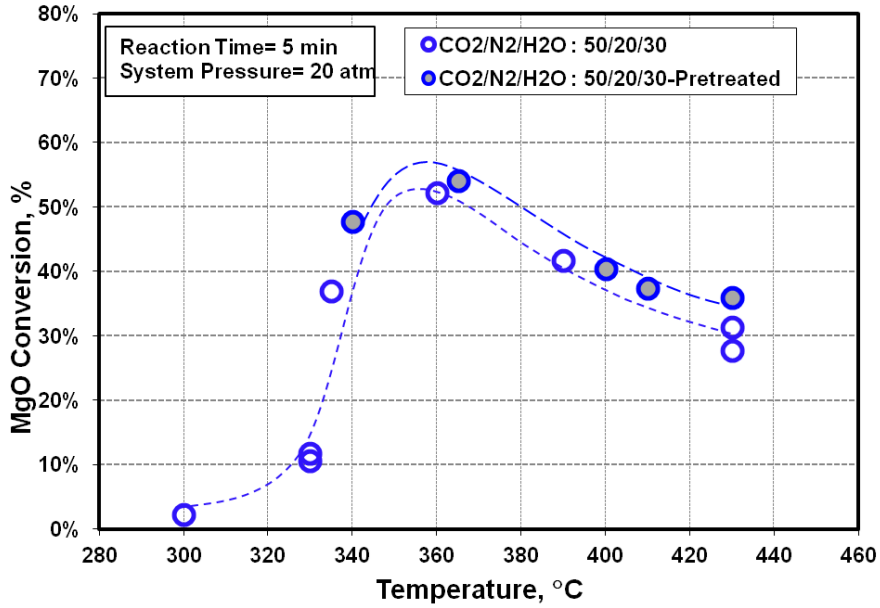

Figure 47. Effect of steam pretreatment on sorbent reactivity at different temperatures

To understand the effect of structural change on the reactivity of the sorbent, samples of the sorbent were exposed to nitrogen environment containing 30% steam at 330°C and 20 atm for 1 hour. After the pretreatment, the sorbent was exposed to CO_2/N_2 (50/50 mol %) mixture at different temperatures. Following each test, the sorbent was removed from the reactor and analyzed by XRD, and X-ray diffraction measurements were performed using a Bruker D2 Phaser diffractometer.

The effect of steam pretreatment on the sorbent reactivity is shown in Figure 48. The results indicate that the presence of steam significantly enhances the sorbent reactivity and capacity, which may be attributed to higher porosity and/or more favorable pore size distribution. Similar results have also been widely reported by others[51-53] for dolomite and limestone.

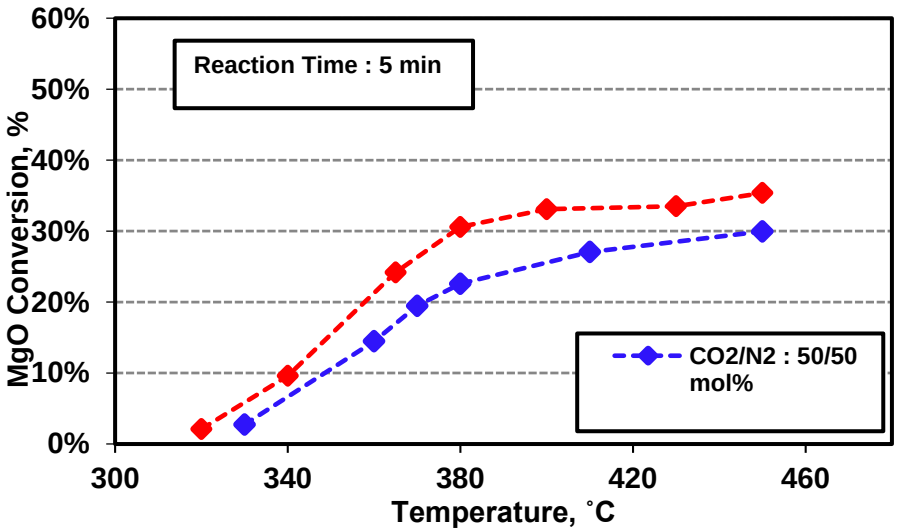

Figure 48. Effect of steam pretreatment on sorbent reactivity and capacity

The effect of steam concentration (10 and 30 mol %) on the reactivity of the sorbent at different temperatures (without pretreatment) was also investigated in the dispersed-bed reactor. The results are presented in Figures 49 and 50, indicating that the reactivity of the sorbent improves with increasing steam concentration in the system. As shown in Figure 50, the sorbent conversions at different temperatures level off at about 50%, which may be attributed to complete carbonation of outer reactive layer of MgO in the sorbent.

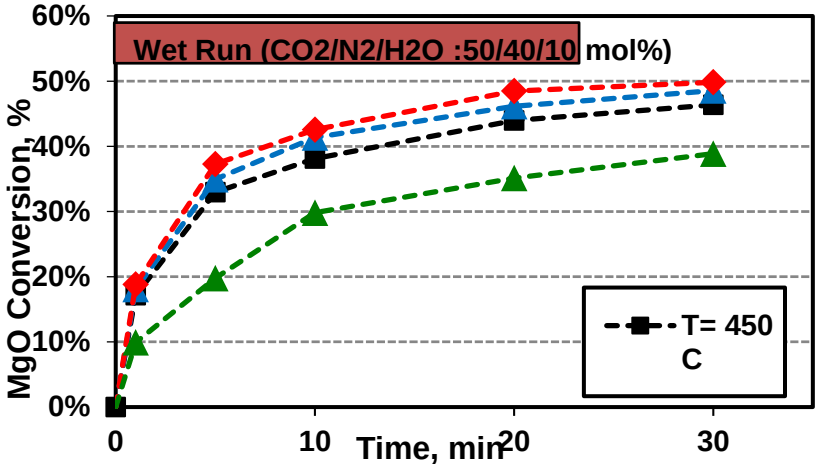

Figure 49. Effect of temperature on the reactivity of the sorbent (30 mol% steam)

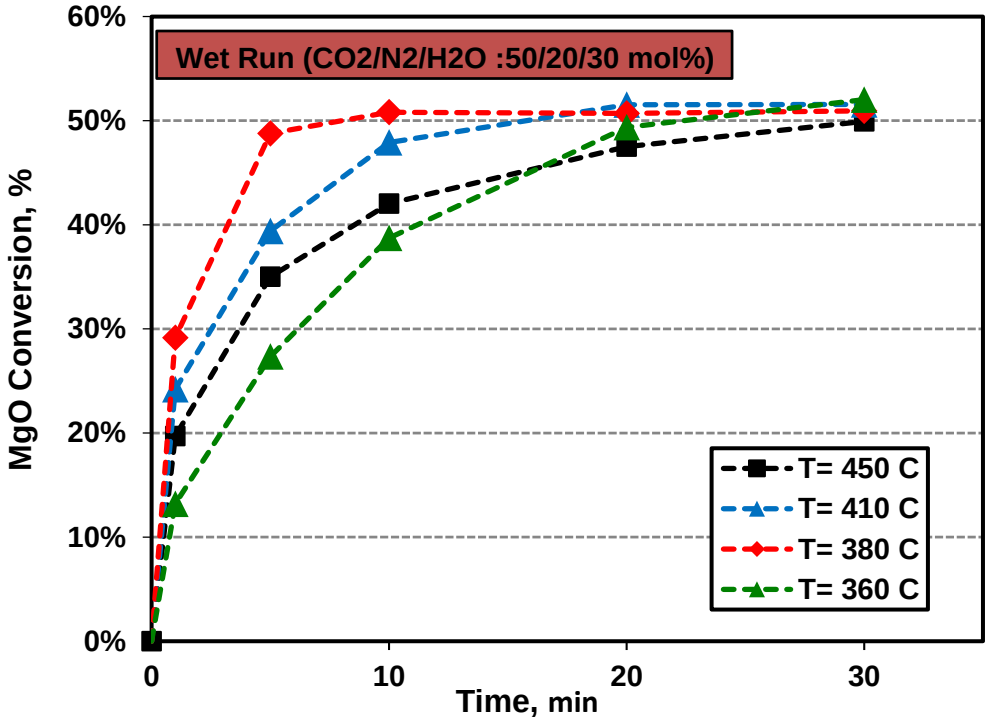

Figure 50. Effect of temperature on the reactivity of the sorbent (30 mol% steam)

To assess the sorbent performance in the regenerative MgO-based process, it is necessary to fit the experimental data to a reaction model that can be used to predict the long-term performance of the sorbent in various reactor configurations. In this study, the variable diffusivity shrinking core Model (VDM) model[34] was selected to capture the behavior of the sorbent at different conditions. A schematic diagram

of the model is illustrated in Figure 51. In this model, the reaction occurs at the interface between the shrinking unreacted core and the product layer. As the reaction proceeds, the difference in the larger molar volumes of the solid product and the smaller molar volume of the reactant leads to decreasing pore volume of the product layer, decreasing the diffusion rate of the gaseous reactant through the sorbent particle. The rate of carbonation reaction at the surface of the shrinking core can be described as--

$$r_{MgO} = -\frac{1}{4\pi r^2}\frac{dN_{MgO}}{dt} = k_s(C_b - C_e) \tag{53}$$

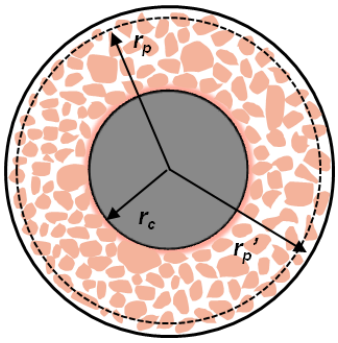

r_c: The radius of the un-reacted core of the particle

r_p: Initial radius of the particle

r'_p: Expanded radius of the particle

Figure 51. Schematic diagram of expanded particle

The governing differential equations describing the transport of CO_2 through the porous particle and its reaction at the surface of the individual particles, along with the relevant initial and boundary conditions are given below:

$$D_e\left[\frac{1}{r^2}\frac{\partial}{\partial r}\left(r^2\frac{\partial C}{\partial r}\right)\right] = 0 \tag{54}$$

$$C = C_R \qquad @\ r = R \tag{55}$$

$$D_e\frac{\partial C}{\partial r} = k_s(C_i\text{-}C_e) \qquad @\ r = r_i \tag{56}$$

$$\frac{dr_i}{dt} = \frac{-k_s}{C_{MgO}}\left[\frac{C_b - C_e}{1+\frac{k_s}{D_e}r_i(1-\frac{r_i}{r_p'})}\right] \tag{57}$$

$$r_p' = \sqrt[3]{r_i^3 + Z_v(r_p^3 - r_i^3)} \tag{58}$$

$$Z_v = \frac{MW_p/\rho_p(1-\varepsilon)}{MW_r/\rho_r(1-\varepsilon_s)} \tag{59}$$

$$\frac{dX}{dt} = -\frac{\frac{3}{r_p}\frac{k_s}{N_{MgO}^o}(C_b - C_e)(1-X)^{\frac{2}{3}}}{1+\frac{k_s}{D_e}r_p(1-X)^{\frac{1}{3}}(1-\sqrt[3]{\frac{1-X}{1-X+XZ}})} \tag{60}$$

In the VDM model, the extent of the non-catalytic gas-solid reaction is dictated by the intrinsic rate of reaction as well as the rate of diffusion of the reactant gas through the solid particle. The reactant gas (i.e.

CO_2) has to diffuse through the particle product layer before reaching the reaction interface. The diffusion rate through this layer changes during the carbonation reaction because of the changes in the product layer properties, which results in changes in the porosity. Therefore, product layer diffusivity can be a significant function of sorbent physical properties affected by changes in the overall conversion and/or the duration of exposure to the reaction environment. In this study, similar to others[3-5], we assumed that the diffusivity through the product layer is an exponential function of the conversion of the particle.

$$D_e = D_{e_0} \exp(-\alpha . X^2) \qquad (61)$$

To model the sorbent behavior in both dry and wet conditions, the reaction rates are determined using the initial slopes of the conversion curves. Figure 52 compares the reaction rate constants (k_s) at different temperatures under the wet and dry conditions. The results indicate that the reaction rate of the sorbent generally increases in the presence of steam in the system. However, as discussed above, this effect is most pronounced at T=380 ˚C

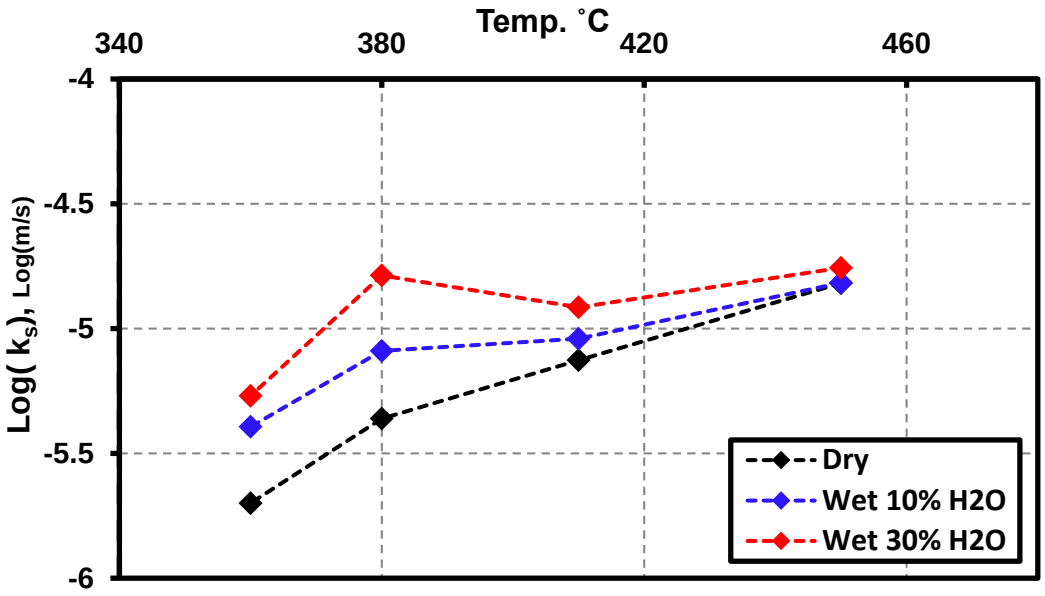

Figure 52. Effect of temperature on reaction constant (wet & dry carbonation)

The VDM model was used to fit the experimental data obtained in dispersed bed reactor at different operating conditions. The two adjustable parameters of the VDM model (D_{e0} and α) were estimated by determination of the best fit to the experimental results through minimization of the least squares of the errors. The results are presented in Figures 53 through 55, which indicate that the model can provide excellent fit to the experimental data. The estimated values of the VDM model parameters (D_{e0} and α) at different temperatures and steam concentrations are presented in Figures 56 and 57. As indicated earlier, the product layer diffusivity is a function of temperature as well as porosity of the sorbent. As expected, the initial product layer diffusivity increases with increasing temperature because both the molecular and Knudsen diffusivity increase with temperature. The presence of steam appears to enhance the product layer diffusivity, which may be attributed to the higher surface area and porosity of the sorbent resulting from the formation and subsequent decomposition of the transient $Mg(OH)_2$ and the structural change imparted by the difference between the larger molar volume of $Mg(OH)_2$ and smaller molar volume of MgO).

The rate of formation of the transient $Mg(OH)_2$, similar to that of MgO carbonation (Equation 53), is dictated by the reaction rate constant, k_s, which increases with increasing temperature (Arrhenius Equation), and the driving force $(C_b\text{-}C_e)$, which decreases with increasing temperature (due to increasing H_2O equilibrium pressure with increasing temperature). In the lower range of temperature (i.e., 360º-380ºC), where the formation of the transient $Mg(OH)_2$ is more favorable, the increase in the reaction rate constant is greater than the decrease in the driving force, resulting in a net increase in the rate of transient $Mg(OH)_2$ formation, while in the middle temperature range (i.e., 380º-410ºC), the reverse appears to be true. However, in the higher temperature range (i.e., 410º-460ºC), as the enhancing effect of steam is diminishing, the rate of carbonation reaction increases because of the reaction rate constant k_s, increases with increasing temperatures (Arrhenius Equation). Furthermore, the smaller values of the model parameter α, in the presence of steam shown in Figure 61 may indicate that the generated product layer has a lower tendency to agglomerate resulting in less pore closure in the presence of steam.

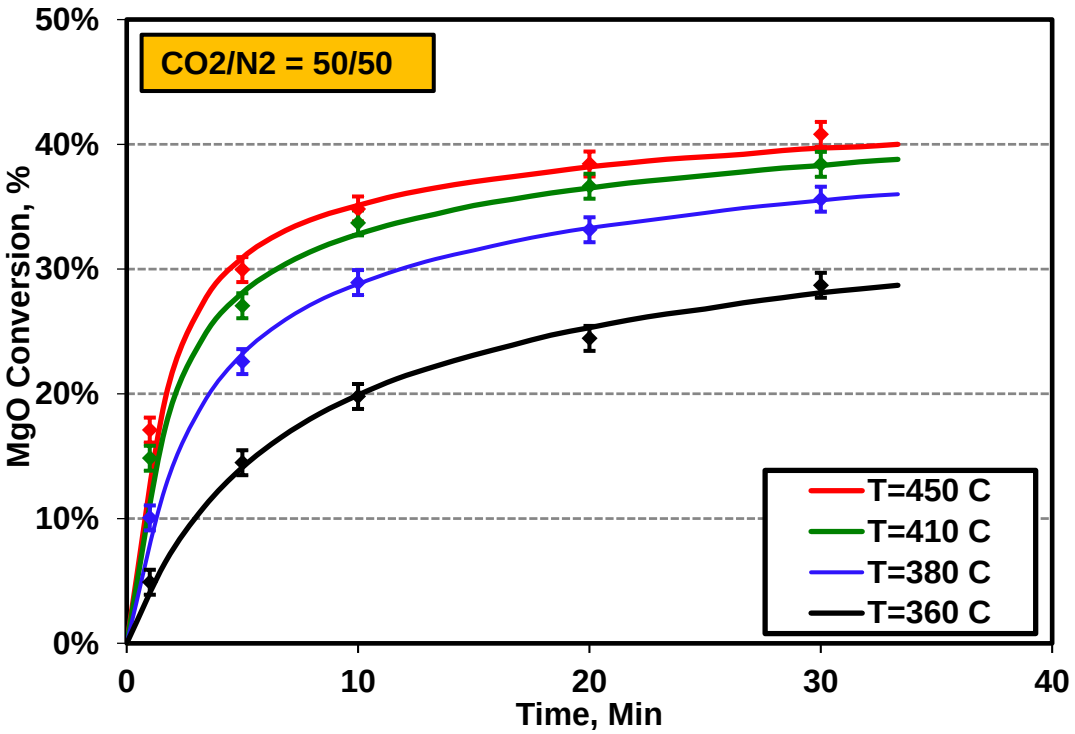

Figure 53. VDM model fit to dispersed bed experiments (dry carbonation)

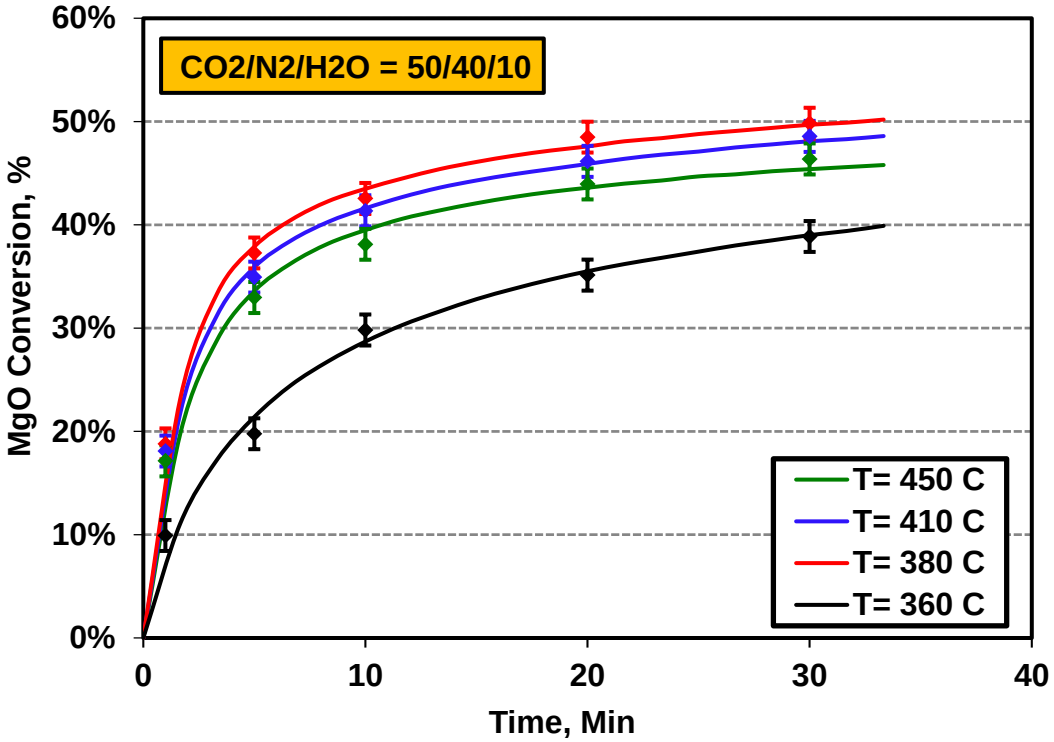

Figure 54. VDM model fit to dispersed bed experiments (10 mol% steam)

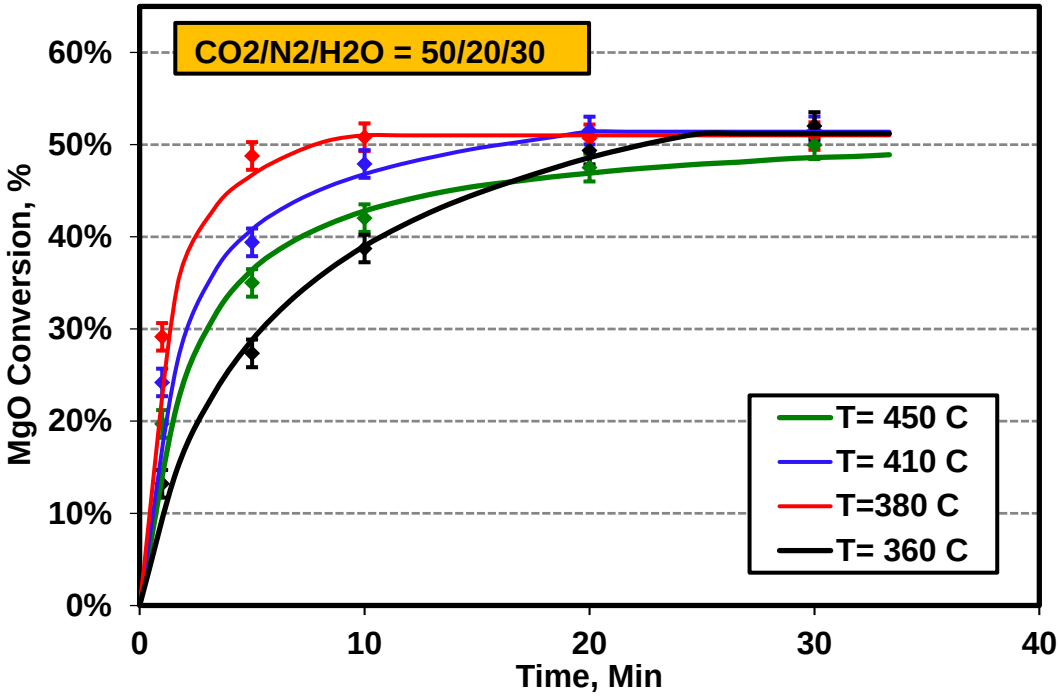

Figure 55. VDM model fit to dispersed bed experiments (30 mol% steam)

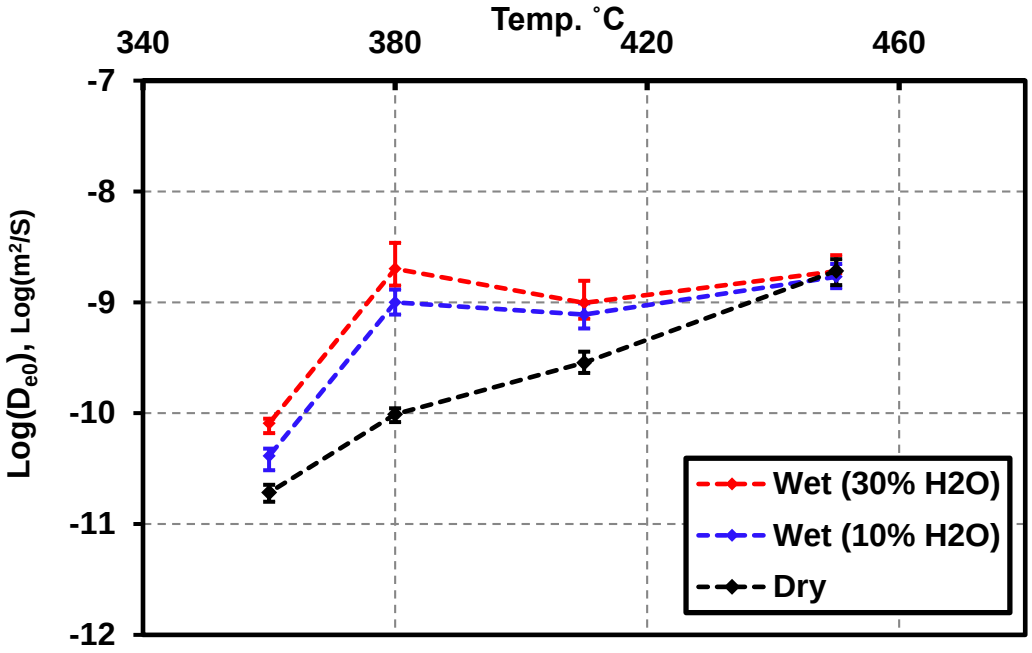

Figure 56. Comparison of D_{e0} (wet and dry carbonations)

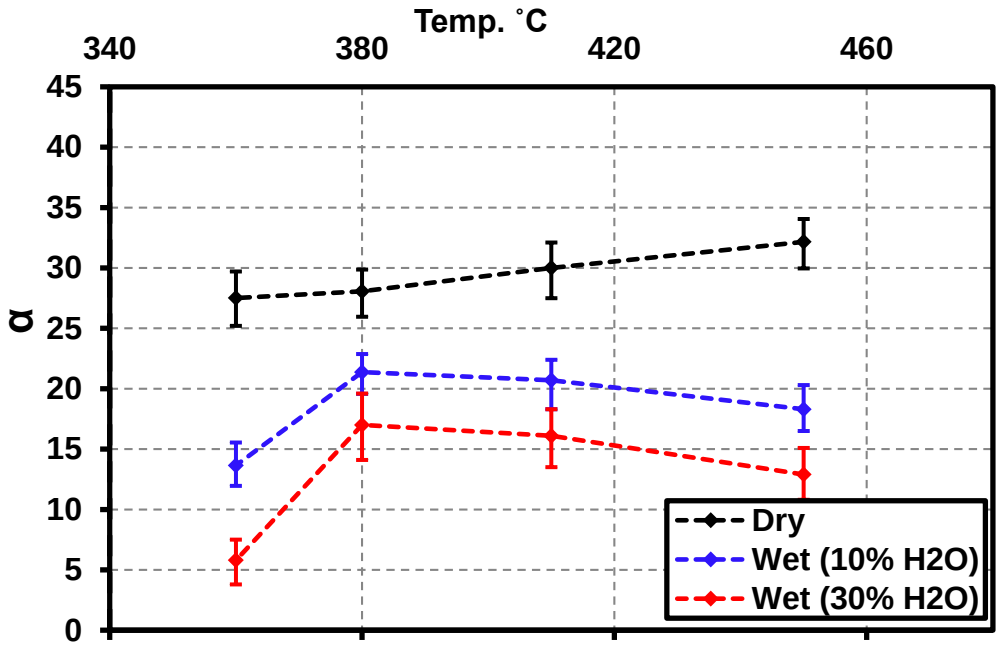

Figure 57. Comparison of α (wet and dry carbonations)

To determine the kinetics of regeneration reaction involving carbonated MgO-based sorbent, about 30 grams of the fresh sorbent was exposed to CO_2/N_2 (50/50 mol %) flow at 430°C and 20 atm for an hour. Fully carbonated sorbents were divided into 1 gram samples for the regeneration studies in the dispersed bed reactor.

To determine the effect of temperature on the rate of the regeneration reaction, the carbonated sorbent was heated in the CO_2/N_2 (50/50 mol %) environment up to the regeneration temperature. The reactor pressure was maintained at 20 atm through the entire regeneration test. The regeneration step was started by switching the gas mixture from 50/50 mixture of CO_2/N_2 to pure nitrogen gas. Following each test, the sorbent was removed from the reactor and analyzed by XRD. X-ray diffraction measurements were performed using a Bruker D2 Phaser diffractometer. The results are shown in Figure 58, indicating that, as expected, the reactivity of the regeneration reaction improves with increasing temperature (i.e. between 450° to 550°C). The decline in the sorbent regenerability at 450°C, shown in Figure 62, is due to the significant increase in the rate of reverse (i.e., carbonation) reaction at this temperature.

To evaluate the sorbent performance in the regenerative MgO-based process, it is necessary to fit the experimental data using a reaction model that can be used to predict the long-term performance of the sorbent in various reactor configurations. In this study, initially, the shrinking core model (SCM) by Yagi and Kunii[32] was selected to capture the behavior of the sorbent at different conditions. A schematic diagram of the model is illustrated in Figure 69. The reaction occurs at a sharp interface, which divides the reacted outer layer (product layer) from the un-reacted core of the solid.

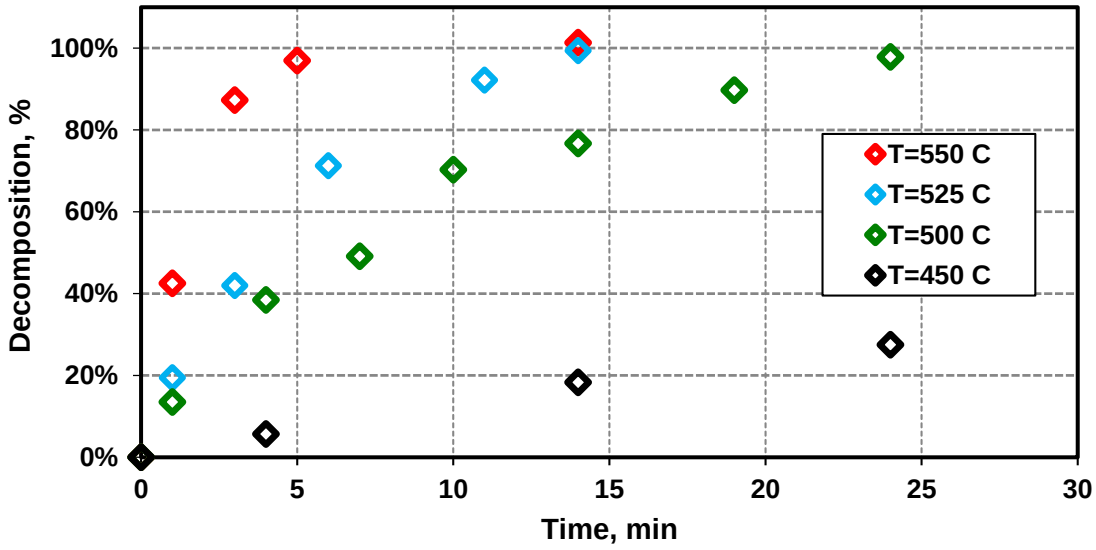

Figure 58. Effect of temperature on regeneration reaction

The rate of carbonation reaction at the surface of the shrinking core can be described as:

$$r_{MgCO_3} = k_d\left(1-\frac{C_i}{C_e}\right) \quad (61)$$

The governing differential equations describing the transport of CO_2 through the porous particle and its reaction at the surface of the individual particles, along with the relevant initial and boundary conditions are given below:

$$D_e[\frac{1}{r^2}\frac{\partial}{\partial r}\left(r^2\frac{\partial C}{\partial r}\right)] = 0 \quad (62)$$

$$C = 0 \quad @\, r = R \tag{63}$$

$$D_e \frac{\partial C}{\partial r} = k_d \left(1 - \frac{C_i}{C_e}\right) \qquad @\, r = r_i \tag{64}$$

$$\frac{\partial X}{\partial t} = \frac{3 r_i^2 k_d}{R^3 N^0_{MgCO_3}} \left(1 - \frac{C_i}{C_e}\right) \tag{65}$$

$$\frac{\partial X}{\partial t} = \frac{\frac{3}{R} \frac{k_d}{N^0_{MgCO_3}} \sqrt[3]{(1-X)^2}}{1 + \frac{k_d}{D_e C_e} R \sqrt[3]{1-X}\,(1 - \sqrt[3]{1-X})} \tag{66}$$

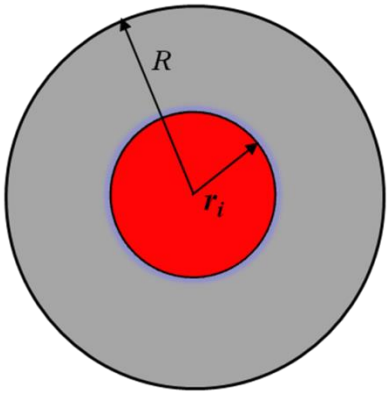

r_i: The radius of the un-decomposed core of the particle

R: Radius of the particle

Figure 59. Schematic diagram of regenerated particle

In the shrinking core model, the extent of the non-catalytic gas-solid reaction is dictated by the intrinsic rate of reaction as well as the rate of diffusion of the reactant gas through the solid particle. The produced gas (i.e. CO_2) has to diffuse out through the particle product layer before reaching the particle surface. The diffusion rate through this layer affects the rate of regeneration reaction by decreasing the driving force for the $MgCO_3$ regeneration reaction, which is the difference between the CO_2 concentration inside the particle and the CO_2 equilibrium pressure at the reaction temperature ($1 - C_i/C_e$).

To model the sorbent regeneration behavior, the reaction rates and diffusion rates were considered as adjustable model parameters. The two adjustable parameters of the shrinking core model (D_e and k_d) were estimated by determination of the best fit to the experimental data through minimization of the least squares of the errors. The results are presented in Figure 60, which indicate that the model can provide excellent fit to the experimental data. The estimated values of the shrinking core model parameters (D_e and k_d) at different temperatures are presented in Figures 61 and 62. The activation energy of the regeneration reaction was obtained through the Arrhenius plot of the intrinsic rate (see Figure 61) to be 173 kJ/mol for the temperature range of 450° to 550°C. The product layer diffusivity increases with increasing temperatures (see Figure 62) because both the molecular and Knudsen diffusivity increase with increasing temperatures.

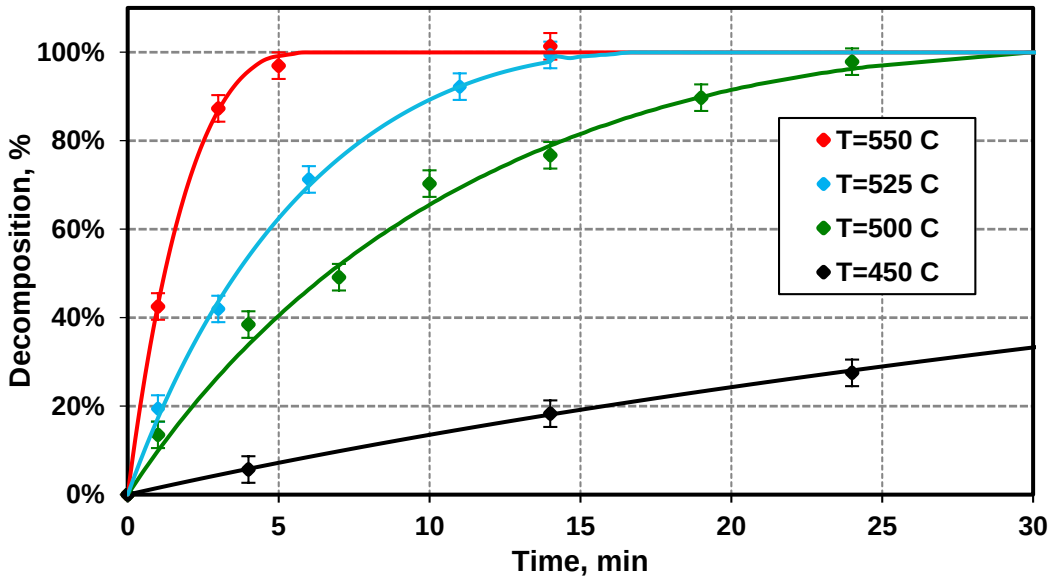

Figure 60. Shrinking core model fit to dispersed bed experiments

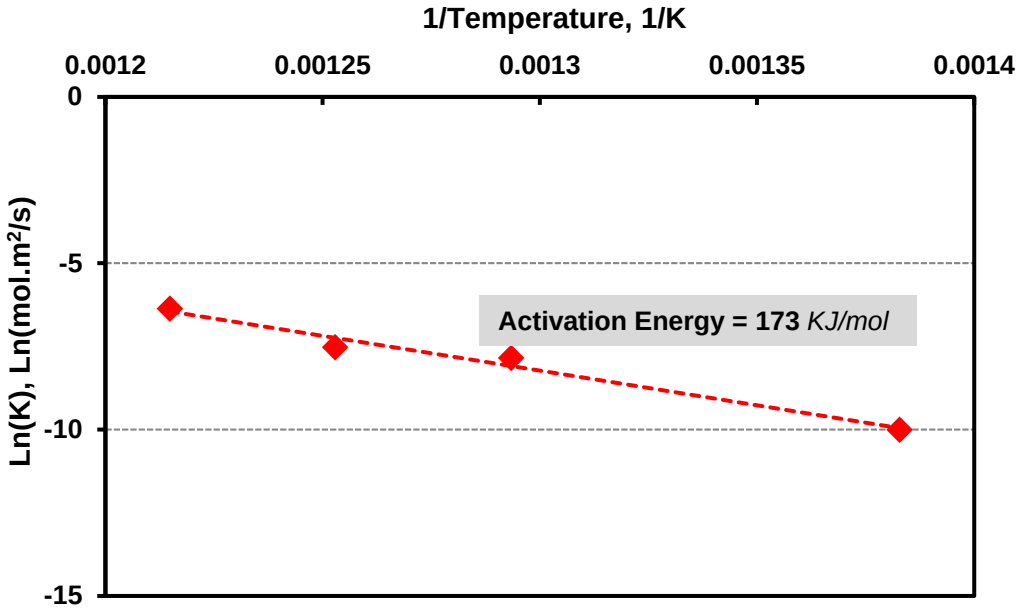

Figure 61. Activation energy of the desorption reaction

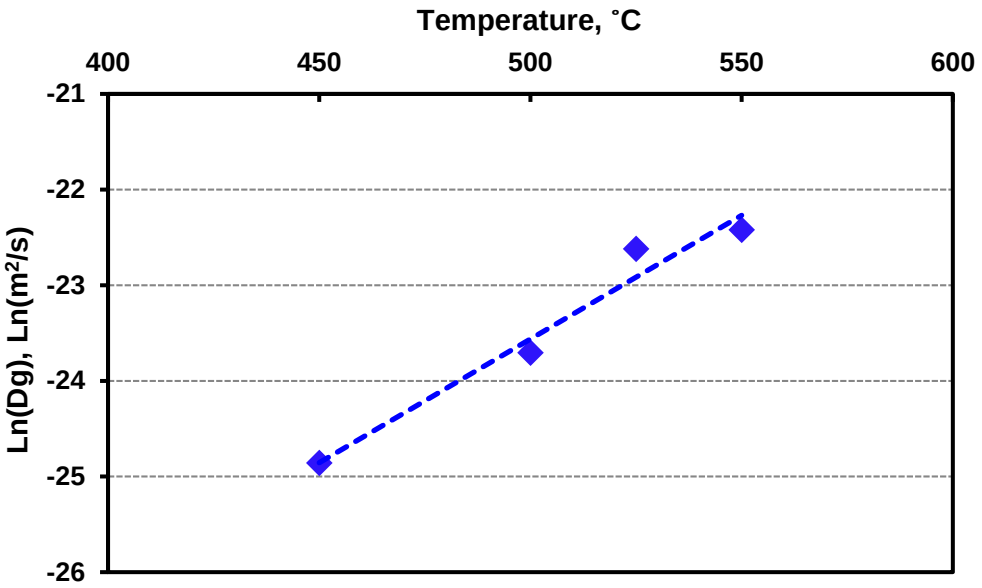

Figure 62. Effect of temperature on product layer diffusivity

To investigate the effect of changes in the pore structure imparted by the presence of steam during carbonation process on the rate of decomposition, a new batch of fresh sorbent was fully carbonated with a mixture of 50/20/30 of $CO_2/N_2/H_2O$ at 430˚C for 30 min. The carbonated sorbent was decomposed in pure nitrogen environment at the desired temperatures (i.e. 500˚C and 550˚C). A comparison of the regenerability of the dry and wet carbonated sorbents are shown in Figure 63, confirming that carbonation of the sorbent in the presence of steam has beneficial effect on the pore structure of the sorbent resulting in higher regenerability of the carbonated sorbents.

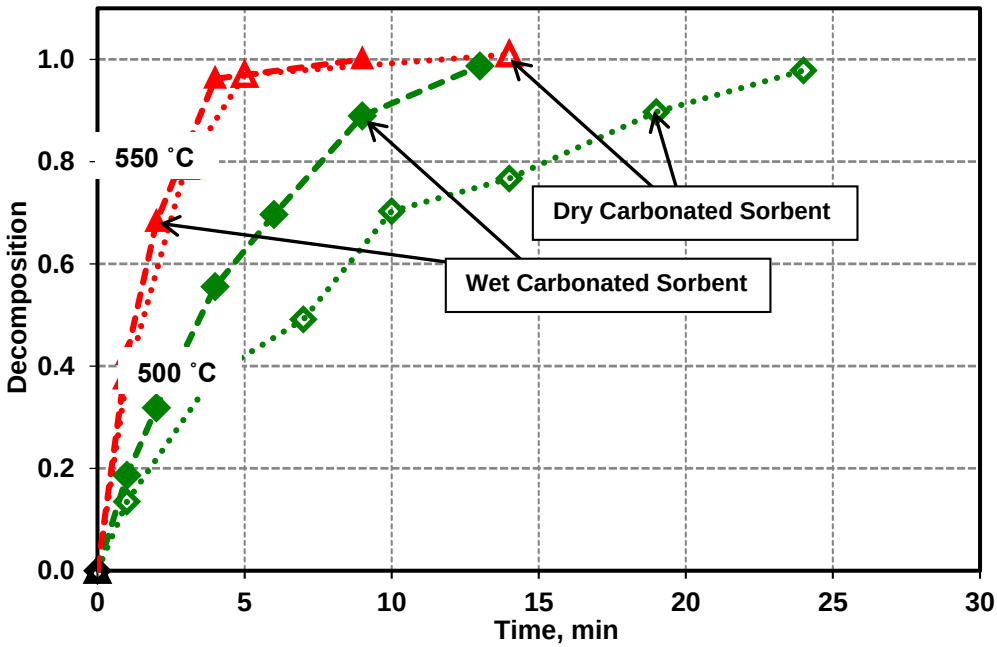

Figure 63. Effect of steam during carbonation on sorbent decomposition

To study the effect of steam on rate of decomposition, a sample of dry carbonated sorbent was regenerated in the presence of steam (30 mol%) at 500˚C and 20 bar. A comparison of the regenerability of the sorbent with and without the presence of steam is presented in Figure 64, indicating that the steam has a beneficial effect on the rate of decomposition reaction. The higher sorbent regenerability in the presence of steam shown in Figure 64 may be attributed to the favorable effect of steam on the pore structure of the sorbent as well as the beneficial effect of steam on kinetics of the decomposition reaction. A comparison of the decomposition rate of dry carbonated sorbent and dry decomposition of wet carbonated sorbent is presented in Figure 65. These results strongly suggest that the beneficial effect of steam is due to its positive effect on the pore structure of the sorbent resulting in higher effective diffusivity of the product layer. Furthermore, the results also suggest that the presence of steam has negligible effect on the kinetics of decomposition, because the rates of the decomposition reaction in the presence of steam at three different conditions are very similar.

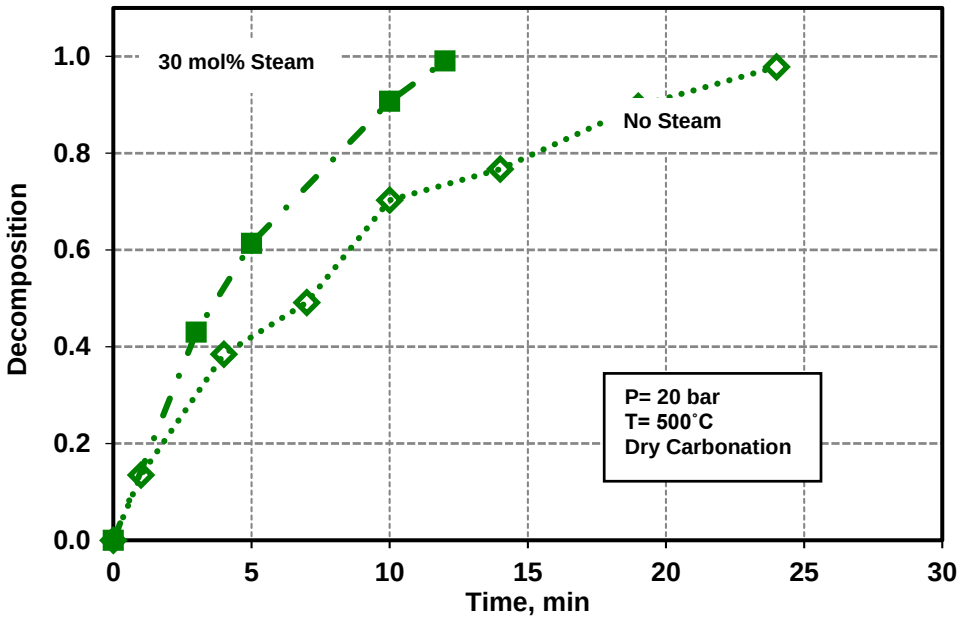

Figure 64. Effect of steam on rate of sorbent regenerability

The effect of CO_2 on rate of decomposition was also investigated by conducting a series of decomposition tests with wet carbonated sorbent using decomposition gases containing 10 and 20 mol% CO_2. The results are presented in Figure 66 and 67 for tests conducted at 500°C and 550°C, respectively, which clearly show that the addition of CO_2 significantly decreases the rate and the extent of regenerability of the sorbent. The lower sorbent regenerability at 500°C and 20 mol% CO_2, shown in Figure 66, is due to the significant increase in the rate of reverse (i.e., carbonation) reaction at the this temperature. Higher CO_2 concentration as well as the decreasing CO_2 equilibrium pressure with decreasing reaction temperature, decreases the driving force ($1-P_{CO2}/P_{CO2e}$) resulting in a significant decrease in the sorbent regenerability.

The long-term durability of the sorbent was investigated over several consecutive absorption/regeneration cycles in the dispersed bed reactor. In this series of tests, the CO_2 absorption steps were carried out at 430°C. The reactor pressure was maintained at 20 atm through the entire absorption and regeneration cycles. The regeneration steps were conducted at 500°C and 550°C by switching the gas mixture from 50/50 mixture of CO_2/N_2 to pure nitrogen gas. The results obtained in these cycles, shown in Figure 68, indicate that the reactivity and capacity of the sorbent decreases in the cycling process (sorbent

deactivation). Furthermore, the results indicate that the sorbents exposure to a higher regeneration temperature expedites the sorbent deterioration in the cyclic process, which may be attributed to either changes in the sorbent's chemical characteristics (i.e. loss of potassium content) or changes in the sorbent's physical characteristics (i.e. sorbent agglomeration and loss of active surface area).

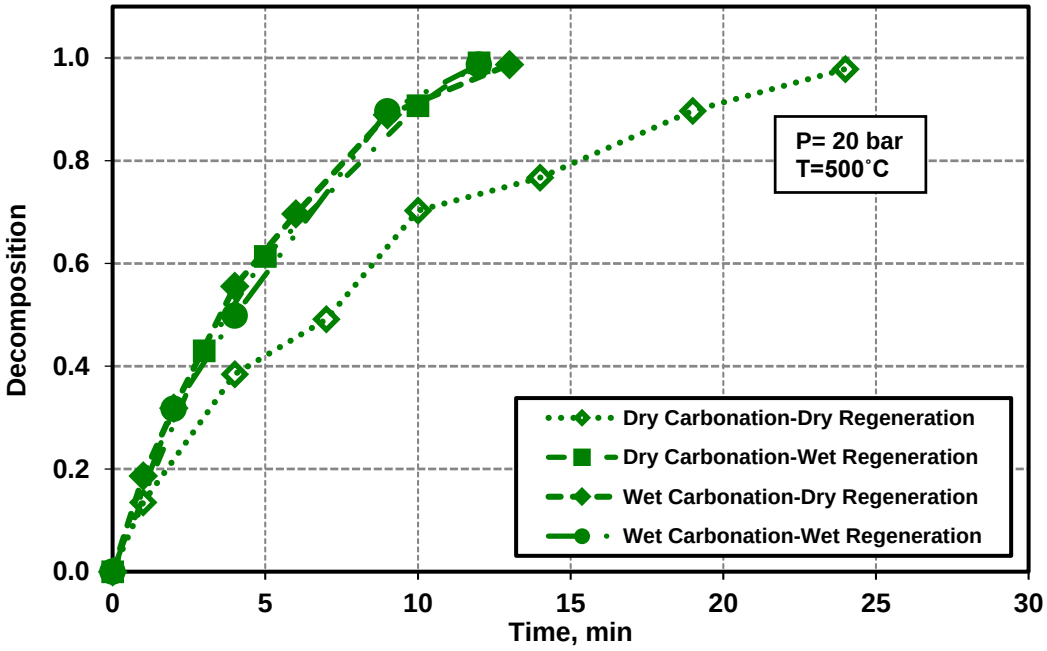

Figure 65. Effect of steam during carbonation and decomposition on rate of decomposition

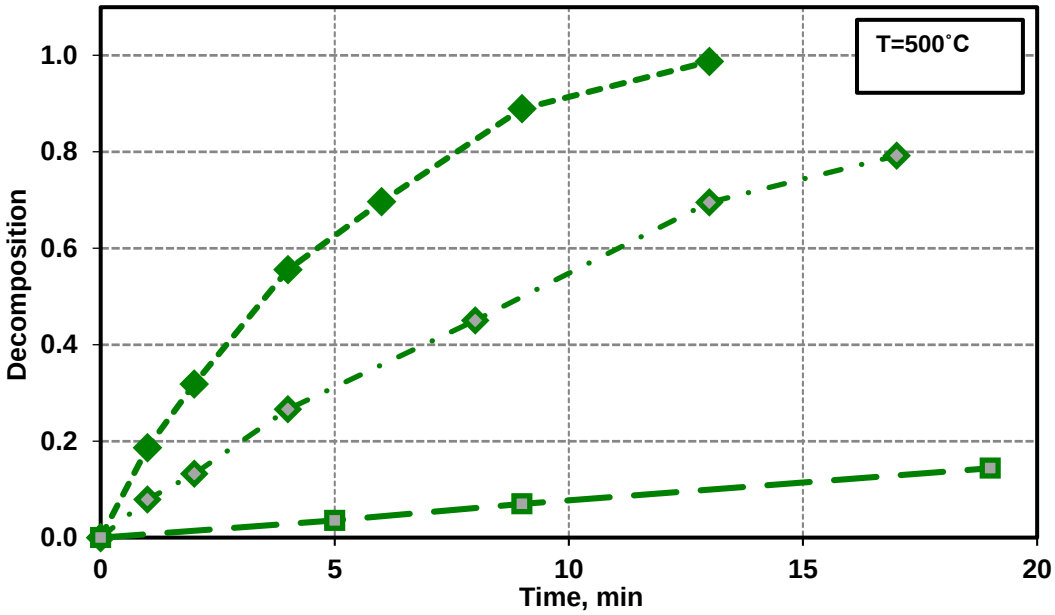

Figure 66. Effect of CO_2 on sorbent regenerability at 500°C

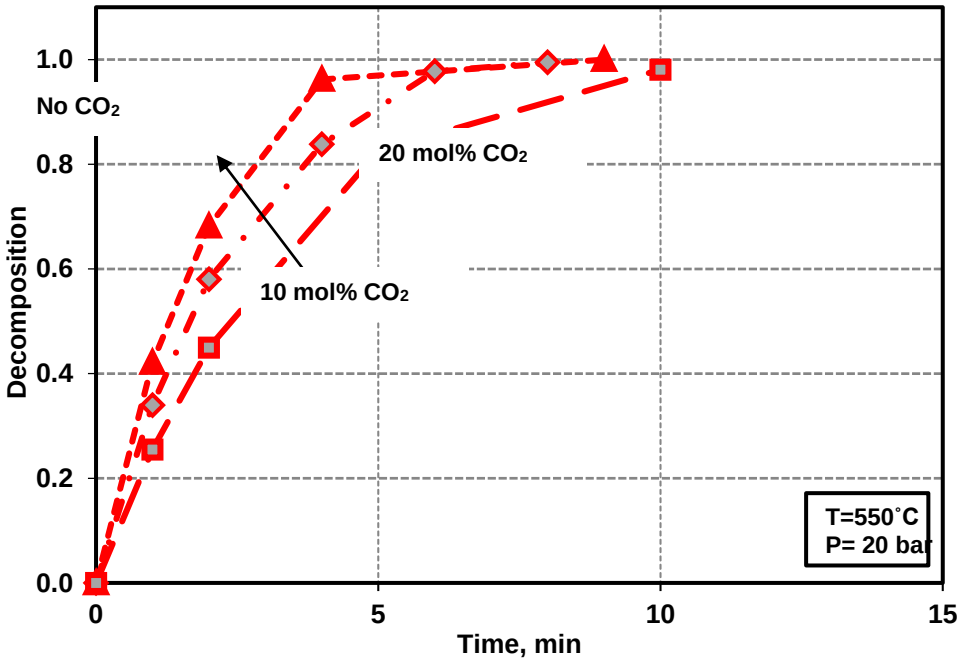

Figure 67. Effect of CO_2 on sorbent regenerability at 550°C

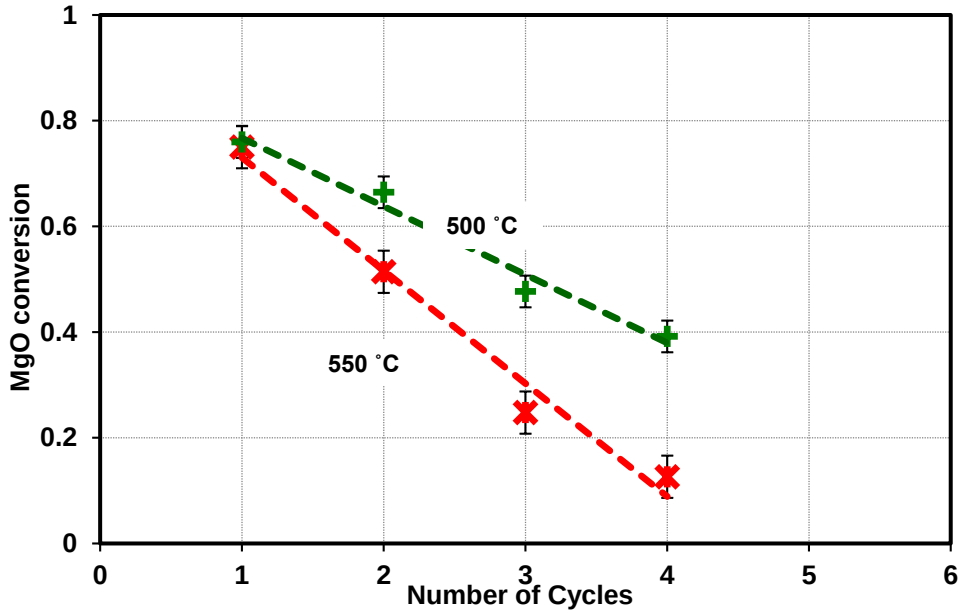

Figure 68. Effect of regeneration temperature on long-term reactivity of the sorbent

To study the effect of steam on durability of the sorbent, two series of tests were conducted. In these tests the CO_2 absorption steps were carried out in the presence of steam and regeneration steps were conducted with and without steam. The results are shown in Figure 69, indicating that the presence of steam can decrease the rate of decline in the sorbent deactivation. The loss of sorbent reactivity can be attributed to

the loss of potassium (due to wear/tear or evaporation) during the cyclic process. The K/Mg molar ratio of the sorbent at different operating conditions (with & without 30 mol% steam) is presented in Figure 70, confirming that the loss of potassium content in the sorbent is an important factor in the rate sorbent deterioration.

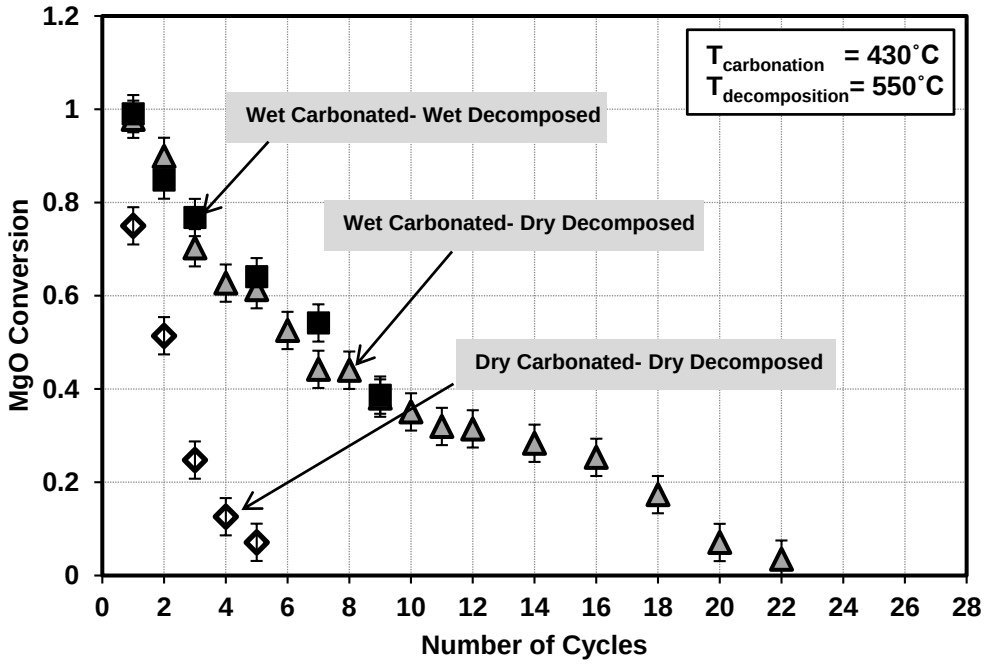

Figure 69. Effect of steam on long-term reactivity of the sorbent

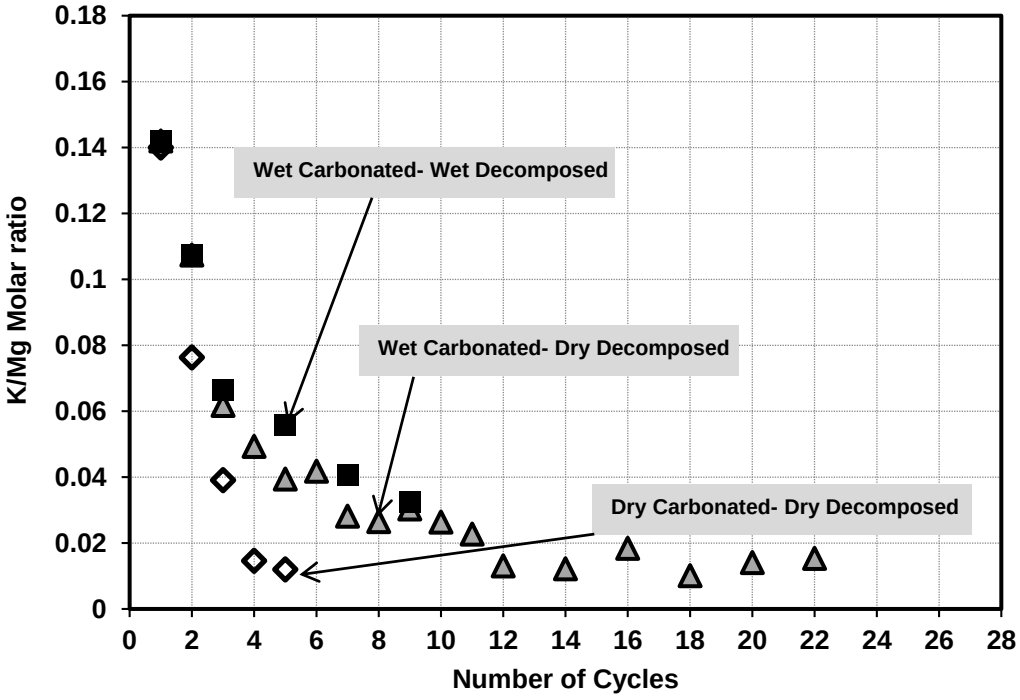

Figure 70. Effect of cycling on K/Mg molar ratio of the sorbent

To evaluate the long-term durability of the sorbents and determine the catalytic activity of sorbent in the water-gas-shift (WGS) reaction, a number of tests were conducted in the lab-scale packed-bed reactor. A

schematic diagram of the packed-bed unit is shown in Figure 25. In a typical packed-bed test, pressurized cylinders of the pure gases are used to feed each of the N_2, CO_2, H_2, and CO gases into the reactor. Pre-calibrated Brooks® Mass Flow Controllers (MFCs), Model 5850i, are used to accurately measure the flow rates of each compound to achieve the desired mixture composition. A high-pressure/high-performance piston pump, manufactured by Chrom Tech, Inc., is used to inject distilled water into the unit. This pump can be operated in flow range of 0.001 to 5.000 mL/min, which is suitable for this experimental work. Stainless steel tubing with 1/8" (0.318 cm) OD is used to deliver the gas mixture to the reactor. These tubes are heated to a temperature range of 240° to 260°C, significantly above the boiling point of water at the operating pressure of the system by heating tapes controlled with temperature controllers. The tubes are completely insulated with a thick layer of wool while the temperature of the tubes is measured by a number of thermocouples placed at the surface of the tubes. These temperatures are monitored and controlled to eliminate any cold/hot zones along the entire tubing line. Downstream of the reactor, a highly-sensitive backpressure regulator was installed to maintain the total pressure of the packed-bed unit at a pre-determined setting. This regulator, which is manufactured by GO-Regulators Company (Model BP-8LF), is comprised of a wide diaphragm-sensing area, which increases its accuracy, and a low-flow rate seat assembly, which damps flow fluctuations. A high-pressure filter housing (knockout pot), manufactured by Parker Hannifin, was installed upstream of the regulator to capture most of the condensed water before entering the backpressure regulator. The pressure of the unit is measured and monitored with a pressure gauge placed between the water knockout pot and the regulator (Figure 25). A Shimatzu Gas Chromatograph (GC), equipped with a Thermal Conductivity Detector (TCD), is used to determine the composition of the product gas downstream of the unit.

The effect of temperature on reactivity of the sorbent was investigated through a few packed bed runs shown in Figures 71, 72 and 73, respectively. The results shows in Figure 71 demonstrates the effectiveness of the bed of sorbent for CO_2 removal at three different operating temperature ranges, indicating that to achieve a high CO_2 removal efficiency, the bed of sorbent should be operated at a temperature lower than 370-410°*C*. The sorbent bed also was exposed to two different CO_2 concentrations (i.e. 25 and 50% mol) at 370-410 °C and 20 atm (Figure 72). As expected, lower CO_2 inlet concentrations delay the bed outlet CO_2 breakthrough curve. Furthermore, comparing the wet and dry runs shown in Figure 73 demonstrates the significant effect of steam in enhancing the reactivity, as well as the capacity of the sorbent. This enhancement effect of steam was also observed in the dispersed bed tests (discussed above), which is attributed to the positive effect of steam on the pore structure of the sorbent.

The bed temperature in the above tests was monitored and measured at four locations along the sorbent bed. A moveable thermocouple inside a thermo-well placed inside the bed was used to measure the temperature as the reaction was occurring inside the sorbent bed. Figure 74 shows the changes in temperature at each of the measuring location for a packed bed. As shown in Figure 74, there was an initial temperature gradient (~20°C), along the bed before the carbonation reaction is started, which has a direct effect on the extent of the CO_2 removal. These temperature profiles were incorporated in the non-isothermal mathematical packed-bed model to predict the effectiveness of the sorbent bed towards CO_2 removal.

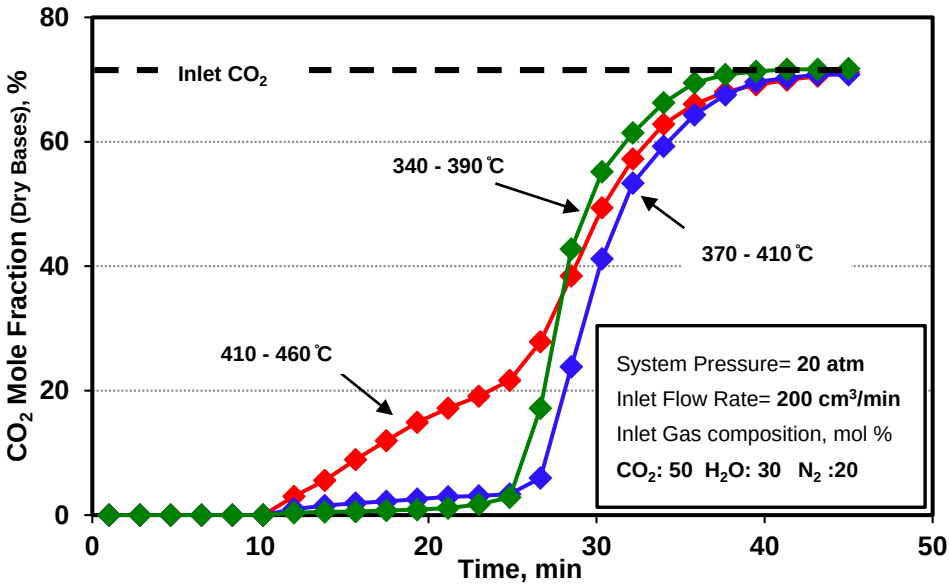

Figure 71. Extent of CO_2 removal at different operating temperatures

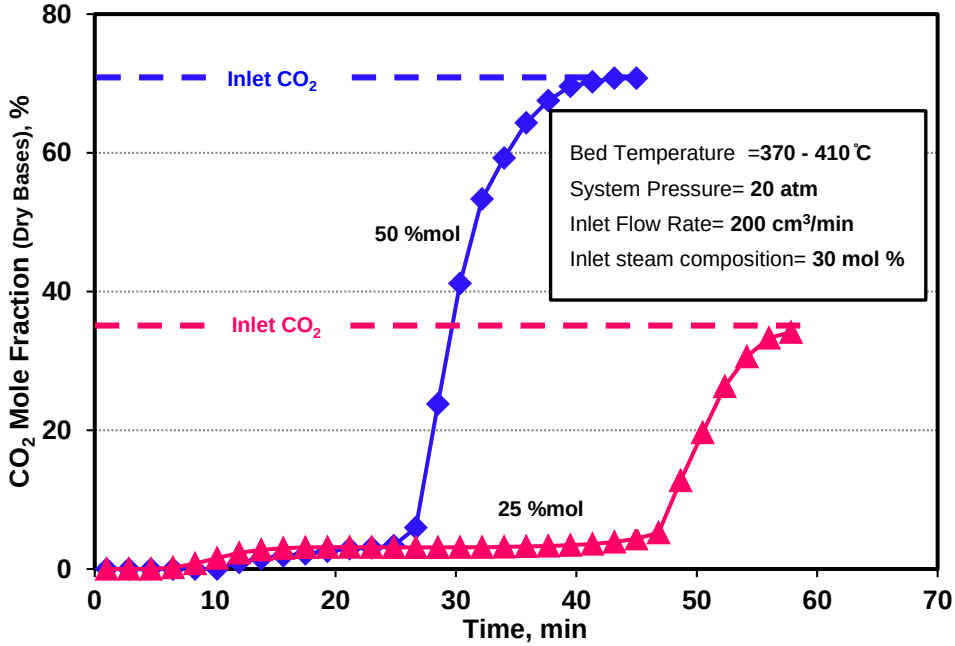

Figure 72. Bed behavior exposed to different inlet CO_2 concentrations

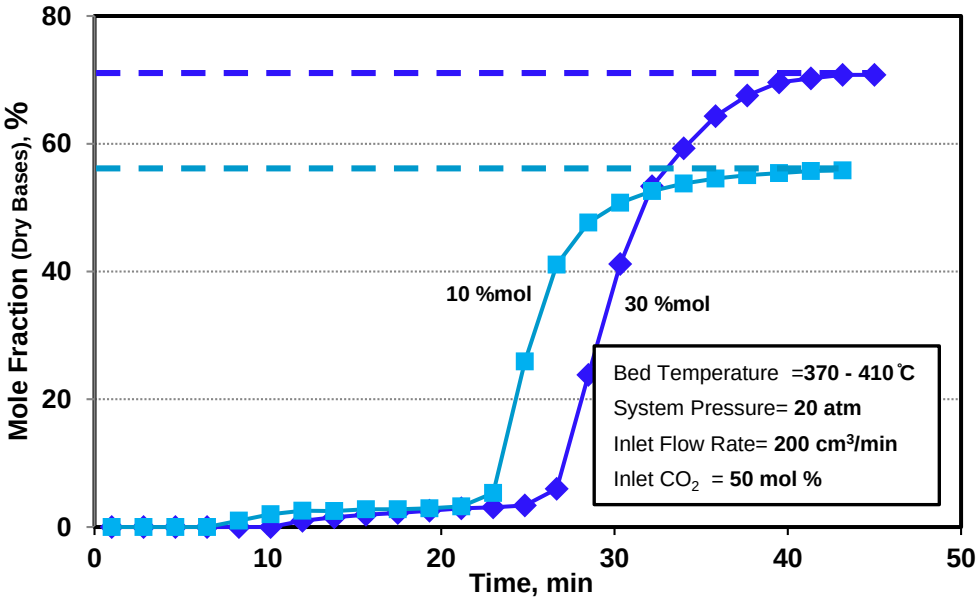

Figure 73. Effect of steam on reactivity and capacity of the sorbent

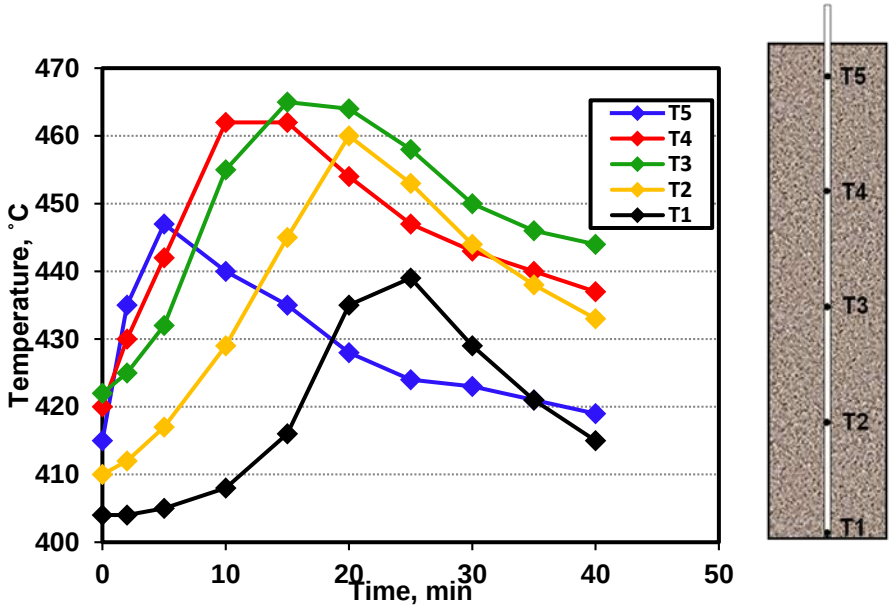

Figure 74. Temperature change along reactor bed during reaction

To determine the effectiveness of the sorbent for CO_2 absorption in presence of syngas as well as its catalytic activity for the water-gas shift (WGS) reaction, the sorbent was exposed to different compositions of syngas mixture (i.e. H_2, CO, H_2O, and CO_2) at different operating temperatures. Figure 75 shows the syngas composition at the outlet of the system in the bed temperature range of 370-410°*C* and 20 atm, measured by the GC unit. Since water is condensed and removed in the knockout pot before reaching the GC, the gas composition data in Figure 75 is on dry basis.

In Figure 75 the experiment was carried out by switching the gas from pure hydrogen to desired syngas composition. To eliminate possible water-gas shift reaction outside the bed, the syngas concentration

introduced to bed corresponded to its equilibrium composition at 370°C. it should be noted that the CO_2 capture by the sorbent from syngas containing CO, H_2, CO_2, and H_2O changes the initial equilibrium composition of the gas and shifts water-gas (WGS) reaction towards production of hydrogen. Figure 76 represents the effectiveness of the bed of sorbent for CO_2 removal at four different operating temperatures. The results indicate that to achieve a high CO_2 removal efficiency, the bed of sorbent should be operated at a temperature range of 370-410°*C* which is also favors production of hydrogen through the WGS reaction.

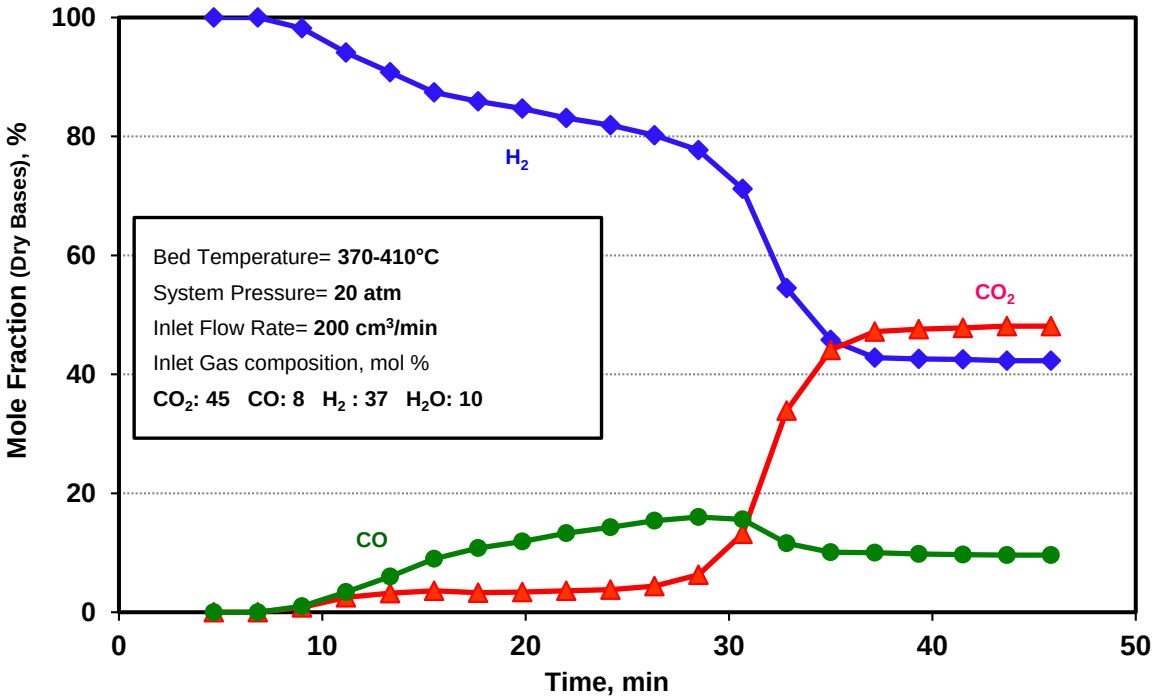

Figure 75. Changes of gas composition measured at gc

The long-time durability of the sorbent was investigated over several consecutive absorption/regeneration cycles in the packed bed unit. The results obtained in five consecutive cycles, shown in Figure 77, indicate that the reactivity of the sorbent gradually decreases in the cycling process (sorbent deactivation). In this series of tests, each of the CO_2 absorption and regeneration steps were carried out at 360-410°*C* and 500°*C*, respectively. The reactor pressure was maintained at 20 atm through the entire absorption and regeneration cycles while the regeneration step was carried out by switching the gas mixture from 45/8/37/10 mixture of $CO_2/CO/H_2/H_2O$ to pure hydrogen gas.

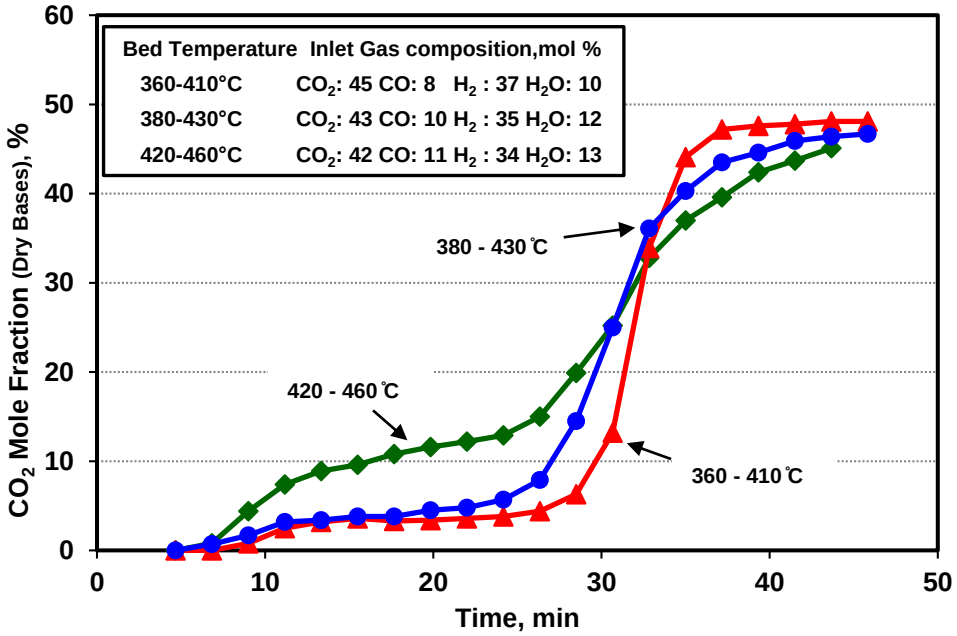

Figure 76. Extent of CO_2 removal at different operating temperatures

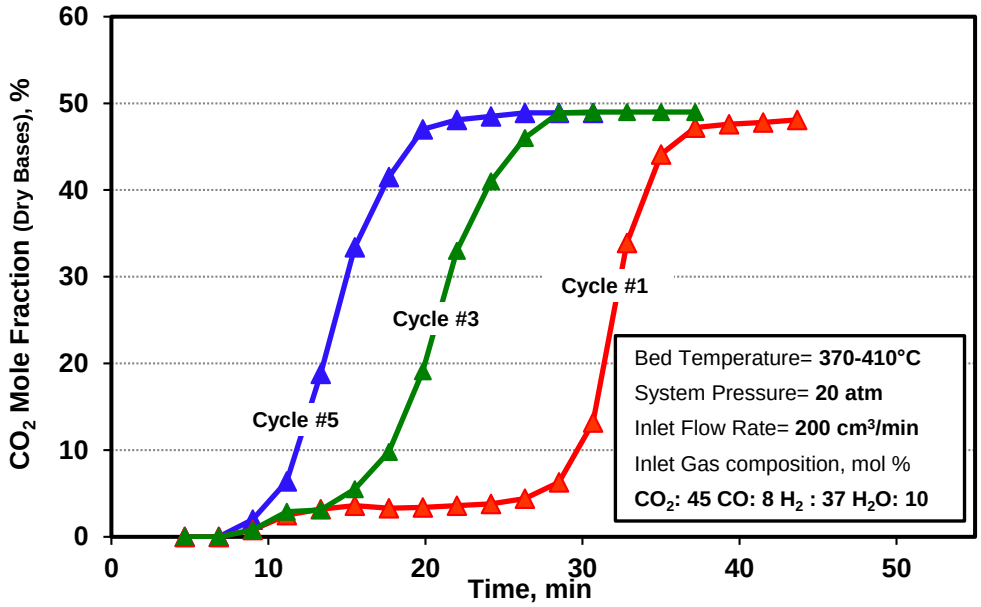

Figure 77. Regenerability and durability of the sorbent

The packed-bed unit consists of three major sections, which impose different residence time distribution (RTD) for the gas mixture to reach the gas analyzer (Gas Chromatograph, GC). These three sections, which include the packed-bed reactor, the water knockout pot, and the backpressure regulator, are shown in Figure 78. Since the concentration of the gases shown in the above figures are measured by the gas chromatograph downstream of the system (Point 5), to determine the concentration profile at the reactor exit (Point 3), the residence time distributions in all three sections of the reactor system were determined by performing a series of blank tests in the packed-bed unit described below.

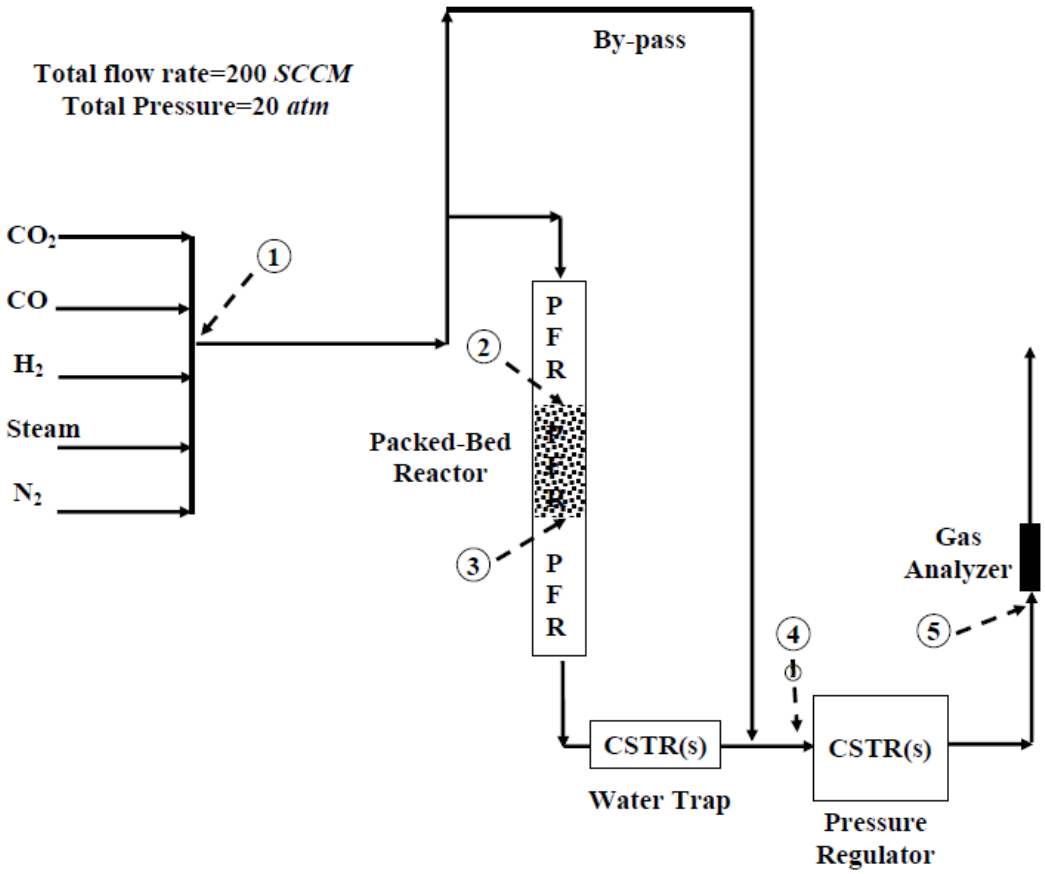

Figure 78. Schematic diagram of major sections of packed-bed unit

In the first blank test, the backpressure regulator was directly connected to the inlet gas mixture, and the reactor and the knockout pot were bypassed (connecting Point 1 to Point 4 directly). A 50/50 gas mixture of N_2 and CO_2, in the form of a step function, was fed to the unit. The changes in the CO_2 concentration at the outlet of the system were measured by the GC, located downstream of the system. Figure 79 shows the residence time distribution of the backpressure regulator involving the connection tubing. After about 20 minutes of the run, the outlet concentrations of CO_2 and N_2 reached their inlet concentrations (~50%mol) and a steady state was achieved. The reproducibility of this blank run is also represented in Figure 79. In the second blank test, the water knockout pot was connected to the unit and the same procedure was applied to the GC data. Figure 80 shows the residence time distribution of the backpressure regulator and water knockout pot involving the connection tubing. To determinate RTD of the entire system, the reactor was connected to the test-line and the reactor bed was packed with inert quartz granules, which were the same particle size and volume as the bed of sorbent used for the actual run. Several blank tests were carried out using the entire packed-bed unit and the results are shown in Figure 81. The results presented in figures 79-81 were used to develop a model describing the RTD of the gas in the entire unit to calculate the concentration of the reactant gas at the reactor exit from that measured by the gas chromatograph.

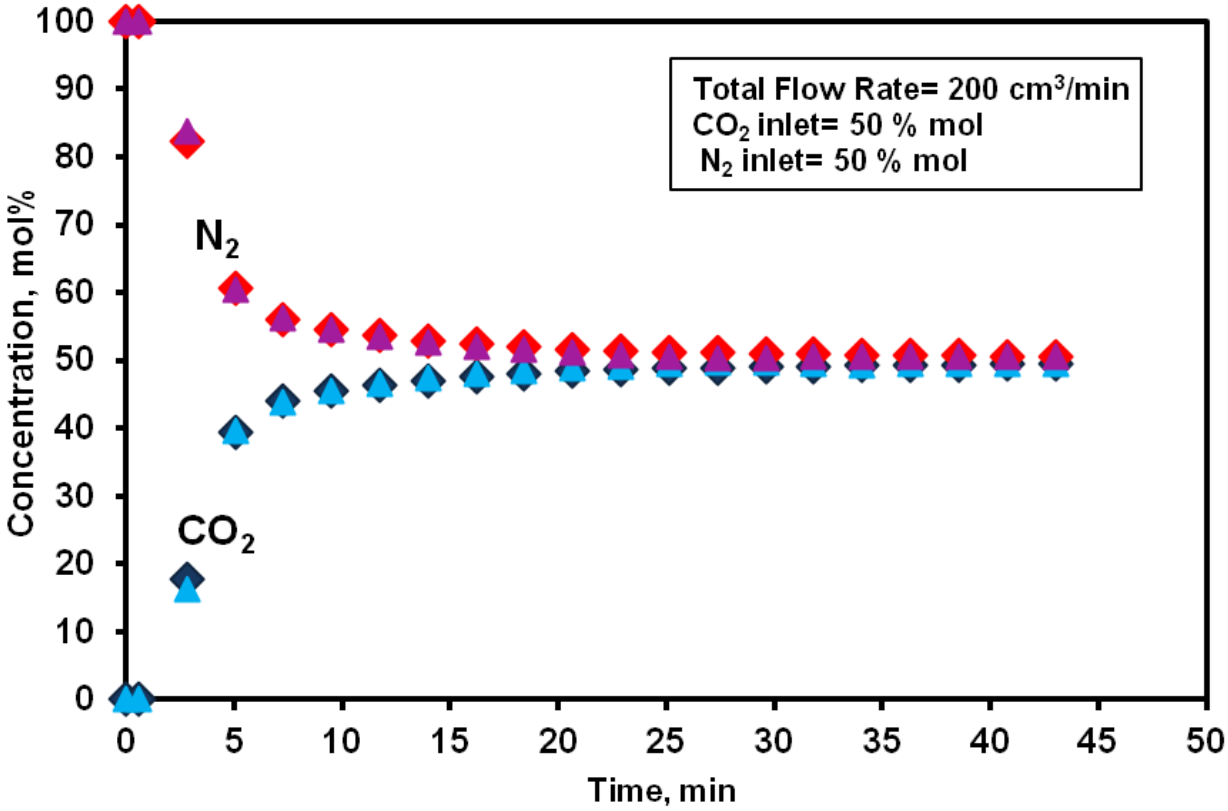

Figure 79. Residence time distribution of backpressure regulator

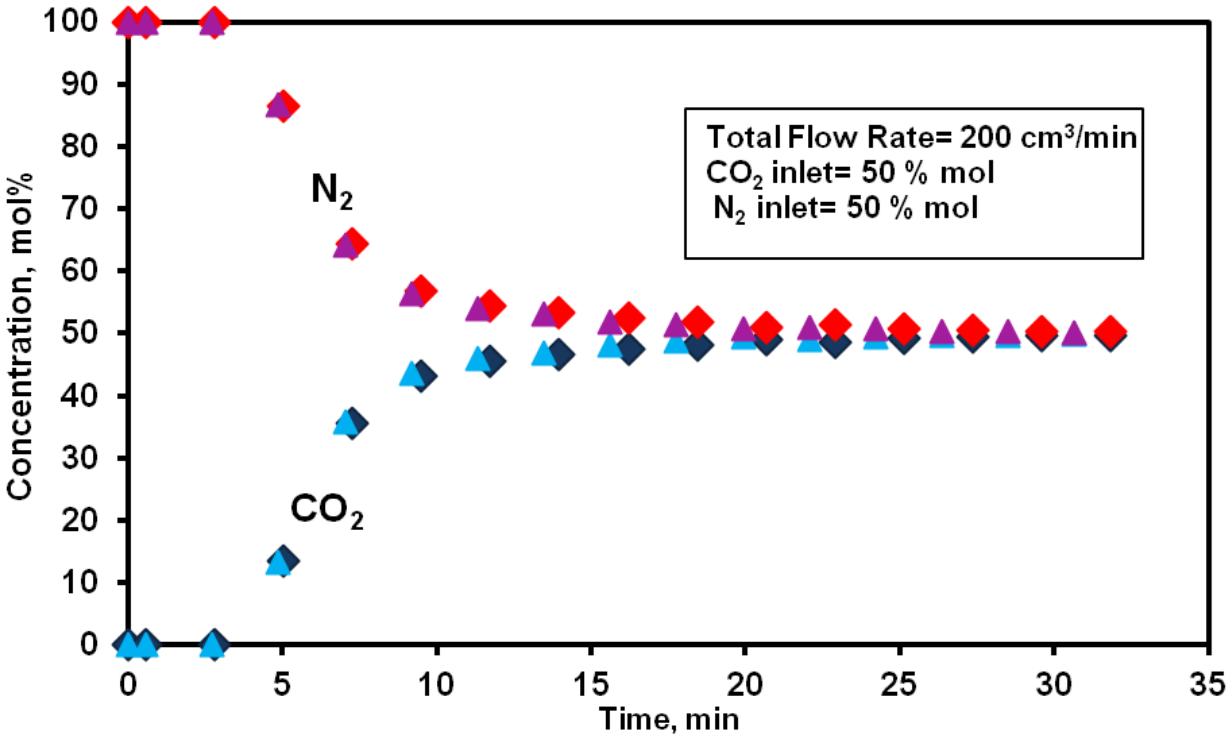

Figure 80. Residence time distribution of backpressure regulator and water knockout pot

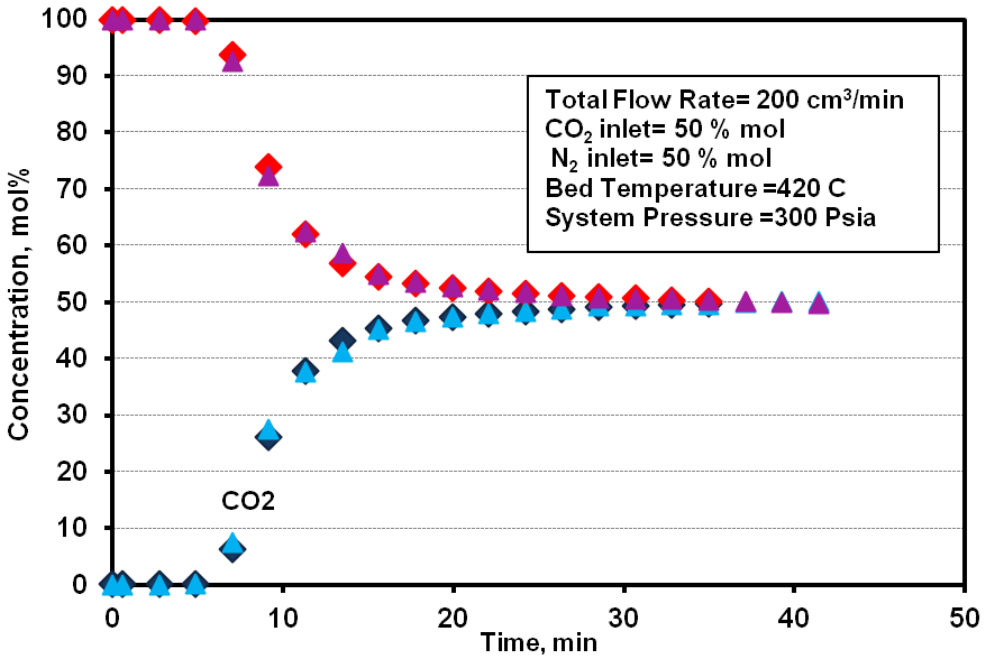

Figure 81. Typical blank run for entire packed-bed system

Also, because of the high CO_2 concentration in the inlet gas mixture, the gas total flow rate significantly changes as CO_2 is removed through the absorption reaction in the bed. This change in the total flow rate significantly affects the residence time distribution of the gas in the packed-bed unit. Therefore, a bubble flow meter was placed at the downstream of the unit to measure the changes in the gas total flow rate as the reaction was taking place. Figure 82 shows the variation in the total gas flow rate (resulting from the carbonation reaction) versus time. The lowest level of the flow corresponds to the maximum CO_2-absorption by the sorbent at that operating condition, which is also related to the CO_2 equilibrium partial pressure in reaction with MgO at each temperature.

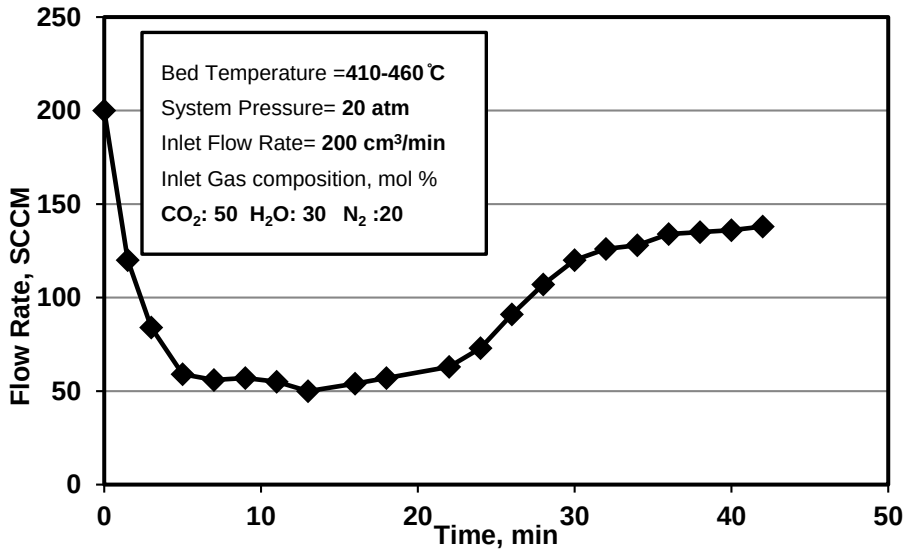

Figure 82. Change in total flow rate of the gas mixture

Packed-Bed unit modeling

Modeling of the packed-bed unit included modeling of the gas mixing flow in each of the unit sections, as well as the modeling of the carbonation reaction in the packed-bed reactor. The reactor model was further developed to include the water-gas shift reaction kinetics and was coupled with the gas mixing model. As mentioned earlier, the packed-bed unit consists of three major sections. The volume of each section imposes a significant residence time distribution (RTD) on the gas mixture to reach the gas analyzer (Gas Chromatograph, GC). The packed-bed reactor, the water knockout pot, and the backpressure regulator are the three major sections in the packed-bed unit, which are shown in Figure 78. Therefore, a residence time distribution (RTD) model was developed using the blank test data presented in Figures 79-81 to determine the composition of the reactor effluent at Point 3. In this model, the inlet concentration to any section is related to the outlet concentration and the RTD through the following equation:

$$C_{out}(t) = \int_0^t C_{in}(t')\,E(t-t')dt' \tag{67}$$

Where, E represents the residence time distribution function. According to the tank-in-series model, the age distribution function that represents N number of CSTRs connected in series is given by the following equation:

$$E(t^*) = \frac{(\theta_i)^{N-1}}{\tau_i(N-1)!}e^{-\frac{t^*}{\tau_i}} \tag{68}$$

$$\tau_i = \frac{V_{CSTR}}{N.Q_{out}} \tag{69}$$

Where τ_i is the mean residence time of a single CSTR.

Figure 83 shows the breakthrough curves resulted in exposing the sorbent to 50%mol CO_2 concentration. Given Y-axis in terms of CO_2 mole fraction at the GC Point 5, the mole fraction of CO_2 at the outlet of the bed can be calculated using tank-in-series model.

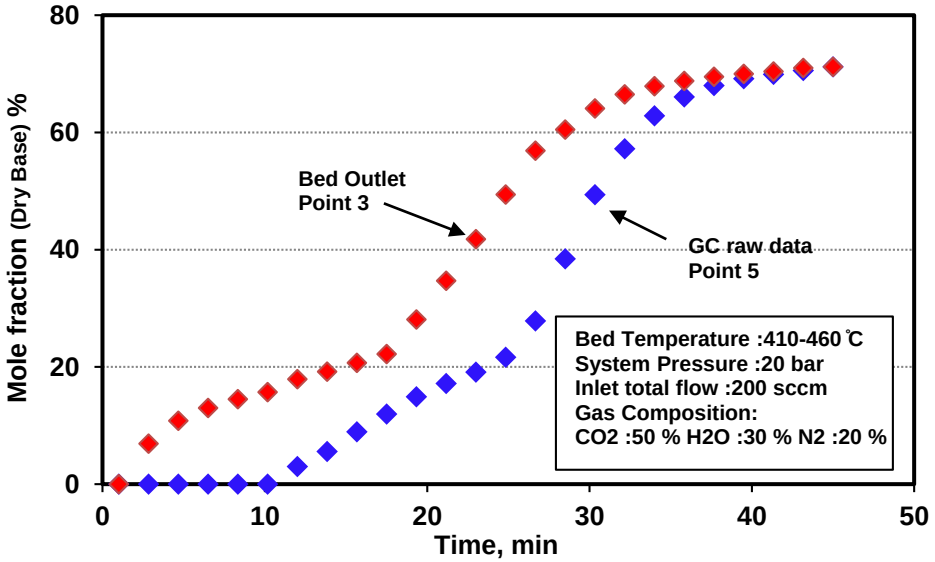

Figure 83. Calculated CO_2 breakthrough mole fractions at different locations

A packed-bed model was developed to predict the extent of CO_2 absorption in a cylindrical reactor with a diameter of 1.9 cm and a length of 8 to 9 cm. An overall mass balance over the entire reactor bed using Navier-Stokes equations can be written as:

$$\varepsilon \frac{\partial C}{\partial t} + \varepsilon \frac{\partial (uC)}{\partial z} = \varepsilon \sum_i \sum_j R_{ij} \tag{70}$$

Where,
C: Overall gas mixture concentration within the bed,
u: Superficial velocity of the gas through the empty reactor
ε: Void fraction of the reactor bed

In Equation 4, the total concentration of the gas can be easily defined as:

(71)

The compressibility factor of the gas mixture at the operating condition of the packed-bed unit (above 300°C at high pressure (20 atm) was calculated to be in the range of 0.985-1.01. Operating the reactor bed at high temperatures significantly decreases the non-ideality of the gas mixture running at high pressure (20 *atm*). Therefore, the gas was assumed to be adequately described by the ideal gas equation of state. $Z_{mixture}$ was assumed to be one ($Z_{mixture}$ = 0.985 to 1.01). As shown in Figure 74, the temperature of the bed changes by 10 to 40°*C* along the bed due to the exothermic carbonation reaction. These small increases in the temperature have a negligible effect on the total concentration of the gas mixture, as represented in Equation 71. Therefore, it is reasonable to assume the total gas concentration is constant along the bed and through time. Then, Equation 70 can be simplified to the following equation, which is a representation of changes in the gas total flow rate along the bed.

$$C \frac{\partial u}{\partial z} = \varepsilon \sum_i \sum_j R_{ij} \tag{72}$$

In the second step of the reactor modeling, mass balances were applied over the sorbent bed for each of the species (*i*) that exist in the gas mixture.

$$\varepsilon \frac{\partial C_i}{\partial t} + \varepsilon \frac{\partial (uC_i)}{\partial z} = \varepsilon \sum_j R_{ij} \tag{73}$$

Other than the assumptions stated before, it was assumed that there is a homogeneous distribution of the gas mixture across the cross-section area of the reactor, because by using a bed of quartz beads before the sorbent bed, the gas is uniformly distributed across the reactor before reaching the bed. As a result, changes in the species concentrations across the bed (in *r* direction) were neglected.

The following boundary and initial conditions was assigned to this mass balance problem:

$$C_i = 0 \qquad @t = 0, z > 0$$

$$C_i = C_{i0} \qquad @z = 0$$
$$u = u_0 \qquad @z = 0$$

As mentioned earlier, there are two reactions that simultaneously occur in the packed-bed reactor. Among the species in the gas mixture (i.e. CO_2, CO, H_2, and H_2O), CO_2 is the only compound that is involved in both the carbonation reaction and the water-gas shift (WGS) reaction. Therefore:

$$\sum_j R_{ij} = \rho_{sorbent} \frac{1-\varepsilon}{\varepsilon} r_{i,WGS} \qquad \text{for } i = \mathrm{CO}, \mathrm{H_2}, \mathrm{H_2O} \qquad (74)$$

$$\sum_j R_{CO_2 j} = \rho_{sorbent} \frac{1-\varepsilon}{\varepsilon} r_{CO_2,WGS} + \rho_{sorbent} \frac{1-\varepsilon}{\varepsilon} r_{CO_2,Cbn} \qquad (75)$$

Where

$$r_{CO_2,Cbn} = \frac{y_{MgO}}{MW_{MgO}} \frac{dX}{dt} \qquad (76)$$

$$r_{CO_2,WGS} = k_{WGS} \left(C_{CO} C_{H2O} - {C_{CO2} C_{H2}}/{K_{eq,WGS}} \right) \qquad (77)$$

Where,

C_i: Mole fraction of species *i* in the gas mixture
K_e: WGS reaction equilibrium constant
k_{WGS}: Forward reaction rate constant

The governing differential equations (i.e. Equations 72 and 73) were numerically solved using the finite difference method. To best fit the model to the experimental data, the WGS reaction rate constant was the model parameter that was determined by minimization of the least squares of the errors. As it was shown in the previous chapters, the rate of the WGS reaction is very dependent on the MgO concentration, which has a significant catalytic affect on promoting the WGS reaction. Therefore, the reaction rate constant is assumed to be a function of the local MgO conversion through the entire sorbent particle. In this study, the following exponential function is used for the changes in the WGS reaction rate constant.

$$k_{WGS} = k^0_{WGS}\, e^{-E_{WGS}/RT} \,.\, e^{-bX_l} \qquad (78)$$

As a result, there are three parameters (k^0_{WGS} , E_{WGS} and b) for the model that were determined by fitting the model to the experiments. In this assumption, the k^0_{WGS} and E_{WGS} are part of an Arrhenius function and depend on temperature, and b is constant for the entire temperature range.

The model was fitted to the experimental data at temperature range of 350° to 425°C and the model parameters were determined for each operating temperature as indicated in Table 27. The activation energy of the WGS reaction is calculated to be 65 kj/mol. Figures 84, 85 and 86 show a comparison among the model fit to the CO_2 , CO and H_2 concentration breakthrough curve at different operating temperatures.

Table 27. WGS Reaction Model Parameters at Different Operating Temperatures

Model Parameter	360-460℃
k^0_{WGS},mol/(g.s)/(mol/m^3)^2	0.000136
b	80
E_{WGS}, kJ/mol	65

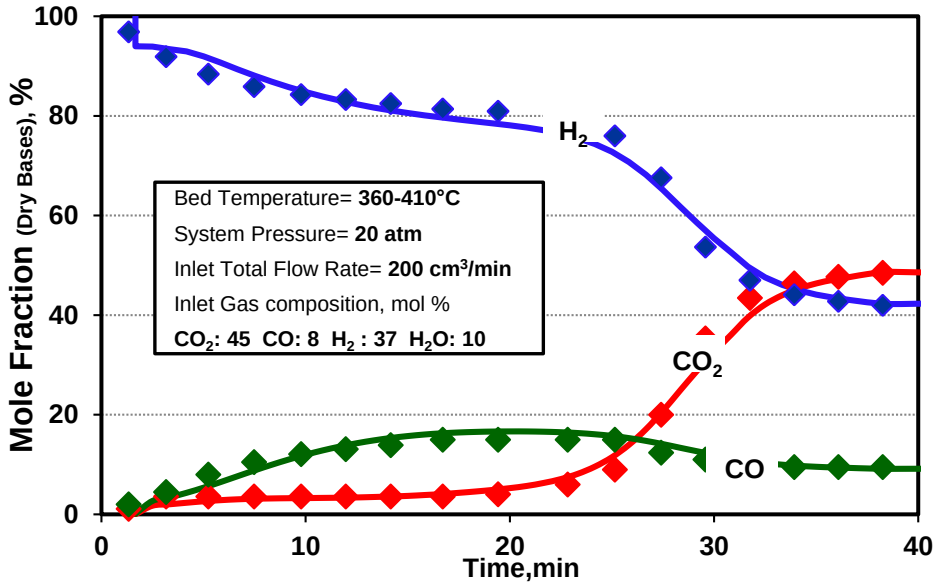

Figure 84. Model fit for CO_2 breakthrough curve in the temperature range of 360-410˚C

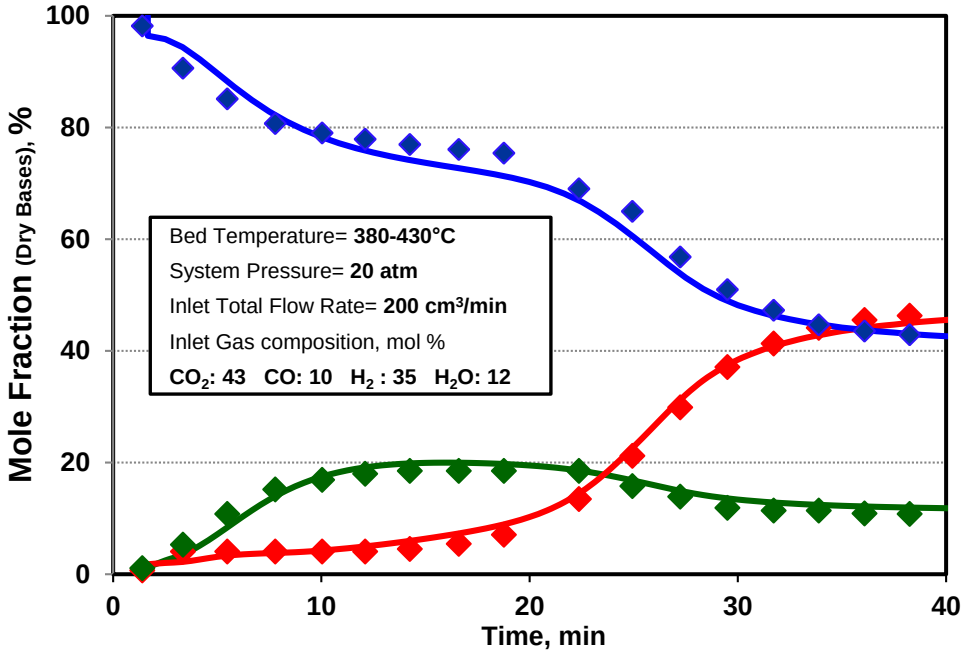

Figure 85. Model fit for CO_2 breakthrough curve in the temperature range of 380-430˚C

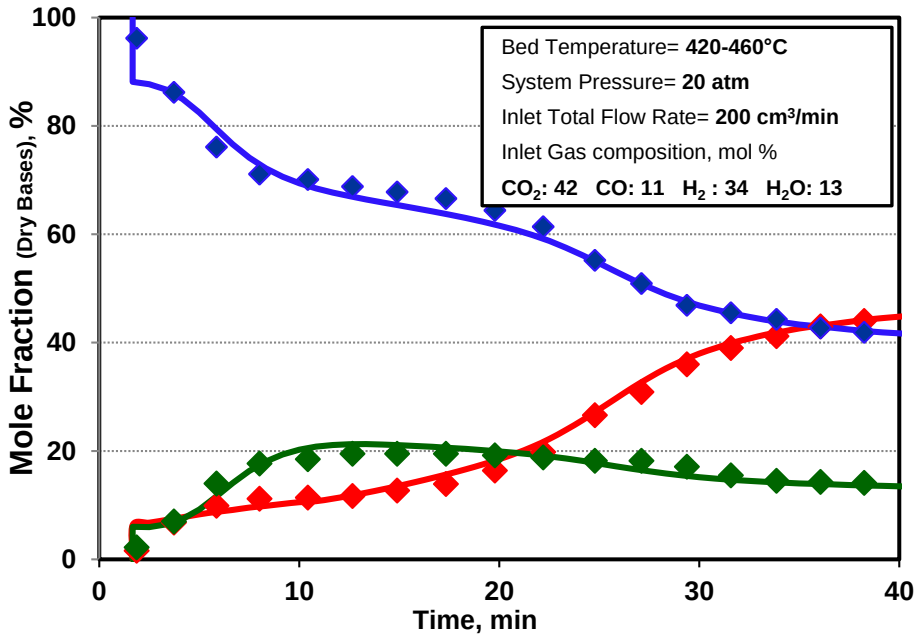

Figure 86. Model fit for CO_2 breakthrough curve in the temperature range of 420-460˚C

The model was also fitted to the experimental data at different cycles and the model parameter, β was determined for each cycle as indicated in Table 28. The model predicts that the reactivity of the sorbent significantly decreases in the cycling process. Figures 87 and 88 show a comparison among the model fit to the CO_2 ,CO, and H_2 concentration breakthrough curve in the cycling process.

Table 28. WGS Reaction Model Parameter at Different Cycle Numbers

Model Parameter	1st Cycle	3rd Cycle	5th Cycle
β	80	110	130

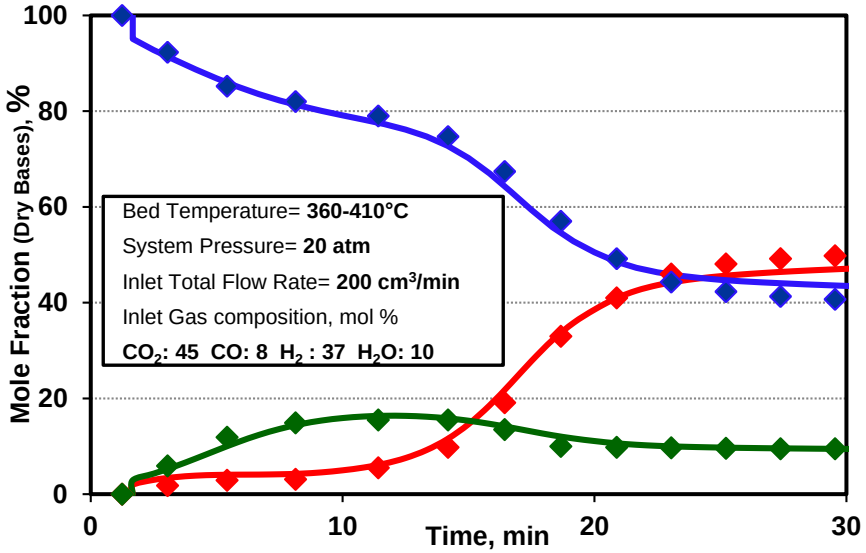

Figure 87. Model fit for CO_2 breakthrough curve in cycle #3

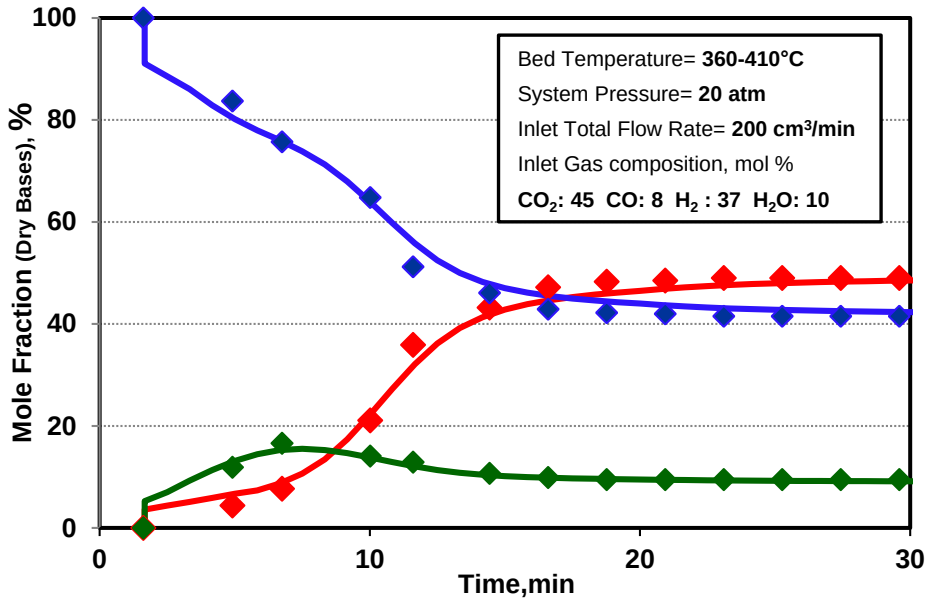

Figure 88. Model fit for CO_2 breakthrough curve in cycle #5

Task 4. CFD simulations of the regenerative carbon dioxide capture process

This task is geared toward incorporation of the PBE model into a computational Fluid Dynamic model to simulate the absorption and the regeneration reactors in the regenerative carbon dioxide capture process.

Simulation of CO_2 capture in a packed-bed

To simulate CO_2 capture in a packed-bed, the experimental obtained by Hassanzadeh[3] in a high-pressure/high-temperature packed-bed with the dry regenerable MgO-based sorbent was utilized. The schematic of the packed-bed reactor used to obtain the experimental data (Hassanzadeh[3]) is shown in Figure 19. The experimental data includes two sets of runs in the packed-bed unit. The first set included the absorption/regeneration cycles in the presence of different concentrations of CO_2, N_2, and steam at different operating conditions that can be used to study CO_2 absorption without the water-gas-shift reaction, while in the second set, syngas mixtures with different compositions were fed into the reactor to evaluate simultaneous CO_2 absorption and enhancement of hydrogen production through the water-gas-shift reaction. The operating conditions of each of these experimental sets are shown in Table 7.

The mathematical model presented above was utilized in a commercial finite volume based CFD code (i.e., ANSYS Fluent) for simulations of the packed bed reactor and investigation of the sorbent's performance at different operating condition. For the reaction kinetic model, the variable diffusivity shrinking core model (also presented above) was implemented in the CFD code using an external subroutine as a user defined function.

As reported by Hassanzadeh[3], because of the exothermic reaction between MgO and CO_2, the temperature of the bed increases as the reaction proceeds. In their experiments there was a 10-30°C temperature rise in the entire packed-bed tests, which significantly affected the CO_2 equilibrium partial pressure (especially at higher temperatures), resulting in an increase in CO_2 concentration at the exit of the bed (not a perfect S-shaped breakthrough curve). Therefore, the

effect of temperature should be considered in the packed model. Because sufficient experimental data were not available for solving the energy equation as part of the model, the experimentally measured temperature profiles reported by Hassanzadeh (Figure 89) were imposed on the bed. Figure 90 shows the locations and temperature measurements along the bed. Figure 91 shows the experimental data (Hassanzadeh[3]) on the extent of CO_2 capture in the packed bed for three different CO_2 inlet concentrations (i.e. 25, 35 and 50%mol) at 425°C and 20 atm.

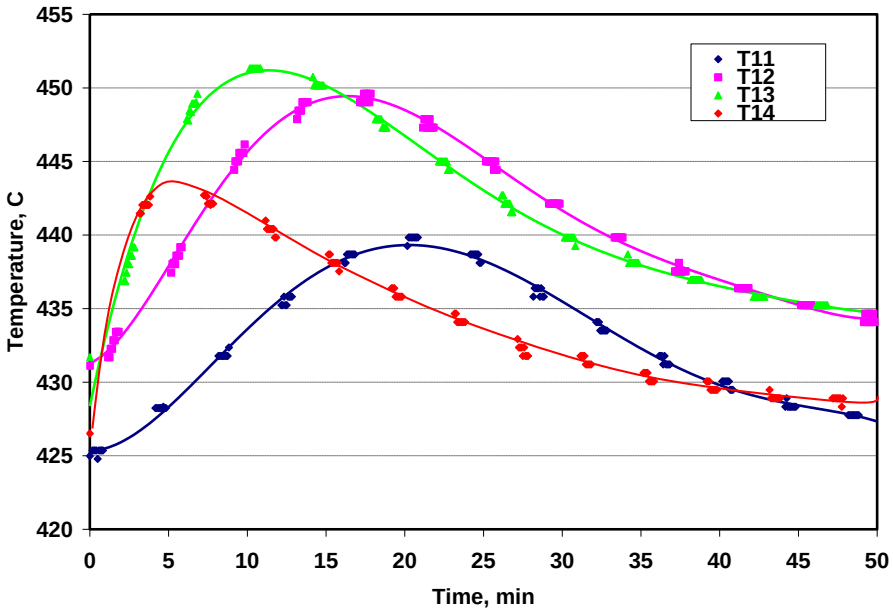

Figure 89. Temperature profile along reactor bed during reaction

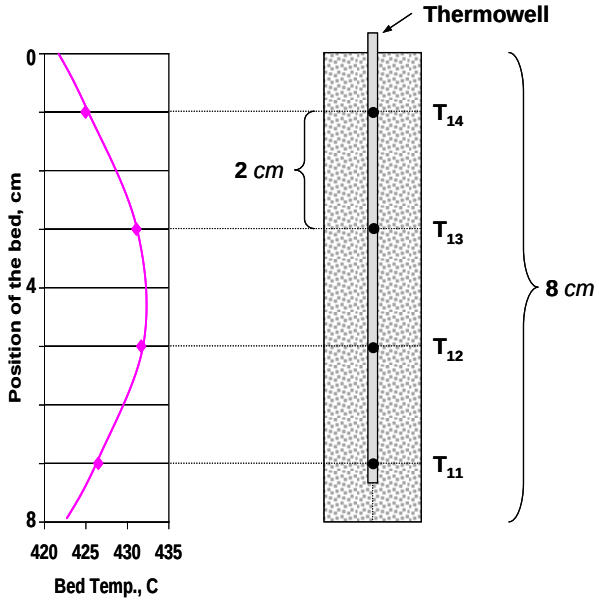

Figure 90. Position of measuring locations and temperature gradient along the bed (at time=0)

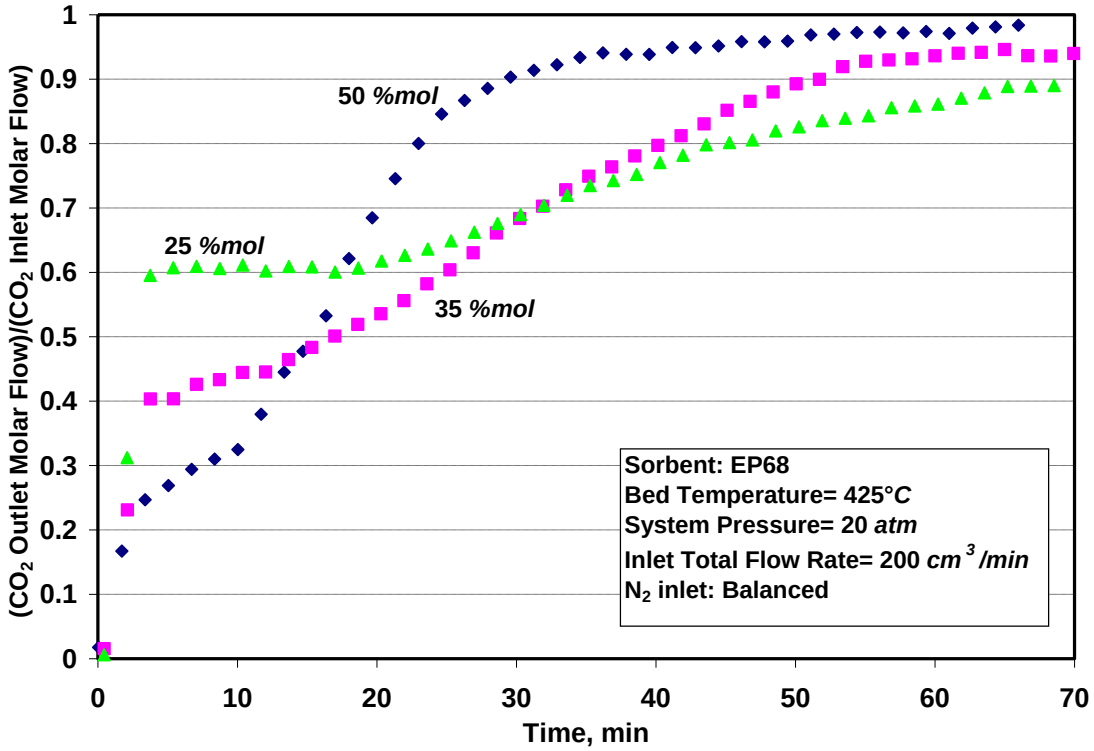

Figure 91. Bed behavior exposed to different inlet CO_2 concentrations

Simulation results for different CO_2 inlet concentrations are presented in Figures 92 through 94. As expected, because of the reaction equilibrium limitation at operating condition of the bed, the extent of CO_2 capture decreases with decreasing CO_2 inlet concentrations, resulting in smaller variations in the temperature within the bed. In these figures, the first breakthrough CO_2 outlet concentration corresponds to the equilibrium concentration of CO_2 at the operating temperature (i.e., about 11.3%). Therefore, because of the equilibrium limitation, the initial ratio of the outlet CO_2 to inlet CO_2 increases with decreasing CO_2 inlet concentration. Although the behavior of the simulated breakthrough curves at different CO_2 inlet concentrations show a similar trend to that exhibited by the experimental data, the simulations under-predicted the extent of CO_2 captured (total area above the curve). The reason may be attributed to the approximation of temperature profiles at different operating conditions by one set of data obtained for the 50% inlet CO_2 concentration, which may be resolved by fine-tuning the temperature profiles.

It should be noted that because of the high CO_2 concentration in the gas mixture, the total flow rate of the gas mixture significantly decreases as the CO_2 is absorbed by the sorbent in the reactor. The developed model can predict the transient changes in the flow rate through the bed. Figures 95 and 96 show the instantaneous gas velocity and CO_2 mole fraction contours in the bed at 10 min after the start of the reaction (at 50% inlet CO_2 concentration).

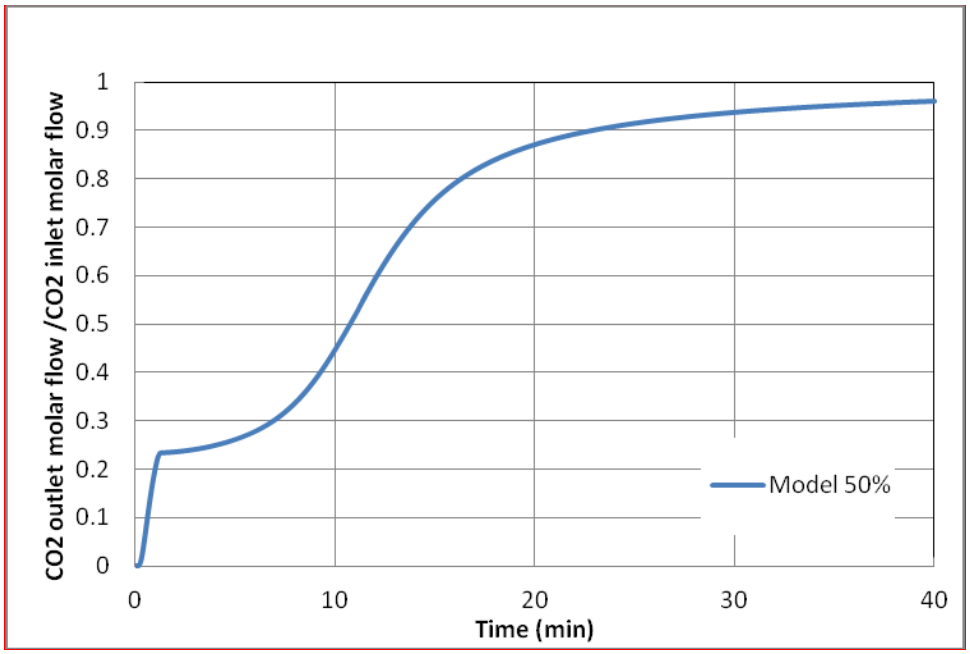

Figure 92. Simulated bed behavior exposed to 50% inlet CO_2 concentrations

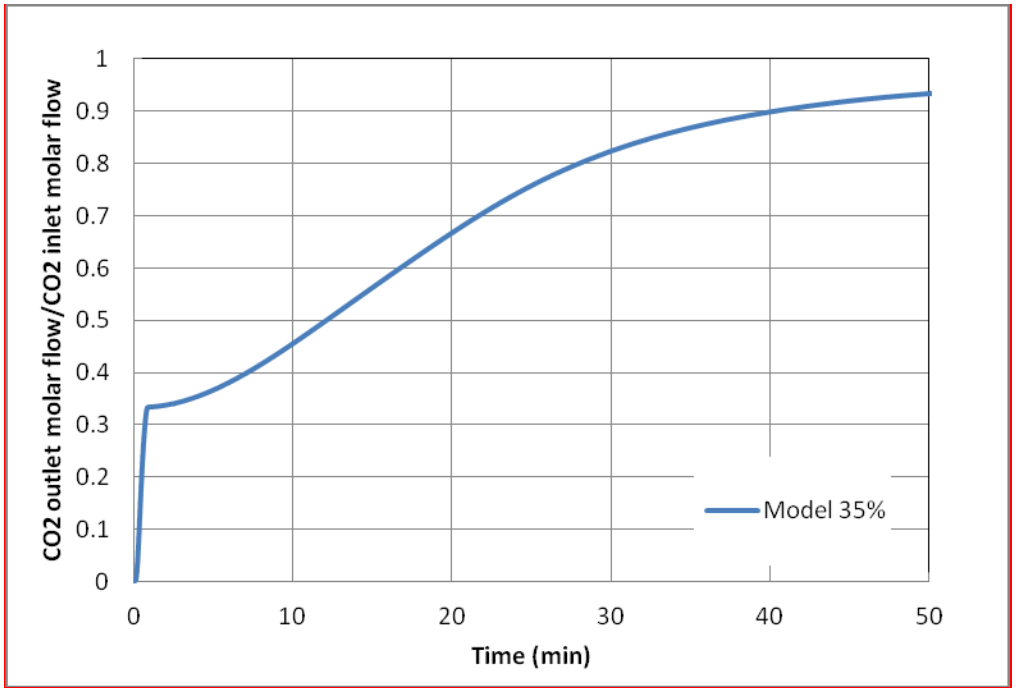

Figure 93. Simulated bed behavior exposed to 35% inlet CO_2 concentrations

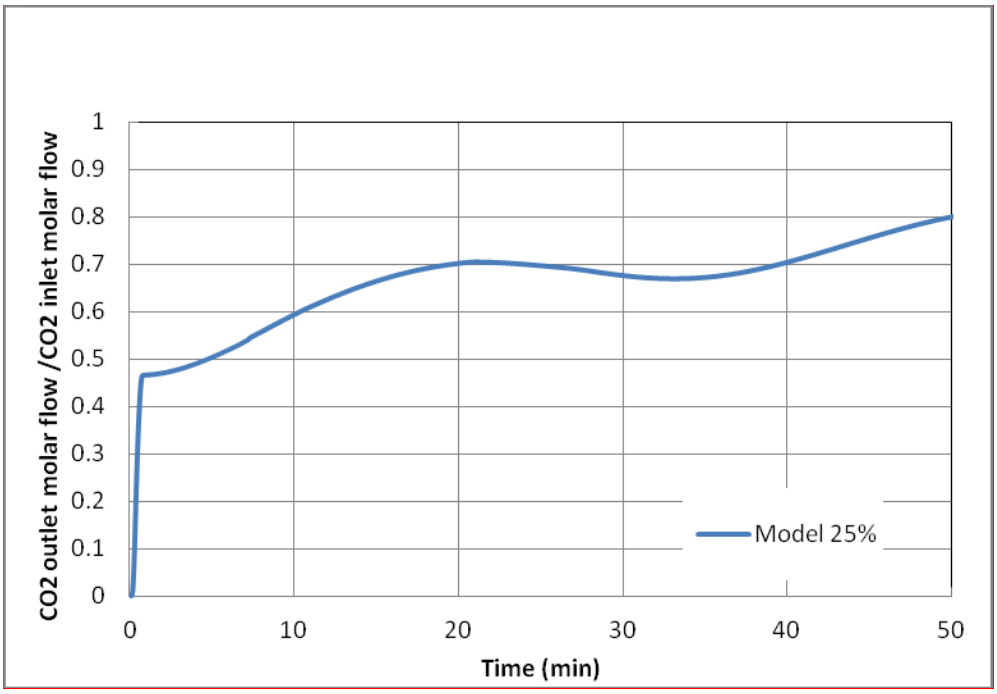

Figure 94. Simulated bed behavior exposed to 25% inlet CO_2 concentrations

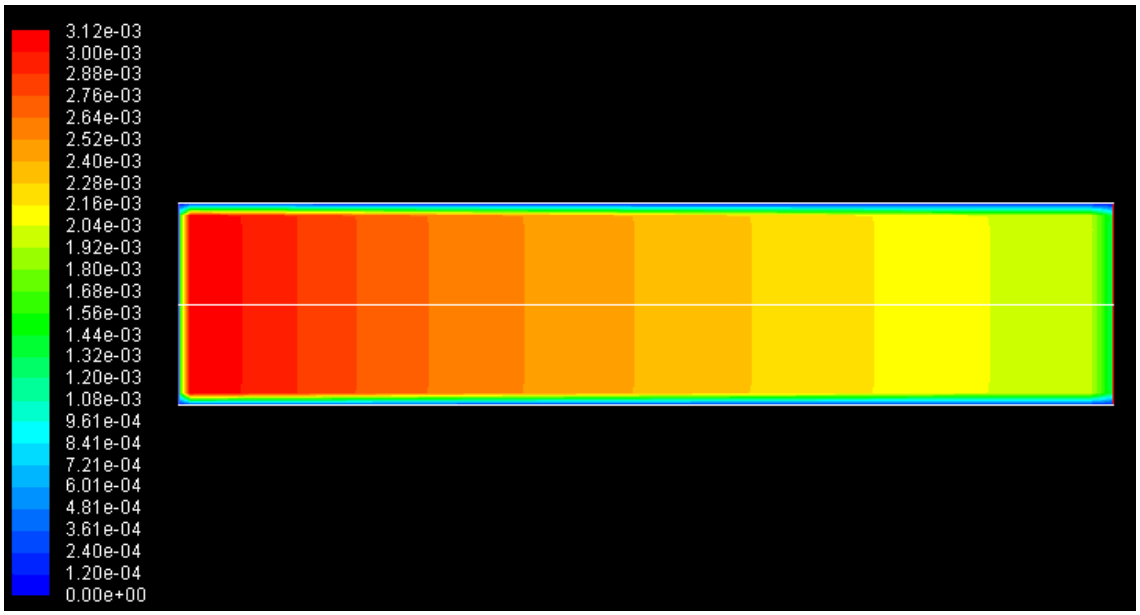

Figure 95. Instantaneous gas velocity (m/s) contours at t = 10 min, for 50% CO_2 inlet concentration.

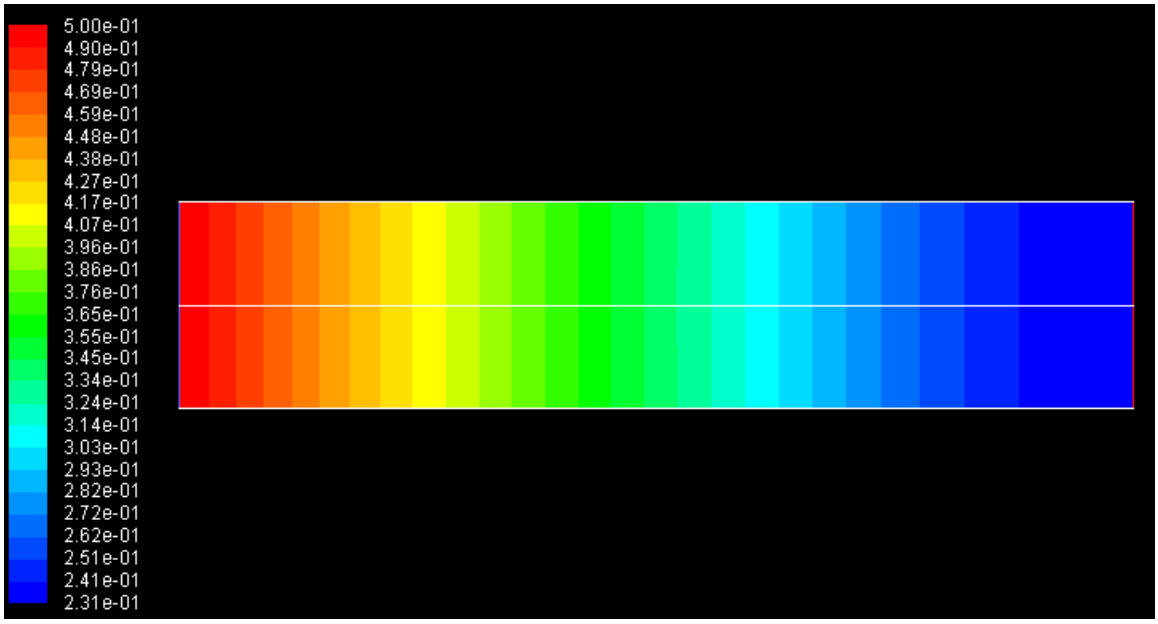

Figure 96. Instantaneous CO_2 mole fraction contours at t = 10 min, for 50% CO_2 inlet concentration.

Verification of the applicability of our CFD-PBE model in simulations of poly-disperse flow

As presented in Task 2, a coupling algorithm based on Finite size domain complete set of trial functions method of moments (FCMOM) was developed and tested in simulations of simple cases with available analytical solutions, showing the accuracy and effectiveness of the method. However, those simple cases did not include particulate processes such as aggregation and breakage phenomena which are responsible for appearance of complex integral terms in population balance equations.

Applicability of the FCMOM method in simulations of complex systems using multiphase CFD approach has not been studied. In this project, we tried to probe the applicability of our CFD-PBE model in simulations of a complex poly-disperse flow. The method was employed in CFD simulations of an oil-water emulsion flow in a backward facing step geometry including aggregation as proposed by Silva et al[57]. The proposed case is a two-dimensional two-phase flow of water in oil emulsion through a Backward Facing Step (BFS) geometry as shown in Figure 97. It was chosen due to its simplicity and the presence of circulation zones with steep gradients in laminar flow. The main circulation region is depicted in Figure 98, showing streamlines of the continuous phase (oil). The results were numerically verified against the simulation results obtained by QMOM model as a reference to evaluate correct implementation of FCMOM in the CFD code, ANSYS/ Fluent 13. It should be noted that this is not an experimental validation, but a numerical analysis and verification test. The coalescence between the water droplets was modeled using the Smoluchowski aggregation model. The continuous form of the Classical Smoluchowski Equation (CSE) can be written as follows

$$\frac{\partial f(v;\mathbf{x},t)}{\partial t} = \frac{1}{2}\int_0^v \beta(v-\eta,\eta).f(v-\eta,t).f(\eta,t)d\eta - f(v,t).\int_0^\infty \beta(v,\eta).f(\eta,t)d\eta \qquad (79)$$

In Eq. (79), the first term on the right-hand side represents the birth of particles due to a binary aggregation between two particles with size ν-η and η; and the second term on the right-hand side represents the death of particles due to aggregation and β is the aggregation kernel.

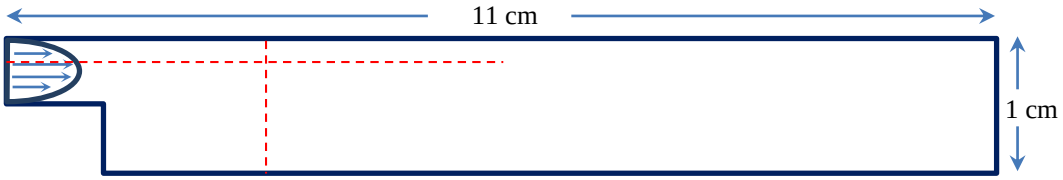

Figure 97. Backward facing step geometry

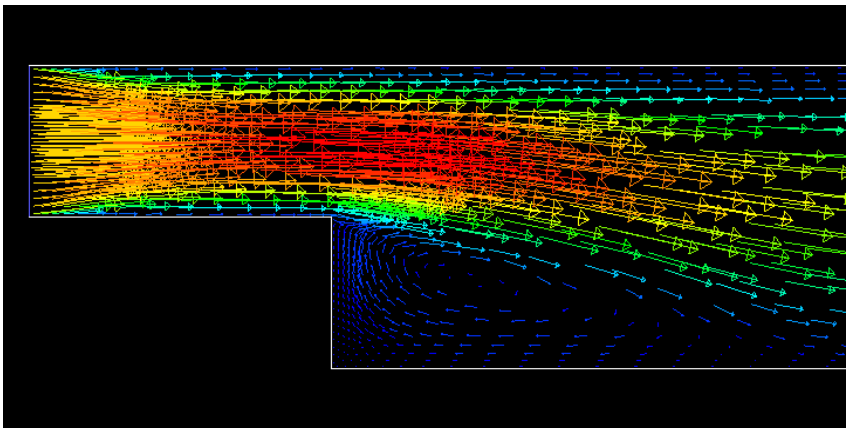

Figure 98. Streamlines of the continuous phase showing the circulation region.

We also define a Finite Smoluchowski Equation (FSE). In FSE, initially a minimum and maximum volumes v_{min} and v_{max} are set. Then, FSE is essentially the same as CSE, the only difference is that in FSE, aggregations leading to particles v larger than v_{max} are neglected. This is accomplished by using $(v_{max} - v)$ (instead of infinity) as upper limit of integration in the second term on the right-hand side of Eq. (79), and introducing the Heaviside step function H in the second term on the right-hand side of Eq.(79) to neglect aggregations involving particles v larger than $(v_{max} - v_{min})$. Therefore, the FSE may be expressed as follows:

$$\frac{\partial f(v;\mathbf{x},t)}{\partial t} = \frac{1}{2} H(v - 2v_{\min}) \int_{v_{\min}}^{v-v_{\min}} \beta(v-\eta,\eta).f(v-\eta,t).f(\eta,t)d\eta - f(v,t).H[(v_{\max} - v_{\min}) - v]. \int_{v_{\min}}^{v_{\max}-v} \beta(v,\eta).f(\eta,t)d\eta \tag{80}$$

The lower boundary (minimum volume) is trivially equal to zero, as in the CSE. Again, in Eq. (80), the first term on the right-hand side represents the birth of particles due to aggregation; the second term on the right-hand side represents the death of particles due to aggregation. The CSE cannot be solved directly using the FCMOM, however, when the value chosen for the v_{max} is large enough, while $v_{min} = 0$, the solution of the FSE model is expected to converge to the solution of the CSE model.

By applying the FCMOM method, final form of the moments transport equation for FSE becomes:

$$\frac{\partial \mu_i}{\partial t} + \nabla.(\mu_i.v_p) = \frac{v_{\max} - v_{\min}}{4} \sum_{n=0}^{M-1}\sum_{m=0}^{M-1} c_m c_n E_{mni}^{FSE} - \frac{v_{\max} - v_{\min}}{2} \sum_{n=0}^{M-1}\sum_{m=0}^{M-1} c_m c_n F_{mni}^{FSE} \tag{81}$$

where:

$$E_{mni}^{FSE} = \int_{-2+v_r}^{1} \int_{-1}^{\bar{v}+1-v_r} \bar{v}^i \beta[\frac{v_{\max}-v_{\min}}{4}.(\bar{v}-\bar{\eta}), \frac{v_{\max}-v_{\min}}{4}.(\bar{\eta}-v_r)]\phi_m(\bar{v}-\bar{\eta}-v_r)\phi_n(\bar{\eta})d\bar{\eta}d\bar{v} \quad (82)$$

$$F_{mni}^{FSE} = \int_{-2+v_r}^{2-v_r} \int_{-1}^{1-\bar{v}-v_r} \bar{v}^i \phi_m(\bar{v}).\beta[\frac{v_{\max}-v_{\min}}{4}.(\bar{v}+v_r), \frac{v_{\max}-v_{\min}}{4}.(\bar{\eta}+v_r)]\phi_n(\bar{\eta})d\bar{\eta}d\bar{v} \quad (83)$$

where $v_r = (v_{max} + v_{min})/(v_{max} - v_{min})$. The coefficients E^{FSE}_{mni} and F^{FSE}_{mni} can be pre-calculated as a function of v_{min} and v_{max}.

In these simulations, all particles share the same velocity field v_p. This assumption is reasonable for small droplets in a liquid–liquid flow with small density difference. As the particle size distribution is convected by the flow, droplet coalescence causes its evolution. Therefore, the change in the size distribution is proportional to the disperse phase residence time. The interphase forces between the continuous and the disperse phases were calculated using the mean diameter (d_{10}) of the particle size distribution obtained through the population balance calculation.

The simulations were performed in hexahedral meshes and the grid independence test was performed using meshes with 8,400, 33,600 and 134,400 elements, referred to as coarse, medium and fine meshes, respectively. Furthermore, the effect of number of moments of size distribution was studied by considering 4, 6 and 8 moments.

The flow was laminar, with a Reynolds number of 500 for the continuous phase (oil) in order to avoid possible uncertainties coming from the turbulence modeling. Water content in the inlet emulsion was 5% with an initial droplet size distribution as:

$$f(\bar{v},0) = a.(\frac{1}{2}+\frac{\bar{v}}{2})^2.(\frac{1}{2}-\frac{\bar{v}}{2})^8 \quad (84)$$

The initial average droplet size was 1.25 mm and the breakage kernel was considered as sum kernel with the form of:

$$\beta = \beta_o(v + \eta) \quad (85)$$

The results are presented on two dashed lines shown in Figure 6, the horizontal line and the vertical line. Figure 99 and Figure 100 show mean droplet size along the vertical line for different mesh resolutions using QMOM and FCMOM. Bothe graphs show identical behaviors, having larger droplet size in the circulation region due to the longer residence time in this region; however FCMOM seems less sensitive to the mesh resolution. Based on the grid independence study, the mesh with medium resolution was chosen for next simulations.

Figure 101 and Figure 102 show mean droplet size along the vertical line for different number of moments (4, 6, 8) using QMOM and FCMOM. These results show that increasing number of moments does not change the QMOM prediction of mean droplet size; however FCMOM is more sensitive to the number of moments. Comparison between the results on FCMOM with 8 moments and those from QMOM are shown in Figures 103 and 104. The results suggest that at least 8 moments are required to capture the same results calculated by QMOM. Figures 105 and 106 show Mean Droplet size contours after 1 sec calculated using FCMOM and QMOM with 8 moments. The identical contours confirm successful implementation of the coupled CFD-PBE model in the CFD code.

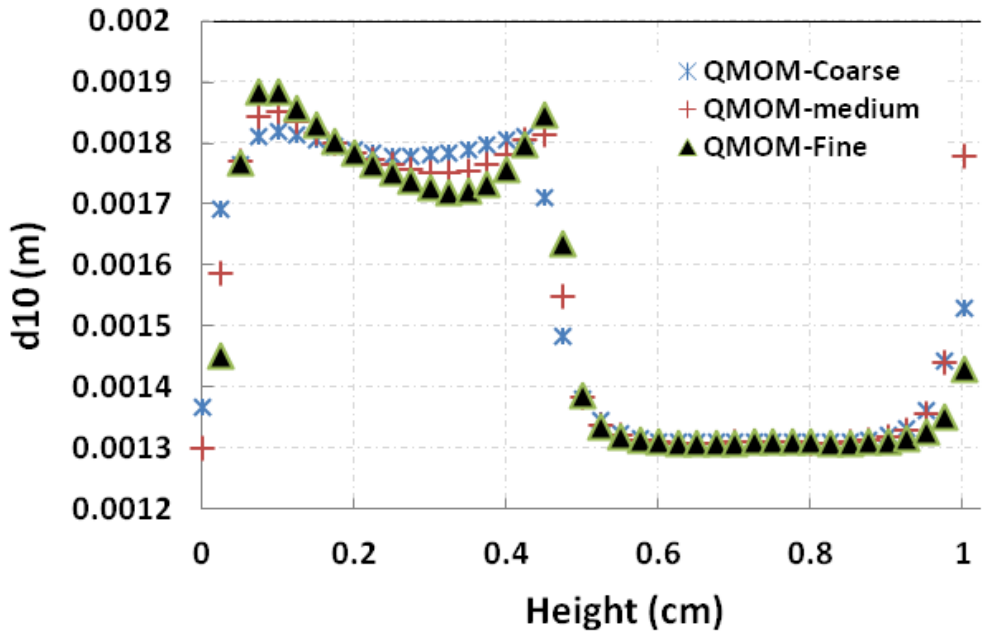

Figure 99. Mean droplet size along the vertical line for different mesh resolutions with QMOM

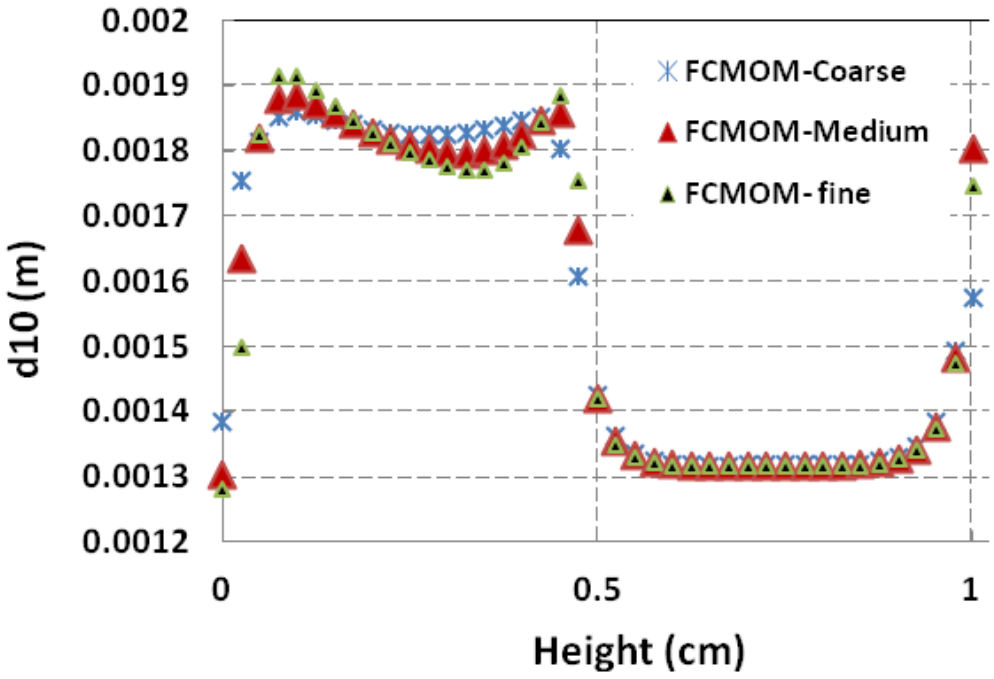

Figure 100. Mean droplet size along the vertical line for different mesh resolutions with FCMOM

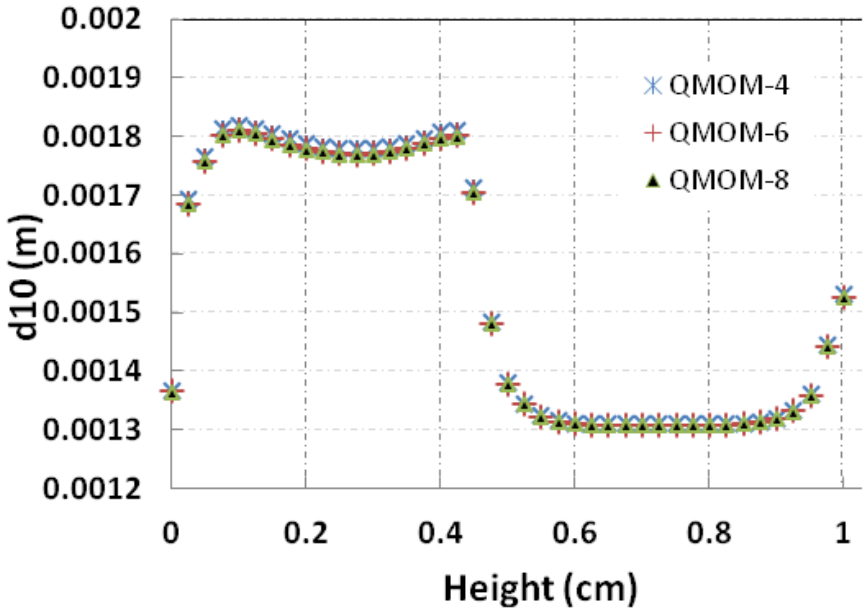

Figure 101. Mean droplet size along the vertical line for different number of moments with QMOM

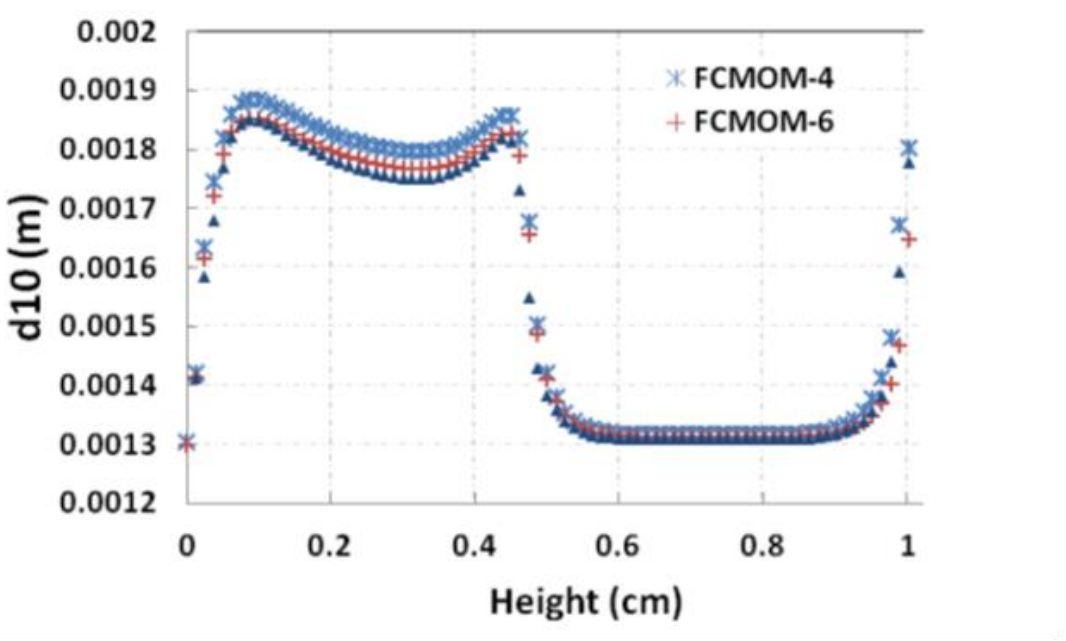

Figure 102. Mean droplet size along the vertical line for different number of moments with FCMOM

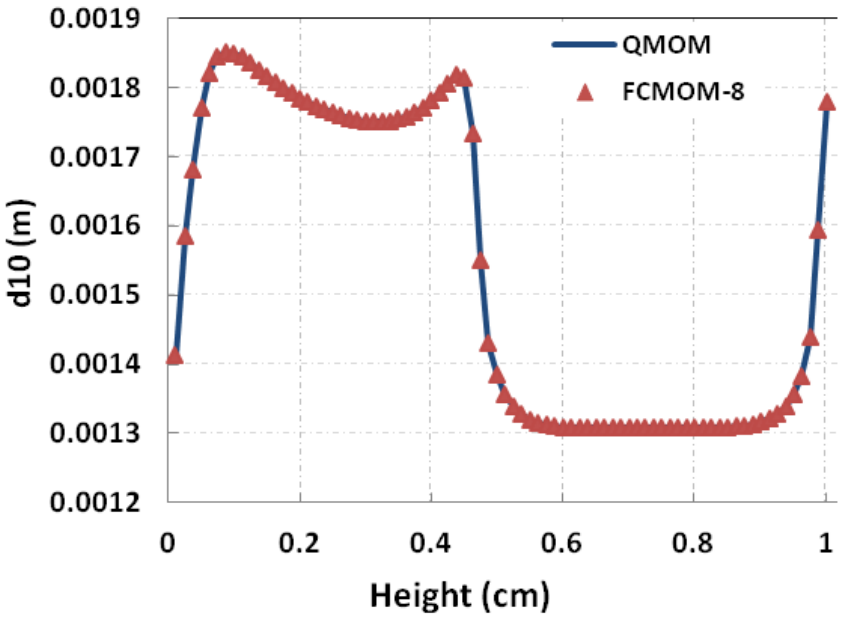

Figure 103. Comparison of the mean droplet size along the vertical line for QMOM and FCMOM (calculated using 8 moments)

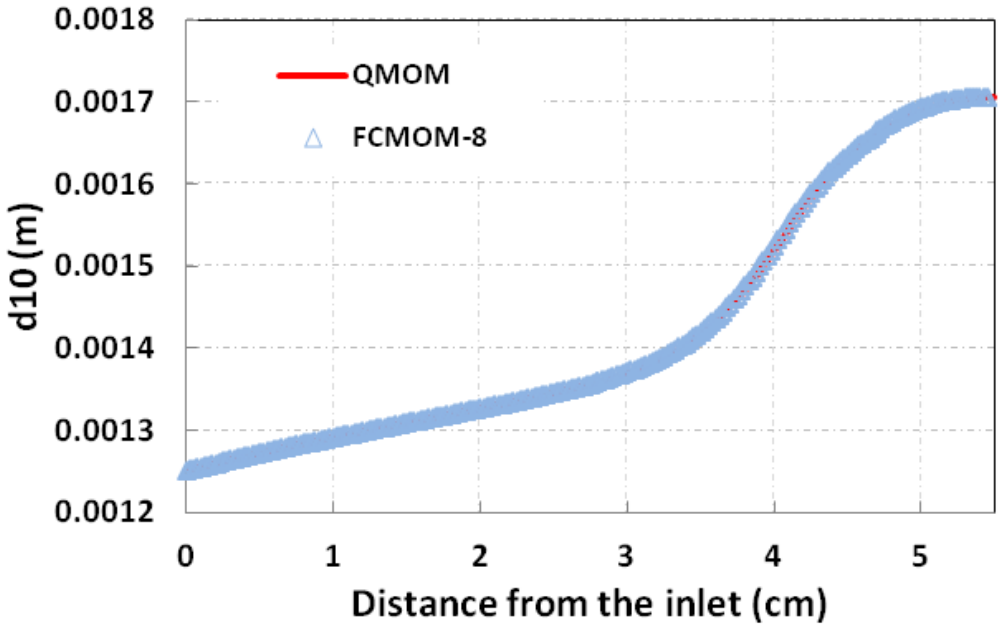

Figure 104. Comparison of the mean droplet size along the horizontal line for QMOM and FCMOM (calculated using 8 moments)

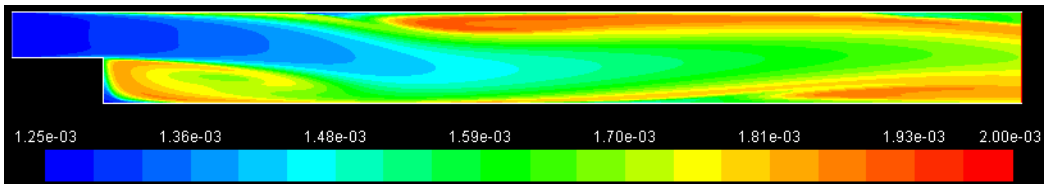

Figure 105. Mean droplet size contours at t= 1 sec calculated using FCMOM and 8 moments

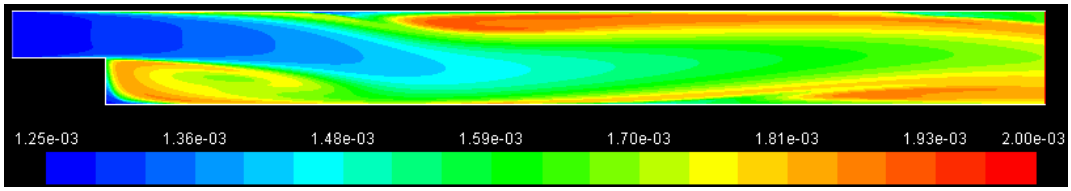

Figure 106. Mean droplet size contours at t= 1 sec calculated using QMOM and 8 moments

Numerical simulation of CO_2 sorption and regeneration process

To assess the performance of the sorbent for capturing CO_2 in a regenerative process and to provide a base case design for a circulating fluidized bed reactor, we used the NETL Carbon Capture Unit (C2U) design as our starting point. The data provided directly by NETL and some detail has been reported by Clark *et al*.[58].

The system is a bench scale post-combustion CO_2 capture unit using a solid sorbent to capture CO_2 from a flue gas stream. The experiment data on hydrodynamics and operation of a continuously looping CO_2 capture system is being used as a baseline for validation of our CFD model. As the first step, we used the cold, non-reacting conditions to study the gas-particle flow behavior of the system. A schematic picture of the experimental unit is shown in Figure 107. The unit has an overall height of 3.35 m, a width of 1.16 m, and a depth of 0.71 m. The system is made of clear polycarbonate material which allows visual observations and image recordings of particle flow. The regenerator and loop seals are 13.97 cm ID clear polycarbonate. Piping is 5.08 cm ID clear polycarbonate except for the 2.54 cm piping from the riser to the cyclone. Two-ring heating coils are located in the regenerator and Loop Seal 1 and reduce to cross-flow area from 152.28 cm^2 to an effective flow area of 105.48 cm^2. The CO_2-containing gas enters the bottom of the absorber and mixes with fresh sorbent. In the cold experiments with inert sorbent, air is used as the fluidization media. The sorbent particles mix with the feed gas adsorbing CO_2 into the particle through chemical reaction. The CO_2 laden particles flow up the riser, turn and flow into the cyclone. In a reacting C2U experiment, CO_2-free gas is separated from particles in the cyclone and exit the system, and the CO_2 laden particles pass through a loop-seal and into the regenerator where CO_2 is released from the sorbent-particles by heating the spent sorbent in a regeneration gas stream (i.e., mainly N_2 or steam). The CO_2 gas exits the C2U system and the regenerated sorbent particles continue through the loop to the next loop-seal. The fresh sorbent particles pass through the loop-seal to the absorber and the process continues. To maintain gas-particle flow in a CO_2 capture loop, gases are injected throughout the system to keep particles fluidized. The main gas inlet is the absorber inlet. Other gases are injected into the system to keep particles fluidized and flowing. In an active CO_2 transport loop, fluidizing gases, injected downstream of the cyclone will be the regeneration gases such as steam. In the non-reacting cold-flow experiment the solid particles are spherical with mean diameter of 185 µm and density of 2480 kg/m^3. The system is operated at room temperature and atmospheric pressure and only air is used as the fluidization media. Table 29 provides the flow rates of gases and injection points throughout the system.

Table 29. Inlet flow rates (positions shown in Figure 107).

Flow Location	Nominal Design Flow Rate (kg/s)
Adsorber	5.0e-03
Loop Seal 1	7.0e-04
Regenerator	1.0e-03
Loop Seal 2	8.0e-4

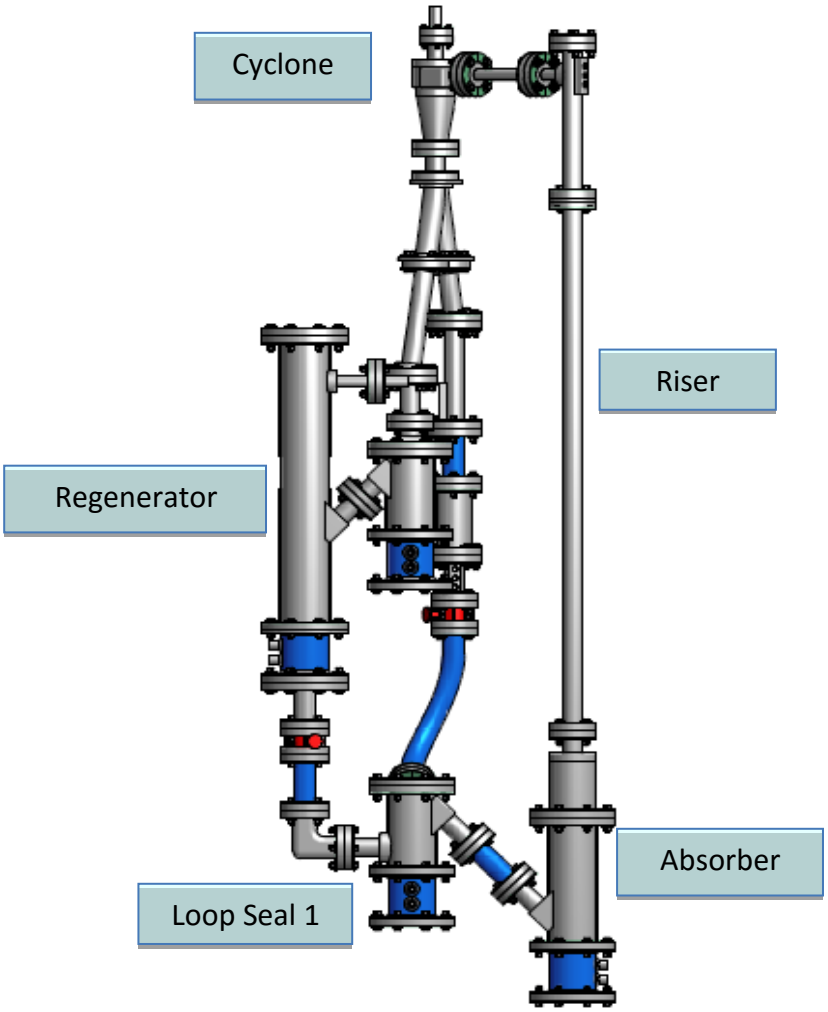

Figure 107. NETL C2U experimental setup

Based on the geometry provided by NETL, we built our 3D CFD mesh and model using Ansys FLUENT CFD code by utilizing our Eulerian-Eulerian CFD model in combination with the kinetic theory of granular flow (Abbasi and Arastoopour[59]), and assuming constant and uniform particle size and density. The 3D mesh consists of 450,000 computational cells.

Our initial focus was directed toward the absorber and riser part of the circulating fluidized bed. For our simulations, the initial solid height in the absorber was set to 30 cm and at minimum fluidization state.

Fluidizing gas was injected from the bottom of the absorber with a mass flow rate of 0.005 kg/s while the solid mass flow rate was set to 0.048 kg/s being injected from the side. Outlet boundary condition was set to atmospheric pressure. The objective of this stage was; 1) to calculate the pressure drop across the absorber and, 2) capturing the chugging effect as observed during the experiments.

According to Clark et al.[58] Chugging occurs when a large mass of particles lifts from the fluidized bed and moves into the cone leading into the riser. The cone-constriction intermittently prevents particles from flowing smoothly into the riser and particles plug the riser pipe. As shown in Figure 108, chugging was observed during the experiment and the same behavior was captured by our CFD model as shown in Figure 109.

A comparison of the predicted pressure drop in the lower mixing zone of the riser with the experimental data is presented in Figure 110, indicating that the model prediction is in good agreement with the experimental data. The average calculated pressure drop from the simulation is 4.29 kPa averaged over 12 sec compare to 3.87 kPa average pressure drop measured in the experiment over 150 sec. One of the factors contributing to the observed discrepancy can be due to the difference in averaging time, while overestimation of drag force between gas and particulate phase (calculated by ordinary drag models) may also be another contributing factor. Ordinary models assume a homogenous dispersion of particle phase in the fluid, and as a consequence, the calculated drag force between phases is higher than the actual drag force, in which particles make clusters in the fluid phase.

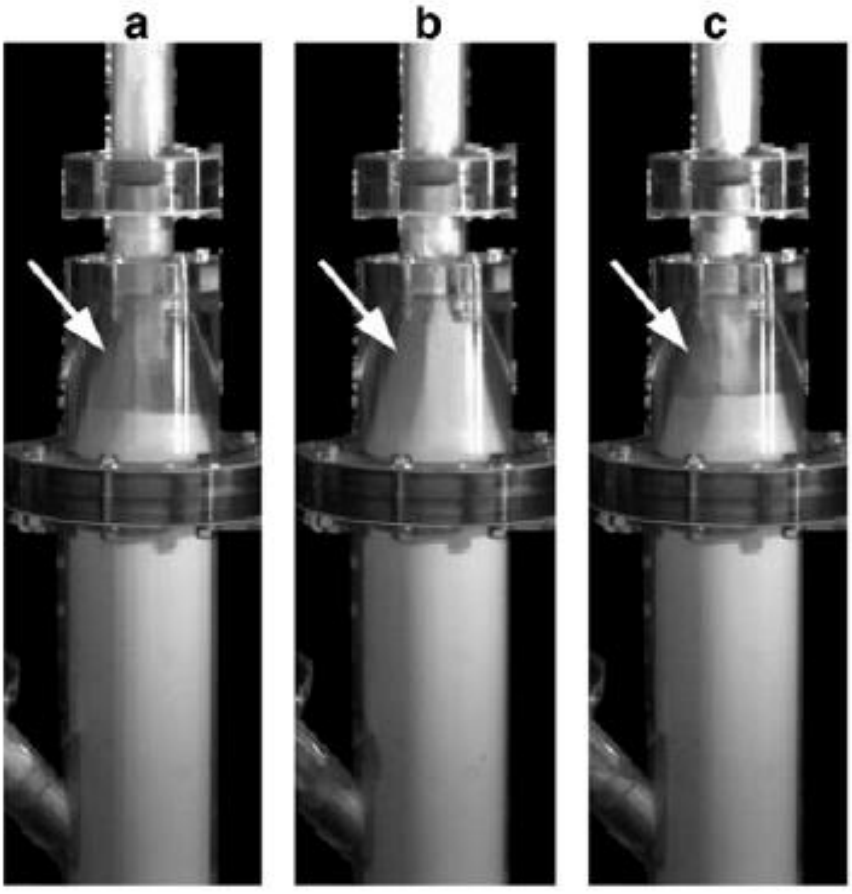

Figure 108. Chugging effect reported during NETL experiments

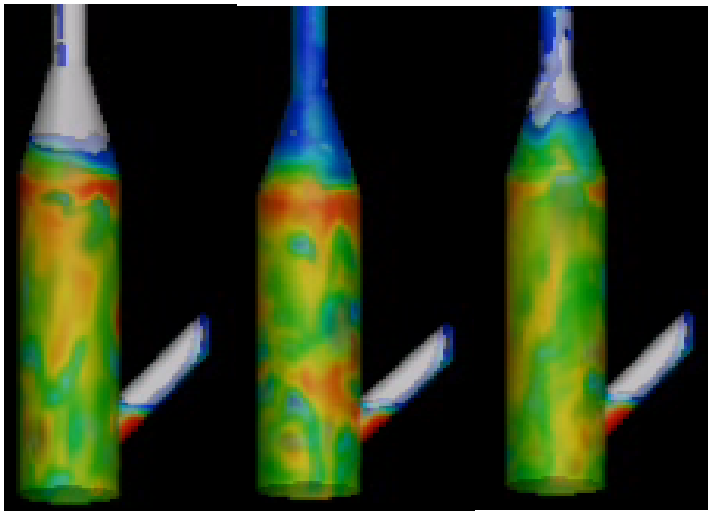

Figure 109. Chugging effect captured in simulations

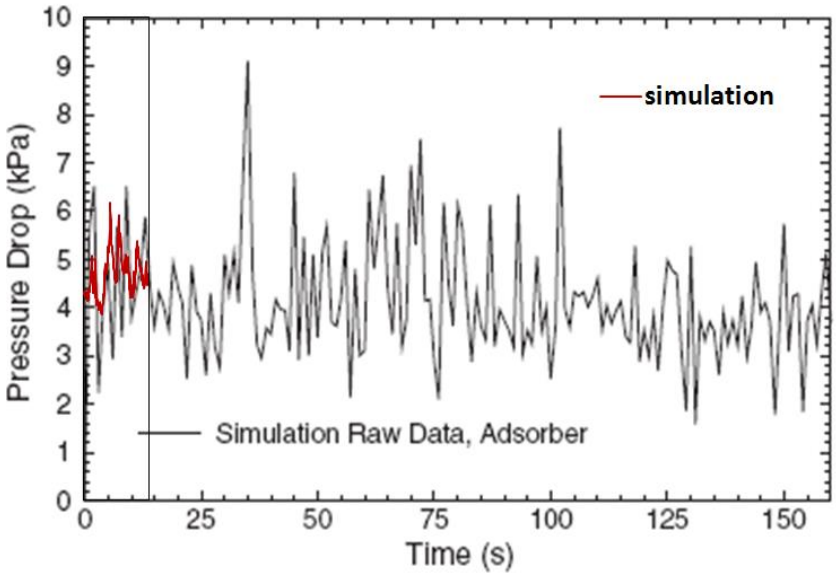

Figure 110. Experimental pressure drop data compare to the simulation results across the lower part of the absorber

To improve the model and achieve higher accuracy, a drag model based on Energy Minimization Multi-Scale (EMMS[60]) approach was used. The EMMS approach is based on the assumption of minimizing energy transfer between the clusters and dilute phase inside a gas-solid environment, while traditional drag models (e.g. Syamlal O'brien[61]) assume a homogenous distribution of solid particles in the gas medium and therefore, neglect all heterogeneities inside the flow.

Figure 111 shows the comparison between EMMS and Syamlal and O'brien[61] model for a bubbling fluidized bed. The results clearly indicate that EMMS provides an accurate prediction of both the instantaneous fluctuations and the average and pressure drop. While Symlal and O'brien[61]model does not

predict any major fluctuation, it can predict the average value with acceptable accuracy. Given the significantly shorter computational time required with the Syamlal and O'brien[61] model, all simulations should be performed with Syamlal and O'Brien[61] model, and EMMS should be used when a more accurate data on instantaneous behavior of flow is required.

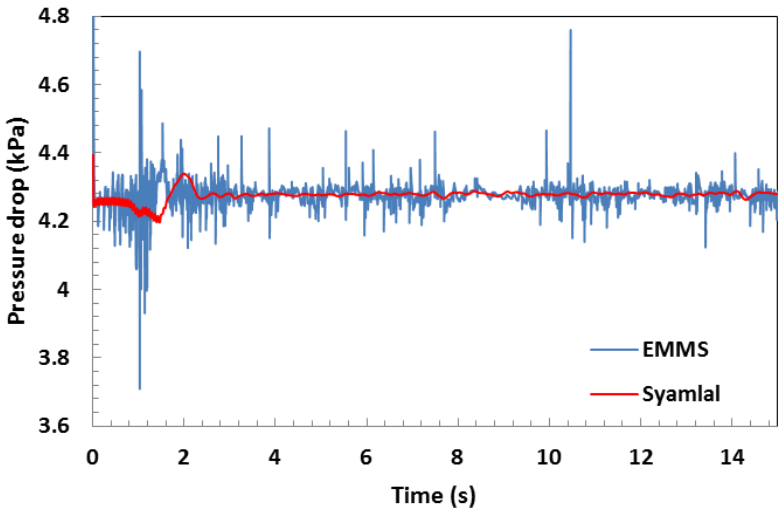

Figure 111. Comparison between EMMS and Syamlal drag models

Following the cold flow simulations of the riser section of the NETL C2U circulating fluidized bed using our 3D Eulerian-Eulerian CFD model (Abbasi and Arastoopour, 2011)[59], the model was used as a base-case for simulations of reactive flow at elevated pressure and temperatures. Given that the hydrodynamics of the system is different at elevated pressures and temperature (because of the effect of temperature and pressure on the viscosity and density of the fluidizing gas), a preliminary study was performed to determine the required gas inlet velocity at the target pressure and temperature (i.e., T=425 °C and P=20 atm). The goal was to find an operating condition that provides the same solid inventory in the riser. Table 30 shows the baseline operating condition for the reactive case.

Table 30. Baseline operating condition

Pressure, atm	20
Temperature, °C	425
Inlet gas velocity, m/s	0.15
Inlet solid rate, kg/s	0.044
Inlet CO_2 mole fraction, v/v%	50

The carbonation reaction between CO_2 and the MgO-based solid sorbent was added to the model using the variable diffusivity shrinking core model (Abbasi et al., 2013)[34]. The details of the model have been presented above. To investigate the effect of different operating conditions on the CO_2 capture performance a set of simulations were performed at different solid circulating rates and also different reaction rates. In all the cases, gas inlet velocity was kept constant. Figure 112 shows the effect of solid circulation rate and also the reaction rate on the CO_2 outlet to inlet mole fraction ratio. In this figure "R" and "S" refer to the baseline reaction rate and solid circulation rate, respectively. At baseline condition (R-S) the CO_2 removal is less than 15%. By increasing the reaction rate by a factor of 10 and keeping the same solid circulation rate (10R-S), CO_2 removal remains in the same level, indicating that in this case, the process is controlled by the amount of solid in the system. By increasing the solid circulation rate by factors of 5 and 10 at high reaction rate (10R-5S and 10R-10S), CO_2 removal increased to 70%, indicating

that the solid hold up in the riser reached to the level that it is no longer controlling the extent of the CO_2 removal. This can be attributed to the denser solid flow in the lower part of the riser and also denser solid flow in the transport zone. Figure 113 shows the contours of instantaneous solid volume fraction, CO_2 mole fraction and Reaction rate at t=20 sec. It clearly shows the dense region in the lower mixing zone of the riser where the reaction rate reaches to its highest values. Another simulation was performed with the original reaction rate and the highest solid circulation rate (R-10S). In this case, as shown in Figure 112, the maximum CO_2 removal was 25%.

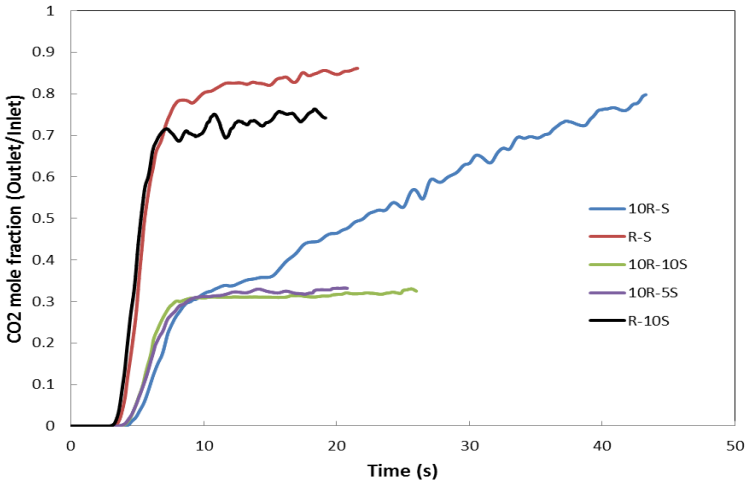

Figure 112. CO_2 outlet to inlet mole fraction ratio vs. time, at different conditions

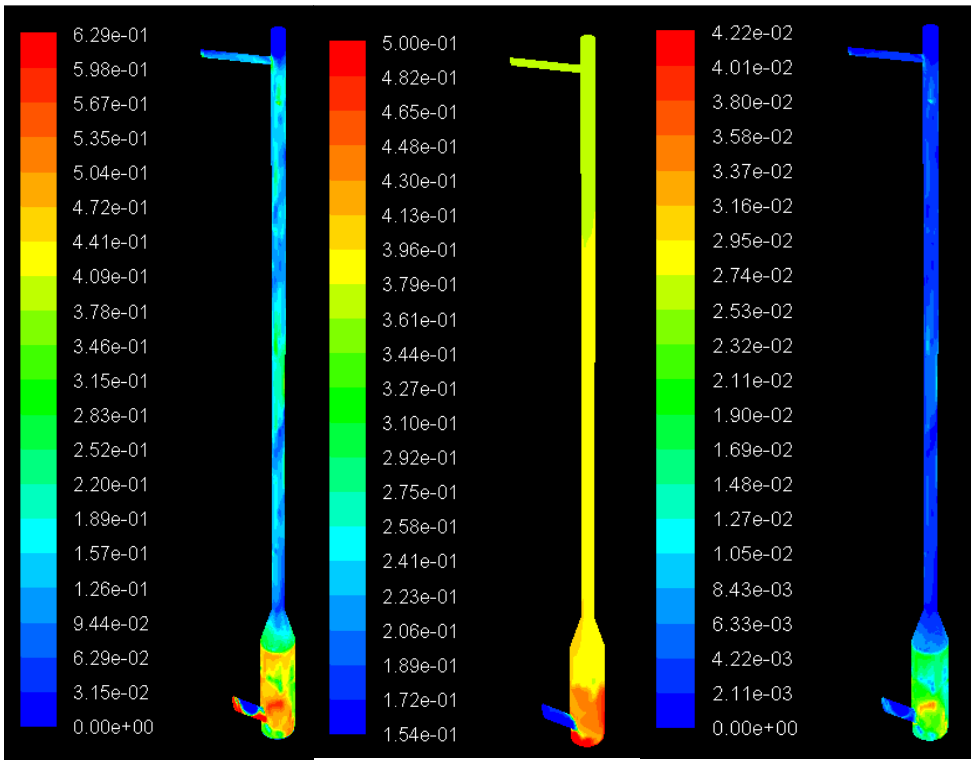

Solid volume fraction CO_2 mole fraction Reaction rate

Figure113. Contours of instantaneous solid volume fraction, CO_2 mole fraction, and reaction rate (t=20 sec)

To investigate the effect of operating conditions on the CO_2 capture performance, a set of simulations were performed at different solid circulating rates and gas residence time. Table 2 shows the inlet gas velocity and solid circulating rates for different cases. Figure 114 shows the effect of solid circulation rate on the CO_2 capture. At the NETL baseline condition, the extent of CO_2 capture is less than 15%. By increasing the solid circulation rate by factors of 5 and 10, the extent of CO_2 capture increased to 40%, indicating that the solid hold up in the riser has reached to the level that it is no longer controlling the extent of the CO_2 capture. This can be attributed to the denser solid flow in the lower part of the riser and also denser solid flow in the transport zone (as shown in Figure 115). Figure 116 shows the effect of gas inlet velocity on the extent of CO_2 capture, indicating that by decreasing gas inlet velocity by 35% (and therefore increasing gas residence time) up to 60 % CO_2 capture can be achieved.

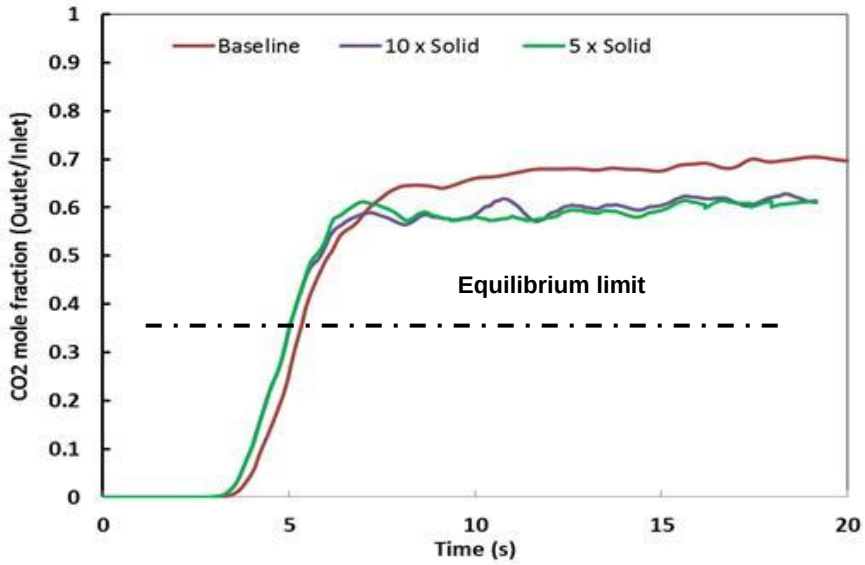

Figure 114. CO_2 outlet to inlet mole fraction ratio vs. time, at different solid circulation rate

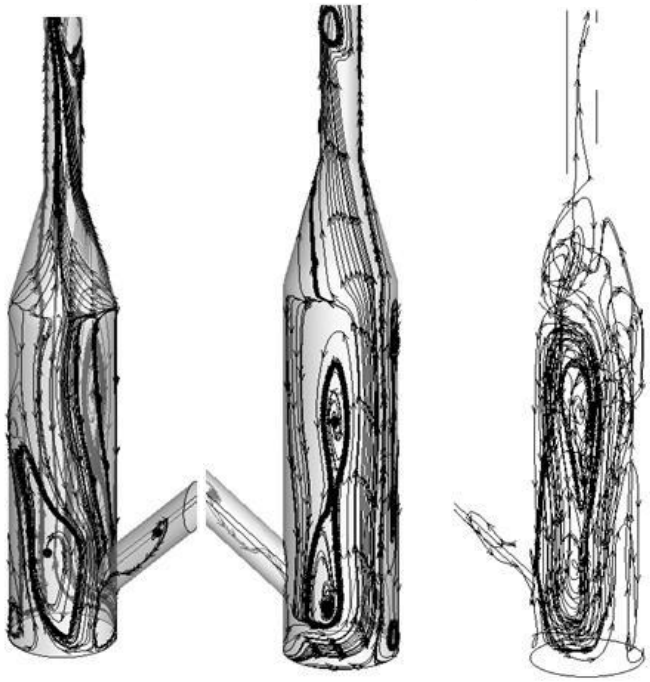

Figure 115. Denser solid flow in the absorber

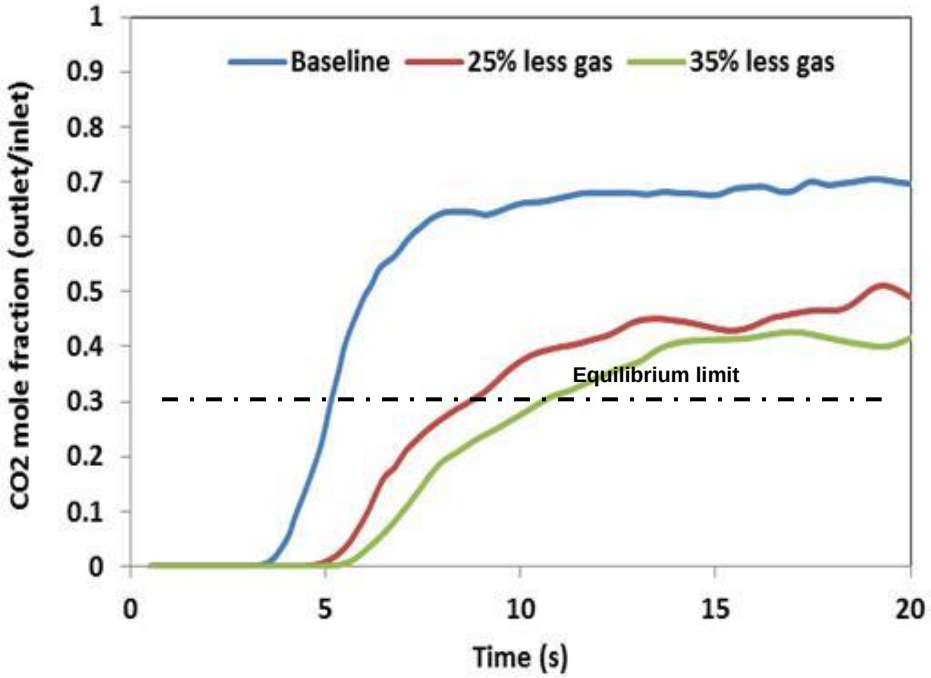

Figure 116. Effect of gas inlet velocity on CO_2 capture

Following the implementation of the carbonation reaction in the model, the water gas shift reaction was added to the reactive system to investigate the performance of the MgO-based solid sorbent in the sorbent enhanced water gas shift (SEWGS) reaction. Hassanzadeh[4] evaluated the same MgO-based dry sorbent in a SEWGS reaction in packed-bed reactor at 350 °C and showed that the sorbent is capable of capturing over 70% of the CO_2 and increase the hydrogen mole fraction from 37 *mol* % (dry basis) in the inlet to 55 *mol* % in the outlet. In this study the same assumptions were made and performance of the sorbent was evaluated for a SEWGS process. In this CFD/PBE simulation model, the inlet gas was a simulated syngas with a composition of 20% CO_2, 20% H_2O, 30% CO, and 30% H_2. Initially, the reactor contained only steam (H_2O). The operating condition corresponds to the "5x Solid" case except the temperature was at 350 °C.

Figure 117 shows the gas composition (wet basis) in the reactor outlet corresponding to about 60% CO_2 capture with and exit gas containing 65% H_2. Since the carbonation reaction is limited by equilibrium, and in this case due to the lower concentration of CO_2, the extent of CO_2 captured by the sorbent is lower than that in the cases with 50% inlet CO_2.

It is well understood that because of the effect of temperature and pressure on the viscosity and density of the fluidizing gas, the hydrodynamics of the system at elevated pressures and temperatures is different than that at ambient condition. One of the important parameters in bubbling fluidized beds is the gas inlet velocity, which should be sufficiently high to fluidize the bed with large number of bubbles to promote good mixing, and sufficiently low to lead to a manageable bed expansion to minimize elutriation and loss of particle from the bed. To stay within these two limits, a gas inlet velocity of 8.4 cm/s (about 3 times the minimum fluidization velocity) was used for simulation of a batch fluidized bed reactor for sorbent regeneration using the shrinking core model. The operating condition of the bed used in the simulation is presented in Table 31. The initial condition of sorbent inside the regenerator is identical to the sorbent

flowing out of the riser part, which are presented in Table 32. The regeneration reaction was added to the model using the shrinking core model, which has been described in detail above.

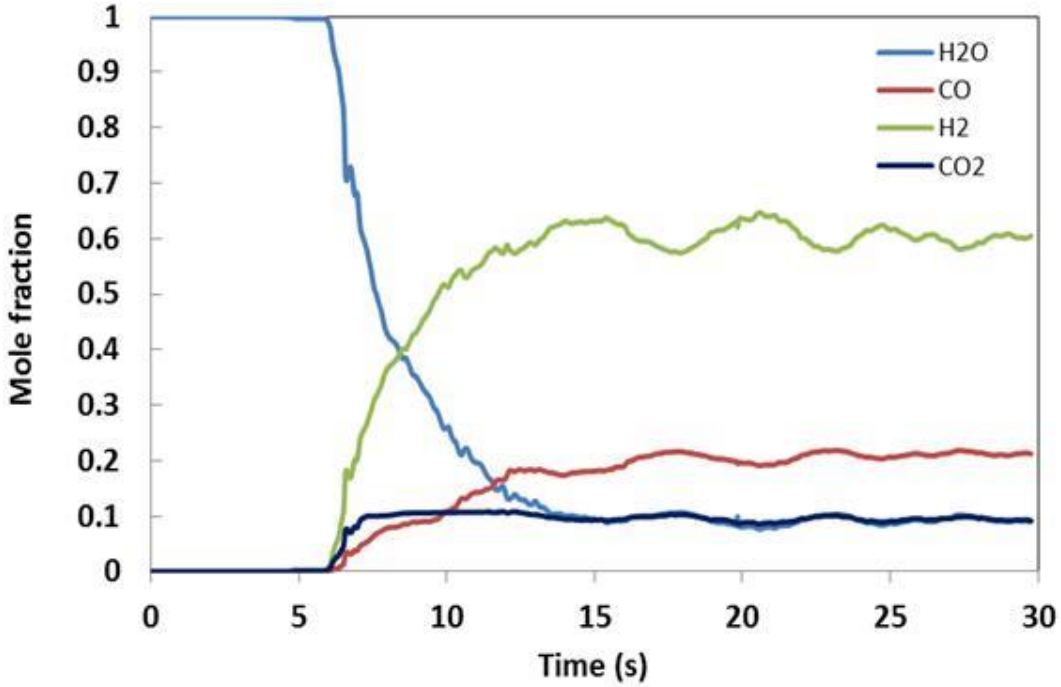

Figure 117. SEWGS gas outlet concentration at 350 ˚C

Table 31. Operating condition

Pressure, atm	20
Temperature, °C	550
Inlet gas velocity, m/s	0.084
Inlet solid rate, kg/s	0
Inlet CO_2 mole fraction	10
Inlet N_2 mole fraction	90

Table 32. Initial condition of particles

Temperature, °C	550
$MgCO_3$ mass fraction	0.248
MgO mass fraction	0.111
Inert mass fraction	0.641
Initial voidage	50%
Initial bed height, m	0.35

Figure 118 shows a schematic diagram of the bed. The impact of the drag law used in this simulation on the bed expansion is presented in Figure 119 (at 10s), which closely matched the experimentally observed

results. Figure 120 shows the heterogeneous behavior of the bed in terms of the velocity vector (presented by length) and solids solid volume fraction (presented by color) at different locations of the bed.

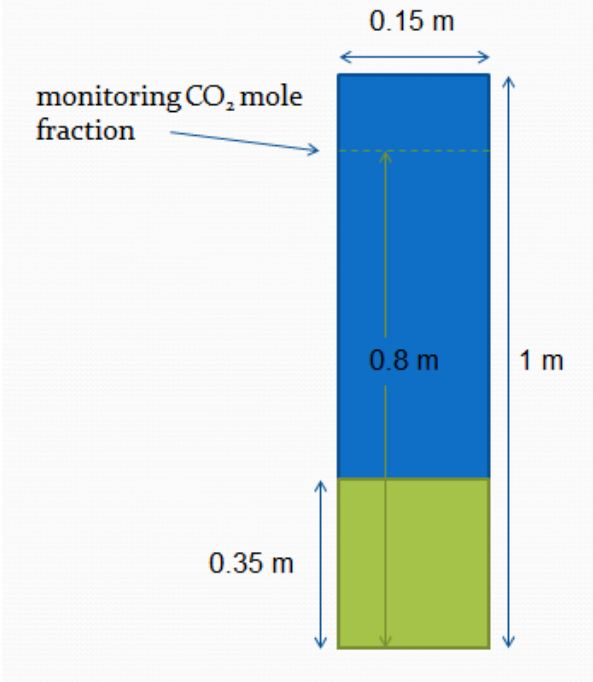

Figure 118. Schematic of the bubbling fluidized bed

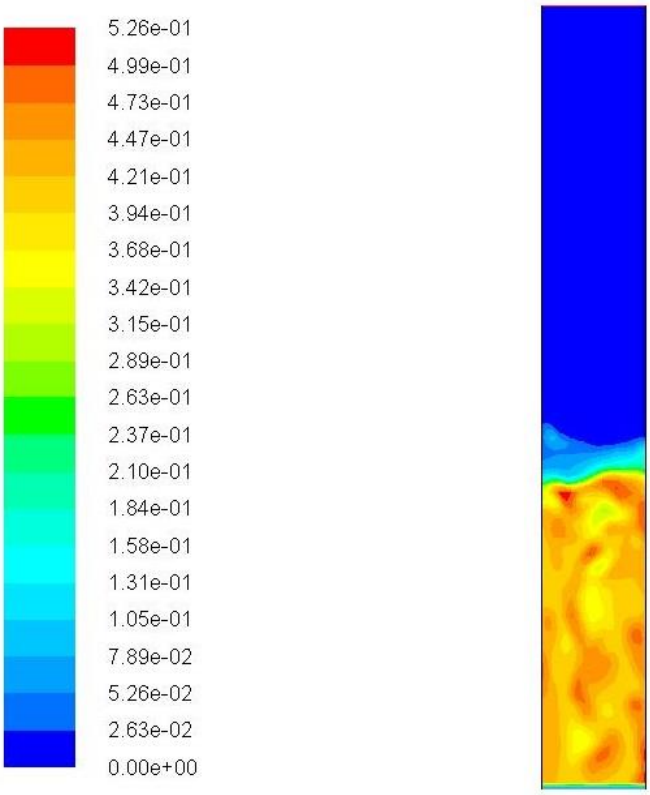

Figure 119. Solid volume fraction contours at 10s

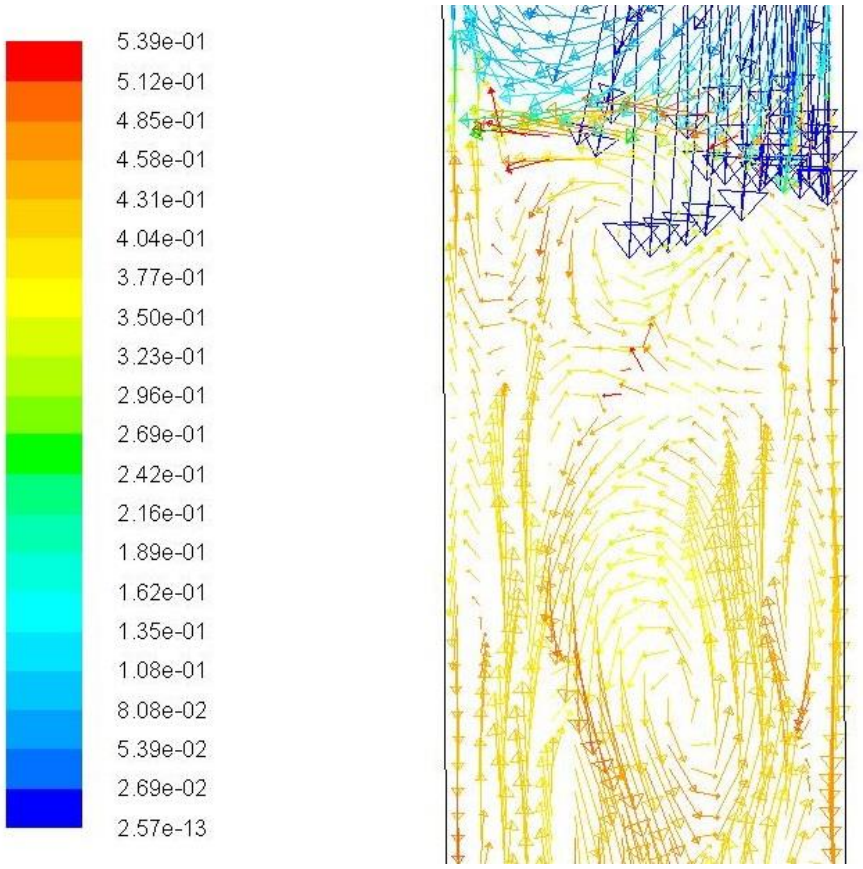

Figure 120. Solid velocity vector colored by solid volume fraction at 10s

The mole fraction of CO_2 leaving the reactor (monitored at a location 0.8 m from the bottom of the reactor) as a function of time is presented in Figure 121. The CO_2 breakthrough concentration consists of an initial period of about 3s, during which no CO_2 is observed at the monitoring location. This period corresponds to the time required for CO_2 leaving the top of the bed to reach the monitoring location. Following this period, there is a sharp rise in CO_2 mole fraction (up to about 0.32), as the CO_2 produced in the bed at different depths reach the monitoring point. The subsequent decrease in CO_2 mole fraction is due to the decrease in the rate of sorbent decomposition as reaction proceeds.

Figure 122 presents the CO_2 mole fraction and conversion vs. time for the same system, indicating that as the carbonated sorbent (i.e., $MgCO_3$) is fully regenerated (after about 300 seconds), the CO_2 concentration at the monitoring location also approached the inlet CO_2 concentration. Figure 123 is a profile of CO_2 mole fraction inside the system after 3 seconds. It clearly shows the hyperbolic profile of gas due to laminarity at these conditions.

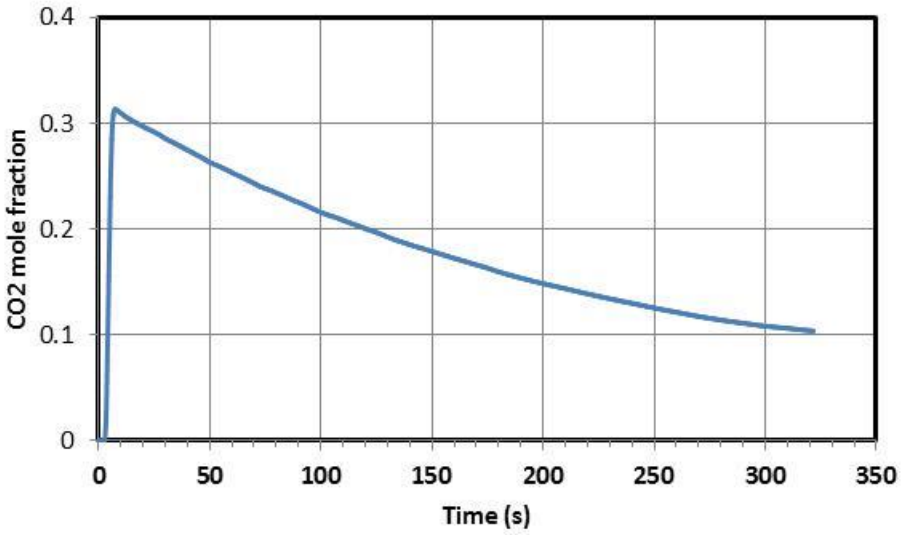

Figure 121. CO_2 mole fraction (30 seconds)

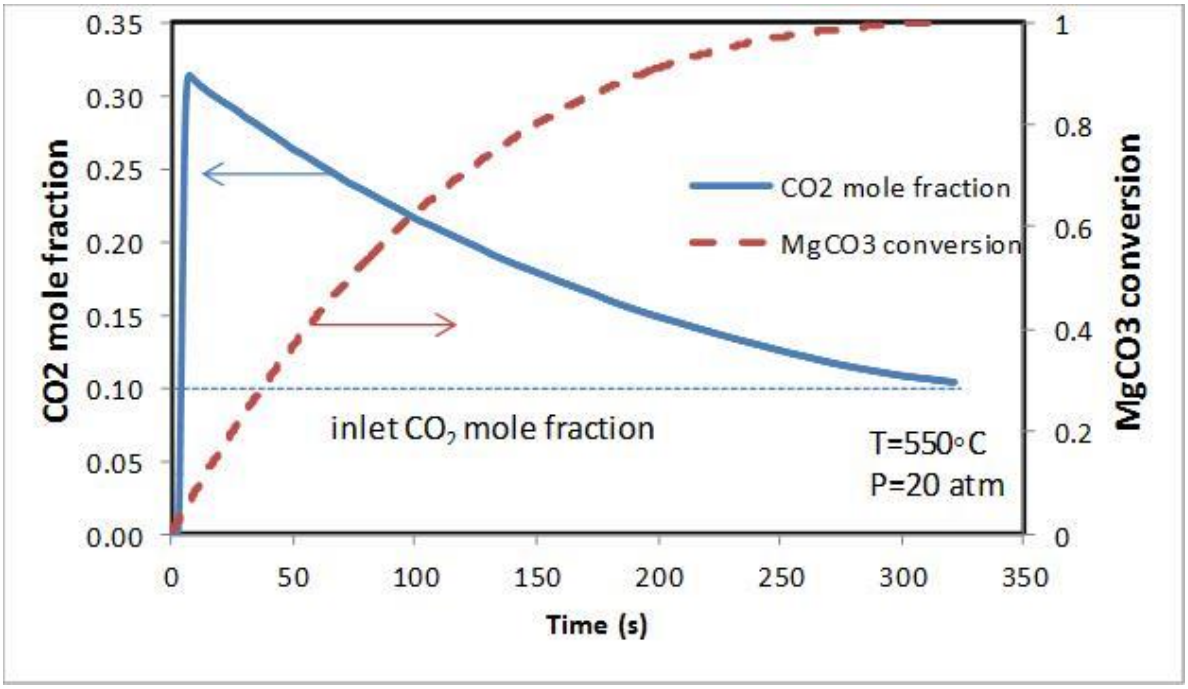

Figure 122. CO_2 mole fraction and sorbent regeneration

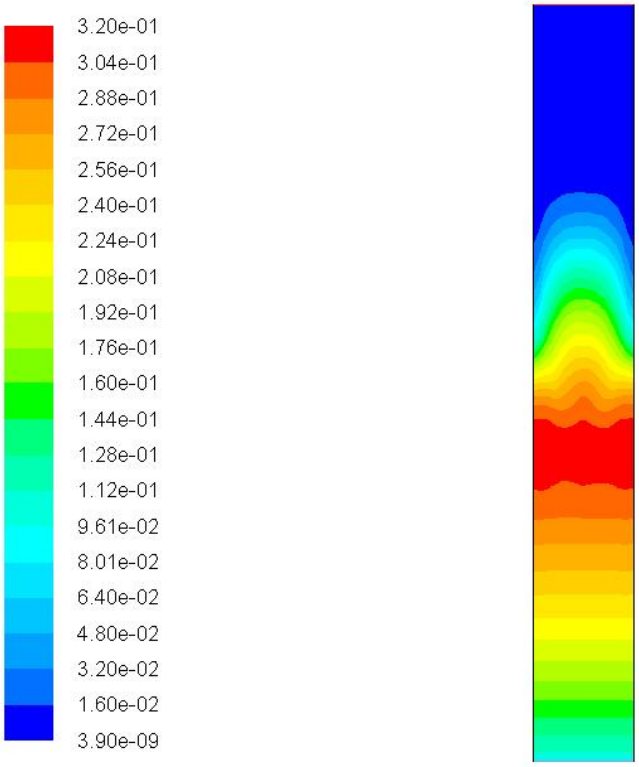

Figure 123. CO_2 mole fraction contours at 3s

Also, as discussed above, steam has a positive effect on both sorbent capacity and rate of regeneration of sorbent. Therefore, steam was used as regenerating continuum to perform CFD simulations. The regeneration reaction was added to the model using the shrinking core model. The details of the model can be found in the preceding part of the report. Two simulations have been performed: The first one regeneration of solids in a batch system and the second one regeneration of solid in continuous system where solids are continuously fed to the system. Table 33 shows the complete operating condition of the bed in the batch mode. The initial condition of sorbent particles inside the regenerator is identical to the fully carbonated particles, which are presented in Table 34.

Table 33. Operating condition for batch system

Pressure, atm	20
Temperature, °C	550
Inlet gas velocity, m/s	0.084
Inlet CO_2 mole fraction, %	0
Inlet H_2O mole fraction, %	100

Table 34. Initial condition of the sorbent in the regenerator

Temperature, °C	550
$MgCO_3$ mass fraction	0.248
MgO mass fraction	0.111
Inert mass fraction	0.641
Initial voidage, %	50
Initial bed height, m	0.35

Figure 118 shows a schematic of the bed indicating its dimension. Figure 124 shows the CO_2 mole fraction leaving the system as well as sorbent conversion as a function of time. Under the operating condition used, it will take about 2 seconds for CO_2 entering the bottom of the reactor to reach the monitoring point located 0.8 m above the bottom of the reactor. The CO_2 mole fraction reaches a value of around 18% and then gradually decreases because the reaction rate will decrease as reaction proceeds. After about 5 minutes the sorbent is fully regenerated and CO_2 mole fraction at the outlet drops to zero.

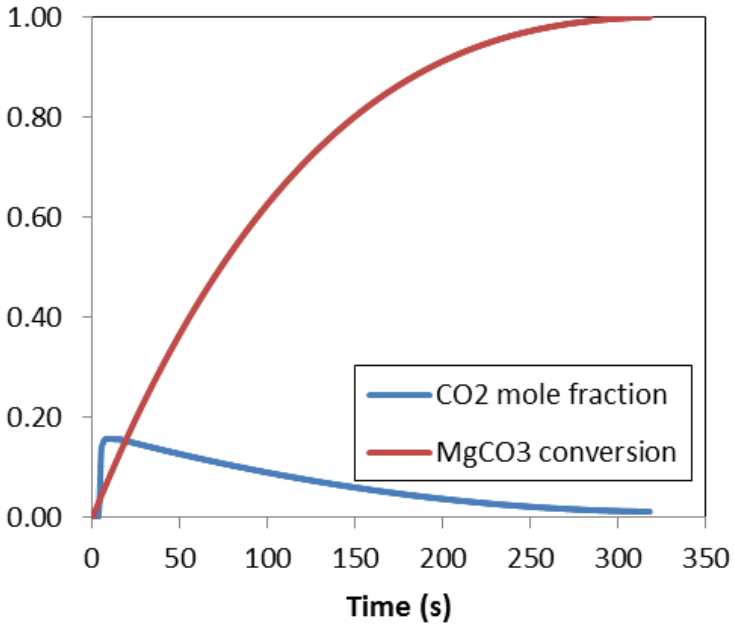

Figure 124. CO_2 mole fraction and sorbent conversion vs time in the batch reactor

The second simulation was carried out for a continuous regenerator reactor. Table 35 shows the operating conditions for continuous system. The initial condition of the bed and sorbent composition in the inlet is the same as batch simulation and is presented in Table 34.

Table 35. Operating condition for continuous system

Pressure, atm	20
Temperature, °C	550
Inlet gas velocity, m/s	0.084
Inlet solid velocity, m/s	0.05
Inlet CO_2 mole fraction, %	0
Inlet H_2O mole fraction, %	100

Figure 125 shows a schematic of the bed indicating its dimension (note that diameter and height of the bed is the same as batch reactor). It should be noted that the sorbent enters the regenerator reactor from the top and leaves from bottom, while gas enters from bottom and leaves from the top of the reactor. Figure 126 shows the CO_2 mole fraction leaving the reactor and sorbent conversion as a function of time. Under the operating condition used, it will take about 4 seconds for the regeneration gas (Steam) entering the bottom of the reactor to reach the monitoring point located 0.8 m above the bottom of the reactor. The CO_2 mole fraction reaches a relatively constant value of about 14% because carbonated solids continuously enters the reactor and reactor reaches a semi-steady state condition at about 20 s which is the

resident time of solids in the reactor. It should be noted that the fluctuation shown in Figure 126 is due to continuous violent nature of the fluidized bed reactor.

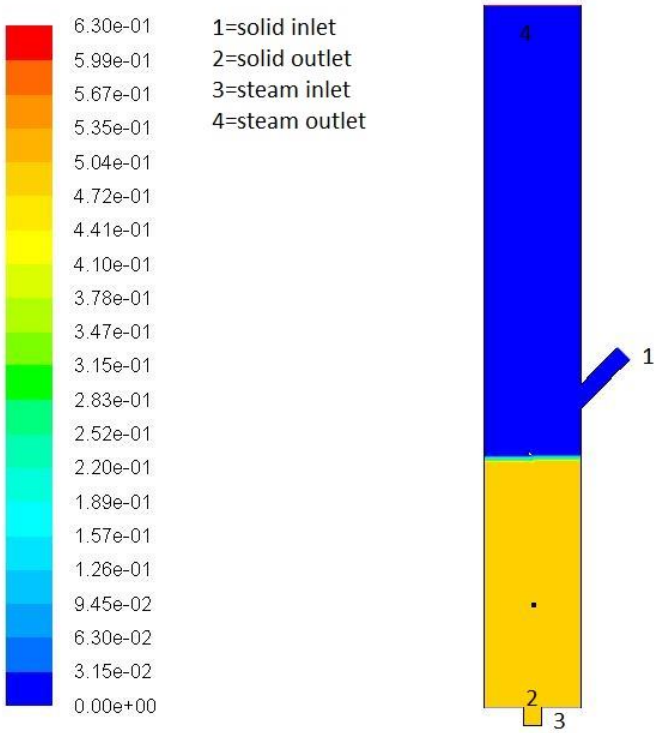

Figure 125. Schematic of continuous reactor

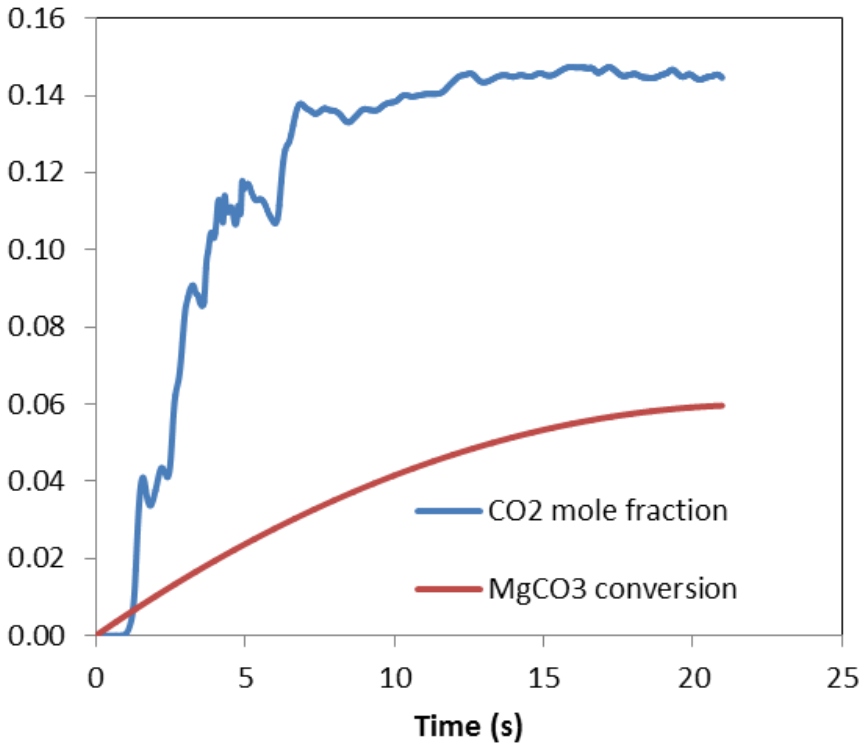

Figure 126. CO_2 mole fraction and sorbent conversion vs time in the continuous reactor

Figure 127 presents the contours of CO_2 mole fraction inside the system after 8 seconds. It shows how CO_2 is produced and carried by steam inside the reactor. Note that the CO_2 mole fraction near the solid inlet is more than CO_2 mole fraction near solid outlet as the rate of reaction is higher near the solid inlet.

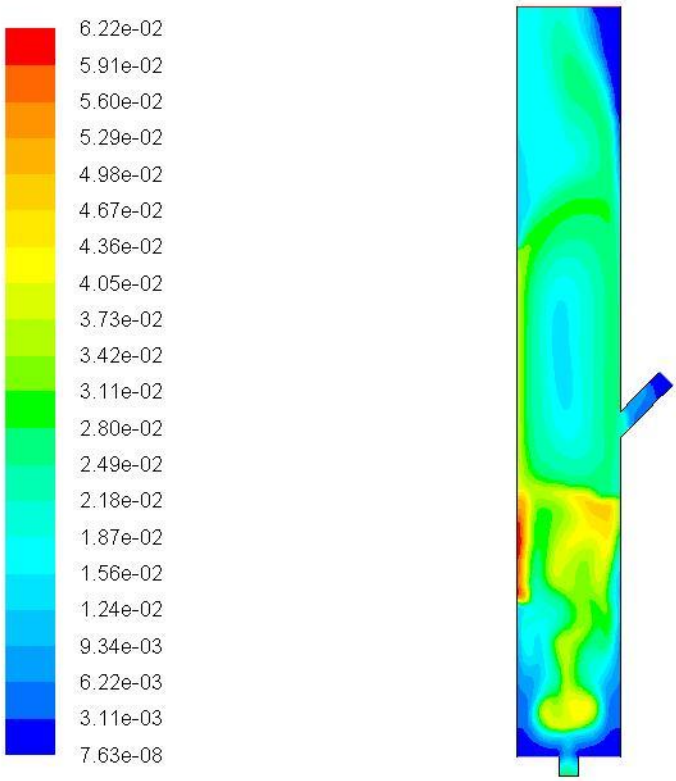

Figure 127. CO_2 mole fraction contour at 8 sec

Task 5. Development of preliminary base-case-design for scale up

The objective of this task is to determine the optimal sorbent size, absorber configuration (i.e., diameter and height), and recycle ratio, in the regenerative CO_2 capture process.

In this task, we developed a base case for a regenerative MgO-based pre-combustion carbon capture process that can be incorporated in a 500 MW Integrated Gasification Combined Cycle (IGCC) power plant. The coal used for this purpose is a typical Illinois #6 bituminous coal. The composition of the coal is presented in Table 36 along with the High Heating Value (HHV) of the coal, which was calculated reported using DuLong correlation.

The overall efficiency of the IGCC plant was assumed to be 40%. The oxygen-blown gasifier was assumed to operate at 1000°C and 50 atm. using a steam-to-carbon ratio of one. The Oxygen requirement and the syngas composition, after high temperature desulfurization (with regenerable mixed metal oxide sorbent) was determined by FlexFuel Gasifier Simulation Model (FFGSM)[62] developed by the co-principal investigator of this project at the process design and gas processing laboratory (PDGPL) at the Illinois Institute of Technology (IIT). The operating condition of the gasifier and the composition of the syngas (calculated by FFGSM) is presented in Table 36. The key properties of the regenerable MgO-based sorbent used in this process are presented in Table 37.

Table 36. Properties of Illinois #6 coal

Ultimate analyses	wt. % (moisture free)
C	70.2
H	4.8
N	0.9
S	3.1
O	9.9
A	11.1
Total	100
Moisture content, %	5
HHV, BTU/lb	12,545

Table 37. Operating condition of the gasifier and syngas composition

Temperature, °C	1000
Pressure, atm	50
Steam-to Carbon Ratio	1
Oxygen-to-Carbon Ratio	0.306
Coal Feed rate, lbm/hr	3.58 e5
Steam Feed rate, lbmol/hr	20.9 e3
Oxidant Feed rate, lbmol/hr	6.4 e3
Product gas, lbmol/hr	4.24 e4
CO content, mol%	25.09
H_2O content, mol%	26.55
CO_2 content, mol%	14.26
H_2 content, mol%	27.16
N_2 content, mol%	balance

Table 38. Key sorbent properties

Particle Diameter, μm	185
Density, kg/m^3	2500
Minimum fluidization velocity, m/s	0.03
Terminal velocity, m/s	1.42

In the regenerative MgO-Based process envisioned, the sorbent is used in a system of Circulating Fluidized Bed (CFB), consisting of a number of carbonators and regenerators, cyclones, L-valves, seal pots and downcomers. The rates of reaction for carbonation and regeneration are based on the reaction models developed in Task 3. The "cleaned" syngas enters the carbonator where the solid sorbent reacts with the gas and captures a significant fraction of the CO_2 in the syngas and the CO_2-lean stream leaves the reactor through a riser. The solid sorbents in the carbonator are carbonated and then accelerated and pneumatically transported through the riser and recycled in a cyclone. A fraction of the carbonated sorbent leaving the cyclone is fed to regenerator and the rest (bypass) is fed to the carbonator to capture

CO_2 in the following cycle. The ratio of flow rate of solids bypassing the regenerator to the flow rate of the sorbent going through regenerator is defined as bypass ratio and is one of the most important parameters of this process. Figure 128 shows the schematic of the system for a single carbonator and a single regenerator. A sorbent make up stream is introduced into the system to make up for deactivation of the sorbent as it goes through multiple cycles, and a deactivated sorbent flow is removed from the system to ensure the steady state operation of the system. Table 39 shows the operating condition of carbonators and risers used in the base case design calculations.

Table 39. Operating and design variables in carbonator and riser

Number of Carbonators and risers	10
Temperature, °C	380
Pressure, atm	50
Carbonator inlet gas velocity, m/s	0.04
Riser gas velocity, m/s	20
Solid circulating rate in each riser, kg/s	20
Bypass ratio	0.15
Desired CO_2 removal, %	90
Make-up flow rate, kg/s	5

The fraction of CO_2 removal determines the change in the sorbent conversion as it passes through the carbonator. The solid circulating rate can be changed over a wide range depending on the application and is determined separately with design of an appropriate L-valve. The temperature of carbonator is set to result in the optimum rate of reaction in carbonator. The flow rate of the sorbent make-up will specify the average number of cycles the solid sorbent will be going through before it leaves the system, which has a strong effect on the reaction rate, and therefore carbonator size. Obviously higher make-up flow rate will result in lower cycle number, higher rate of reaction, and the lower reactor size, but will increase the sorbent cost. The gas velocity in the carbonator should be higher than minimum fluidization velocity of sorbents to ensure a smooth flow of solid in the carbonator. The gas velocity in the riser is also selected to be higher than terminal velocity of the solids to effectively transport the solids up to the cyclone. The riser gas velocity has a direct impact on the solid hold up in the riser. A proper design will have solid hold up less than 5% in the riser. The height of the riser, on the other hand, should be long enough to be able to accelerate the solids to the specified velocity. Table 40 shows the sizing and design calculations of each carbonator and riser.

Table 40. Carbonator and riser sizing and design conditions

Carbonator diameter, m	4.3
Carbonator height, m	20.7
Riser diameter, m	0.19
Riser height, m	3
Riser solid hold up, %	0.05
Sorbent Cycle number	33
Sorbent inlet conversion	10
Sorbent outlet conversion	65
CO_2 inlet concentration, kmol/m^3	0.13
CO_2 outlet concentration, kmol/m^3	0.02

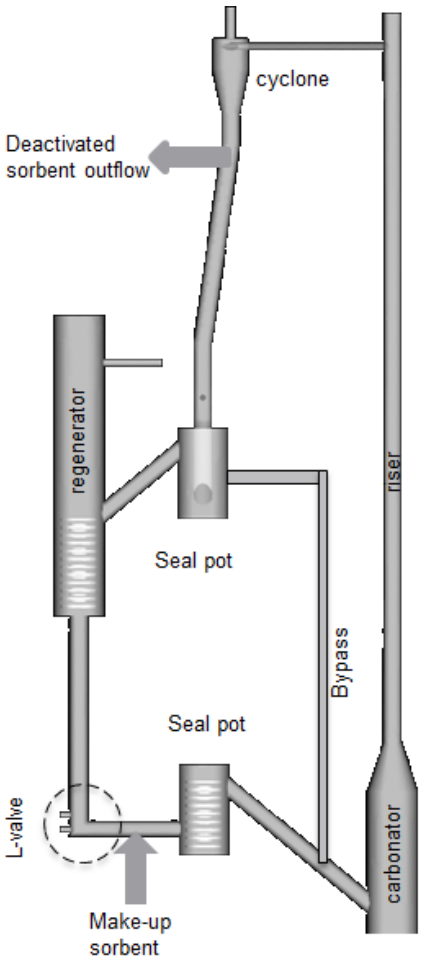

Figure 128. Schematic diagram of the process

Steam is used as regeneration medium, main because the presence of steam improves the rate of regeneration reaction (as discussed in Task 3), cost of the gas, and the ease of separation of CO_2 from steam (in a condenser). Also the steam temperature in the inlet of regenerator should be higher than regenerator temperature in order to compensate partially for energy needed to warmup the solids to regenerator temperature and provide the energy required for endothermic regeneration reaction. The operating conditions of the regenerator are presented in Table 41:

Table 41. Regenerator operating and design conditions

Number of Carbonator and risers	2
Temperature, °C	500
Pressure, atm	50
Regenerator inlet gas velocity, m/s	0.13
Each regenerator steam flow rate, kg/s	10.07
Solid circulating rate in each regenerator, kg/s	82.5
Extent of reaction, %	100
Solid loss percentage in the Cyclone, %	0

The flow rate of steam was calculated based on energy needs in the system and will be discussed below. Since the rate of regeneration is higher than rate of carbonation, the number of regenerators is considerably less than number of carbonators. The regeneration temperature was assumed to be 500 °C because of significantly lower rate of sorbent deterioration (compared to the sorbents regenerated at 550 °C) as discussed above. In the base-case-design, the rate of solid loss in the cyclone was assumed to be negligible. It should be noted that as long as the rate of solid loss is lower than the fresh sorbent make-up rate, any loss incurred in the cyclone can be offset by a reduction in the rate of spent sorbent removal from the system. The extent of sorbent regeneration is the major parameter in specifying the regenerator size. Table 42 shows the sizing and design calculations of each regenerator.

Table 42. Regenerator sizing and design conditions

Regenerator diameter, m	5
Regenerator height, m	15
Sorbent inlet conversion	65
Sorbent outlet conversion	0
CO_2 inlet concentration, kmol/m^3	0
CO_2 outlet concentration, kmol/m^3	0.12

To produce the steam required in the regenerator, water is used and heated through an extensive heat integration network inside the system as well as utilization of external fuel (e.g., natural gas). The heat integration network was developed in Aspen/HYSYS® and is shown in Figure 129. A make-up water stream is used and some water is also purged to prevent CO_2 accumulation inside the system. Table 43 shows the important parameters of the heat integration network. The liquid CO_2 produced is at 50 atm pressure and can easily be pumped and sequestered or stored.

Table 43. Heat integration parameters

Fuel energy, kJ/s	7.68e4
Steam temperature in the inlet of Regenerator, °C	592
Regenerator out flow temperature, °C	500
Make-up water flow rate, kg/s	0.3
Make-up water temperature, °C	30
Purge flow rate, kg/s	0.1
Purge temperature, °C	95
Liquid CO_2 flow rate, kg/s	19.6
Liquid CO_2 temperature, °C	15

In the preliminary economic analyses performed in this task, the cost associated with the process consisted of operating costs and capital investment costs. The major components of the operating costs included sorbent cost, labor cost, and fuel cost, while the major components of the capital costs included those associated with the carbonators and regenerators and heat integration network. Table 44 shows cost analysis for three different scenarios. The cost of carbon capture (liquid CO_2 at 50 atm) was determined under three scenarios presented in Table 44 and the calculated costs of the major cost components of the process are presented in Table 45.

Table 44. Cost Basis

	Scenarios		
Cost Basis	Optimistic	Average	Pessimistic
Sorbent cost, $ /ton	60	80	100
Spent Sorbent disposal cost, $/ton	-15*	10	25
Cost of electricity, $/kW	0.1	0.1	0.1
Cost of natural gas$/MMBTU	5	5	5
Useful plant life, years	50	50	50

* Salable byproduct

Table 45. Major cost component of the process

	Scenarios		
Costs	Optimistic	Average	Pessimistic
Sorbent cost, $million/yr	6.42	12.8	17.8
Labor cost, $million/yr	4	4	4
Fuel cost, $million/yr	10.4	10.4	10.4
Operating life of the system, yrs.	50	50	50
Total Bare-module cost of the equipment, $million	68.1	68.1	68.1
Total capitalized cost, $million/yr	5.91	5.91	5.91
CO_2 capture cost, $/ton CO_2	**31**	**38**	**44**
Increase in the cost of electricity, %	**9.65**	**11.97**	**13.77**

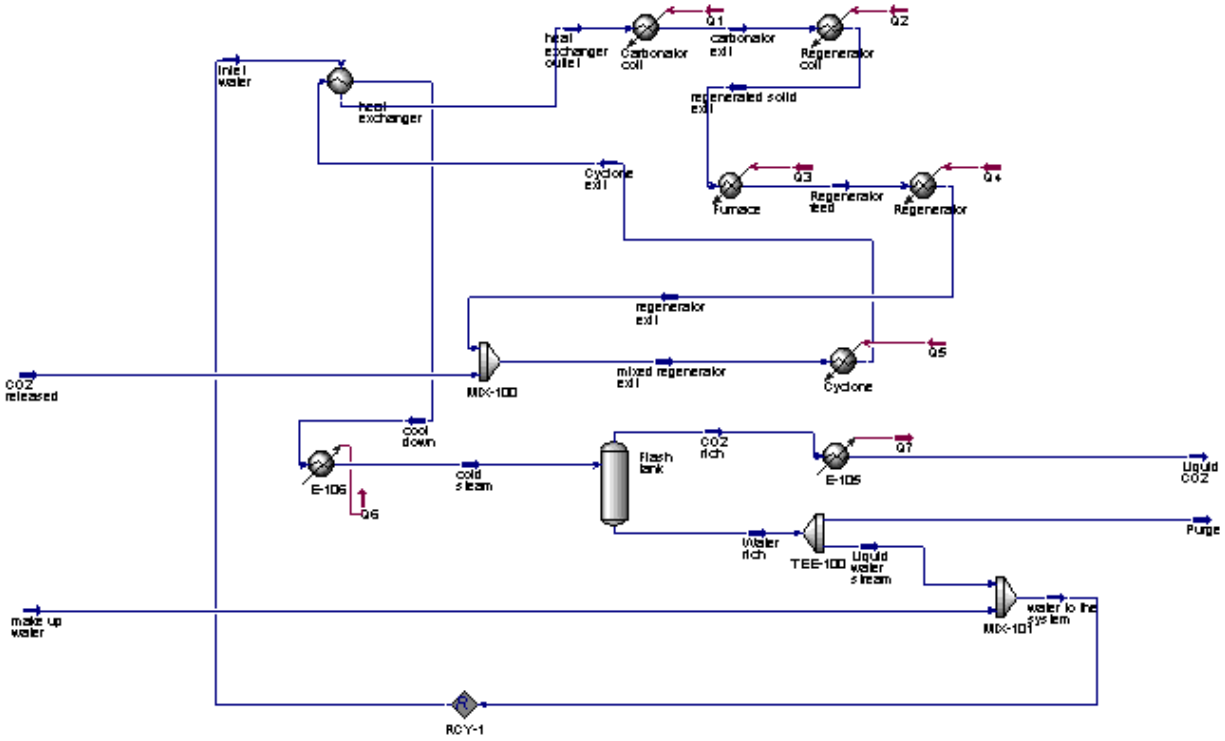

Figure 129. Heat integration scheme in the process

CONCLUSIONS AND RECOMMENDATIONS

A highly reactive and mechanically strong MgO based sorbent was developed in this project that is capable of removing CO_2 from pre-combustion coal gas in IGCC process. Among various preparation parameters, the potassium to magnesium ratio (K/Mg) appears to be the most important parameter affecting the CO_2 capacity of the sorbent. The optimum K/Mg ratio is about 0.15. Furthermore, the optimum range of temperature for drying during sorbent preparation appears to be in the range of 70°-100°C, while the optimum re-calcination temperature is around 500°C.

The rate of carbonation of the sorbent improves with increasing temperature in the range of 340° to 450°C, above which, thermodynamic equilibrium limitation results in lower reaction rate at higher temperatures. The order of the carbonation reaction with respect to CO_2 concentration was determined to be one with an activation energy of 134 kJ/mol. The results of carbonation tests also indicate that the presence of steam significantly enhances the sorbent reactivity and capacity and that the highest impact of steam occurs 360°C, which also favors production of hydrogen through the WGS reaction. Steam also has a beneficial effect on the rate of regeneration reaction and the optimum regeneration temperature is around 550°C.

The variable diffusivity shrinking core model (VDM) developed in this project, was shown to accurately fit the experimental data. An important advantage of this model is that the changes in the sorbent conversion with time can be expressed in an explicit manner, which will significantly reduce the CFD computation time.

A computational fluid dynamic/population balance equations (CFD/PBE) model was developed in this project. The PBE model was implemented in a commercial CFD code (i.e., Ansys Fluent 13.0) and the code was verified against analytical solutions reported in the literature for simple cases. The code was also validated against experimental data for CO_2 capture obtained in a packed-bed reactor. Furthermore, the CFD/PBE model was shown to predict hydrodynamics of the cold flow gas/solid system in the NETL Carbon Capture Unit (C2U). The pressure drop predicted by the model was shown to be in good agreement with the experimental data, and the model is able to predict the chugging behavior, which was experimentally observed in the C2U.

The model predictions for the extent of CO_2 capture at elevated pressure and temperatures indicate that by controlling the solid circulation rate, up to 70% CO_2 removal can be achieved, and that solid hold up in the riser is one of the main factors controlling the extent of CO_2 removal. The CFD/PBE simulation model indicates that by using a simulated syngas with a composition of 20% CO_2, 20% H_2O, 30% CO, and 30% H_2, the composition (wet basis) in the reactor outlet corresponded to about 60% CO_2 capture with an exit gas containing 65% H_2.

The results of a preliminary base-case-design analyses developed for a regenerative MgO-based pre-combustion carbon capture process for a 500 MW IGCC power plant indicate that liquid CO_2 can be produced at 50 atm can easily be pumped and sequestered or stored. The results of the preliminary economic analyses indicate that the estimated cost of carbon capture is in the range of $31-$44/ton, suggesting that a regenerative MgO-Based process can be a viable option for pre-combustion carbon dioxide capture in advanced gasification based power systems.

REFERENCES

1. US Department of Energy, Carbon Sequestration Technology Roadmap and Program Plan, 2007.
2. US Department of Energy, Financial Assistance Funding Opportunity Announcement for "Support of Advanced Coal Research at U.S. Colleges and Universities", FOA Number: DE-FOA-0000146, 2009.
3. Hassanzadeh A., Abbasian J., A Regenerative Process for Pre-Combustion CO2 Capture and Hydrogen Production in IGCC, Proceedings of the 26th annual International Pittsburgh Coal Conference, 2009.
4. Hassanzadeh A., A regenerative process for carbon dioxide removal and hydrogen production in IGCC [dissertation], Chicago (IL): Illinois Institute of Technology, 2007.
5. Hassanzadeh A., Abbasian J. Regenerable MgO based sorbents for high-temperature CO2 removal from syngas: 1. Sorbent development, evaluation, and reaction modeling. Fuels 2010; 89 (6): 1287-1297.
6. Benyahia S., Syamlal M., O'Brien T.J., Summary of MFIX equations 2005-4, from URL http://www.mfix.org/documentation/MfixEquations2005-4-3.pdf. July 2007.
7. Benyahia, S., Arastoopour, H., Knowlton, T.M., Massah, H., "Simulation of particle and gas flow behavior in the riser section of a circulating fluidized bed using the kinetic theory approach for the particulate phase", Powder Technology, 112, 24-33, 2000.
8. Arastoopour H. Numerical simulation and experimental analysis of gas/solid flow, Powder Technology, 119, 59-67 (2001).
9. Strumendo M., Arastoopour H., Solution of PBE by MOM in Finite Size Domains, Chemical Engineering Science, 63, 2624-2640 (2008).
10. Strumendo M., Arastoopour H., "Solution of population balance equations by the FCMOM for in-homogeneous systems", Industrial and Engineering Chemistry Research, 49, 11, 2010.
11. Arastoopour, H., "Numerical simulation and experimental analysis of gas/solid flow systems: 1999 Flour-Daniel Plenary Lecture" Powder Technology, 119, 59-67, 2001
12. Garg, R., Shahnam, M. and Huckaby, E. D., "Continuum simulations of CO2 capture by dry regenerable Potassium based sorbents", 7th International Conference on Multiphase Flow, ICMF 2010, Tampa, FL, May 30 – June 4, 2010
13. Li et al (11)
14. Gidaspow D., Multiphase Flow and Fluidization, Academic Press, San Diego, 1994.
15. Nikolopoulos, A., Atsonios, K., Nikolopoulos, N., Grammelis, P., Kakaras, E., "An advanced EMMS scheme for the prediction of drag coefficient under a 1.2MWth CFBC isothermal flow—Part II: Numerical implementation", Chem. Eng. Science 65, 4089–4099, 2010
16. Beruto, D. T., Vecchiattini, R and Giordani, M. Solid products and rate-limiting step in the thermal half decomposition of natural dolomite in a CO2 (g) atmosphere, Thermochimica Acta 405, 183-194, 2003.
17. Galai H., Pijolat M., Nahdi K., and Trabelsi-Ayadi M., Mechanism of growth of MgO and CaCO3 during a dolomite partial decomposition, Solid State Ionics 178, 1039-1047 (2007).
18. Hashimoto H., Komaki E., Hayashi F., and Uematsu T., "Partial decomposition of dolomites in CO2", Journal of Solid State Chemistry 33, 181-188, 1980.

19. Yi, C., K., Jo, S., J., Seo, Y., Lee, J., B., Ryu, C. K., “Continuous operation of the potassium-based dry sorbent CO2 capture process with two fluidized-bed reactors”, International journal of greenhouse gas control, 1, 31-36, 2007

20. Randolph, A. D., and M. A. Larson, “Theory of Particulate Process”, 2nd ed., Academic Press, New York, 1988.

21. Hulburt, H. M.; Katz, S., “Some Problems in Particle Technology”, Chemical Engineering Science, 19, 555, 1964.

22. Marchisio, D. L.; Pikturna, J. T.; Fox, R. O.; Vigil, R. D., “Quadrature Method of Moments for Population-Balance Equations”, AIChE Journal., 49, 1266, 2003a.

23. Marchisio, D. L.; Vigil, R. D.; Fox, R. O., “Quadrature Method of Moments for Aggregation-Breakage Processes”, Journal of Colloid and Interface Science, 258, 322, . 2003b.

24. Ramkrishna, D., “Population Balances: Theory and Applications to Particulate Systems in Engineering”, Academic Press, London, 2000.

25. Vanni, M., ‘‘Approximate Population Balance Equations for Aggregation- Breakage Processes’’, Journal of Colloid and Interface Science, 221, 143, 2000.

26. McGraw, R., “Description of Aerosol Dynamics by the Quadrature Method of Moments”, Aerosol Science and. Technology, 27, 255, 1997.

27. Barrett, J.C., Webb, N.A., “A comparison of some approximate methods for solving the aerosol general dynamic equation”, Journal of Aerosol Science, 29, 31–39, 1998.

28. Diemer, R.B., Olson, J.H., “A moment methodology for coagulation and breakage problems: part 1—analytical solution of the steady state population balance”, Chemical Engineering Science, 57, 2193–2209, 2002a.

29. Diemer, R.B., Olson, J.H., “A moment methodology for coagulation and breakage problems: part 2—moments models and distribution reconstruction”, Chemical Engineering Science, 57, 2211–2228, 2002b.

30. Marchisio, D. L.; Fox, R. O., “Solution of Population Balance Equations Using the Direct Quadrature Method of Moments”, Journal of Aerosol Science, 36, 43, 2005.

31. Strumendo, M.; Arastoopour, H., “Solution of Bivariate Population Balance Equations Using the Finite Size Domain Complete Set of Trial Functions Method of Moments (FCMOM)”, Industrial and Engineering Chemistry Research, 48, 262, 2009.

32. Yagi, S. and Kunii, D. 5th Int. Symposium on Combustion (Reinhold, New York, 1955), p. 231

33. Levenspiel, O. 1999, Chemical Reaction Engineering, 3rd Ed., John Wiley & Sons, New York

34. Abbasi, E., Hassanzadeh, A., Abbasian, J., “Regenerable MgO-based sorbent for high temperature CO2 removal from syngas: 2. Two-zone variable diffusivity shrinking core model with expanding product layer”, Fuel, 105, pp. 128-134, (2013)

35. Haul, R., Stein L. H., Diffusion in calcite crystals on the basis of isotopic exchange with carbon dioxide. Trans. of the Faraday Soc., 1955; 51:1280–1290.

36. Anderson, T. F., Self-Diffusion of Carbon and Oxygen in Calcite by Isotope Exchange with Carbon Dioxide. J. Geophys. Res., 74(15), pp. 3918 – 3932, 1969.

37. Szekely, J. and Evans, J. W., Studies in Gas–Solid Rreactions: Part I. A Structural Model for the Reaction of Porous Oxides with a Reducing Gas. Met. Trans. ,2 (1971), p. 1691.

38. Krishnan, S.V. and Sotirchos, S.V., A Variable Diffusivity Shrinking-Ccore Model and its Application to the Direct Sulfation of Limestone. Can. J. Chem Eng., 71 (1993), pp. 734–745.

39. Stendardo, S. and Foscolo, P. U., Carbon dioxide capture with dolomite: A model for gas–solid reaction within the grains of a particulate sorbent. Chem. Eng. Sci., 64 (2009), pp. 2343–2352

40. Marquaradt, D. W., Nonlinear Chemical Engineering Model. Chem Eng Prog 1959;55.6:65.

41. Kuester, J. L. and Mize, J. H., Optimization Techniques with FORTRAN, McGraw-Hill, New York (1973).

42. Borgwardt R H. Calcium Oxide Sintering in Atmospheres Containing Water and Carbon Dioxide, Ind Eng Chem Res 1989; 28: 493-500.

43. Adanaz J, Garcia-Lbiano F, Abad A, de Diego LF, Gayan P. Regeneration of sulfided dolomite with steam and carbon dioxide. Energy Fuels 2001; 15:85–94.

44. Ranade PV, Harrison DP. The Variable Property Grain Model Applied to the Zinc Oxide-Hydrogen Sulfide Reaction, Chem Eng Sci 1981; 36: 1079-1089.

45. Mess D, Sarofim AF, Longwell JP. Product Layer Diffusion During the Reaction of Calcium Oxide with Carbon Dioxide. Energy, Fuels 1999; 13 (5): 999-1005.

46. Dobner S, Sterns L, Gralf RA, Squires AM. Cyclic Calcination and Recarbonation of Calcined Dolomite. Ind Eng Chem 1977; 16.4: 479-486.

47. Hughes RW, Lu D, Anthony EJ, Wu Y. Improved Long-Term Conversion of Limestone-Drived Sorbents for In Situ Capture of CO2 in a Fluidized Bed Combustor, Ind Eng Chem Res 2004; 43: 5529-5539.

48. Laursen K, Duo W, Grace JR., Lim CJ. Cyclic Steam Reactivation of Spent Limestone, Ind Eng Chem Res 2004; 43: 5715-5720.

49. Cater, E.D., and P.R. Buseck. "Mechanism of Decomposition of Dolomite in the Electron Microscope." Ultramicroscopy 18, 241-252, 1985.

50. Chase, M. W. (1998). NIST - JANAF Thermochemical Tables (Fourth ed.). Journal of Physical and Chemical Reference Data. ISBN 1-56396-831-2.

51. Dobner, S., Sterns, L., Gralf, R. A., and A. M. Squires. “Cyclic Calcination and Recarbonation of Calcined Dolomite.” Ind. Eng. Chem. 16.4 (1977): 479-486.

52. Hughes, R.W., Lu, D., Anthony, E.J., and Y. Wu. “Improved Long-Term Conversion of Limestone-Drived Sorbents for In Situ Capture of CO2 in a Fluidized Bed Combustor.” Ind. Eng. Chem. Res. 43 (2004): 5529-5539.

53. Laursen, K., Duo, W., Grace, J. R., and C. J. Lim. “Cyclic Steam Reactivation of Spent Limestone.” Industrial and Engineering Chemistry Research 43 (2004): 5715-5720.

54. Wolff, E. H. P., Gerritsen, A. W., and P. J. T. Verheijen. “Attrition of an Alumina-Based Sorbent for Regenerative Sulfur Capture from Flue Gas in a Fixed Bed.” Powder Technol 76 (1993): 47.

55. C. Liu and S. Shih. “Kinetics of the Reaction of Iron Blast Furnace Slag/Hydrated Lime Sorbents with SO2 at Low Temperatures: Effects of the Presence of CO2, O2, and NO”Ind. Eng. Chem. Res., 2009, 48, 8335–8340.

56. Kato, Y., N. Yamashita, K. Kobayashi and Y. Yoshizawa; “Kinetic Study of the Hydration of Magnesium Oxide for a Chemical Heat Pump,” Appl. Therm. Eng., 16, 853–862 (1996).

57. Silva, L.F.L.R. Damian, R.B., Lage, P.L.C., “Implementation and analysis of numerical solution of the population balance equations in CFD packages”, Computers & Chemical Engineering, 32- 12 (2008): 2933–2945

58. Clark, Samuel, Dale M. Snider, and James Spenik. "CO2 Adsorption loop experiment with Eulerian–Lagrangian simulation." Powder Technology (2013).

59. Abbasi, E. and Arastoopour, H. “CFD Simulation of CO2 Sorption in a Circulating Fluidized Bed using the deactivation kinetic model”, Proceeding of the 10th International Conference on Circulating Fluidized Beds and Fluidization Technology, CFB 10, Oregon, USA, 2011.

60. Nikolopoulos, A., Nikolopoulos, N., Charitos, A., Grammelis, P., Kakaras, E., Bidwe, A.R, Varela, G., “High-resolution 3-D full-loop simulation of a CFB carbonator cold model”, Chemical Engineering Science,Volume 90,pp. 137-15, (2013)

61. Syamlal, M. O'Brien T. J., "Fluid dynamic simulation of O3decomposition in a bubbling fluidized bed",AIChE JournalVolume 49,Issue 11,pages 2793–2801, (2003).

62. FFGSM, http://mypages.iit.edu/~abbasian/ffgsm.html